JOHANNES KEPLER
UNIVERSITÄT LINZ

Student
**Konstantin Kosenko**

Submission
**Institute of Organic Chemistry**

Supervisor
**Assoc. Univ.-Prof. Dr. Wolfgang Schöfberger**

Co-supervisor
**Assoc. Univ.-Prof. Dr. Ian Teasdale, PhD**

Co-supervisor
**RNDr. Ján Štěrba Ph.D.**

September 2025

# SYNTHESIS AND APPLICATION OF IMIDAZOQUINOLINE TLR7/8 AGONISTS CONJUGATED WITH POLYPHOSPHAZENE POLYMERS

Master's thesis
to obtain the academic degree
Master of Science
in the Master's program
Biological Chemistry

**JOHANNES KEPLER UNIVERSITY OF LINZ**
Altenberger Strasse 69
4040 Linz, Austria
jku.at

Kosenko, K., 2025: Synthesis and application of imidazoquinoline TLR7/8 agonists conjugates with polyphosphazene polymers. Mgr. Thesis, in English, - 190 p., Faculty of Science, University of South Bohemia, České Budějovice, Czech Republic.

**Annotation**

The focus of this thesis was the preparation of a novel imidazoquinoline ligand and its conjugation with biodegradable PGA polyphosphazene. This conjugate has the potential to overcome certain limitations associated with the application of immune response modifiers such as resiquimod. Another part of the thesis is dedicated to studying the mechanistic differences between resiquimod and the novel agonist SA-401. Cell culture and biochemical experiments were performed to prepare samples suitable for MS proteomics, which can theoretically provide a comprehensive overview of these differences. Furthermore, we utilized bioinformatics and molecular dynamics simulations to supplement the analysis and evaluate the differences between these ligands.

**Declaration**

I declare that I am the author of this qualification thesis and that in writing it I have used the sources and literature displayed in the list of used sources only.

I further declare that I have used Perplexity AI generative artificial intelligence tool and Grammarly Proofreader in accordance with academic ethics for the purpose of grammar proofreading.

Linz, 10.08.2025 ……

Konstantin Kosenko

## Acknowledgment

Many people have contributed to this project over its 2.5-year duration. First, I would like to thank my supervisor, Prof. Wolfgang Schöfberger, who provided me with the opportunity to work on this project and consistently offered support and assistance whenever needed. I am also very grateful to other members of the Organic Chemistry Institute, in particular Prof. Mario Waser, Dr. Beate Hager, Christian Rückl, and Ghaffar Pasdar. I am especially thankful to Prof. Matthias Bechmann for his support and assistance with NMR.

I spent a significant amount of my practical work at the Polymer Chemistry Institute, and I would like to thank Prof. Ian Teasdale for his supervision and engagement in this project, as well as Dr. Paul Strasser and Pauline Stadler for their assistance and patient teaching.

Special thanks go to Prof. Markus Himmelsbach and the Analytical Chemistry Institute for his help with HPLC-MS measurements and for his excellent lectures in mass spectrometry.

I would like to thank Dr. Oliver Drews for his active and insightful consulting throughout this project, particularly regarding cell culture and biochemical assays aimed at analyzing samples by MS proteomics.

I also want to thank Prof. Jindřich Chmelař for his support in the biological experiments. I am incredibly grateful to Dr. Radka Lencová for her help and great assistance with cell culture work. Finally, I would like to thank Dr. Eva Výletová and Dr. Anna Kovaříková, as well as the other members of the Department of Medical Biology, for their assistance and support.

I am grateful to Prof. Ján Štěrba and his team from the Laboratory of Applied Biochemistry, particularly Dr. Jarmila Štěrbová, Dr. Hana Tykalová, and Dr. Pavlína Věchtová, for teaching me and assisting me with all the biochemical techniques I have learned throughout this project. Prof. Ján Štěrba has always been ready to help, teach new things, and discuss results. Additionally, I would like to thank Prof. Ján Štěrba and Ms. Jindřiška Trefná for their ongoing support with organizational matters.

I would like to thank Prof. Roman Tůma for his active support, guidance, and assistance in the MD simulation part of this project, as well as for providing all the necessary infrastructure for these calculations.

I am also truly grateful to my awesome family, great friends (especially my man, Tobi, and Angi), and, of course, my love, Masha. On the other hand, I have to admit that Tobi and Masha are part of my family too. Thank you all for your help and support - it is simply invaluable and means so much to me. Without you, this thesis would not have been possible. I love you all! You are the best!

## Abstract

Cancer treatment can be approached in various ways, one of which is based on the concept of immune surveillance. The immune system can recognize and destroy tumor cells, but the tumor microenvironment is often immunosuppressive, allowing tumors to evade immune detection. Reprogramming innate immune cells by targeting pathogen recognition receptors, such as Toll-like receptors (TLRs), offers a promising approach. However, the clinical application of immune response modifiers is frequently limited by their systemic action and associated side effects. In previous studies, we demonstrated that the conventional TLR7/8 agonist resiquimod could be substituted with our drug candidate SA-401 *in vivo*. In this project, we focused on preparing SA-401 conjugates using biodegradable bottlebrush polyphosphazene polymers to enable more selective application in cancer immunotherapy. A secondary aim was to investigate the mechanistic differences between resiquimod and SA- 401. We synthesized a novel polymer and characterized it using NMR, GPC, DLS, and UV-Vis spectroscopy. Subsequently, we developed a conjugation procedure to attach SA-401 to the polymer via a pH-sensitive hydrazone bond. To assess the differences between resiquimod and SA-401 in vitro, we employed cell culture techniques and biochemical assays, supplemented by *in silico* molecular dynamics simulations. Our results indicate that the developed conjugation procedure yields a product with the desired characteristics for biological application.

## Table of Contents

**Acknowledgment** ..... **II**
**Abstract** ..... **III**
**Table of Contents** ..... **IV**
**1 Introduction** ..... **1**
Cancer: From Ancient Theories to Modern Therapies ..... 1
Understanding Cancer: Fundamentals and Hallmarks ..... 1
From Proto-Oncogenes to Oncogenes: Mechanisms of Activation ..... 3
Dysregulation of Growth Factor Signaling in Cancer ..... 4
Tumor Suppressor Genes: Guardians Against Cancer ..... 5
Apoptosis Pathways and Their Dysregulation in Tumorigenesis ..... 7
Bypassing Hayflick's Limit: Telomere Maintenance in Cancer ..... 9
Angiogenesis and the Angiogenic Switch in Cancer ..... 10
From Local Invasion to Colonization: Mechanisms of Metastasis ..... 11
Reprogramming Energy Pathways: Glycolysis in Cancer ..... 12
Immune Surveillance and Evasion in Cancer ..... 13
Innate and Adaptive Immunity: An Overview ..... 14
Pathogen Recognition and Phagocytosis in Innate Immunity ..... 14
Initiation of cellular innate response: inflammation ..... 16
From Pathogen Recognition to NF-κB Activation: TLR Signaling Mechanisms ..... 17
The Dual Role of NF-κB Signaling in Cancer Progression ..... 19
TLR7/8 Signaling Pathways and Their Regulation by IRF5 ..... 20
Cytokines and Chemokines Induced by TLR7/8 ..... 21
The Dual Role of Inflammation in Cancer ..... 23
TLR7/8-Targeted Immunotherapy ..... 24
TLR7/8 Agonists in Clinical Trials ..... 26
Drug Delivery Strategies and the EPR Effect ..... 27
Polymer-Based Drug Delivery ..... 28
Polyphosphazene Polymers for Drug Delivery ..... 29
**2 Aims of the study** ..... **31**
**3 Experimental part: synthesis of TLR7/8 agonist SA-401** ..... **36**
**3.1 Materials and methods** ..... 36
**3.2 Synthesis procedures** ..... 36
3.2.1 Synthesis of S1 and S2 ..... 36
3.2.2 Synthesis of S3 ..... 37
3.2.3 Synthesis of S4 ..... 38

3.2.4 Synthesis of S5 ..... 39
3.2.5 Synthesis of S6 ..... 39
3.2.6 Synthesis of S7 ..... 40
3.2.7 Synthesis of S8 ..... 41
3.2.8 Synthesis of S9 ..... 42
**4 Experimental part: synthesis of the polyphosphazene (PPz) polymer and conjugation with SA-401 ..... 44**
**4.1 Materials and methods** ..... 44
**4.2 Synthesis procedures** ..... 45
4.2.1 Synthesis of tert-butyl (2-(2-(2-aminoethoxy)ethoxy)ethyl)carbamate ..... 45
4.2.2 Synthesis of Boc-protected macrosubstituted PPz (P1) ..... 46
4.2.3 Boc-deprotection of macrosubstituted PPz (P2) ..... 47
4.2.4 Synthesis of Bn-protected PPz-PGA (P3) ..... 48
4.2.5 Bn-deprotection of PPz-PGA ..... 49
4.2.6 Synthesis of Cbz-protected β-Ala-Boc-hydrazide linker ..... 50
4.2.7 Cbz-deprotection of β-Ala-Boc-hydrazide linker ..... 50
4.2.8 Synthesis of β-Ala-Boc-hydrazide linked PPz-PGA ..... 51
**4.3 Conjugation procedure** ..... 52
4.3.1 Boc-deprotection of β-Ala-Boc-hydrazide linked PPz-PGA ..... 52
4.3.2 Conjugation of β-Ala-hydrazide linked PPz-PGA with SA-401 ..... 52
4.3.3 Drug loading quantification ..... 53
**5 Experimental part: *in vitro* cell culture assays ..... 54**
**5.1 Materials and methods** ..... 54
**5.2 Isolation of the bone marrow** ..... 55
**5.3 Differentiation of bone marrow derived macrophages** ..... 56
**5.4 Flow cytometry** ..... 56
**5.5 Cell seeding for the activation with ligands** ..... 57
**5.6 Activation of cells with ligands** ..... 57
**5.7 Cell harvesting and counting** ..... 59
**5.8 Lysis of the cells, measurement of the protein concentration** ..... 60
**5.9 SDS PAGE quality control** ..... 60
**6 Experimental part: *in silico* modeling, MD simulations on TLR7/8, comparison of SA-401 and R848 ..... 61**
**6.1 Identification of residues involved in the interaction** ..... 61
**6.2 Multiple sequence alignment (MSA)** ..... 61
**6.3 Molecular dynamics simulations** ..... 61
**6.4 Overview of the simulated systems** ..... 64

**6.5 Analysis of MD simulation runs** ... 64
**7 Results and discussion** ... **67**
**7.1 Synthesis of SA-401** ... 67
7.1.1 Synthesis of S1 and S2 ... 67
7.1.2 Synthesis of S3 ... 68
7.1.3 Synthesis of S4 ... 68
7.1.4 Synthesis of S5 ... 69
7.1.5 Synthesis of S6 ... 70
7.1.6 Synthesis of S7 ... 71
7.1.7 Synthesis of S8 ... 74
7.1.8 Synthesis of S9 (SA-401) ... 74
**7.2 Synthesis of polyphosphazene polymer** ... 76
7.2.1 Summary of results ... 76
7.2.2 Synthesis of tert-butyl (2-(2-(2-aminoethoxy)ethoxy)ethyl)carbamate ... 76
7.2.3 Synthesis of Boc-protected macrosubstituted polyphosphazene (PPz) (P1) ... 77
7.2.4 Boc-deprotection of macrosubstituted PPz ... 78
7.2.5 Synthesis of Bn-protected PPz-PGA (P3) ... 79
7.2.6 Bn-deprotection of PPz-PGA ... 80
7.2.7 Synthesis of Cbz-protected β-Ala-Boc-hydrazide linker ... 81
7.2.8 Cbz-deprotection of β-Ala-Boc-hydrazide linker ... 81
7.2.9 Synthesis of β-Ala-Boc-hydrazide linked PPz-PGA ... 82
**7.3 Conjugation procedure** ... 82
7.3.1 Boc-deprotection of of β-Ala-Boc-hydrazide linked PPz-PGA ... 82
7.3.2 Conjugation of β-Ala-hydrazide linked PPz-PGA with SA-401 ... 83
7.3.3 Drug loading quantification ... 84
**7.4 Isolation of bone marrow and differentiation of BMMs** ... 85
**7.5 Cell lysis results** ... 86
7.5.1 BCA concentration measurement ... 86
7.5.2 SDS PAGE results ... 88
**7.6 Bioinformatics and MD simulations** ... 90
7.6.1 Amino acid residues involved in receptor-ligand interactions ... 90
7.6.2 Analysis of MD simulation results: RMSD and RMSF graphs ... 92
7.6.3 MM/PBSA and MM/GBSA results ... 95
**8 Conclusion** ... **99**
**9 List of abbreviations** ... **100**
**10 References** ... **102**

**11 Appendix ..... 108**
**Synthesis of SA-401** ..... 108
Characterization of S2 ..... 108
Characterization of S3 ..... 110
Characterization of S4 ..... 113
Characterization of S5 ..... 116
Characterization of S6 ..... 119
Characterization of S7 ..... 122
Characterization of S8 ..... 125
Characterization of S9 ..... 128
HPLC-MS analysis of the synthesis of product S7 ..... 133
**Synthesis of polyphosphazene polymer** ..... 136
Characterization of tert-butyl (2-(2-(2-aminoethoxy)ethoxy)ethyl)carbamate ..... 136
Characterization of Boc-protected macrosubstituted PPz ..... 137
Characterization of Boc-deprotected macrosubstituted PPz ..... 139
Characterization of Bn-protected PPz-PGA ..... 140
Characterization of Bn-deprotected PPz-PGA ..... 142
Characterization of Cbz-protected β-Ala-Boc-hydrazide linker ..... 144
Characterization of Cbz-deprotected β-Ala-Boc hydrazide linker ..... 146
Characterization of β-Ala-Boc-hydrazide-linked PPz-PGA ..... 148
**Conjugation with SA-401** ..... 156
Characterization of Boc-deprotected of β-Ala-Boc-hydrazide linked PPz-PGA ..... 156
Characterization of SA-401-conjugated β-Ala-hydrazide-linked PPz-PGA ..... 158
**Microscopy imaging of bone marrow-derived macrophages (BMMs)** ..... 163
Day 0 ..... 163
Day 3 ..... 164
Day 7 ..... 166
Day 8 ..... 168
Day 9 ..... 170
**MD simulation inputs** ..... 177
Ionizaton of the system (ions.mdp) ..... 177
Energy minimization (em.mdp) ..... 178
NVT equilibration (nvt.mdp) ..... 179
NPT equilibration (npt.mdp) ..... 180
MD production run (md.mdp) ..... 181

# 1 Introduction

## Cancer: From Ancient Theories to Modern Therapies

Cancer is not a novel disease; it has been known to humanity for centuries. It is believed that the first theory of cancer was proposed by Hippocrates approximately 2400 years ago[1]. He hypothesized that an excess of black bile could cause cancer. Much later, in the 19th century, scientists discovered that cancer is a disease of the cell. In 1863, Rudolf Virchow observed tumor-infiltrating leukocytes and suggested a connection between inflammation and cancer[2]. He also noted that cancer cells often resemble the tissue cells from which they originated[3]. At the beginning of the 20th century, cancer research began to develop rapidly[1].

Despite significant advances in the field, treating cancer remains a challenging task. In 2022, cancer was responsible for approximately 9.7 million deaths worldwide. Around 20 million new cases were diagnosed that same year[4]. Over the last century, various methods for treating cancer have been developed. Conventional approaches include surgery, radiotherapy, and chemotherapy. These remain the most widely used methods today[5]. Nevertheless, none of these methods is flawless. Surgery and radiotherapy effectively treat solid primary tumors, but are largely ineffective against metastases[5]. Chemotherapy, on the other hand, often causes severe side effects and may even result in therapy-induced secondary tumors[6].

Recently, promising approaches such as immunotherapy, hormone therapy, targeted therapy, and stem-cell therapy have emerged[7]. In 1891, William B. Coley, considered the father of immunotherapy, first tried to use immunotherapy to treat cancer[8]. He injected streptococcal bacteria into inoperable tumors and observed shrinkage. Today, immunotherapy is viewed as an innovative approach that offers many advantages over traditional treatments[9]. The fundamental concept of immunotherapy is to modulate the immune system, enabling it to target and destroy cancer cells[10].

Although immunotherapy is conceptually straightforward, applying it effectively is complex. This requires understanding how immune response mechanisms work and how they can be manipulated. Before discussing these aspects, it is essential to introduce the fundamental nature of cancer and the concept of cancer hallmarks, which are common characteristics shared by most malignancies.

## Understanding Cancer: Fundamentals and Hallmarks

Cancer is generally described as a disease in which the body's own cells become highly proliferative, invasive, and capable of spreading to other parts of the body through

metastasis[11]. However, defining cancer precisely is challenging because of its highly heterogeneous nature. Cancer exhibits phenotypic, genetic, epigenetic, and metabolic variations across different types[12]. Additionally, tumors are not solely composed of cancerous cells. They also include tumor-associated stromal cells, immune cells, and other cell types, collectively forming the tumor microenvironment (TME)[13].

Despite this vast variability, most cancers share certain defining features that enable cells to become cancerous. These characteristics, known as the hallmarks of cancer, were first proposed by D. Hanahan and R.A. Weinberg in 2000, who highlighted six main features of cancer cells[14]. Later, in 2011, they identified two new emerging hallmarks and two enabling characteristics[13]. Currently, eight main hallmarks are recognized (two of them were described earlier in 2011 and were added to the main set in 2022)[15]. Furthermore, in 2022, four emerging hallmarks and enabling characteristics were proposed by D. Hanahan[15]. Notably, cancer cells are characterized by the following capabilities[15]:

1) Sustaining proliferative signaling
2) Evading growth suppressors
3) Activating invasion and metastasis
4) Enabling replicative immortality
5) Inducing angiogenesis
6) Resisting cell death
7) Reprogramming cellular metabolism (added in 2022)
8) Avoiding immune destruction (added in 2022)

Two recognized enabling characteristics:

1) Genome instability and mutation
2) Tumor-promoting inflammation

Four new emerging hallmarks and enabling characteristics[15]:

1) Unlocking phenotypic plasticity
2) Non-mutational epigenetic reprogramming
3) Polymorphic microbiomes
4) Senescent cells

These hallmarks provide a framework for understanding how normal cells transform into malignant cells. They also serve as a foundation for developing targeted therapies. The following chapters will examine each hallmark in detail.


**Figure 1:** Eight cancer hallmarks adapted from Hanahan[15]

**From Proto-Oncogenes to Oncogenes: Mechanisms of Activation**

As mentioned previously, cancer cells arise when normal cells acquire characteristics like uncontrolled proliferation, invasiveness, and other malignant traits. These changes occur due to genetic and epigenetic modifications that dysregulate cancer-critical genes. Such genes can be broadly categorized into two groups[16]. The first group includes proto-oncogenes, which can promote tumor formation when overexpressed or hyperactivated. Typically, these genes encode growth factors, components of cellular signaling pathways, or transcription factors[17]. The second group consists of tumor-suppressor genes, which contribute to tumorigenesis when they undergo loss-of-function mutations.

Proto-oncogenes can be transformed into oncogenes through several mechanisms. One mechanism is gene amplification, which increases the number of copies of a specific gene. For example, amplification of the *HER2* gene is observed in approximately 20-25% of breast cancers and is linked to a poor prognosis[18]. Point mutations can also convert a proto-oncogene into an oncogene. Notably, *Ras* oncogenes – implicated in approximately 30% of all tumors – can be activated by this mechanism[19]. Furthermore, mutations in regulatory regions may work together with mutations in coding regions[20]. Finally, chromosomal translocations can deregulate gene expression by placing a gene under the control of a different promoter. This is one of the mechanisms that activates the *Myc* oncogene[21]. In addition, chromosomal translocations can fuse two genes together, producing hybrid oncoproteins. A classic example is the BCR-ABL fusion protein formed by a translocation between chromosomes 9 and 22.

This rearrangement results in the Philadelphia chromosome, a hallmark of chronic myeloid leukemia[22].

After discussing the various mechanisms by which proto-oncogenes can become oncogenes, these transformations can be broadly categorized into two types. The first type comprises structural mutations leading to protein hyperactivation. For instance, point mutations in the coding region or gene fusion due to chromosomal translocations. The second type involves deregulating mutations leading to the overexpression of oncoproteins. It can be achieved through point mutations in the regulatory region, gene amplification, or chromosomal translocations that bring a specific gene under the control of a strong promoter or enhancer[20].

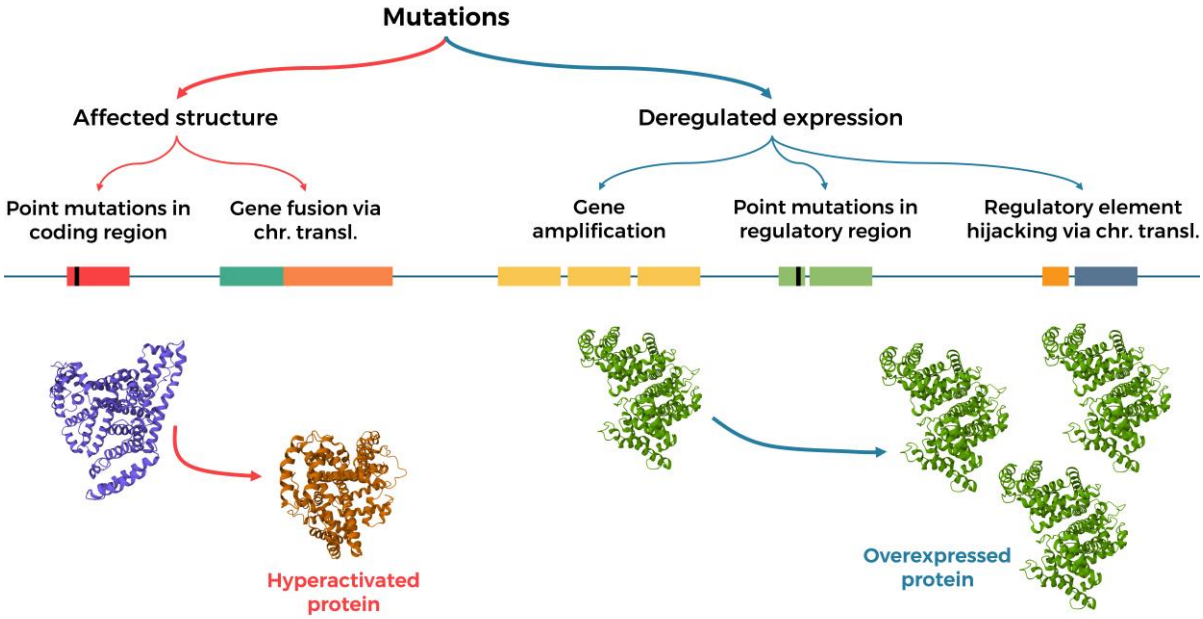


**Figure 2:** Possible mechanisms underlying oncogene activation

### Dysregulation of Growth Factor Signaling in Cancer

It is known that the cell growth-and-division cycle is tightly regulated by various growth factors (GFs), which help limit the number of cells and maintain tissue architecture. In contrast, cancer cells can bypass these regulatory mechanisms in multiple ways. For example, they can produce GF ligands themselves, promoting proliferation through autocrine signaling[23]. They can also stimulate stromal cells within TME to produce specific growth factors. In addition, cancer cells may increase the expression of GF receptors or acquire mutations that lead to their continuous activation.

Many receptors that recognize growth factors and cytokines belong to the receptor tyrosine kinase (RTK) family, which includes epidermal growth factor receptors (EGFRs) and fibroblast growth factor receptors (FGFRs) among others[24]. In most cancer types, one or more downstream components of growth factor signaling pathways are mutated. For example, pancreatic cancer frequently involves mutations in the RAS pathway, breast cancer is often driven by HER2 signaling, while melanomas commonly exhibit alterations in B-RAF signaling[23]. Interestingly, direct mutations affecting growth factors themselves (e.g., enhanced expression level) are rather rare[23].

Previously, we discussed oncogene activation, which can lead to either protein overexpression or hyperactivation. The same principles apply to growth factor receptors such as EGFRs. These receptors can be amplified and overexpressed (e.g., HER2 in breast cancer) or become constitutively active[25]. For example, truncated EGFR that lacks the extracellular ligand-binding domain is permanently active without ligand stimulation. Similar mechanisms also explain the dysregulation of other components in growth factor signaling pathways.

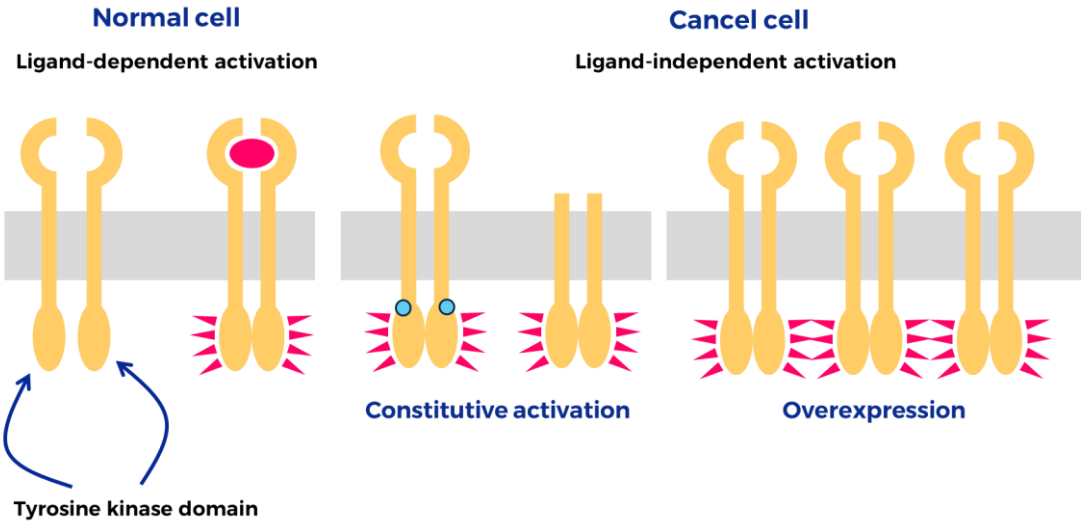


**Figure 3**: Mechanisms of growth factor receptor dysregulation in cancer, including overexpression and constitutive activation. Adapted from *The Biology of Cancer*[20]

### Tumor Suppressor Genes: Guardians Against Cancer

In addition to sustaining proliferative signaling, cancer cells must bypass mechanisms that inhibit this signaling and restrict proliferation. The genes that control these inhibitory mechanisms are called tumor-suppressor genes (TSGs), and two of the most prominent examples are *TP53* and *Rb1*[13]. Loss-of-function mutations in these genes are common in cancer. In fact, *TP53* is the most frequently mutated gene in cancer[26].

The first TSG identified was the retinoblastoma gene *Rb1*[27]. The Rb protein is a key regulator of cell cycle progression, capable of arresting cells at the G1-S transition. Rb can also interact with various chromatin regulators and transcription factors. In turn, Rb activity is regulated by reversible phosphorylation by cyclin-dependent kinases (CDKs)[28]. Phosphorylation of Rb releases E2F transcription factors and promotes cell cycle progression[29]. While extensive research has uncovered many functions of the Rb protein, its precise role in cancer prevention remains unclear[30]. Interestingly, evidence suggests that loss of Rb function may trigger apoptosis. This implies that *Rb* has specific pro-survival properties, and its loss during early carcinogenesis may be disadvantageous.

Importantly, both *Rb1* alleles must be inactivated for loss-of-function. While the probability of two independent mutations is extremely low, this can occur through mitotic recombination[20]. This event, which happens at a frequency of $10^{-5}$ to $10^{-4}$ (compared to a mutational inactivation frequency of $10^{-6}$), results in loss of heterozygosity (LOH). Mitotic recombination is therefore one mechanism by which a cell can lose both wild-type *Rb1* alleles.

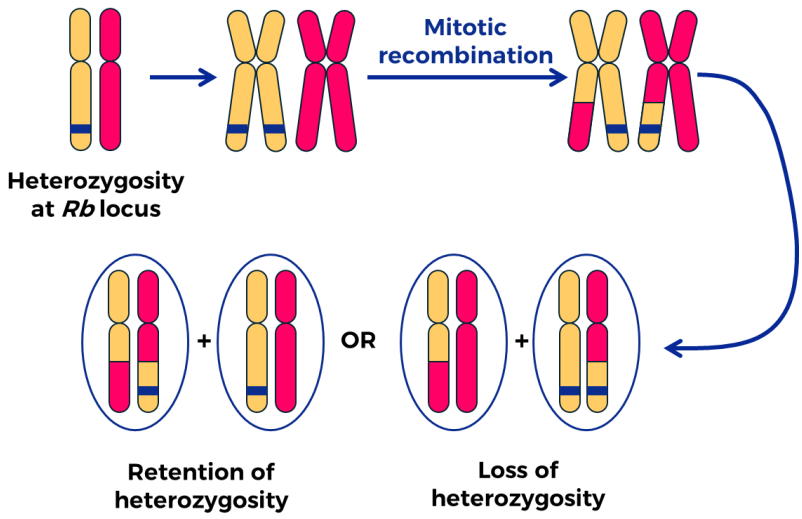


**Figure 4**: Mitotic recombination leading to loss of heterozygosity (redrawn from *The Biology of Cancer*[20])

Another important tumor suppressor, p53, is deleted or mutated in half of all cancer cases[31]. Even when p53 remains intact, other components of its signaling pathway are often mutated. As a transcription factor, p53 regulates crucial cellular processes, including cell cycle control and apoptosis. Additionally, it is responsible for the genomic stability and is widely treated as "guardian of the genome"[26]. Interestingly, mutated p53 is not only non-functional in terms of tumor suppression, but can also gain oncogenic properties. Evidence suggests that the mutated p53 protein can promote tumor cell survival by regulating cell stress response mechanisms[32].

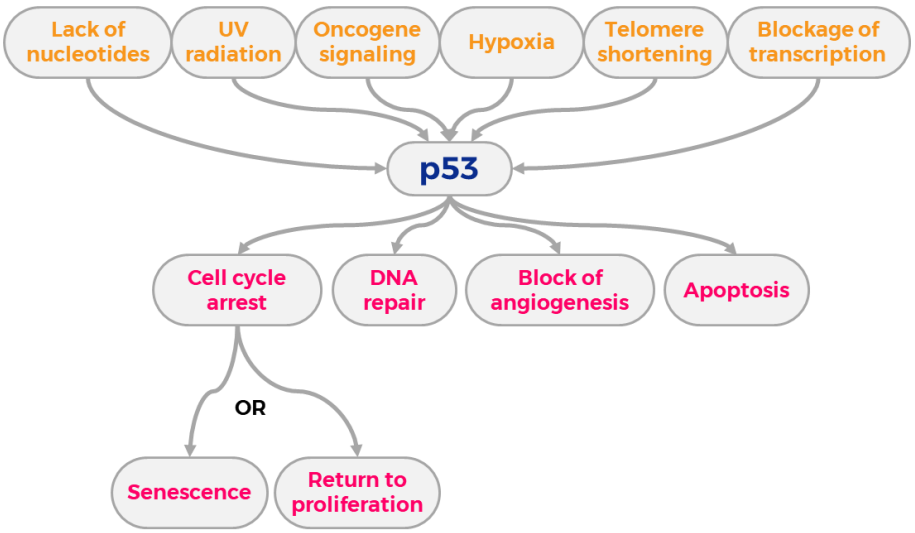


**Figure 5**: Activation of p53 by stress signals triggers downstream responses (redrawn from *The Biology of Cancer*[20])

**Apoptosis Pathways and Their Dysregulation in Tumorigenesis**

In 1988, researchers discovered that the BCL-2 protein, previously isolated from patients with B-cell lymphoma, has a fundamental prosurvival function and plays a central role in the concept of programmed cell death[33]. Today, *BCL-2* is recognized as an anti-apoptotic oncogene, and anti-apoptotic members of the Bcl-2 family are frequently upregulated in cancer, enabling resistance to cell death – one of the central hallmarks of cancer [13]. Over the last 30 years, research has shown that evasion of apoptosis is closely linked to tumor progression, carcinogenesis, and resistance to anticancer therapies[34].

Apoptosis is a type of programmed cell death essential for eliminating unwanted cells. Beyond its homeostatic function, apoptosis is now recognized as a key mechanism of the immune response, providing defense against certain pathogens[35]. During apoptosis, cells condense and shrink, often fragmenting into apoptotic bodies. Eventually, phagocytes such as macrophages engulf them. In contrast to necrosis, another form of cell death in which cells burst and release their contents into the extracellular space, apoptosis doesn't trigger an inflammatory response[16].

The mechanism underlying apoptosis is driven by cysteine proteases. These proteases cleave proteins at specific aspartic acid residues – these enzymes are collectively known as caspases. Caspases are divided into initiator caspases (e.g., caspases 8, 9, and 10) and effector caspases (e.g., caspases 3, 6, and 7). Upon activation by initiator caspases, effector caspases cleave thousands of proteins, thus mediating apoptosis[36]. Important targets of caspases are nuclear lamins, components of the cytoskeleton (e.g., actin), the inhibitor of caspase-activated DNase (ICAD), and various regulatory proteins[37].

There are two main pathways leading to the activation of initiator caspases: the intrinsic and extrinsic. The intrinsic pathway is initiated by mitochondrial outer membrane permeabilization (MOMP), which releases cytochrome *c* to the cytoplasm. After this step, the apoptosome forms and activates caspase-9, which in turn activates effector caspase-3. Proteins of the Bcl-2 family play a central role in regulating cytochrome *c* release. This family contains pro-apoptotic members (e.g., BAK1, BAX, BIM, BID, and PUMA) as well as anti-apoptotic proteins (e.g., BCL-2, BCL-$X_L$, and MCL1)[36].

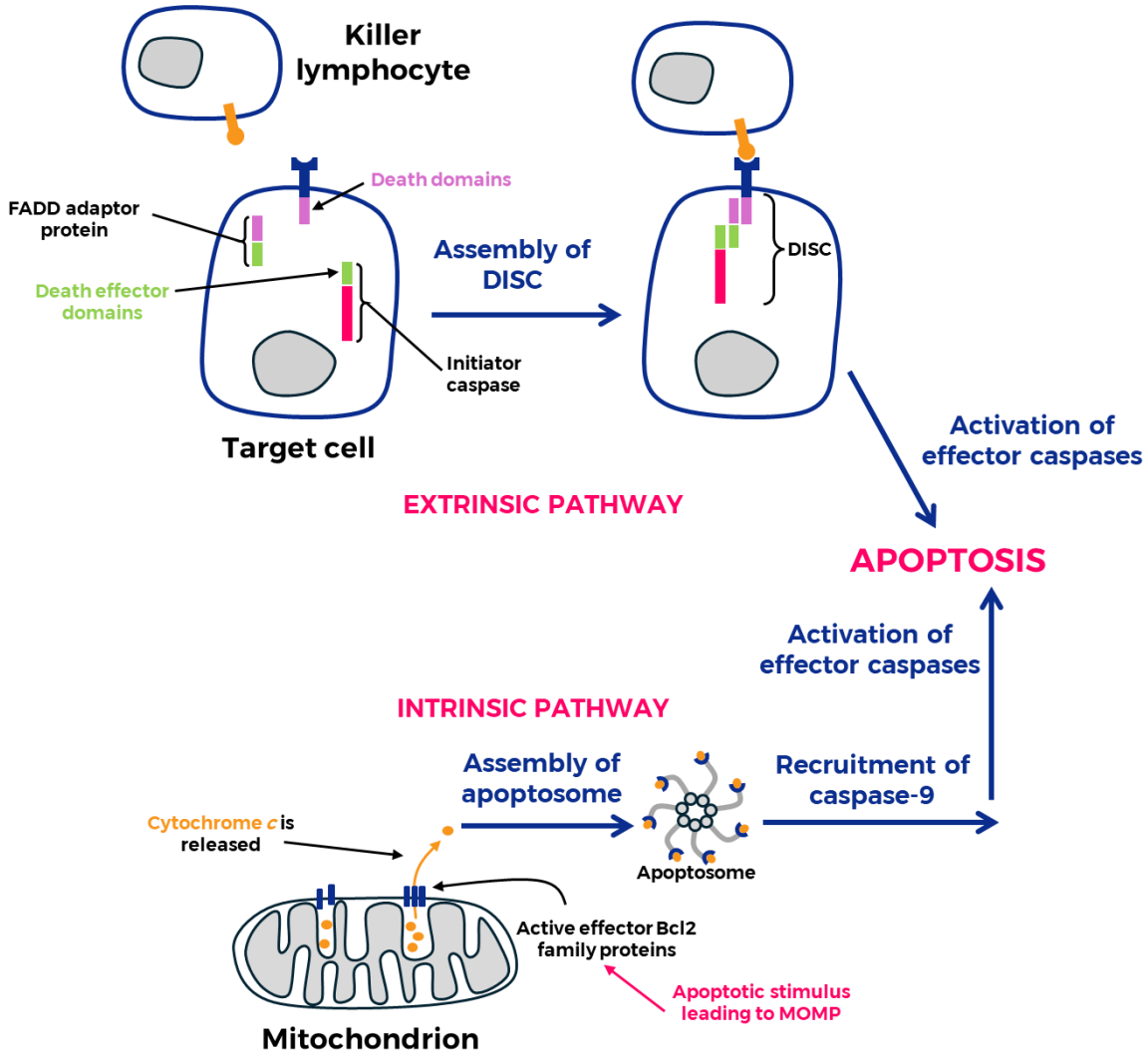


**Figure 6**: Overview of the extrinsic and intrinsic apoptosis pathways. Adapted from *Molecular Biology of the Cell*[16]

Pro-apoptotic members are further divided into two groups: BH3-only proteins and effector Bcl family proteins. BAX and BAK are two main effector proteins, and at least one is required to induce apoptosis. Once activated, they oligomerize in the outer mitochondrial membrane, facilitating MOMP. The function of BH3-only proteins is to promote the oligomerization of effector proteins and induce apoptosis in response to apoptotic stimuli. One

such stimulus is DNA damage, which leads to the accumulation of p53, subsequently facilitating the expression of BH3-only proteins such as Noxa and Puma. On the other hand, anti-apoptotic members bind to and inhibit pro-apoptotic members, preventing inappropriate apoptotic responses[16].

Another important mechanism leading to apoptosis is the extrinsic pathway. It relies on death receptors belonging to the tumor necrosis factor (TNF) receptor family. Two important members of this family are the TNF receptor itself and the Fas death receptor. The Fas receptor is activated by Fas ligand on the surface of cytotoxic T lymphocytes (CTLs), triggering the activation of the intracellular death domains of the death receptors. These death domains then activate initiator caspases via adaptor proteins such as FADD, forming the death-inducing signaling complex (DISC). DISC is responsible for the activation of effector caspases 3, -6, and -7, ultimately mediating apoptosis. Similar to the intrinsic pathway, various mechanisms exist to prevent apoptosis. One example is the FLIP protein, which resembles an initiator caspase but lacks protease activity, thereby inhibiting apoptosis.

Given the critical role of these pathways in cell survival, apoptosis has become an important target for a novel class of therapeutics. BH3 mimetics are one example. These compounds bind to anti-apoptotic members of the intrinsic pathway and promote apoptosis. Various molecules that inhibit proteins, such as BCL-2 and BCL-$X_L$, have demonstrated therapeutic potential in cancer therapy[36]. Another class of therapeutics targets and stimulates death receptors, thus utilizing the extrinsic pathway of apoptosis. These approaches can be combined with other therapeutic strategies, further enhancing their potential efficacy.

**Bypassing Hayflick's Limit: Telomere Maintenance in Cancer**

In 1965, Leonard Hayflick observed and postulated that somatic cells can undergo only a certain number of cell divisions[38]. This limitation is now known as Hayflick's limit. Normally, cells eventually enter senescence (a non-proliferative state) and do not divide anymore. This phenomenon is explained by the progressive shortening of telomeres during each division cycle. In contrast, cancer cells can bypass this limit, thereby gaining replicative immortality. It has been demonstrated that cancer cells – along with embryonic stem cells and other self-renewing cells, such as activated T cells – can maintain telomere length and avoid this shortening[39].

Cancer can sustain telomere length through two main mechanisms. The first one (observed in approximately 85% of cancer cases) involves the activation of telomerase, an enzyme that elongates telomeres after each replication cycle. The second mechanism,

alternative lengthening of telomers, is telomerase-independent and relies on homologous recombination.

Telomeres protect chromosome ends and are crucial for unlimited cell proliferation; their progressive shortening in non-immortalized cells leads to end-to-end fusions and genomic instability, triggering crisis[13]. Telomere shortening can induce cellular senescence via multiple pathways. One proposed mechanism involves the activation of p53 induced by DNA damage. In turn, p53 induces the transcription of cyclin-dependent kinase inhibitor (CKI) p21[40], which inhibits cyclin-dependent kinase 4 (CDK4) and CDK6[41]. When CDK4 and CDK6 are inactive, they cannot phosphorylate the Rb protein, and thus, transcription factor E2F is kept sequestered by Rb.

Notably, the role of CDK4/6 in cancer progression is widely recognized. These kinases are often hyperactivated in cancers, making them promising therapeutic targets[42]. Thus, by maintaining telomere length, cancer cells gain replicative immortality, a key hallmark of cancer.

**Angiogenesis and the Angiogenic Switch in Cancer**

Similar to normal tissues, tumors require nutrients and oxygen to survive. They also require the removal of waste products. This is facilitated by angiogenesis – the formation of new blood vessels. Normal tissues only undergo transient angiogenesis during processes like wound healing. In contrast, tumor progression activates an angiogenic switch, leading to continuous sprouting of new vessels to support tumor growth[13]. Notably, angiogenesis is often triggered early in invasive cancer development, even during microscopic premalignant phases such as dysplasias and in situ carcinomas. This early activation of the angiogenic switch highlights its role as a key hallmark of cancer[43]

Angiogenesis is a complex process regulated by multiple factors that can either promote or inhibit it[44]. Currently, there are six molecular mechanisms of tumor angiogenesis. While all six mechanisms contribute to cancer vascularization, sprouting angiogenesis is generally described as the most predominant and well-characterized mechanism in most tumors[45]. This mechanism relies on several interconnecting signaling pathways, with vascular endothelial growth factor (VEGF) and its corresponding receptor VEGFR being crucial players. Other important factors include fibroblast growth factor (FGF), delta-like ligand 4, and platelet-derived growth factor (PDGF).

Notably, the VEGF protein family includes several members: VEGF-A, VEGF- B, VEGF-C, VEGF-D, VEGF-E, VEGF-F, and placental growth factor (PIGF)[46]. VEGF-A is

the most characterized among them, and at least sixteen isoforms of this protein have been identified[47]. VEGF is produced by various cell types, including endothelial cells, tumor cells, activated platelets, lymphocytes, macrophages, and others[44]. It binds to the corresponding receptors (e.g., VEGFR2) on the endothelial cells and facilitates proliferation, survival, vasodilation, and migration of these cells towards tumors[48].

It is known that due to its rapid growth, the tumor environment is often hypoxic in the interior. The larger the distance from the blood vessels, the smaller the amount of oxygen that can diffuse in[49]. In addition, tumor remodeling might lead to the deformation of blood vessels. This can further enhance the hypoxic environment inside many tumors. Under hypoxic conditions, tumors produce hypoxia-inducible factor 1 (HIF-1) – an important transcription factor. Once produced, it drives the expression of different genes which encode angiogenic factors (e.g., VEGF), glycolytic enzymes, glucose transporters, and invasion factors[50].

**From Local Invasion to Colonization: Mechanisms of Metastasis**

Another important phenomenon commonly observed in cancer is metastasis. It is the process by which cancer cells spread from the primary tumor to other parts of the body through the blood or lymphatic system, forming secondary tumors. This significantly complicates cancer treatment and, in fact, metastasis is responsible for 90% of cancer-related deaths[51]. Many studies have shown that metastasis is a complex phenomenon requiring multiple steps that comprise the invasion-metastatic cascade[52].

First, cancer cells need to invade local tissues and vessels. After that, cancer cells travel through the bloodstream into the distant organs, where they eventually escape from blood vessels. This phase is referred to as dissemination. Disseminated tumor cells (DTCs) that survive till this point may enter the dormancy phase. It is characterized by halted cell expansion, which can be achieved, for instance, via the growth arrest of DTCs[53]. At this stage, micrometastases are not detectable using current clinical methods. Then, after some time – sometimes decades, cancer cells start to colonize in the distant organ, forming macrometastases[54].

A crucial process facilitating metastasis is epithelial-mesenchymal transition (EMT). The EMT is naturally involved in various biological processes, including embryonic development, stem cell differentiation, tissue repair, and cancer development. During the process, immotile epithelial cells acquire invasive and migratory traits[55]. In particular, loss of cell polarity, reorganization of the cytoskeleton, altered expression of adhesion molecules, and disruption of intercellular junctions are commonly observed[56]. Notably, the process is

reversible, and these cells can regain traits of the epithelial cells[57]. This phenomenon of mesenchymal-epithelial transition (MET) plays a crucial role in the colonization process when cancer cells have reached distant sites. Interestingly, in many cases, cells undergo only partial EMT and exhibit mixed traits of both epithelial and mesenchymal phenotypes[58].

EMT is regulated by various microRNAs (miRNAs) and transcription factors (TFs) such as Snail, Slug, Zeb, and Twist[59]. These TFs generally activate transcription of mesenchymal genes and also inhibit the expression of epithelial genes. For example, Snail1 blocks the expression of adhesion molecules such as E-cadherin and recruits histone modifiers that epigenetically silence these genes. On the other hand, Snail1 facilitates the expression of mesenchymal markers such as fibronectin and vitronectin[60]. Notably, expression of E-cadherin is also suppressed by other TFs such as Slug, Zeb1, and Twist1[56]. Evidence suggests that these transcription factors are important regulators of metastasis.

**Reprogramming Energy Pathways: Glycolysis in Cancer**

Around 100 years ago, in 1923, Otto Warburg observed that tumors often upregulate glucose consumption and produce more lactate than normal cells[61]. He discovered that cancer cells largely rely on glycolysis, even under aerobic conditions. In contrast, normal cells depend on glycolysis only under anaerobic conditions, while under aerobic conditions, oxidative phosphorylation is the primary source of energy[62]. Now this effect is known as the Warburg effect or aerobic glycolysis. Today, this characteristic is recognized as a separate cancer hallmark[63].

Building on this hallmark, it is notable that glycolysis is significantly less efficient, providing only two ATP molecules from one glucose molecule. In contrast, oxidation of glucose via oxidative phosphorylation may result in up to 38 ATP molecules. However, cancer cells maintain the levels of ATP similar to normal cells[64]. This metabolic adaptation is driven by key regulators such as c-Myc and HIF-1α, which promote glycolysis and the Warburg effect[65]. They upregulate and increase expression of glucose transporters and various glycolytic enzymes such as hexokinase, phosphoglycerate mutase, pyruvate kinase, and lactate dehydrogenase[66]. Conversely, tumor suppressor p53 can inhibit glycolysis by reducing the expression of glucose transporters GLUT1 and GLUT4, thus limiting glucose uptake. Thus, loss of p53 can promote anaerobic glycolysis and cancer progression[67].

Expanding on these regulatory changes, mutations in both mitochondrial DNA (mtDNA) and nuclear DNA that affect mitochondrial energy metabolism are frequently observed in cancer, contributing to alterations in cellular metabolism[68]. On the other hand,

the shift towards glycolysis can be reversible. Inhibiting glycolysis alone is not sufficient to kill tumor cells. In this situation, they upregulate oxidative phosphorylation and use it as a main energy production metabolism[69]. Some types of cancer can upregulate the influx of amino acids, such as glutamine, into the tricarboxylic acid cycle (TCA) to support oxidative phosphorylation.

Considering the inefficiency of glycolysis for energy production, it may seem counterintuitive for cancer cells to favor this pathway. It is also known that even enhanced glycolysis is not capable of supporting cancer progression if oxidative phosphorylation is dysfunctional[70]. However, glycolysis supplies cancer cells with metabolic intermediates needed for the biosynthesis of macromolecules (such as nucleotides, lipids, proteins). This is especially critical for rapidly proliferating cells[71]. Another reason would be a hypoxic environment in the tumor interior, and thus, glycolysis would be advantageous in these conditions. Finally, deregulation of oxidative phosphorylation decreases the production of toxic reactive oxygen species (ROS)[72], which could result in apoptosis[73].

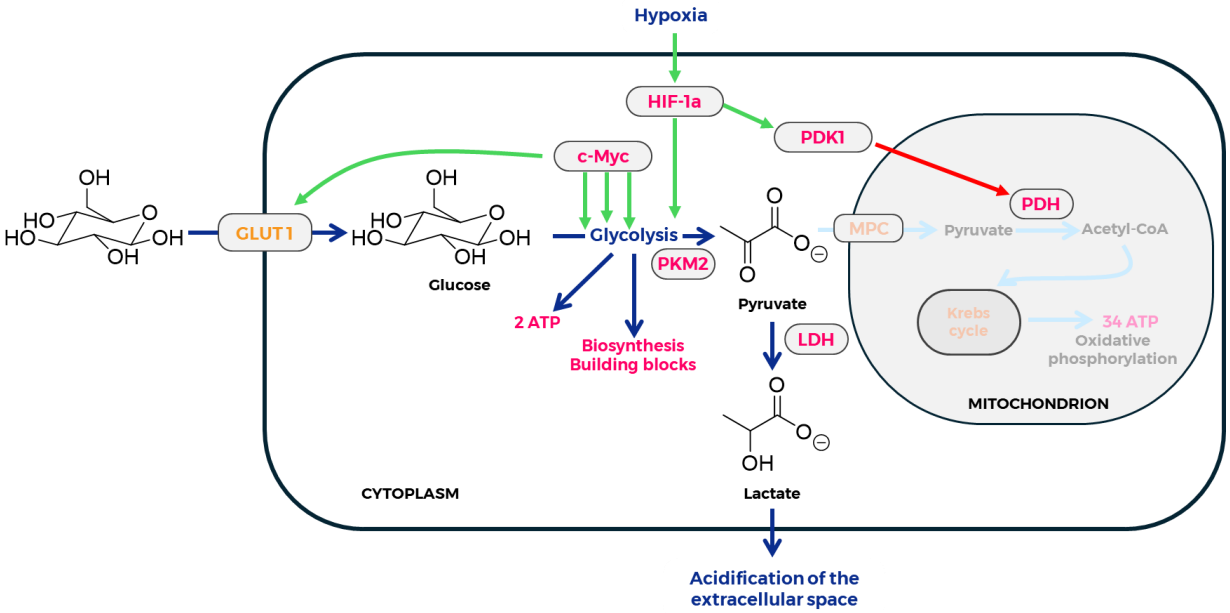


**Figure 7**: Molecular mechanisms of the Warburg effect: HIF-1α and c-Myc increase glucose transporter (GLUT1) and upregulate glycolytic enzymes (PKM2, LDH), boosting glycolysis and lactate production. PDK1 inhibits PDH, limiting mitochondrial oxidation. ATP is primarily generated via glycolysis, while the intermediates feed into biosynthetic pathways.

### Immune Surveillance and Evasion in Cancer

Throughout evolution, humans developed a highly sophisticated immune system. This system constantly monitors and eliminates pathogens, a process known as immune surveillance[74]. It must also distinguish between harmful pathogens and the body's own cells and tissues, a principle known as self-tolerance. In fact, the immune system can recognize and destroy most

incipient cancer cells; however, some cancer cells can evade immune surveillance[13]. Research has identified various mechanisms that enable cancer cells to escape detection and destruction by the immune system[75]. Recently, this ability has been recognized as one of the primary hallmarks of cancer[15].

This thesis examines the interactions between cancer cells and immune cells, the mechanisms by which cancer cells evade immune detection, and strategies to activate immunity against cancer. To provide a foundation for these discussions, it is necessary to outline the general functions of the immune system first. The following chapters will address the basics of the immune system and its dual role in cancer progression and suppression.

**Innate and Adaptive Immunity: An Overview**

All organisms, including bacteria, must protect themselves against harmful invaders known as pathogens. Different organisms use various strategies to achieve this protection. In vertebrates, such as humans, the immune system operates through two primary types of immunity: innate and adaptive[16]. Innate immunity acts as a rapid, general defense mechanism. It protects against a wide range of pathogens and involves nearly all cell types. In contrast, adaptive immunity is more specific and relies on B and T lymphocytes. It typically requires some time to initiate its response, but it is more targeted and efficient in eliminating pathogens. Notably, adaptive immunity can be further categorized into cell-mediated immunity and humoral immunity[76].

Innate immunity is the evolutionarily older and more general form of immune response. Typically, it provides the first line of defense and consists of multiple components[77]. All multicellular organisms except vertebrates – invertebrates, plants, and fungi – rely exclusively on the innate type of immunity[78]. It includes physical barriers, such as epithelial layers of the skin and mucosa, chemical barriers such as antimicrobial proteins and peptides (e.g., lysozyme, S100 proteins, defensins, interferons, surfactant proteins SP-A and SP-D), and cellular responses like inflammation and phagocytosis[76]. Notably, in most cases, innate immunity is required to establish a more sophisticated adaptive immune response[79]. Interestingly, recent evidence suggests that innate immunity can exhibit a form of immunologic memory, enhancing its response to repeated exposures, although this is traditionally associated with adaptive immunity[80].

**Pathogen Recognition and Phagocytosis in Innate Immunity**

Most pathogens that cross epithelial layers are rapidly detected by sentinel immune cells, such as macrophages and dendritic cells. These cells are equipped with various pathogen

recognition receptors (PRRs), which sense different molecules derived from bacteria, viruses, fungi, and parasites[81]. These specific molecules are referred to as pathogen-associated molecular patterns (PAMPs).

Currently, five main classes of PRRs have been identified: Toll-like receptors (TLRs), nucleotide-binding domain (NOD)-like receptors (NLRs), C-type-lectin receptors (CLRs), RIG-I-like receptors (RLRs), and AIM-2-like receptors (ALRs)[82]. In addition, sentinel cells can sense molecules that are released upon tissue damage – so-called damage-associated molecular patterns (DAMPs), which are host molecules that signal injury or stress[83]. Notably, tissue-resident macrophages constantly survey their environment and phagocytose pathogens when they are encountered[84].

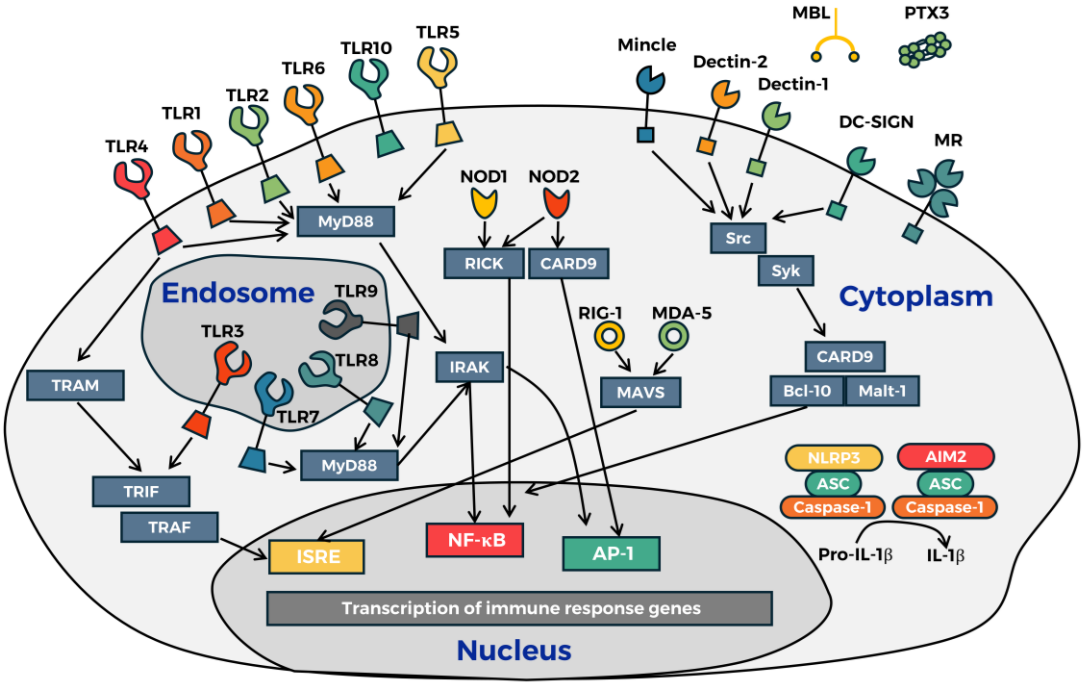


**Figure 8**: Overview of different PRRs; adapted from M. Jaeger et al[82].

Macrophages, monocytes, neutrophils, and dendritic cells are classified as professional phagocytes due to their high efficiency in phagocytosis. These cells are distinct from non-professional phagocytes, such as epithelial cells, endothelial cells, and fibroblasts, which have more limited roles in phagocytosis[85]. Macrophages and other professional phagocytes rely generally on two types of receptors: phagocytic receptors and PRRs mediating inflammatory signal transduction and enhancing phagocytosis[86]. The first group includes non-opsonic receptors, which recognize pathogens directly, such as CLRs and scavenger receptors. Additionally, there are opsonic receptors that recognize host-derived molecules bound to

pathogens. Examples of these include complement receptors (CRs) and Fc receptors, which recognize antibodies (Abs) bound to pathogens.

The second group of receptors, including TLRs and NLRs, does not directly participate in phagocytosis but cooperates with phagocytic receptors to activate inflammation. This cooperation enhances the overall immune response by triggering cytokine production and coordinating microbial killing and antigen presentation[87].

**Initiation of cellular innate response: inflammation**

Inflammation is a biological response triggered by pathogens during infection (via PAMPs), tissue damage (via DAMPs), or toxic compounds. The three main pathways mediating inflammation are NF-kB, MAPK, and JAK-STAT[88]. When PRRs on sentinel cells are activated, they trigger signaling cascades that lead to the expression of pro-inflammatory cytokines such as tumor necrosis factor (TNF), interleukin-1β (IL-1β), and IL-6, along with various chemokines including IL-8[89]. In addition, PRR signaling often leads to the expression of cyclooxygenase-2 (COX-2)[90], which catalyzes the production of prostaglandins, and inducible nitric oxide synthase (iNOS), required for generating nitric oxide (NO), which is used to kill phagocytosed pathogens[91].

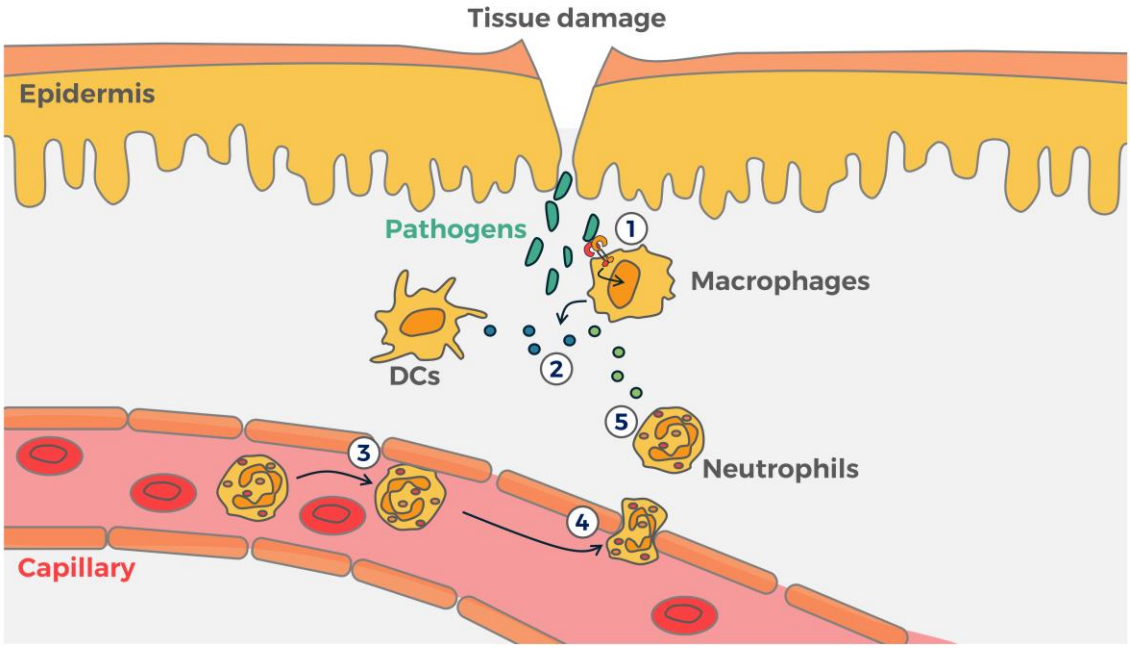


**Figure 9**: Overview of the inflammatory response (adapted from *Kuby Immunology* [76]). The process includes: (1) activation of pattern recognition receptors (PRRs); (2) production of cytokines and vasoactive molecules; (3) activation of endothelial cells in blood capillaries, initiating the leukocyte recruitment cascade; (4) transmigration of leukocytes across the endothelium; and (5) chemotaxis-driven migration of leukocytes (e.g., neutrophils) toward the site of inflammation.

Chemokines function as chemoattractants released by sentinel cells along with vasoactive compounds to recruit other leukocytes, such as neutrophils, to the site of inflammation. This leukocyte recruitment requires endothelial activation, which occurs through two distinct mechanisms. Type I involves a rapid response mediated by various factors such as histamine (released by activated mast cells) via GPCR signaling[92]. That leads to vasodilation and vasopermeability. In contrast, type II activation relies on cytokine receptor signaling (such as TNFR and IL-1R1). This signaling upregulates adhesion molecules, facilitating leukocyte retention and extravasation[93].

Various adhesion molecules participate in the leukocyte recruitment cascade. P-selectin and E-selectin expressed on endothelial cells mediate the first step of the cascade – leukocyte capture and rolling. They do this by binding to P-selectin glycoprotein ligand-1 (PSGL-1) and E-selectin ligand-1 (ESL-1) on leukocytes[94]. This interaction initiates transient adhesion, slowing leukocytes to facilitate subsequent activation steps. The process continues with slow rolling, arrest, and crawling driven by integrins (such as LFA-1, VLA-4, and MAC-1) on leukocytes. Integrins bind immunoglobulin superfamily proteins (e.g., ICAM-1, ICAM-2, and VCAM-1) on the endothelial cells, enabling firm adhesion. Finally, activated leukocytes migrate through the endothelium using transcellular or paracellular diapedesis and start moving towards the inflammatory site guided by chemotactic signals[95].

**From Pathogen Recognition to NF-κB Activation: TLR Signaling Mechanisms**

As previously noted, the innate immune system recognizes pathogens using pattern recognition receptors (PRRs) like Toll-like receptors (TLRs). Humans encode at least ten TLRs, which are found either on the cell surface (e.g., TLR1, TLR2) or inside the cell within compartments called endosomes (e.g., TLR7/8, TLR9)[96]. Each TLR detects specific molecules via its leucine-rich repeat (LRR) domain, which relays signals to the Toll/interleukin-1 receptor (TIR) domain, initiating immune responses[97].

TLR signaling occurs through two primary pathways: MyD88-dependent and MyD88-independent (the latter specific to TLR3 and TLR4 and excluded here). In the MyD88-dependent pathway, TLR activation triggers MyD88 recruitment to the TIR domain[98]. Discovered in 1990 but linked to immunity later, MyD88 contains three domains: a death domain (DD), an intermediate domain (INT), and a TIR domain[99]. The MyD88 TIR domain binds TLRs, while its DD interacts with IL-1R-associated kinase 4 (IRAK4). IRAK4 phosphorylates IRAK1, a step critical for downstream signaling, as evidenced by IRAK4-deficient mice failing to produce cytokines upon TLR stimulation[100].

MyD88 belongs to the TIR domain adaptor family. Some TLRs (TLR5, TLR7, and TLR9) rely solely on MyD88. Others (TLR1, TLR2, and TLR6) require TIRAP as a co-adaptor. TLR3 uniquely uses TRIF and TRAM (MyD88-independent pathway), whereas TLR4 employs both pathways: MyD88/TIRAP for early responses and TRAM/TRIF for delayed interferon production[98].

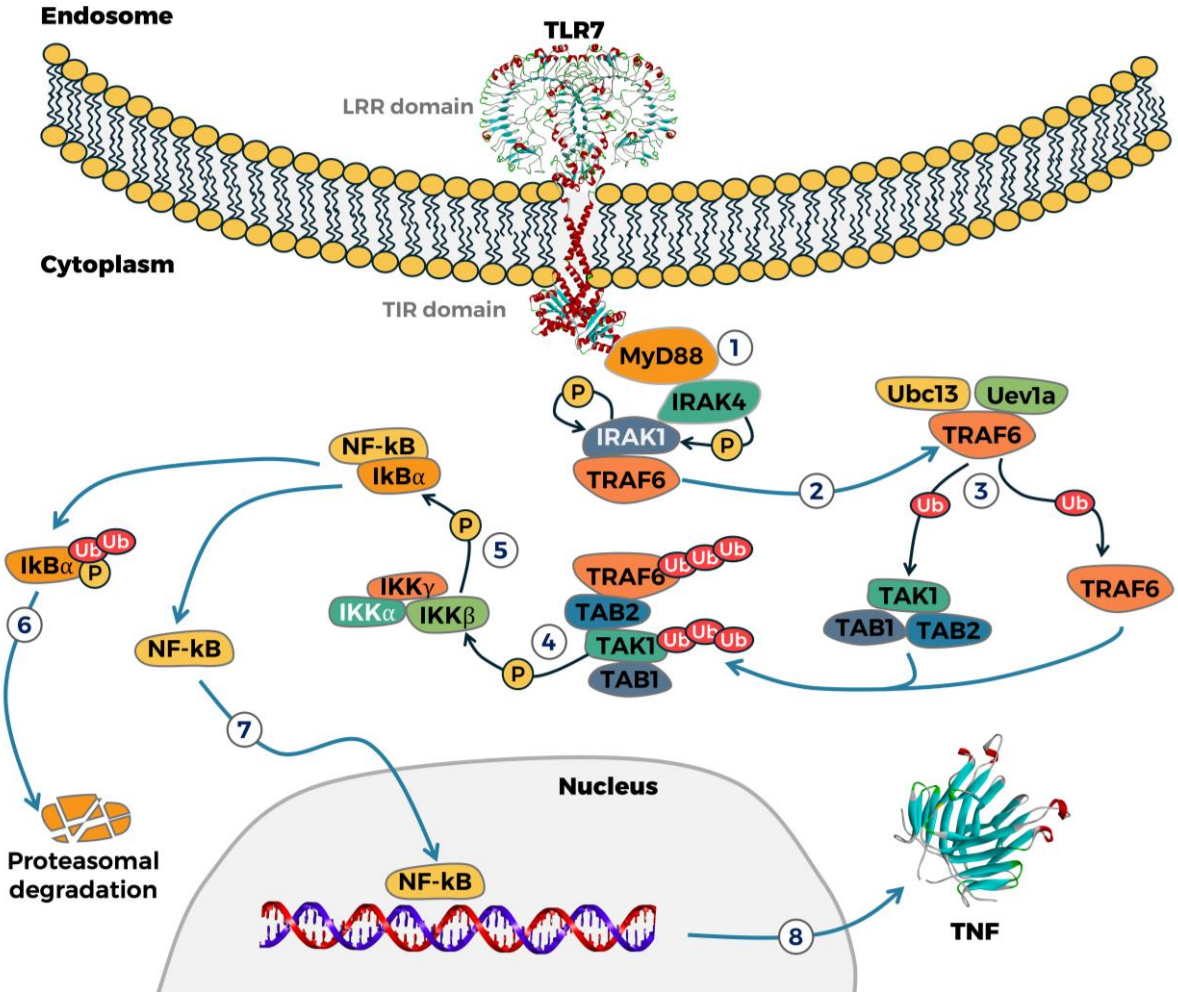


**Figure 10**: The MyD88-dependent Toll-like receptor (TLR) signaling pathway begins when a ligand, such as a pathogen-associated molecular pattern, binds to the leucine-rich repeat domain of the TLR. This interaction leads to the recruitment **(1)** of myeloid differentiation primary response protein 88 (MyD88), which interacts with the TLR through its Toll/IL-1R (TIR) domain. Subsequently, interleukin-1 receptor-associated kinase 4 (IRAK4) is recruited and phosphorylates IRAK1. Phosphorylated IRAK1 then recruits the E3 ubiquitin ligase tumor necrosis factor (TNF) receptor-associated factor 6 (TRAF6), after which IRAK1 and TRAF6 dissociate **(2)** from the receptor. TRAF6, with the assistance of the ubiquitin-conjugating enzymes Uev1a and Ubc13 (acting as E2 enzymes), undergoes polyubiquitination **(3)**. Ubiquitinated TRAF6 recruits transforming growth factor-β (TGF-β)-activated kinase 1 (TAK1) along with TAK1-binding proteins (TABs) to form the TAK1-TAB complex. TAK1 then phosphorylates **(4)** the inhibitor of nuclear factor kappa B (IκB) kinase (IKK) complex, which in turn phosphorylates IκBα **(5)**. Phosphorylated IκBα is subsequently ubiquitinated and degraded by the proteasome **(6)**, releasing nuclear factor κB (NF-κB) to translocate to the nucleus **(7)** and activate the transcription of target genes such as TNF **(8)**.

Activated IRAK1 undergoes autophosphorylation, which enables the recruitment of TNF receptor-associated factor 6 (TRAF6)[98]. After recruitment, TRAF6 – an E3 ubiquitin ligase – dissociates from IRAK1 and forms a complex with ubiquitin-conjugating enzyme 13 (Ubc13) and ubiquitin-conjugating enzyme E2 variant 1 (Uev1a)[101]. This complex catalyzes K63-linked ubiquitination of substrates such as IRAK1, TRAF6 itself, and TGF-β-activated kinase 1 (TAK1). In contrast to K48-linked ubiquitination, which targets proteins for proteasomal degradation, K63-linked ubiquitin chains serve as scaffolds to recruit proteins containing ubiquitin-binding domains[101].

Polyubiquitinated TAK1 binds TAK1-binding protein 1 (TAB1) and TAB2 or TAB3[102], with TAB2 serving as a bridge between TRAF6 and TAK1[103]. This complex activates the IκB kinase (IKK), which consists of catalytic subunits (IKKα and IKKβ) and regulatory subunit IKKγ (also known as nuclear factor-κB (NF-κB) essential modulator (NEMO))[98]. The TAK1-TABs complex phosphorylates IKKβ, activating IKK. Notably, TAK1's role varies by cell type: its deficiency may impair responses in some cells or paradoxically enhance cytokine production in others[104].

Once activated, IKK phosphorylates the inhibitor of the NF- κB (IκBα), which tightly binds to NF-κB and inhibits its activity. Subsequent ubiquitination and phosphorylation of IκBα trigger its proteasomal degradation, releasing NF-κB[105]. Activated through this process, NF-κB translocates to the nucleus, where it induces transcription of target genes. The specific pattern of expressed genes depends on the mechanism of NF-κB activation[105].

**The Dual Role of NF-κB Signaling in Cancer Progression**

The mechanism described above corresponds to the classical (canonical) NF-κB signaling pathway, which can be activated by Toll-like receptors (TLRs), certain pro-inflammatory cytokines, and other types of pattern recognition receptors (PRRs). In contrast, the alternative NF-κB pathway is triggered by signaling molecules such as lymphotoxin and CD40 ligand and typically results in a slower cellular response. Upon activation, the classical NF-κB pathway induces the expression of pro-inflammatory cytokines (e.g., TNF, IL-1β, and IL-6), chemokines (e.g., IL-8, CCL-2, CCL-5, and CXCL2), anti-apoptotic proteins, growth factors, pro-inflammatory enzymes (e.g., COX-2 and iNOS), and adhesion molecules (e.g., VCAM1 and ICAM1)[106].

Building upon these activation mechanisms, it is essential to note that more than 500 cancer-critical genes are regulated by NF-κB signaling [107]. Thus, NF-κB can contribute to cancer initiation, promotion, and metastasis. For example, it may activate the enzyme

activation-induced cytidine deaminase (AID), which causes cytosine-to-thymine mutations that can initiate cancer[108]. Another example is NF-κB-induced upregulation of Snail, Slug, and Twist1, transcription factors closely associated with EMT and metastasis[109]. Furthermore, NF-κB upregulates matrix metalloproteinase 9 (MMP9), thereby further increasing cancer invasiveness[110]. Some phytochemicals (e.g., flavonoids) have demonstrated anti-cancer effects, which can be explained by their inhibition of NF-κB signaling and anti-inflammatory properties[111].

However, in addition to its role in promoting cancer, NF-κB is an activator of the innate immune response, which is required for tumor elimination. Therefore, it can be either tumor-suppressing or tumor-promoting, and its role in cancer is rather complex[112].

**TLR7/8 Signaling Pathways and Their Regulation by IRF5**

In this project, we focus on TLR7 and TLR8. Both receptors are located in the endosomes and recognize single-stranded RNA (ssRNA) as their natural ligand, playing a key role in the antiviral response. They both signal through the MyD88-dependent pathway; however, their signaling differs significantly and is also influenced by the specific cell type. The two main signaling pathways involved are the NF-κB pathway and the interferon regulatory factor (IRF) pathway[113]. Evidence suggests that TLR7 activation initially induces IFN-β and NF-κB-regulated inflammatory cytokines, followed by IFN-α production, whereas TLR8 activation triggers a stronger early response characterized by the production of IFN-β and a broad range of inflammatory cytokines, leading to sustained inflammation despite declining IFN-β levels[113].

IRFs are a family of transcription factors that coordinate the expression of type I interferons and certain chemokines such as IP-10[114]. IRF3 and IRF7 are activated by various viruses as well as by ligands of TLR3 and TLR4. In contrast, activation of TLR7 and TLR8 by the agonist resiquimod results in the activation of IRF5 and IRF7, but not IRF3. Silencing IRF5 significantly reduces interferon production, suggesting that IRF5 is a central mediator of TLR7/8 signaling. Interestingly, IRF5 functions differently from IRF7 and IRF3: while IRF3 and IRF7 are primarily responsible for the antiviral response and type I interferon production, IRF5 mainly modulates the production of pro-inflammatory cytokines such as TNF, IL-6, and IL-12[115].

For activation, IRF5 typically undergoes post-translational modifications – such as phosphorylation or ubiquitination - that promote homodimerization and nuclear translocation. Upon TLR activation by their respective ligands, IRF5 interacts with TRAF6 and MyD88 to

form a signaling complex[116]. Phosphorylation of the C-terminal region of IRF5 by IKK-β is considered a crucial step for its activation and transcriptional activity[117]. Beyond pro-inflammatory cytokines, IRF5 also regulates the expression of chemokines like CXCL10 and CCL5, as well as co-stimulatory molecules including CD40 and CD86[115].

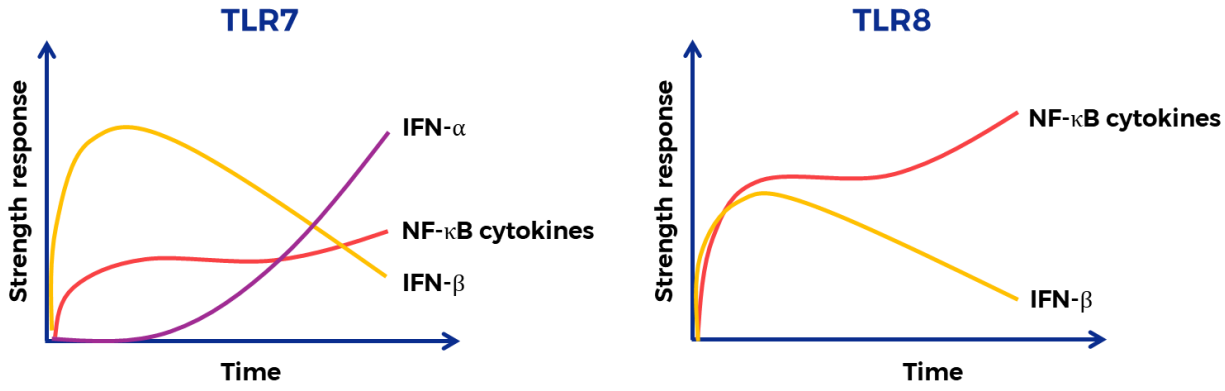


**Figure 11**: Difference in cytokine expression profile between TLR7 and TLR8. Redrawn from Bender et al.[113]

### Cytokines and Chemokines Induced by TLR7/8

TLR7/8 signaling primarily involves the transcription factors NF-κB and IRFs, resulting in the production of multiple cytokines, chemokines, interferons, and interferon-stimulated genes. This chapter summarizes the most important and relevant genes upregulated by TLR7/8 ligands.

**IL-1α** acts through the IL-1 receptor (IL-1R) to induce inflammatory responses. IL-1R is expressed by many cell types, including T cells, monocytes, macrophages, and dendritic cells[118], and its activation induces the production of pro-inflammatory mediators such as COX-2, TNF, and IL-6, which further stimulate the production of IL-1α and IL-1β, thereby amplifying the inflammatory signal. IL-1α is constitutively expressed by various hematopoietic and non-hematopoietic cells and functions as an alarmin in sterile inflammation[119]. The IL-1α precursor is biologically active.

**IL-1β** is mainly expressed by macrophages, dendritic cells, and monocytes as a precursor that requires activation by caspase-1 via the inflammasome. Like IL-1α, it binds to IL-1R and exhibits similar biological activity. IL-1β is an important mediator of inflammation; it is responsible for inducing fever, thereby facilitating lymphocyte functions. It also induces acute phase proteins and mediates B and T cell proliferation. Furthermore, IL-1β stimulates the production of pro-inflammatory cytokines and chemokines such as IL-8 and MCP-1. Additionally, it promotes the generation of reactive oxygen species (ROS) and nitric oxide (NO)[120].

**IL-6** is produced mainly by B and T cells but also by other cell types, including fibroblasts, keratinocytes, and dendritic cells. It binds to the IL-6 receptor (IL-6R), which is primarily expressed on immune cells and hepatocytes. Upon production, IL-6 acts on the liver to trigger the synthesis of acute-phase proteins such as C-reactive protein (CRP) and fibrinogen. It also increases the production of megakaryocytes in the bone marrow. Moreover, IL-6 is an important pyrogenic cytokine and controls the expression of macrophage colony-stimulating factor. It serves as a growth factor for B cells and induces the production of IL-4, which is responsible for Th2 polarization[121].

**TNF** is a multifunctional cytokine that plays an important role in cell proliferation, survival, differentiation, and death. It is synthesized as a membrane-bound precursor (pro-TNF), which is then released by the TNF-converting enzyme. TNF may have both anti-cancer and pro-cancer properties. It is expressed primarily by macrophages but also by T and B cells, mast cells, and dendritic cells. Its action is transmitted via TNF receptor 1 (TNFR1). Activation of TNFR1, depending on the adaptor proteins involved, leads to the activation of NF-κB, MAPKs, or cell death pathways[122].

**IL-10** is mainly expressed by T cells, dendritic cells, monocytes, and macrophages. In macrophages and dendritic cells, its expression is regulated by type I interferons and TLR signaling. IL-10 has strong immunosuppressive properties on macrophages, monocytes, and dendritic cells, inhibiting the production of pro-inflammatory cytokines and chemokines. Furthermore, it downregulates the expression of MHC class II molecules and co-stimulatory molecules, including CD80. On the other hand, IL-10 has immune-stimulatory effects on B cells and mast cells and promotes the proliferation of NK cells[123].

**IL-18** is a proinflammatory cytokine produced by monocytes, macrophages, keratinocytes, and mesenchymal cells. It stimulates both innate and adaptive immunity. IL-18 is produced as an inactive precursor that is activated by caspase-1. Upon binding to receptors on T cells and NK cells, it induces IFN-γ production via STAT4. Furthermore, IL-18 signaling results in the activation of NF-κB. The overall effect of IL-18 depends on its environment; for example, increased IFN-γ production requires the co-presence of IL-12. IL-18 also enhances the cytotoxic activities of CD8+ T cells and NK cells[124].

**Chemokines** comprise a large family of cytokines that function via G-protein-coupled receptors and stimulate the attraction of different immune cell types. Upon TLR7/8 activation, various chemokines are upregulated, including CXCL1 and IL-8, which are very potent neutrophil attractants; CCL2, which attracts monocytes and memory T cells; CCL3, a strong

chemoattractant for monocytes and lymphocytes; CCL4, which attracts NK cells, T cells, and monocytes; and CCL5, a very potent attractant for T cells and eosinophils[125].

**Interferons** can also be upregulated upon TLR7/8 activation. In particular, type I interferons, including IFN-β are rapidly expressed within one hour, while some types of IFN- α are released to a lesser extent or more slowly compared to IFN-β. This induction depends on IRF7, as mentioned earlier. Type I interferons bind to the receptor IFNAR, which is associated with the tyrosine kinases JAK1 and TYK2. Activation of these kinases leads to phosphorylation of STAT1 and STAT2, which form a complex with IRF9 that binds to interferon-stimulated response elements (ISREs), activating the transcription of interferon-related genes[126]. The IFNAR receptor is expressed by various cell types, but monocytes and B cells show the highest expression levels[127]. Through JAK/STAT signaling pathways, type I interferons induce the expression of 200 to 500 different genes (depending on cell type, interferon dose, and treatment duration). Collectively, these are called interferon-stimulated genes (ISGs). Three classical examples of ISGs are MX1, OAS, and PKR[128].

**The Dual Role of Inflammation in Cancer**

The relationship between inflammation and cancer is complex and context-dependent. In 1863, Rudolf Virchow proposed that chronic inflammation can cause cancer, and it is now estimated that up to 25% of cancer cases are linked to chronic inflammation[129]. As described above, NF-κB is involved in the regulation of many cancer-related genes. In addition, other inflammatory pathways, such as MAPK, JAK-STAT, and PI3K-AKT, may also contribute to cancer development and progression[107]. Interestingly, while certain infections are strongly associated with cancer (e.g., Helicobacter pylori or hepatitis C virus), chronic inflammation does not always lead to cancer. Furthermore, therapies such as surgery, chemotherapy, and radiotherapy can cause tissue injury and necrotic cell death, leading to inflammation that may eventually facilitate resistance to therapy[106].

There are two main types of inflammation: chronic and acute. Acute inflammation serves as an important first line of defense, recruiting inflammatory cells such as macrophages, neutrophils, and dendritic cells, and ultimately helping to establish an adaptive immune response. Both innate and adaptive immune responses can inhibit cancer initiation and progression by eliminating nascent tumor cells-a process known as immune surveillance.

However, if acute inflammation is not resolved, it can progress to chronic inflammation, which is a well-established risk factor for cancer development and progression. Chronic, unresolved inflammation creates an immunosuppressive tumor microenvironment (TME),

fostering conditions that support tumor growth, immune evasion, and resistance to therapy[107]. The TME is often infiltrated by immunosuppressive cells, such as regulatory T cells, myeloid-derived suppressor cells, and tumor-associated macrophages (mainly M2-polarized), all of which suppress effective anti-tumor immune responses[130].

In summary, while acute inflammation and immune surveillance can protect against cancer, chronic inflammation promotes an immunosuppressive microenvironment that facilitates tumor progression and resistance to therapy.

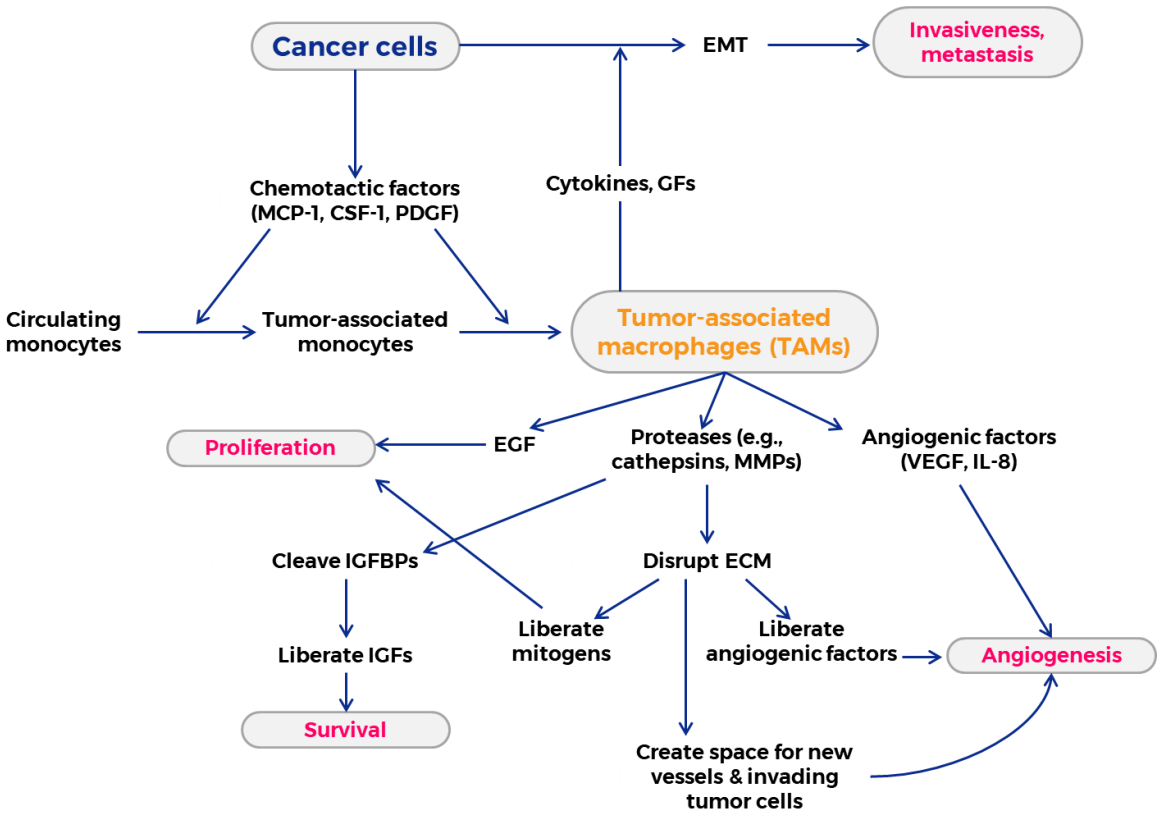


**Figure 12**: Tumor-associated macrophages (TAMs) are recruited by cancer cell–derived chemotactic factors and, in turn, promote tumor progression through the secretion of growth factors, proteases, and angiogenic factors.

### TLR7/8-Targeted Immunotherapy

As mentioned, TLR agonists can induce an inflammatory response that may be beneficial under certain conditions and exhibit anti-cancer effects. Broadly, this class of drugs is referred to as immune response modifiers. One such drug, imiquimod – TLR7 agonist – is FDA-approved for the treatment of superficial basal cell carcinoma, where it is applied as a 5% cream[131]. Furthermore, although surgery is the most common treatment for melanoma, topical 5% imiquimod cream has been successfully used in some cases where surgery was not feasible or failed[131].

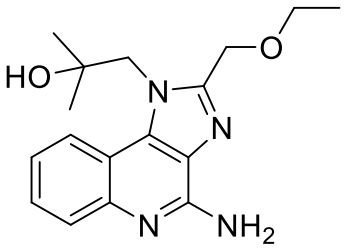


Resiquimod

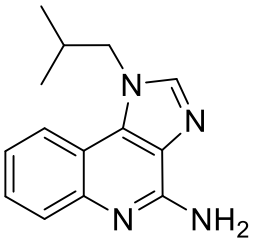


Imiquimod

The immune-activating properties of imiquimod have been demonstrated both *in vivo* and *in vitro*. In particular, its antitumor effects are linked to the recruitment of pDCs, which release type I interferons. Specifically, IFN-α exerts multiple antitumor actions, such as upregulating MHC class I Ags and increasing the expression of adhesion molecules like ICAM-1[132]. In addition, imiquimod induces the expression of other proinflammatory cytokines, including TNF, IL-6, and IL-8, as well as certain chemokines such as CCL2 and CCL3[133].

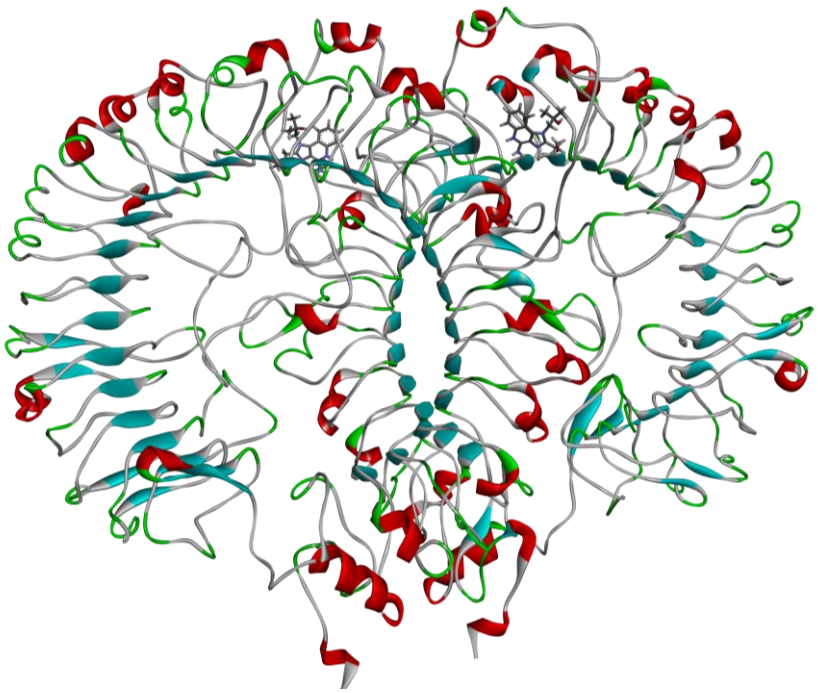

**Figure 13**: Ectodomain of TLR7 shown with the docked ligand R848. Image generated with *Discovery Studio 2024*

Resiquimod is another immune response modifier that activates both TLR7 and TLR8. It shares similar anticancer effects with imiquimod and can activate both pDCs and mDCs, which, upon activation, produce various proinflammatory cytokines. Moreover, resiquimod upregulates costimulatory molecules such as CD80, CD86, and CD40 as well as MHC class II molecules on the surface of DCs, which are essential for the activation of adaptive immunity[134]. It has also been shown to induce polarization from Th2 to Th1 phenotype[135].

Furthermore, resiquimod stimulates IL-12 production from monocytes and dendritic cells, a cytokine that bridges innate and adaptive immunity. Overall, resiquimod is approximately 100 times more effective than imiquimod in inducing cytokine production[136].

As previously mentioned, imiquimod is a more selective activator of TLR7, while resiquimod activates both TLR7 and TLR8. This difference results in significantly different biological effects. Stimulation of TLR7 with imiquimod upregulates the production of IFN-α and chemokines, including CXCL10 and CXCL11. On the other hand, stimulation of TLR8 with resiquimod induces NF-κB signaling and the production of corresponding cytokines such as TNF, IL-1, IL-6, IL-12, and macrophage inflammatory protein (MIP-1).

Moreover, resiquimod can be synergistically combined with other TLR ligands such as poly I:C (a TLR3 ligand). This combination effectively induces M1 polarization of macrophages within TME and has been shown to be successful in a lung cancer model[137]. Resiquimod has also been successfully combined with chemotherapeutics like Taxol, which activates TLR4. Interestingly, the combination of LPS (a potent activator of TLR4) with Taxol can accelerate tumor growth[138]. Another promising combination was demonstrated by Caisova et al., who applied resiquimod together with poly I:C and lipoteichoic acid (LTA, a TLR2 ligand), observing a synergistic antitumor effect in pancreatic adenocarcinoma mouse model in vivo[139].

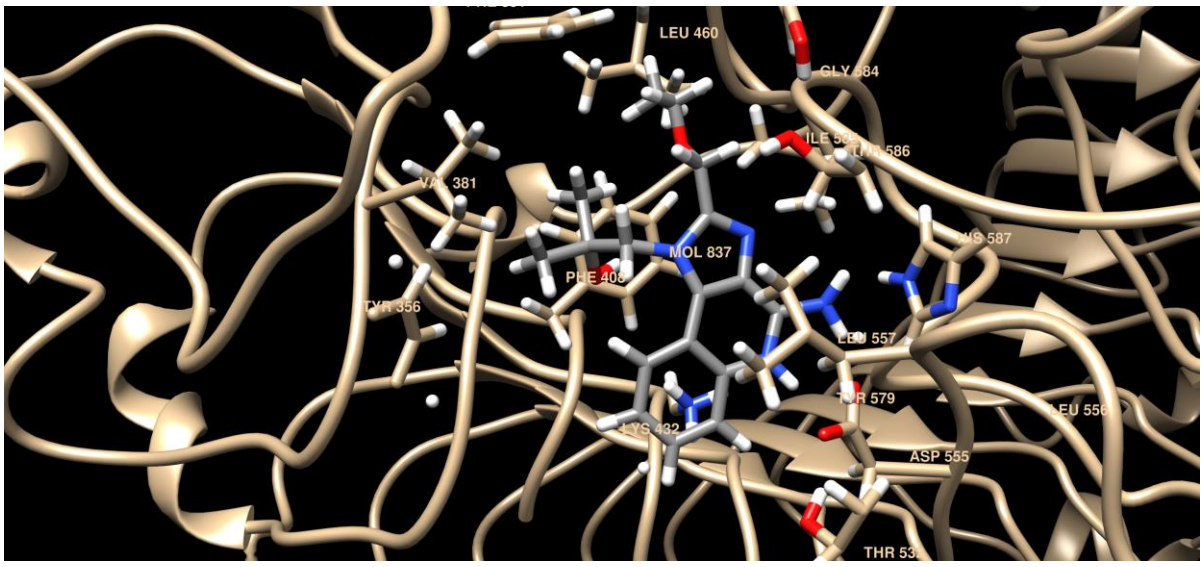


**Figure 14**: R848 bound in the ligand-binding pocket of TLR7, with key interacting residues highlighted. Image generated with *Chimera 1.19*

### TLR7/8 Agonists in Clinical Trials

Despite the pronounced anti-cancer effects of TLR7/8 agonists, only imiquimod is currently FDA-approved for local topical application, available as a 5% cream[140]. Resiquimod has been

tested in phase II dose-ranging clinical trials as a topical gel at concentrations of 0.01%, 0.03%, 0.06%, and 0.1% to treat actinic keratosis – skin lesions that may progress to skin cancer[141]. The therapeutic efficacy did not depend on concentration; however, higher concentrations were associated with increased incidence of adverse effects. Specifically, 13% and 12% of patients treated with 0.06% and 0.1% resiquimod, respectively, experienced side effects such as influenza-like symptoms. A similar trend was observed with local skin reactions.

Resiquimod was also evaluated in phase II clinical studies administered orally at doses of 0.01 mg/kg and 0.02 mg/kg for the treatment of hepatitis C virus infection[142]. The 0.01 mg/kg dose was generally well tolerated, whereas many patients receiving 0.02 mg/kg experienced side effects, including fever, shivering, and headache. These results suggest that although enhanced side effects compared to imiquimod may contribute to therapeutic benefit, they also pose challenges, indicating that the application method and dosing regimen must be carefully optimized.

**Drug Delivery Strategies and the EPR Effect**

As mentioned earlier, the application of many drugs - including imiquimod and resiquimod – is limited by their systemic side effects, which represent a significant bottleneck in cancer therapy. Immune response modifiers such as resiquimod broadly activate the immune system but lack tumor specificity. Consequently, local administration methods such as topical or intratumoral delivery are preferred to minimize systemic toxicity. However, these approaches are inefficient for targeting secondary tumors and small metastases. Therefore, advanced drug delivery systems can be employed to selectively deliver drugs to tumors, thereby reducing systemic side effects while improving pharmacokinetic properties, such as solubility, bioavailability, and half-life[143].

Today, various strategies are available that enable more selective drug delivery to tumors. Among these, encapsulation of drugs into nanoparticles has gained particular importance and relevance. Nanoparticles (also called nano-sized drugs), including liposomes, micelles, and some polymeric materials, serve as drug carriers. Some liposome-based drugs, such as liposomal doxorubicin, have been approved by the FDA[143].

The selectivity of nano-sized drugs is linked to the enhanced permeability and retention (EPR) effect[144]. Unlike normal tissues, tumor vasculature is more permeable due to the presence of large pores formed by incomplete endothelial lining. Furthermore, the extent of pericyte coverage on vessels is reduced in tumor vasculature. This allows nanoparticles to preferentially escape the bloodstream in tumors, leading to the accumulation of the active

pharmaceutical ingredient (API). In addition, drug retention inside the tumor is increased due to poor lymphatic drainage[145].

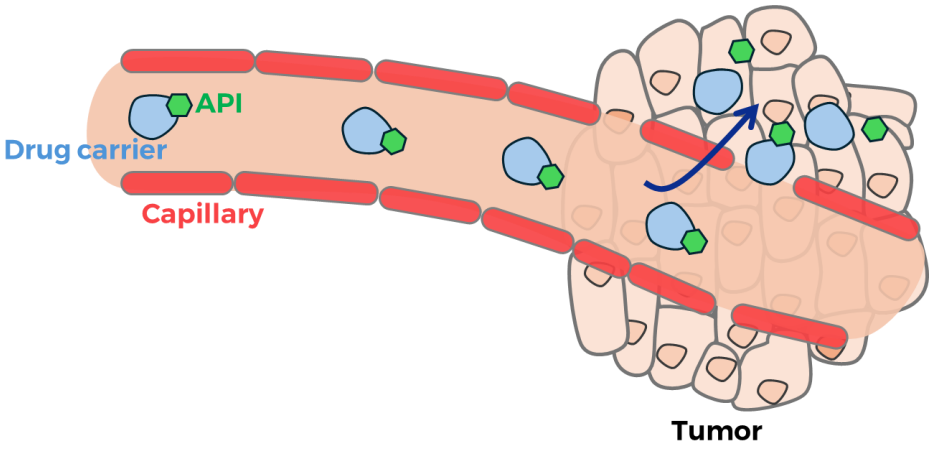


**Figure 15**: Illustration of the EPR effect and its use in tumor-selective drug delivery

However, it is worth mentioning that the EPR effect is rather limited. Although it can significantly reduce side effects, it provides only about a two-fold increase in selectivity[145]. Furthermore, drug uptake is still slow, meaning that a large portion of the drug will be metabolized and excreted before reaching the tumor. That is why the EPR effect alone is usually insufficient, and additional strategies must be employed.

For example, stimuli-responsive delivery represents a promising approach. Such stimuli can include pH (triggering release under certain pH conditions), enzymes (enzymatic release), or reactive oxygen species (ROS-sensitive release). In these cases, additional selectivity factors – such as the upregulation of specific enzymes or an acidic pH in the tumor microenvironment – are exploited to enhance targeted drug release[145].

**Polymer-Based Drug Delivery**

Polymers are frequently used as macromolecular carriers for targeted drug delivery. These conjugates typically consist of the polymer itself, a linker, and the active pharmaceutical ingredient (API)[146]. The linker is often designed to provide controlled, stimuli-sensitive release of the drug. The choice of linker depends on the specific application and desired release mechanism. For example, the commonly used hydrazone linker is acid-labile, making it suitable for targeting endosomes due to the acidic environment of late endosomes.

One of the most widely used polymers in drug development is polyethylene glycol (PEG)[147]. PEG is employed to prolong circulation time, increase solubility, and enhance various pharmacokinetic properties. It can be conjugated to proteins, peptides, and small

molecules. Many PEGylated products, such as PEGylated asparaginase and PEGylated doxorubicin in liposomes, are FDA-approved[148].

A polymer intended for use as a drug carrier should possess several key properties[149]. First, it should be biodegradable, non-toxic, and non-immunogenic. Second, its molecular weight must be high enough to ensure prolonged circulation time. The overall geometry, including size and shape, is also crucial, as these factors influence biodistribution and cellular uptake[150]. Third, the linker should be sensitive and selective, allowing the API to be released in a controlled manner. The drug loading capacity of the polymer is another important consideration. Finally, the polymer should be capable of passive or active targeting to the desired site, such as cancer tissues.

**Polyphosphazene Polymers for Drug Delivery**

In this project, we focused on improving drug delivery by conjugating the active pharmaceutical ingredient (API) with a polyphosphazene polymer. These polymers have a nitrogen-phosphorus alternating backbone, with two side chains attached to each phosphorus atom. When organic side chains are introduced, the resulting polymers are referred to as poly(organo)phosphazenes (POPZ). Due to the vast possibilities for functionalizing these side chains, the properties of POPZ can be finely tuned[151]. Furthermore, the P–N backbone is biodegradable and eventually hydrolyzes to ammonium and phosphate[152]. For these reasons, polyphosphazene polymers are used in biomedical applications, including tissue engineering, drug delivery, and bioimaging[151].

Poly(organo)phosphazenes can be synthesized by two main methods: ring-opening polymerization of hexachlorocyclotriphosphazene or living cationic polymerization of trichloro(trimethylsilyl)phosphoranimine[152]. The latter method allows for the production of polymers with lower molecular weights and narrow dispersity. The number of repeating units is controlled by the ratio of monomer to initiator. After polymerization, macromolecular substitution of the chloride atoms is performed, enabling further functionalization of the polymer.

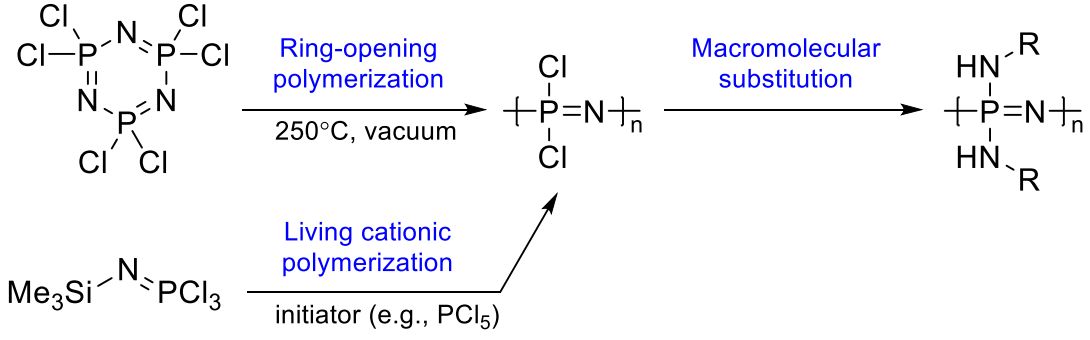

As mentioned earlier, polyphosphazenes are extremely versatile and can adopt various architectures. In particular, graft polymers with organic side chains forming brush-type architectures are especially important[153]. Macrosubstituted polyphosphazenes can serve as macroinitiators for preparing densely grafted structures composed of polymers such as polystyrene or polyglutamic acid (PGA). Such PPz-PGA polymers show great potential as drug carriers due to their excellent aqueous solubility, biodegradability, and high loading capacity[154]. They demonstrate improved biodistribution and pharmacokinetics, prolonged circulation half-life, and promote the accumulation of drugs in tumors.

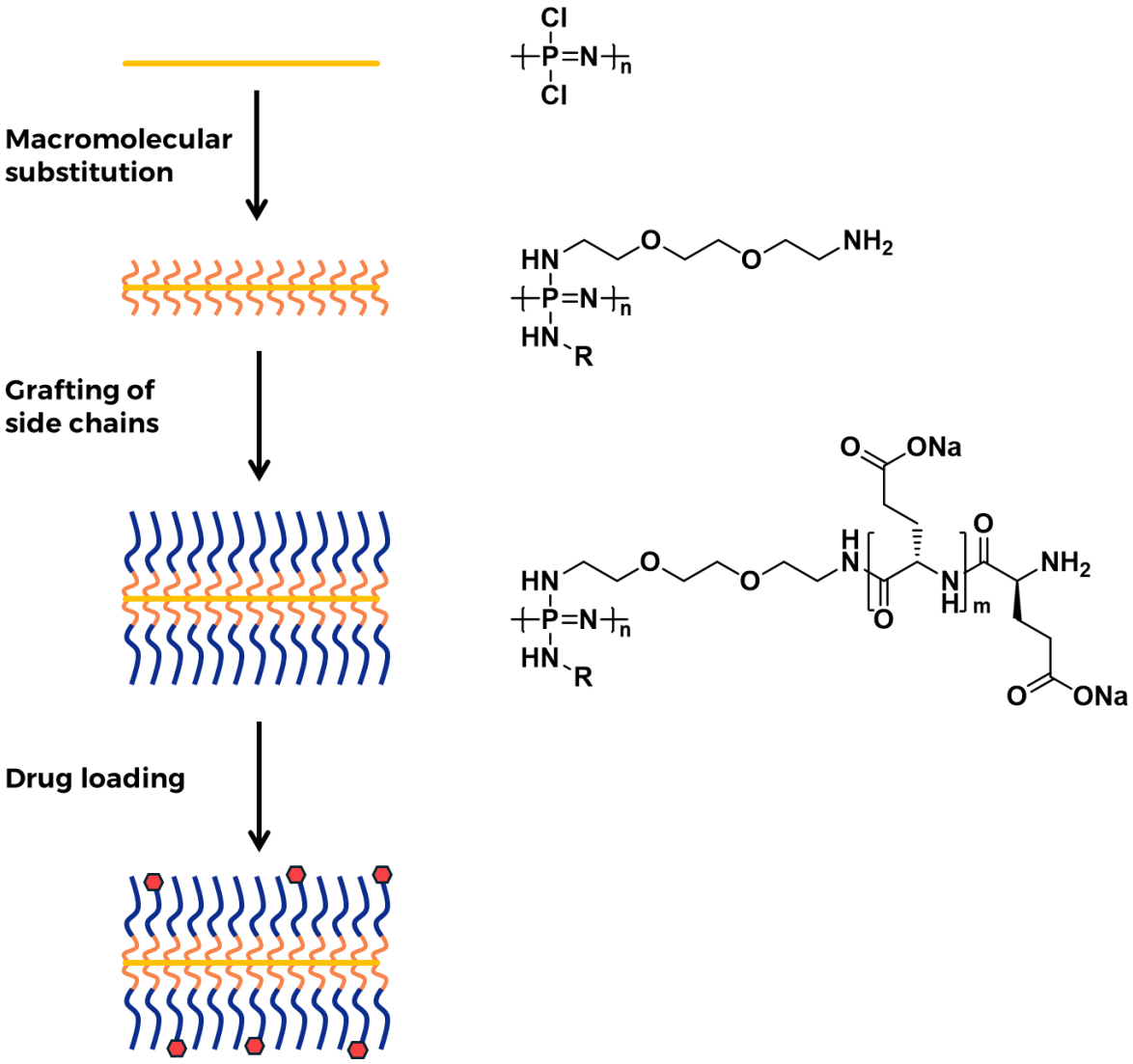


**Figure 16**: Schematic representation of the preparation of the polyphosphazene drug conjugate, illustrating polymer assembly and subsequent drug

## 2 Aims of the study

Previously, we demonstrated that resiquimod (R848) and SA-401 exhibit similar efficacy in vivo against a murine pancreatic adenocarcinoma model. No significant differences were observed in terms of tumor shrinkage or survival outcomes. These results are provided below.

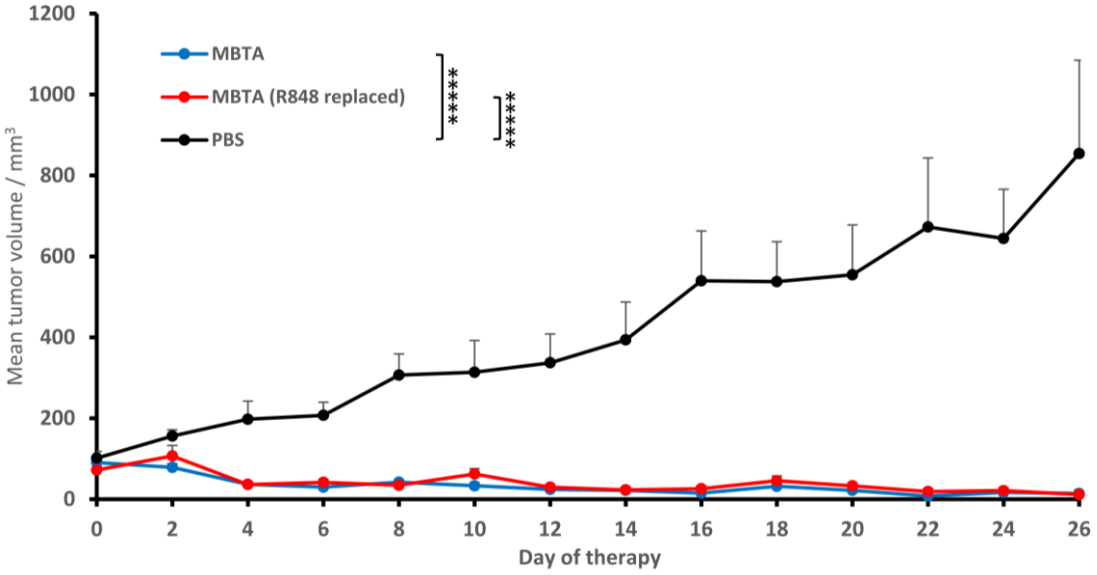


**Figure 17:** 400 000 Panc02 cells were injected into the right flanks of C57BL/6 mice. After 12 days, the mice were randomly assigned to three groups (eight mice in each group): MBTA (tumors were treated with MBTA therapy), MBTA where resiquimod (R848) was replaced with SA-401, and PBS (control group). Tukey's HSD test has been performed (*****$p \leq 0.0005$).

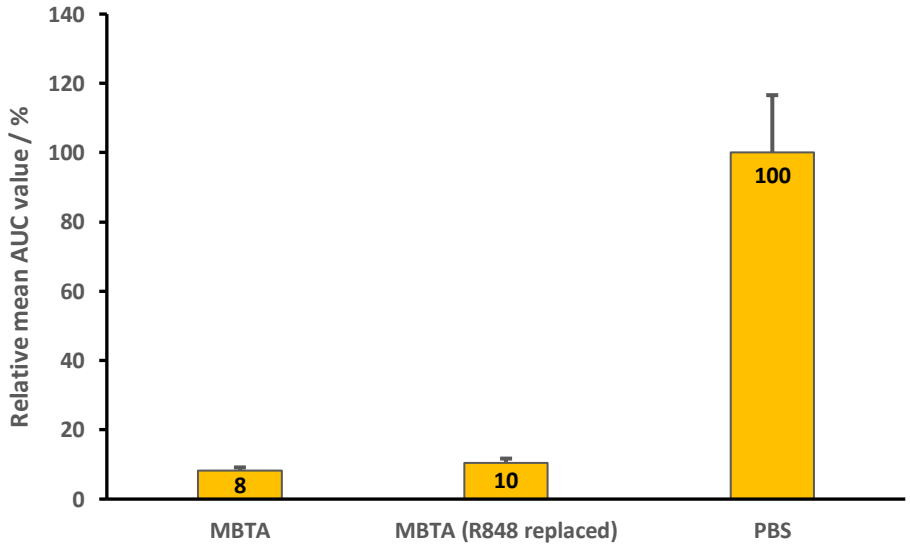


**Figure 18**: Relative mean AUC of tumor volume over therapy, normalized to PBS control (100%), derived from averaged volume curves

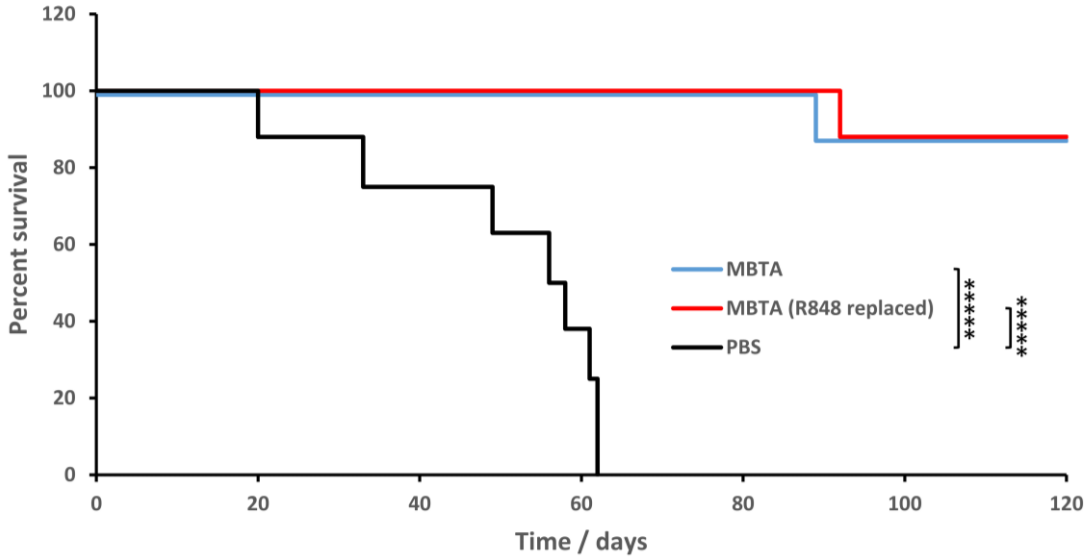


**Figure 19**: 400 000 Panc02 cells were injected into the right flanks of C57BL/6 mice. After 12 days, the mice were randomly assigned to three groups (eight mice in each group): MBTA (tumors were treated with MBTA therapy), MBTA where resiquimod (R848) was replaced with SA-401, and PBS (control group). The results were shown as Kaplan-Meier curves. Log-rank test has been performed (*****$p \leq 0.0005$).

In this master's thesis, we focused on the preparation of a novel bottlebrush polyphosphazene polymer designed to be conjugated with SA-401 via a hydrazone bond. This conjugate is designed to enable more selective targeting to endosomes, potentially allowing systemic administration with improved pharmacokinetic properties. The pH-sensitive hydrazone bond is labile under the acidic conditions of endosomes, facilitating slow release of SA-401 once endocytosed. This strategy aims to reduce side effects commonly associated with immune response modifiers by enhancing targeted delivery.

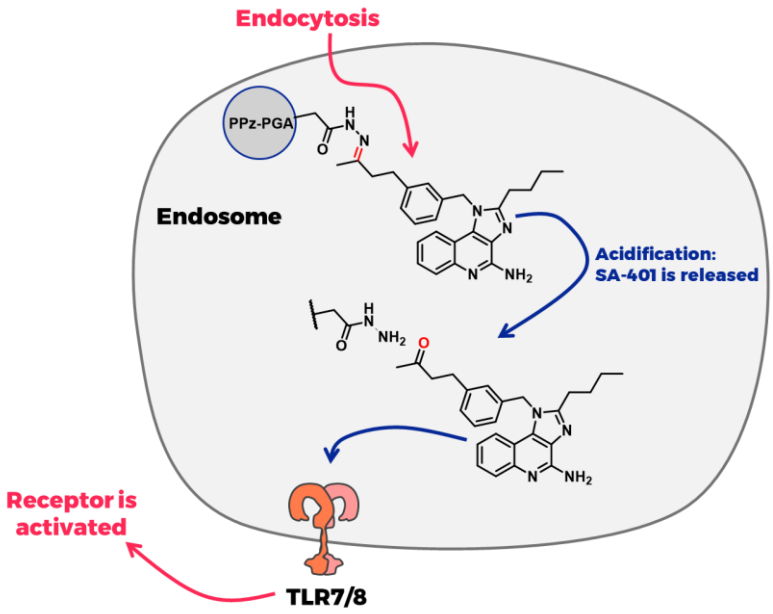


**Figure 20**: Acidification in endosomes leads to release of SA-401 and subsequent activation of TLR7/8

SA-401 was synthesized following a modified procedure previously reported by Stephan Aichhorn, while the polyphosphazene polymer was prepared according to the method published by Paul Strasser et al. Therefore, the first two aims of this thesis were to synthesize SA-401 and prepare the polymer conjugate.

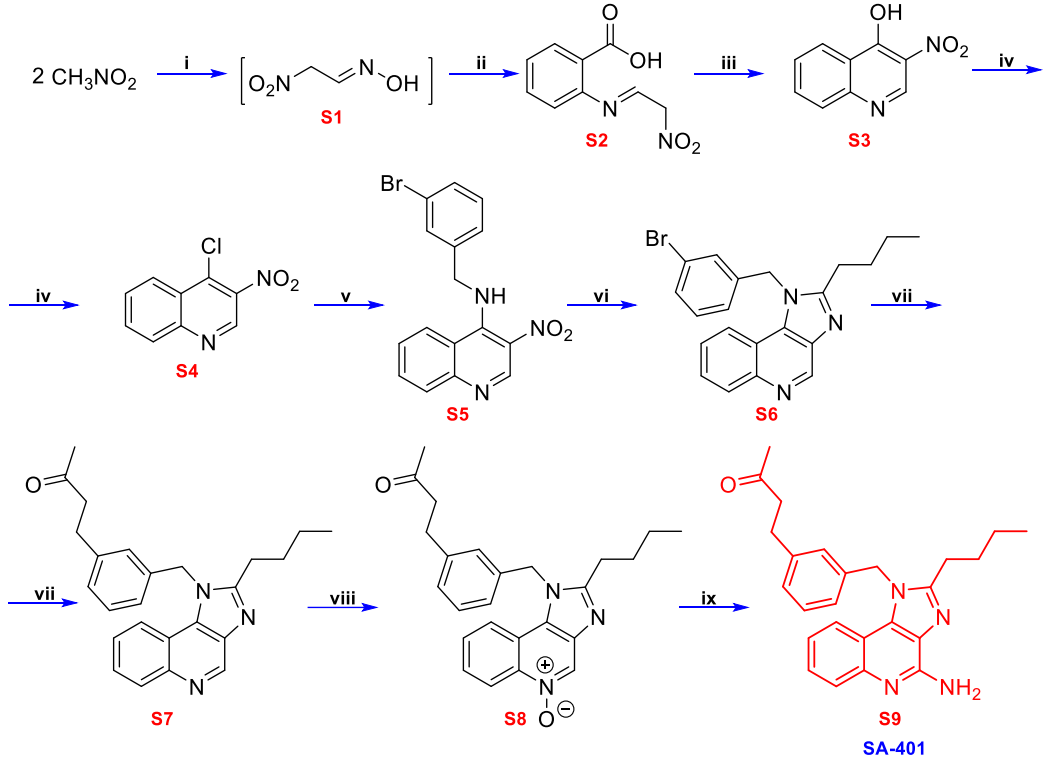


**Figure 21**: Synthesis of TLR7/8 agonist SA-401

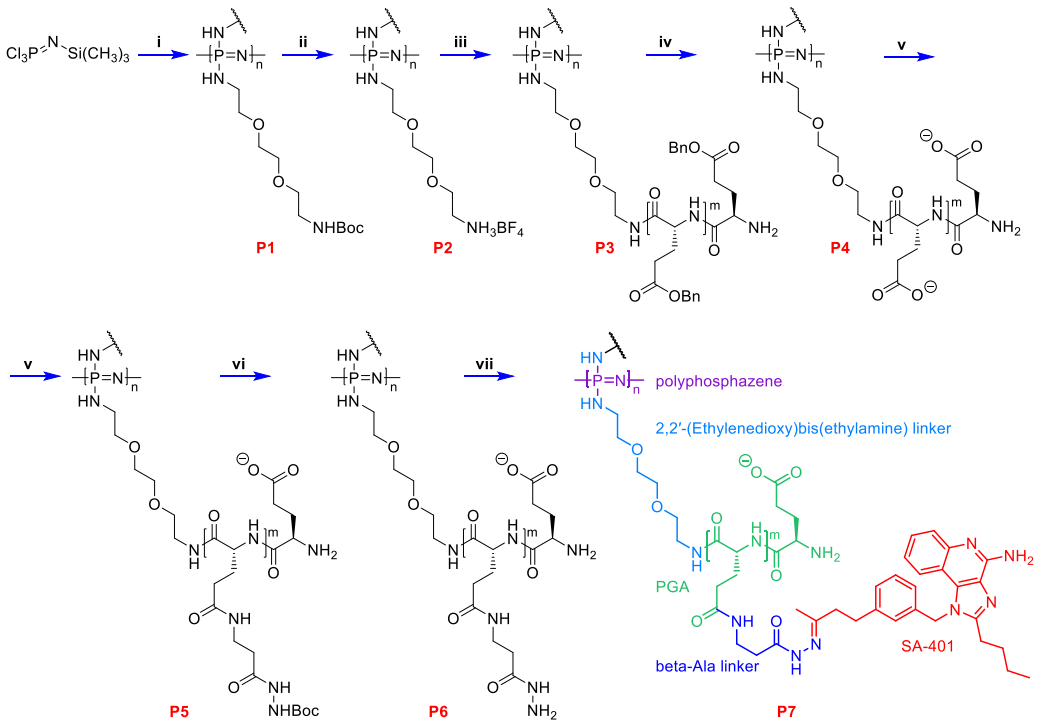


**Figure 22**: Synthesis of SA-401-conjugated β-Ala-hydrazide linked PPz-PGA

Additionally, we conducted *in vitro* characterization of SA-401 alone and compared its effects to those of the conventional TLR7/8 agonist resiquimod (R848). This involved differentiating isolated myeloid precursor cells into bone marrow-derived macrophages using LCCM, followed by activation of these macrophages with SA-401 and R848. After activation, the cells were lysed and analyzed biochemically using techniques such as SDS-PAGE and Western blotting. Differences in cellular responses and activation states were further assessed through mass spectrometry-based proteomics.

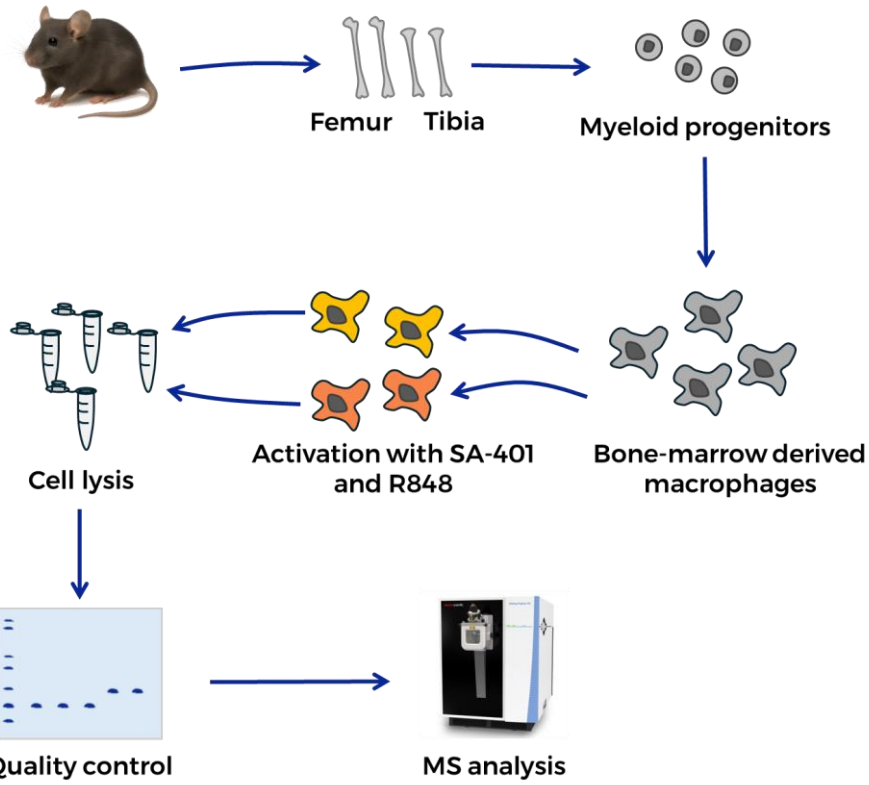


**Figure 23**: Schematic workflow for the *in vitro* comparison of SA-401 and R848

Finally, we compared these molecules *in silico* using molecular dynamics (MD) simulations performed with GROMACS. Various systems were simulated under different conditions, and binding affinities were calculated using the MM-PBSA method to gain insight into their molecular interactions. Through our analysis, we determined that a simulation length of 200 ns is sufficient for these systems, and this duration was applied to all simulations.

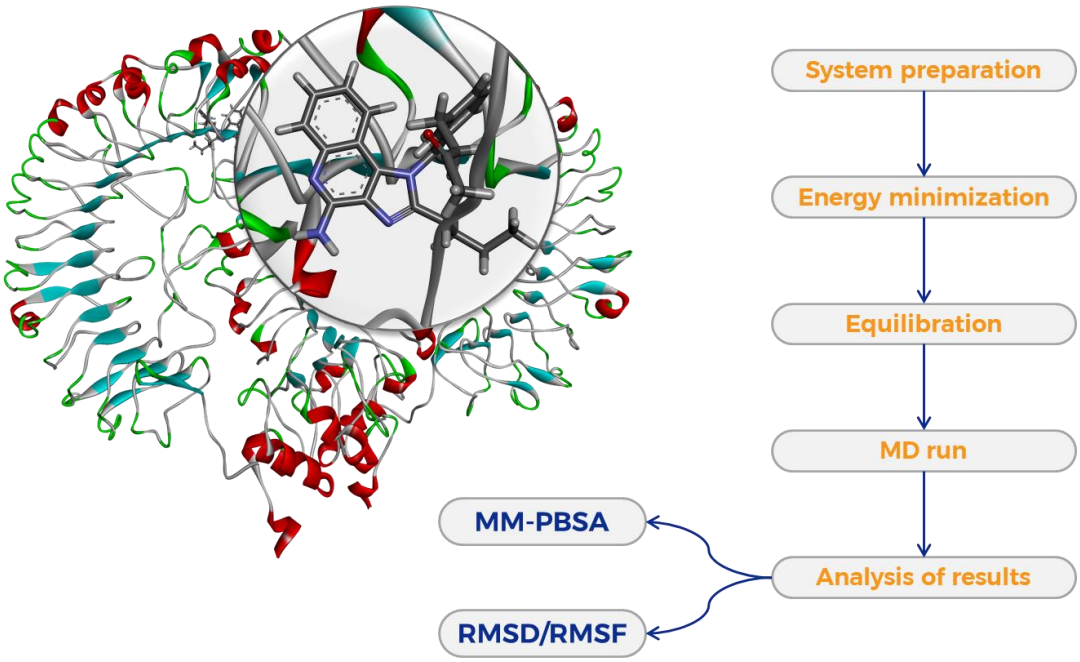


**Figure 24**: Simplified workflow of the molecular dynamics simulation performed in GROMACS

# 3 Experimental part: synthesis of TLR7/8 agonist SA-401

## 3.1 Materials and methods

**Materials**: All chemicals and solvents were purchased from commercial suppliers and used without further purification.

**NMR spectroscopy**: NMR spectra were recorded on a Bruker Avance III 300 MHz spectrometer (equipped with a BBO probe) or a Bruker Avance III 500 MHz NMR spectrometer (equipped with a BBO probe). Chemical shifts were referenced to the residual non-deuterated solvent. Chemical shifts (δ) are reported in parts per million (ppm), and coupling constants (J) are given in hertz (Hz). All chemicals and solvents were purchased from commercial suppliers and used without further purification. The acquired data were processed and analyzed using TopSpin 4.4.0 software.

**ESI-MS**: MS data were acquired using a Shimadzu LCMS-2020 single quadrupole mass spectrometer via a CAMAG TLC-MS interface 2. The flow rate was set to 0.4 mL/min. MS measurements were performed at a maximum scan speed of 15 000 u/sec and in both positive and negative ion modes. The ESI-MS eluent was prepared by dissolving 631 mg of ammonium formate and 0.3 mL of formic acid in 29.3 mL of water, then diluting the mixture to 1000 mL with methanol. Results were analyzed by averaging the signal data and subtracting the baseline, and were subsequently plotted using Shimadzu LabSolutions software.

**HPLC-MS system:** Agilent Technologies 1260 Infinity II HPLC system with Agilent Technologies 6560 DT-IM-QTOF mass spectrometer. Solvent A was 0.1% formic acid, and solvent B was acetonitrile. All measurements were run in positive and negative modes.

## 3.2 Synthesis procedures

### 3.2.1 Synthesis of S1 and S2

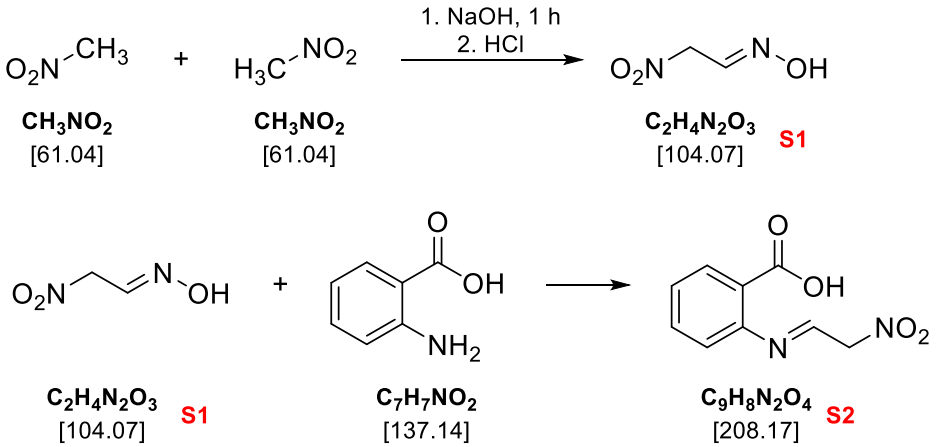


5.25 mL of $CH_3NO_2$ (98 mmol, 1.1 equiv.) was added dropwise to an ice-cold solution of NaOH (12 g, dissolved in 24 mL of distilled water) with stirring. A white precipitate formed

during the addition. After the $CH_3NO_2$ was added, the mixture was heated to 40 °C and then cooled to 20 °C. Upon heating, the solution turned red. Subsequently, another 5.25 mL of $CH_3NO_2$ (98 mmol, 1.1 equiv.) was added dropwise. The mixture spontaneously heated up; when it reached 65 °C, cooling was applied to bring the temperature down to 55 °C, after which it was allowed to cool to room temperature. The mixture was then poured over 27 g of ice and acidified with 30 mL of concentrated HCl, resulting in the formation of a yellow solution of compound **S1**.

The solution of **S1** obtained in the previous step was added to a solution of anthranilic acid (12.3 g, 90 mmol, 1.0 equiv.) in HCl (11 mL of conc. HCl + 200 mL of distilled water). A yellow precipitate formed immediately. The mixture was left overnight at room temperature, then the precipitate was filtered off and washed with cold water. The precipitate was dried in an oven at 75 °C to yield product **S2** as a bright yellow powder (16.15 g, 78 mmol, 86%). The product was characterized by NMR.

$^1$H NMR (300 MHz, DMSO, 298K): δ=6.76 (d, J=6.0 Hz, 1H), 7.24 (dt, J=1.3, 7.5 Hz, 2H), 7.68 (dt, J=1.5, 7.7 Hz, 2H), 7.76 (d, J=8.6 Hz, 1H), 8.10–8.01 (m, 2H), 13.05 (d, J=13.7 Hz, 1H), 13.75 ppm (br s, 1H).

$^{13}$C NMR (75 MHz, DMSO, 298K): δ=113.6, 115.4, 116.6, 123.6, 131.8, 134.6, 137.4, 140.9, 168.5 ppm.

### 3.2.2 Synthesis of S3

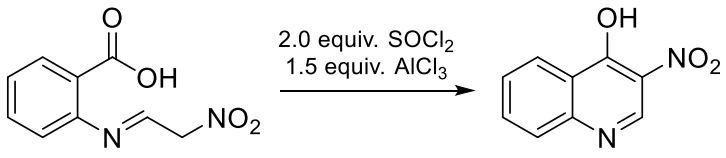


$C_9H_8N_2O_4$ [208.17] **S2**

$C_9H_6N_2O_3$ [190.16] **S3**

Product **S2** (15.0 g, 72 mmol, 1.0 equiv.) was dissolved in 60 mL of DMF, forming a blood-red solution. The mixture was heated to 60 °C, and $AlCl_3$ (14.4 g, 108 mmol, 1.5 equiv.) was added slowly while maintaining the temperature below 65 °C. After stirring at 60 °C for 1 hour, the solution was cooled to 45 °C, and $SOCl_2$ (10.2 mL, 140 mmol, 1.9 equiv.) was added dropwise (note: a rapid temperature increase occurred during the addition). The reaction was stirred at 105 °C for 1 hour, cooled to 70 °C, and diluted with 15 mL of DMF. Further cooling to 40 °C was followed by quenching with 180 mL of ice-cold deionized water. After 5 minutes, the precipitate was collected by filtration, washed sequentially with water and hot DCM, and dried overnight at 75 °C to yield the product **S3** as a brown powder (8.1 g, 43 mmol, 59%), characterized by NMR and ESI-MS.

$^{1}$H NMR (300 MHz, DMSO, 298K): δ=7.53 (tdd, J=2.3, 4.6, 4.6 Hz, 1H), 7.73 (d, J=8.1 Hz, 1H), 7.81 (tdd, J=2.5, 5.0, 5.0 Hz, 1H), 8.27 (dd, J=1.2, 8.0 Hz, 1H), 9.21 (s, 1H), 13.05 ppm (s, 1H);

$^{13}$C NMR (75 MHz, DMSO, 298K): δ=113.6, 115.4, 116.6, 123.6, 131.8, 134.6, 137.8, 140.9, 168.5 ppm.

### 3.2.3 Synthesis of S4

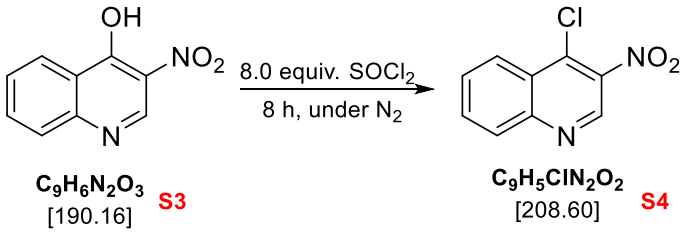


$C_9H_6N_2O_3$ [190.16] **S3**

$C_9H_5ClN_2O_2$ [208.60] **S4**

8.00 g of product **S3** (42 mmol, 1.0 equiv.) was placed in a three-necked round-bottom flask under a nitrogen atmosphere. Next, 655 µL of DMF (6 mmol, 0.2 equiv.) and 70 mL of DCM were added via a dropping funnel. Subsequently, 25.06 mL of $SOCl_2$ (345 mmol, 8.2 equiv.) was added dropwise to the mixture. The reaction mixture was then refluxed for 8 hours under a nitrogen atmosphere. After cooling in an ice-water bath, 225 mL of ice-cold 1.67 M NaOH solution was added. The mixture was stirred for 50 minutes and then extracted four times with DCM. The combined organic layers were washed three times with saturated $NaHCO_3$ solution and dried over anhydrous $Na_2SO_4$. Removal of the solvent by rotary evaporation yielded the product as a brown powder (6.57 g, 31 mmol, 75%). The crude product was purified by column chromatography (silica, DCM, Rf = 0.75), affording 4.84 g of **S4** as a tan powder (23 mmol, 55%). The product was characterized by NMR and ESI-MS.

$^{1}$H NMR (300 MHz, $CDCl_3$, 298K): δ=7.81 (tdd, J=2.4, 4.9, 4.9 Hz, 1H), 7.94 (tdd, J=2.5, 4.9, 4.9 Hz, 1H), 8.20 (d, J=8.2 Hz, 1H), 8.42 (dd, J=1.1, 8.5 Hz, 1H), 9.25 ppm (s, 1H).

$^{13}$C NMR (75 MHz, $CDCl_3$, 298K): δ=125.5, 126.0, 129.7, 130.2, 133.1, 136.6, 141.3, 144.5, 149.2 ppm.

### 3.2.4 Synthesis of S5

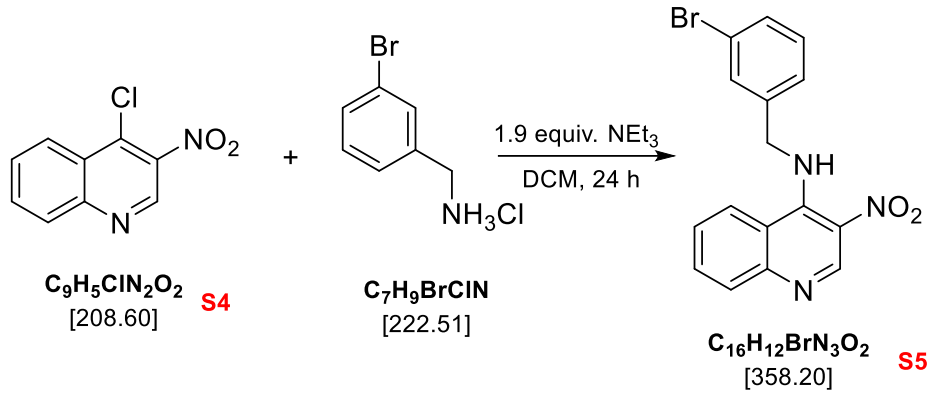


$C_9H_5ClN_2O_2$ **S4**
[208.60]

$C_7H_9BrClN$
[222.51]

$C_{16}H_{12}BrN_3O_2$ **S5**
[358.20]

A mixture of 4.84 g of **S4** (23 mmol, 1.0 equiv.) and 6.23 g of 3-bromobenzylamine hydrochloride (28 mmol, 1.2 equiv.) in a three-necked round-bottom flask equipped with a condenser was treated with 6.26 mL of $Et_3N$ (44 mmol, 1.9 equiv.) and 132 mL of DCM. The reaction was refluxed under an $N_2$ atmosphere for 24 hours. After concentration under reduced pressure, the residue was taken up in pentane (440 mL), yielding a yellow precipitate upon stirring for 30 minutes. The precipitate was collected via vacuum filtration, washed with pentane, and redissolved in DCM. The resulting solution was washed with a half-saturated $NaHCO_3$, and the organic layer was concentrated using a rotary evaporator to afford the product as a bright yellow powder (7.48 g, 21 mmol, 90% yield). The product was characterized by NMR and ESI-MS.

$^1$H NMR (300 MHz, $CDCl_3$, 298K): δ=5.06 (d, J=6.0 Hz, 2H), 7.38–7.28 (m, 2H), 7.44 (tdd, J=2.5, 4.9, 4.9 Hz, 1H), 7.52 (td, J=1.7, 7.4 Hz, 1H), 7.58 (t, J=1.7 Hz, 1H), 7.77 (tdd, J=2.4, 4.8, 4.8 Hz, 1H), 8.02 (dd, J=1.2, 8.4 Hz, 1H), 8.17 (dd, J=0.9, 8.6 Hz, 1H), 9.39 (s, 1H), 9.79 ppm (t, J=4.5 Hz, 1H);

$^{13}$C NMR (126 MHz, $CDCl_3$, 298K): δ=52.4, 119.2, 123.6, 125.7, 125.9, 126.7, 126.7, 130.3, 130.7, 131.1, 131.8, 133.0, 139.3, 147.4, 150.8, 151.1 ppm.

### 3.2.5 Synthesis of S6

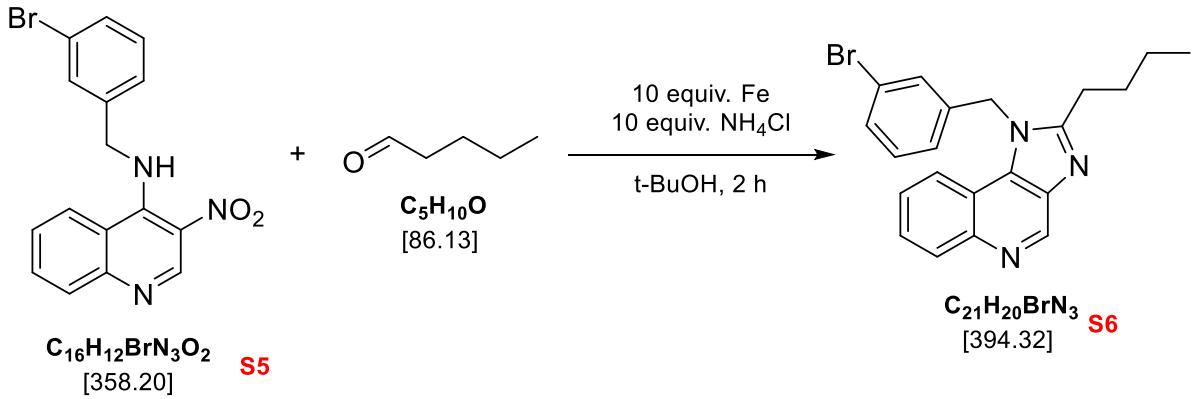


$C_{16}H_{12}BrN_3O_2$ **S5**
[358.20]

$C_5H_{10}O$
[86.13]

$C_{21}H_{20}BrN_3$ **S6**
[394.32]

A suspension of **S5** (2.0 g, 20 mmol, 1.0 equiv.), $NH_4Cl$ (10.5 g, 195 mmol, 10.0 equiv.), iron powder (10.96 g, 195 mmol, 10.0 equiv.), and pentanal (9.38 mL, 88 mmol, 4.5 equiv.) in 203 mL of isobutanol was refluxed for 2 hours, during which the color changed from yellow to red; after cooling to room temperature, the mixture was filtered through a glass filter (vacuum filtration, pore size 2).

Subsequently, 1 M NaOH was added to the flask, and after vigorous shaking, the mixture was filtered again through a glass filter with a pore size of 4 (this step is performed to remove iron salts, which otherwise hinder separation during the extraction process). The layers were separated, and the aqueous phase was extracted twice with EtOAc. The combined organic extracts were washed twice with 1 M NaOH, dried over anhydrous $Na_2SO_4$, and concentrated.

The residue was heated to 60 °C, then 175 mL of heptane was slowly added; after freezing the mixture overnight, no precipitation was observed, so the mixture was concentrated again (70 °C, 30 mbar) and kept under high vacuum for 15 minutes. The flask was then heated to 60 °C, at which point precipitation was observed, and 105 mL of heptane was slowly added using a Pasteur pipette. A yellow precipitate formed, and the flask contents were placed in the freezer; the precipitate was subsequently filtered off, washed with cold heptane, and dried under vacuum to afford the product as a mango yellow powder (5.6 g, 14 mmol, 73%). The product was characterized by NMR and ESI-MS.

$^1$H NMR (500 MHz, $CDCl_3$, 298K): δ=0.94 (t, J=7.3 Hz, 3H), 1.46 (sext, J=6.9 Hz, 2H), 1.88 (pent, J=7.4 Hz, 2H), 2.91 (t, J=7.5 Hz, 2H), 5.78 (s, 2H), 6.88 (d, J=7.6 Hz, 1H), 7.18 (t, J=7.8 Hz, 1H), 7.29 (s, 1H), 7.48–7.43 (m, 2H), 7.61 (t, J=7.4 Hz, 2H), 7.87 (d, J=8.3 Hz, 1H), 8.26 (d, J=8.2 Hz, 1H), 9.36 ppm (s, 1H);

$^{13}$C NMR (126 MHz, $CDCl_3$, 298K): δ=13.8, 22.5, 27.2, 29.6, 48.4, 117.5, 119.6, 123.6, 124.0, 126.6, 127.0, 128.6, 130.9, 131.0, 131.5, 134.0, 136.6, 137.5, 144.8, 145.0, 155.7 ppm.

### 3.2.6 Synthesis of S7

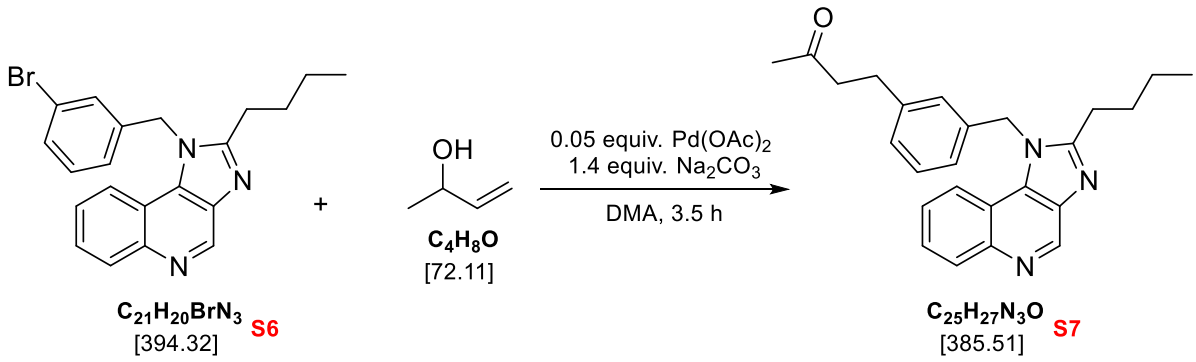


$C_{21}H_{20}BrN_3$ **S6**
[394.32]

$C_{25}H_{27}N_3O$ **S7**
[385.51]

A solution of **S6** (5.0 g, 12.7 mmol, 1.0 equiv.) in 90 mL of DMA was treated with but-3-en-2-ol (1690 µL, 17.8 mmol, 1.4 equiv.), $Pd(OAc)_2$ (150 mg, 0.6 mmol, 0.05 equiv.), and $Na_2CO_3 \cdot 10H_2O$ (2.8 g, 25.4 mmol, 2.0 equiv.*). The mixture was heated to 135 °C under an $N_2$ atmosphere for 3.5 hours, cooled to room temperature, and diluted with EtOAc. The solution was washed with a saturated $NaHCO_3$ solution, and the aqueous phase was extracted three times with EtOAc. The combined organic phase (a slightly yellowish liquid) was washed twice with brine, dried over anhydrous $Na_2SO_4$ overnight, and concentrated under reduced pressure (60 °C, 200 mbar). The resulting brownish oil was purified by column chromatography (silica, DCM:MeOH:7N $NH_3$ in MeOH = 11:0.6:0.4) to yield the product as a yellow crystalline solid (3.20 g, 8.3 mmol, 65%), characterized by ESI-MS and NMR.

* $Na_2CO_3 \cdot 10H_2O$ was dried at 75 °C overnight prior to use, and the equivalent amount was adjusted to account for its hydrated form.

$^1$H NMR (500 MHz, $CDCl_3$, 298K): δ=0.94 (t, J=7.4 Hz, 3H), 1.46 (sext, J=7.5 Hz, 2H), 1.89 (pent, J=7.8 Hz, 2H), 2.03 (s, 3H), 2.62 (t, J=7.3 Hz, 2H), 2.81 (t, J=7.3 Hz, 2H), 2.93 (t, J=7.7 Hz, 2H), 5.76 (s, 2H), 6.90–6.83 (m, 2H), 7.11 (d, J=7.9 Hz, 1H), 7.22 (t, J=7.7 Hz, 1H), 7.42 (tdd, J=2.3, 4.7, 4.7 Hz, 1H), 7.59 (tdd, J=2.4, 4.8, 4.8 Hz, 1H), 7.91 (d, J=8.5 Hz, 1H), 8.25 (d, J=8.3 Hz, 1H), 9.35 ppm (s, 1H);

$^{13}$C NMR (126 MHz, $CDCl_3$, 298K): δ=13.8, 22.5, 27.2, 29.4, 29.6, 30.0, 44.7, 49.0, 117.6, 120.0, 123.3, 125.5, 126.3, 126.8, 128.2, 129.6, 130.8, 134.2, 135.4, 136.6, 142.4, 144.7, 144.9, 155.9, 207.3 ppm.

### 3.2.7 Synthesis of S8

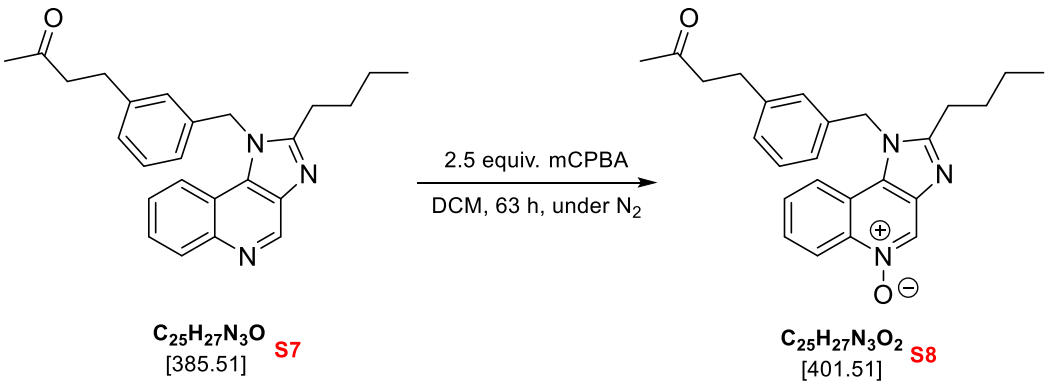


**S7** (3.0 g, 7.77 mmol, 1.0 equiv.) was dissolved in 350 mL of anhydrous DCM in a three-necked round-bottom flask under an $N_2$ atmosphere. 3-Chloroperbenzoic acid (mCPBA, 77% purity, 4.39 g, 19.58 mmol, 2.5 equiv.) was added, and the reaction mixture was refluxed for 65 hours. The solvent was removed under reduced pressure, and the residue was treated with

125 mL of EtOAc, followed by 125 mL of saturated $NaHCO_3$ solution. The mixture was stirred vigorously for 2 hours, after which the aqueous layer was extracted three times with EtOAc. The combined organic phase was dried over anhydrous $Na_2SO_4$, and the solvent was evaporated to afford the final product **S8** as a brown oil (3.6 g, 8.97 mmol, 115% yield), characterized by ESI-MS and NMR.

$^1H$ NMR (500 MHz, $CDCl_3$, 298K): δ=0.94 (t, J=7.2 Hz, 3H), 1.50–1.42 (m, 3H), 1.86 (pent, J=7.7 Hz, 2H), 2.04 (s, 3H), 2.64 (t, J=7.3 Hz, 2H), 2.83 (t, J=7.3 Hz, 2H), 2.93 (t, J=7.7 Hz, 2H), 5.74 (s, 2H), 6.83 (d, J=8.1 Hz, 1H), 6.90 (s, 1H), 7.13 (d, J=8.2 Hz, 1H), 7.23 (d, J=7.8 Hz, 1H), 7.54 (t, J=7.8 Hz, 1H), 7.67 (t, J=7.7 Hz, 1H), 7.89 (d, J=8.0 Hz, 1H), 9.01 (d, J=8.5 Hz, 1H), 9.15 ppm (s, 1H);

$^{13}C$ NMR (126 MHz, $CDCl_3$, 298K): δ=13.7, 22.5, 27.2, 29.4, 29.6, 30.0, 44.7, 49.0, 117.9, 120.5, 121.9, 123.1, 125.5, 128.0, 128.2, 128.5, 128.8, 129.7, 131.2, 134.7, 135.8, 138.3, 142.6, 158.0, 207.2 ppm.

### 3.2.8 Synthesis of S9

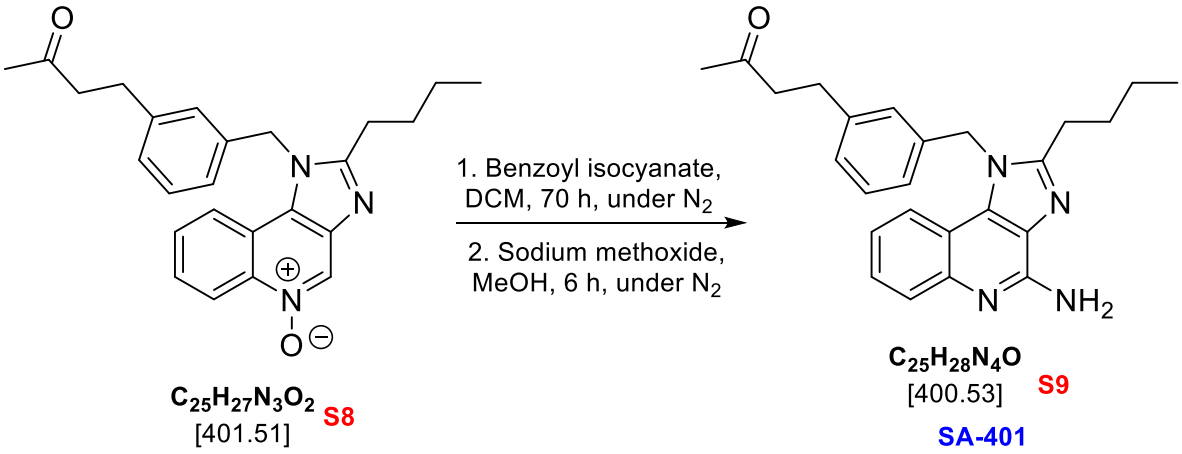


Benzoyl isocyanate (4.4 g, 90% purity, 26.84 mmol, 3.0 equiv.) was placed in a three-necked flask, evacuated for 20 minutes, and subjected to three $N_2$/vacuum cycles. 300 mL of DCM (purified with MBRAUN solvent purification system) was added under a steady $N_2$ flow, followed by a solution of **S8** (3.6 g, 8.94 mmol, 1.0 equiv.) in 73 mL of DCM (same grade). The mixture was refluxed under $N_2$ for 90 hours, after which the solvent was removed by rotary evaporation. The residue was redissolved in 300 mL of MeOH, treated with sodium methoxide (2.4 g, 44.78 mmol, 5.0 equiv.), and refluxed for 6 hours.

The solvent was evaporated, and the crude product underwent two column chromatographies: the first using silica gel with DCM (1% 7N $NH_3$ in MeOH) and a methanol gradient (0→10%), and the second using EtOAc with a methanol gradient (0→23%, then

50%). This yielded 1.72 g (4.31 mmol, 48%) of intermediate material, characterized by ESI-MS. Final purification via column chromatography (silica, DCM:MeOH:TFA = 10:0.3:0.2) afforded a slightly yellowish powder, which was recrystallized from EtOAc/MeOH (25 mL:0.4 mL) to remove an impurity (m/z 387). The resulting white powder, **S9** (SA-401) (1.1 g), was characterized by HPLC-MS, ESI-MS, and NMR.

$^{1}$H NMR (500 MHz, $CDCl_3$, 298K): δ=0.92 (t, J=7.4 Hz, 3H), 1.43 (sext, J=7.4 Hz, 2H), 1.79 (pent, J=7.7 Hz, 2H), 2.03 (s, 3H), 2.62 (t, J=7.4 Hz, 2H), 2.81 (t, J=7.5 Hz, 2H), 2.87 (t, J=7.9 Hz, 2H), 5.55 (s, 2H), 5.68 (s, 2H), 6.87–6.84 (m, 2H), 7.10 (tdd, J=2.3, 4.6, 4.6 Hz, 2H), 7.22 (t, J=7.6 Hz, 1H), 7.42 (tdd, J=2.4, 4.9, 4.9 Hz, 1H), 7.69 (dd, J=0.9, 8.4 Hz, 1H), 7.79 ppm (dd, J=0.9, 8.4 Hz, 1H);

$^{13}$C NMR (126 MHz, $CDCl_3$, 298K): δ=13.7, 22.5, 27.2, 29.5, 30.0, 30.0, 44.7, 48.8, 115.3, 119.8, 122.2, 123.4, 125.5, 126.7, 126.9, 127.0, 128.1, 129.5, 134.0, 135.6, 142.3, 144.6, 151.1, 154.0, 207.4 ppm.

# 4 Experimental part: synthesis of the polyphosphazene (PPz) polymer and conjugation with SA-401

## 4.1 Materials and methods

**Materials**: All chemicals and solvents were purchased from commercial suppliers and used without further purification.

**NMR spectroscopy:** NMR spectra were recorded on a Bruker Avance III 300 MHz spectrometer (equipped with a BBO probe) or a Bruker Avance III 500 MHz NMR spectrometer (equipped with a BBO probe). Chemical shifts were referenced to the residual non-deuterated solvent. Chemical shifts (δ) are reported in parts per million (ppm), and coupling constants (J) are given in hertz (Hz). All chemicals and solvents were purchased from commercial suppliers and used without further purification. The acquired data were processed and analyzed using TopSpin 4.4.0 software.

**GPC analysis in DMF**: For GPC analysis, a sample containing 2 mg/mL of polymer in DMF was prepared. Samples were filtered through a 0.2 μm PTFE filter prior to analysis. Measurements were performed on a Viscotek GPCmax instrument using a PFG column from Polymer Standard Service GmbH (300 mm × 8 mm, 5 μm particle size). The instrument was operated and data were processed using OmniSEC 5.12 software. The mobile phase was DMF with 10 mM LiBr, and the column temperature was maintained at 60 °C. Detection was performed using refractive index (RI), right- and low-angle light scattering (RALS and LALS), and intrinsic viscosity (IV) detectors. Results were plotted using Origin 2024 software.

**Aqueous GPC**: Analysis was performed on an Agilent Technologies 1260 Infinity II system equipped with a Shodex OHpak LB-802.5 (300 mm × 8 mm, 6 μm particle size) and a Shodex OHpak LB-804 (300 mm × 8 mm, 10 μm particle size) column. The mobile phase consisted of 0.1 M $NaNO_3$ with 0.025% $NaN_3$, delivered at a flow rate of 0.5 mL/min. Samples with a final concentration of 2 mg/mL in Milli-Q water were filtered through a 0.2 μm nylon filter prior to analysis. Data were processed using Astra 7.3.2.21 software and plotted in Origin 2024.

**IR spectroscopy**: IR spectra were recorded on a Bruker Alpha II FT-IR spectrometer using OPUS 8.2.28 software, and the spectra were subsequently plotted in Origin 2024 software.

**DLS analysis**: DLS analysis was performed using a Malvern Zetasizer Nano ZSP instrument at a fixed scattering angle (173°) at 25 °C. Samples with a final concentration of 0.2 mg/mL in 1× PBS solution were filtered through a 0.2 µm nylon filter prior to analysis.

**UV-Vis spectroscopy**: UV-Vis spectra were recorded using a Molecular Devices SpectraMax M2e Multimode Microplate Reader, operated with SoftMax Pro 7.0.3 software. The spectra were subsequently plotted using Origin 2024 software.

### 4.2 Synthesis procedures

#### 4.2.1 Synthesis of tert-butyl (2-(2-(2-aminoethoxy)ethoxy)ethyl)carbamate

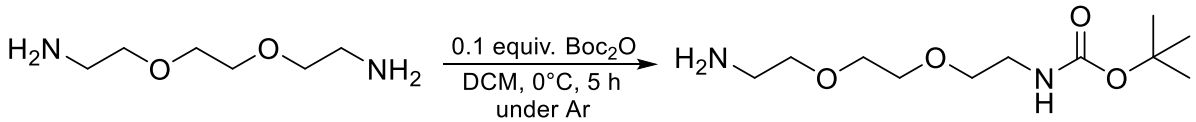


$C_6H_{16}N_2O_2$
[148.21]

$C_{11}H_{24}N_2O_4$
[248.32]

27 mL of 2,2′-(ethylenedioxy)bis(ethylamine) (0.184 mol, 1.0 equiv.) was dissolved in 200 mL of DCM and cooled to 0°C. Separately, 4.00 g of di-*tert*-butyl dicarbonate ($Boc_2O$, 0.0183 mol, 0.10 equiv.) was dissolved in 200 mL of DCM. Over 5 hours, the $Boc_2O$ solution was added dropwise to the cooled solution (0°C) of 2,2′- (ethylenedioxy)bis(ethylamine) under an argon atmosphere. After complete addition, the mixture was stirred overnight at room temperature (RT).

The reaction mixture was then concentrated to approximately 100 mL and diluted with 150 mL of DCM and 150 mL of deionized water. The phases were separated, and the organic phase was washed twice with 100 mL of deionized water. The combined aqueous phase was extracted once with 100 mL of DCM. The combined organic phase was washed once with brine and then dried over anhydrous $MgSO_4$. Evaporation of the solvent afforded 4.86 g (0.0196 mol, 107%) of a colorless, clear liquid.

$^1$H NMR (300 MHz, $CDCl_3$, 298K): δ=1.43 (s, 9H), 1.68 (s, 2H), 2.87 (t, J=5.3 Hz, 2H), 3.29 (q, J=5.3 Hz, 2H), 3.56-3.48 (m, 4H), 3.63–3.57 (m, 4H), 5.19 ppm (br, 1H).

### 4.2.2 Synthesis of Boc-protected macrosubstituted PPz (P1)

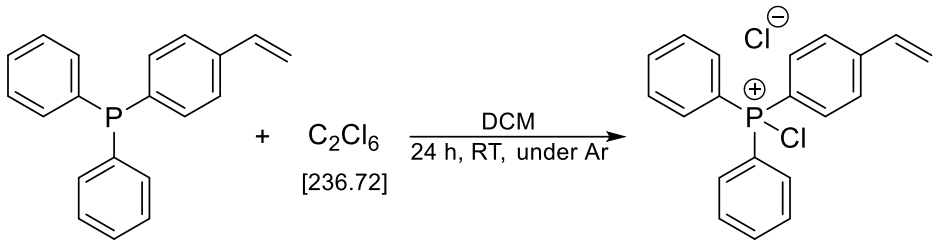


$C_{20}H_{17}P$
[288.33]

$C_{20}H_{17}Cl_2P$
[359.23]

**Initiation reaction**: 4-(diphenylphosphino) styrene (10.03 mg, 0.03479 mmol, 1.0 equiv) was dissolved in 1 mL of anhydrous DCM and combined with a solution of $C_2Cl_6$ (9.08 mg, 0.03836 mmol, 1.1 equiv.) in 1 mL of anhydrous DCM. The reaction mixture was stirred for 24 hours under an argon atmosphere (inside a glovebox) at RT.

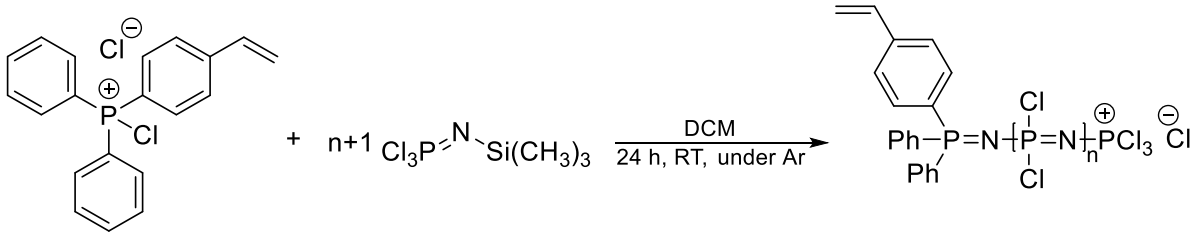


$C_{20}H_{17}Cl_2P$
[359.23]

$C_3H_9Cl_3NPSi$
[224.52]

**Polymerization reaction**: 584.02 mg of monomer $Cl_3P$=N-$Si(CH_3)_3$ (2.60 mmol, 74.8 equiv.) was dissolved in 2 mL of anhydrous DCM. The solution obtained from the previous step (initiator) was then quickly added to the monomer solution. The reaction mixture was stirred for 24 hours under an argon atmosphere (inside a glovebox) at RT.

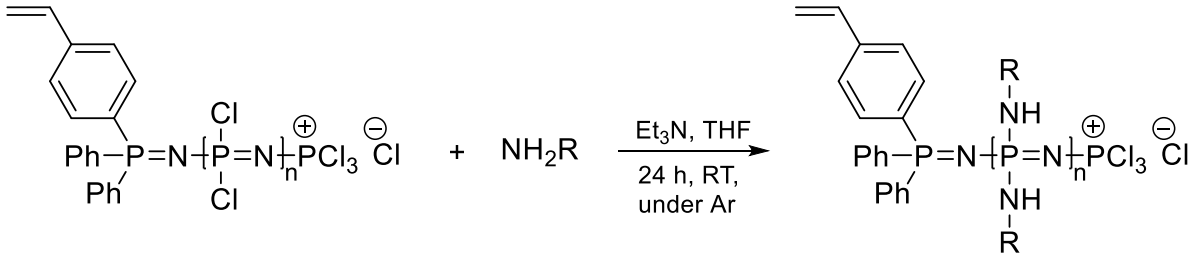


$C_{11}H_{24}N_2O_4$
[248.32]

**P1**

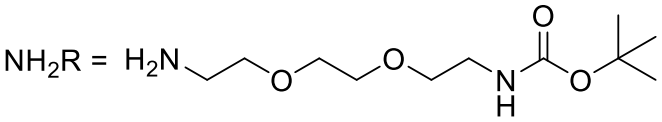


**Macrosubstitution reaction**: tert-butyl (2-(2-(2-aminoethoxy)ethoxy)ethyl) carbamate (1.615 g, 6.504 mmol, 187.0 equiv.) was dissolved in 50 mL of anhydrous THF, followed by the addition of 0.91 mL of $Et_3N$ (6.529 mmol, 187.7 equiv.). The previously obtained polymerization reaction solution was then added dropwise, resulting in the formation of a

white precipitate of $Et_3N{\cdot}HCl$. The reaction mixture was stirred for 24 hours under an argon atmosphere (inside a glovebox) at RT.

The mixture was filtered using a paper filter, and the filtrate was concentrated under reduced pressure to yield a yellowish viscous liquid. The crude polymer was purified by dialysis (MWCO 3.5 KDa; 2 hours in deionized water followed by 22 hours in ethanol), affording 1.098 g (2.03 mmol, 78%) of a yellowish viscous substance. The final product was characterized by NMR spectroscopy ($CDCl_3$) and GPC (DMF).

$^1$H NMR (300 MHz, $CDCl_3$, 298K): δ=1.43 (br, 9H), 3.08 (br, 2H), 3.32 (br, 2H), 3.46 (br, 4H), 3.60 ppm (br, 4H).

$^{31}$P NMR (122 MHz, $CDCl_3$, 298K): δ=2.22, 4.67, 11.454 ppm.

### 4.2.3 Boc-deprotection of macrosubstituted PPz (P2)

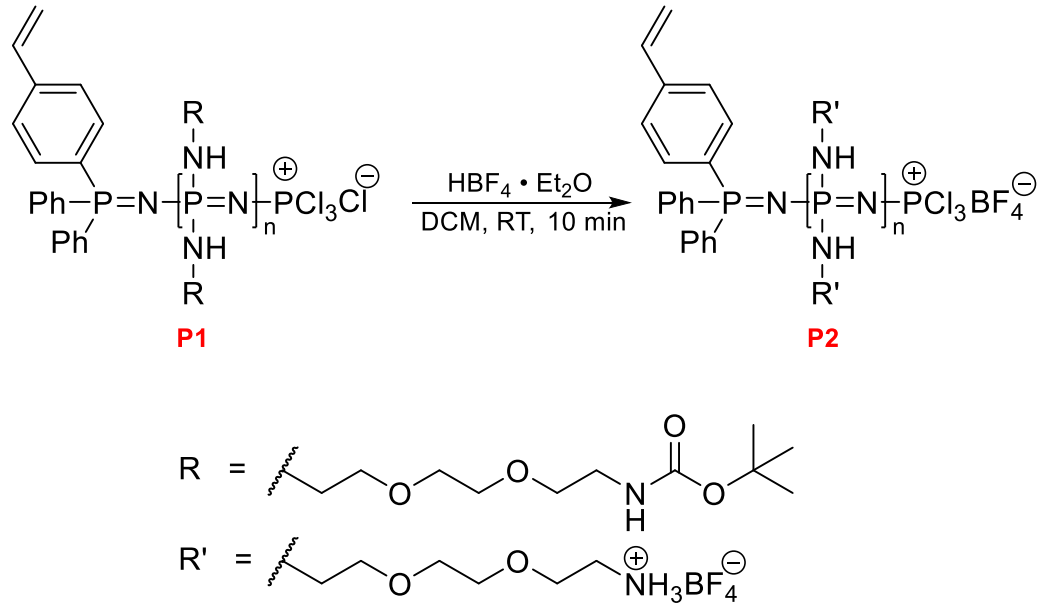


Boc-protected macrosubstituted PPz (202.8 mg, 0.3758 mmol, 1.0 equiv.) was dissolved in 50 mL of anhydrous DCM, followed by slow addition of 300 µL of $HBF_4{\cdot}Et_2O$ (354 mg, 2.186 mmol, 5.8 equiv.) upon vigorous stirring. Formation of white precipitate was observed. After 10 minutes, the reaction mixture was filtered, and the precipitate was washed with ice-cold diethyl (5 × 50 mL).

The washed precipitate was then redissolved in methanol, and the solvent was removed under reduced pressure. The resulting material was further dried under vacuum to remove residual solvents, affording 212.6 mg of a viscous, colorless, transparent substance (0.413 mmol, 110%). The material was characterized by NMR spectroscopy ($D_2O$).

$^1$H NMR (500 MHz, $D_2O$, 298K): δ=3.26-3.17 (br m, 4H), 3.81–3.65 ppm (br m, 8H).

$^{31}$P NMR (202 MHz, $D_2O$, 298K): δ=4.47 ppm.

$^{19}$F NMR (471 MHz, $D_2O$, 298K): δ= - 149.98, - 150.03 ppm.

### 4.2.4 Synthesis of Bn-protected PPz-PGA (P3)

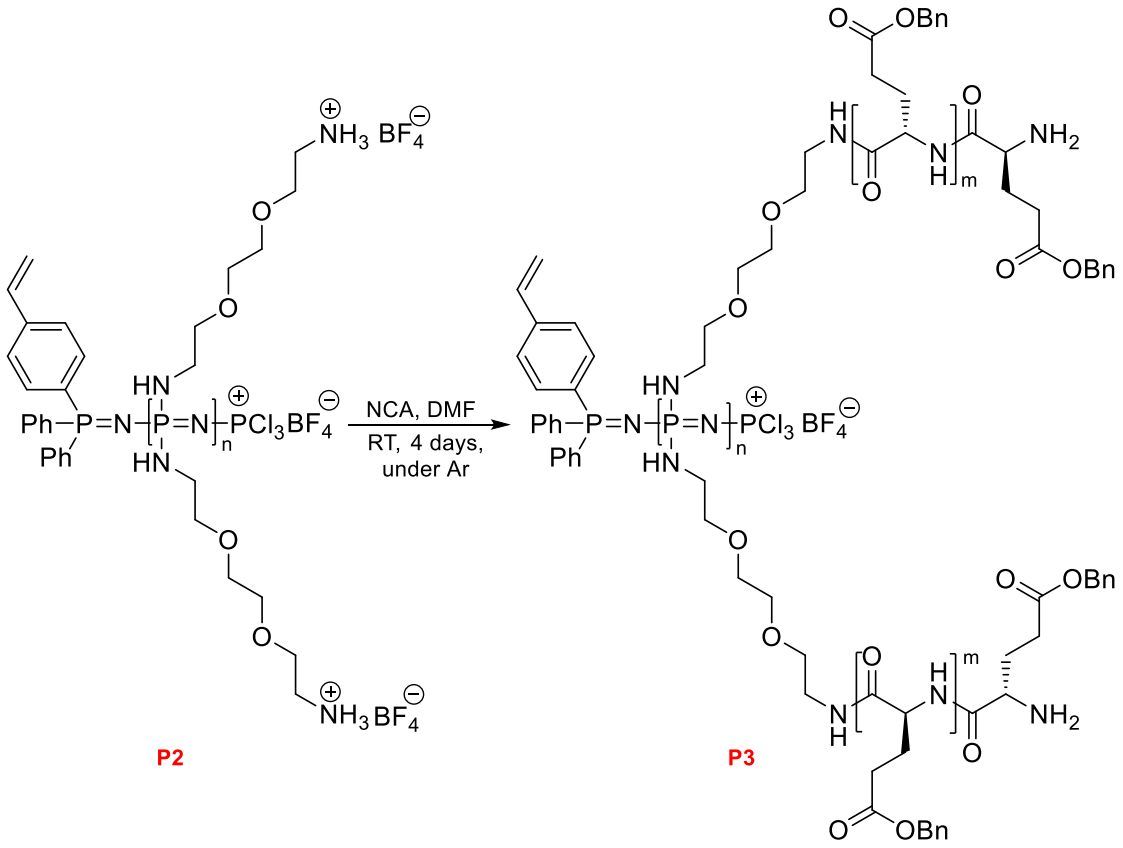


Boc-deprotected PPz (30.5 mg, 0.059 mmol, 1.0 equiv.) was dissolved in 1.6 mL of anhydrous DMF. Separately, 5-benzyl L-glutamate N-carboxyanhydride (NCA) (1.641 g, 6.234 mmol, 105.7 equiv.) was dissolved in 14 mL of anhydrous DMF, which had been previously dried over 3 Å molecular sieves and purged with nitrogen. This NCA solution was then added to the PPz solution. The reaction mixture was stirred at room temperature under an argon atmosphere inside a glovebox for 4 days.

The mixture was then poured into 156 mL of cold diethyl ether, inducing the formation of a white precipitate. The suspension was centrifuged (10 min, 4000 rpm), and the collected solid was dried in a desiccator to afford 437 mg (0.0196 mmol, 33%) of a transparent, rigid material. The product was characterized by NMR spectroscopy (DMSO) and GPC (DMF).

Important note: it is crucial to transfer the collected solid to a separate vial before drying in a desiccator, as it becomes difficult to scrape once dried in centrifuge tubes.

$^{1}$H NMR (300 MHz, DMSO): δ=2.47–1.70 (br m, 4H), 4.26-3.21 (br, 1H), 5.03 (br, 2H), 7.32 ppm (br, 5H).

$^{31}$P NMR: attempt failed

### 4.2.5 Bn-deprotection of PPz-PGA

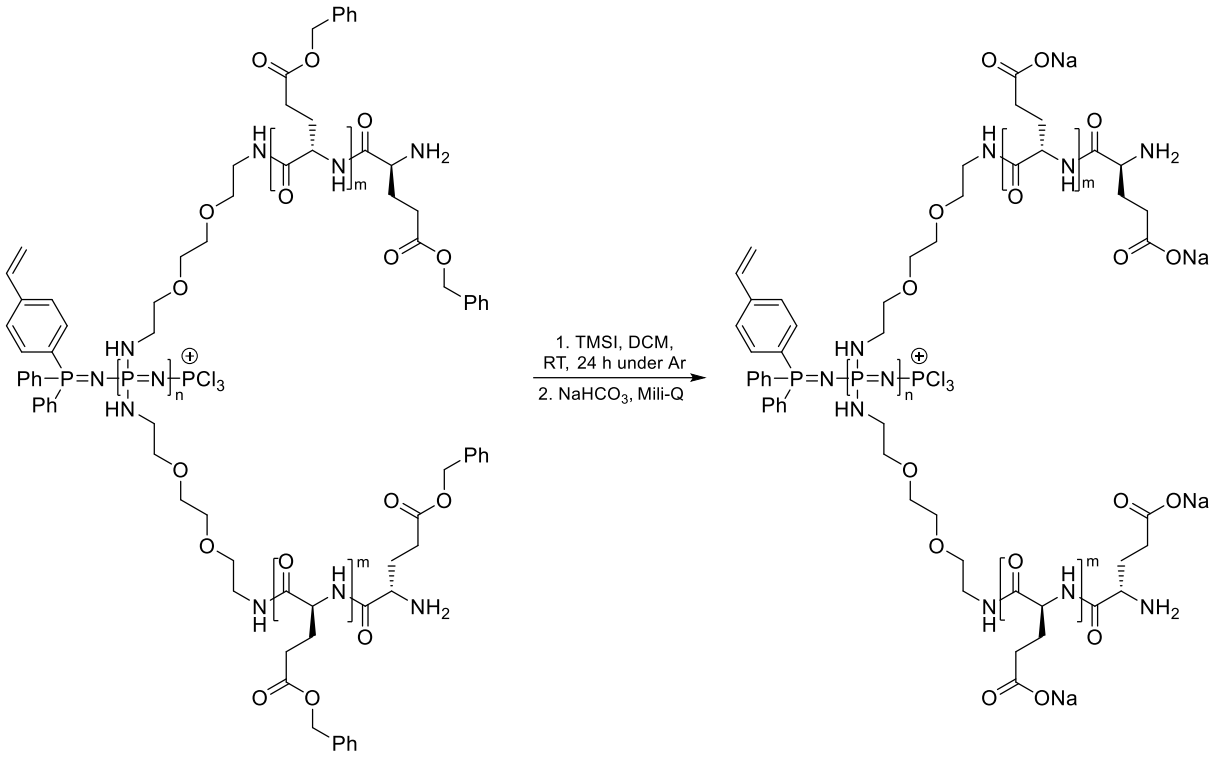


P3 P4

Bn-protected PPz-PGA (416.6 mg, 0.0187 mmol, 1.0 equiv.) was placed in a flat-bottom flask and dissolved in 20 mL of anhydrous DCM (vortexing and prolonged stirring were required, but the polymer remained partially undissolved). 1.6 mL of iodotrimethylsilane (TMSI, 2.25 g, 11.20 mmol, 598.9 equiv., 6 equiv. per glutamic acid) was added, and the reaction was stirred for 24 hours at RT under argon atmosphere (inside a glovebox).

DCM was evaporated, and the residue was suspended in 10 mL of Mili-Q water and 10 mL of saturated $NaHCO_3$ solution. Two crystals of sodium thiosulfate were added, changing the suspension color from yellowish to white. The mixture was stirred for 24 hours at RT, washed with $Et_2O$ (3 × 10 mL), and dialyzed against deionized water (3.5 kDa MWCO) for 48 hours. The dialyzed solution was freeze-dried, yielding a bluish solid.

For further purification, the material was redissolved in Milli-Q water and divided equally into four Vivaspin 6 centrifugal concentrators (30 kDa MWCO), pre-washed three times with Milli-Q water. A total of 200 mL of Mili-Q water was passed through the concentrators. The retained product was freeze-dried, affording 167.5 mg (0.0108 mmol, 58% yield) of a white, fluffy substance. The purified material was characterized by GPC (aqueous) and NMR spectroscopy ($D_2O$).

$^1$H NMR (500 MHz, $D_2O$, 298K): δ=2.01 (br m, J=57.6 Hz, 2H), 2.42-2.30 (br m, 2H), 4.34 ppm (s, 1H).

$^{31}$P NMR (500 MHz, $D_2O$, 298K): δ=4.11, 11.20, 20.34 ppm.

### 4.2.6 Synthesis of Cbz-protected β-Ala-Boc-hydrazide linker


$C_{11}H_{13}NO_4$ [223.23] $C_5H_{12}N_2O_2$ [132.16] $C_{16}H_{23}N_3O_5$ [337.38]

Cbz-β-alanine (1.501 g, 6.72 mmol, 1.0 equiv.), tert-butyl carbazate (0.888 g, 6.72 mmol, 1.0 equiv.), and EDC·HCl (1.353 g, 7.06 mmol, 1.05 equiv.) were combined in a round-bottom flask and dissolved in 60 mL of anhydrous DCM. The mixture was stirred at RT under a $N_2$ atmosphere for 2 hours.

After completion, the reaction mixture was washed with 60 mL of 0.1M acetic acid (AcOH). The aqueous layer was extracted three times with 30 mL of DCM. The combined organic layers were then washed sequentially with 60 mL of AcOH (twice), followed by 60 mL of saturated $NaHCO_3$ solution, and finally with 60 mL of water. The organic phase was dried over anhydrous $Na_2SO_4$, filtered, and concentrated under reduced pressure. Drying under vacuum afforded a white solid (crude yield: 2.018 g, 5.98 mmol, 89%). The crude product was characterized by NMR ($CDCl_3$) and ESI-MS.

$^1$H NMR (500 MHz, $CDCl_3$, 298K): δ=1.46 (s, 9H), 2.50 (td, J=5.7, 50.4 Hz, 2H), 3.54–3.46 (m, 2H), 5.09 (s, 2H), 5.58 (s, 1H), 6.52 (s, 1H), 7.37–7.28 (m, 5H), 7.58 ppm (s, 1H).

$^{13}$C NMR (75 MHz, $CDCl_3$, 298K): δ=28.1, 34.1, 40.0, 66.7, 82.2, 128.0, 128.1, 128.5, 136.5, 155.5, 156.6, 171.2 ppm.

### 4.2.7 Cbz-deprotection of β-Ala-Boc-hydrazide linker

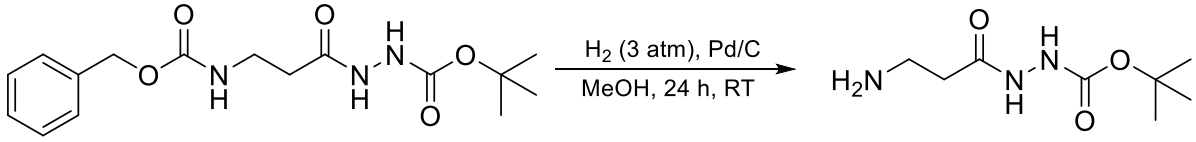


$C_{16}H_{23}N_3O_5$ [337.38] $C_8H_{17}N_3O_3$ [203.24]

Cbz-β-alanyl-boc-hydrazide (1.989 g, 5.88 mmol, 1.0 equiv.) was dissolved in 150 mL of methanol (MeOH). To this solution, 125.85 mg of wet Pd/C catalyst was added, ensuring it was premixed with methanol to prevent dispersion. The mixture was then subjected to hydrogenation at 3 atm for 24 hours at RT. The reaction mixture was then filtered through Celite to remove the catalyst, and the filtrate was concentrated using rotary evaporation. This process yielded 0.976 g of the product (4.80 mmol, 82%) in the form of a white foam. The product was characterized by NMR ($CDCl_3$), ESI-MS, and IR spectroscopy.

$^{1}$H NMR (500 MHz, $CDCl_3$, 298K): δ=1.45 (s, 9H), 2.39 (t, J=5.6 Hz, 2H), 3.05 (t, J=5.6 Hz, 2H), 4.69 ppm (s, 3H).

$^{13}$C NMR (125 MHz, $CDCl_3$, 298K): δ=28.2, 36.3, 37.7, 81.5, 155.7, 172.1 ppm.

### 4.2.8 Synthesis of β-Ala-Boc-hydrazide linked PPz-PGA

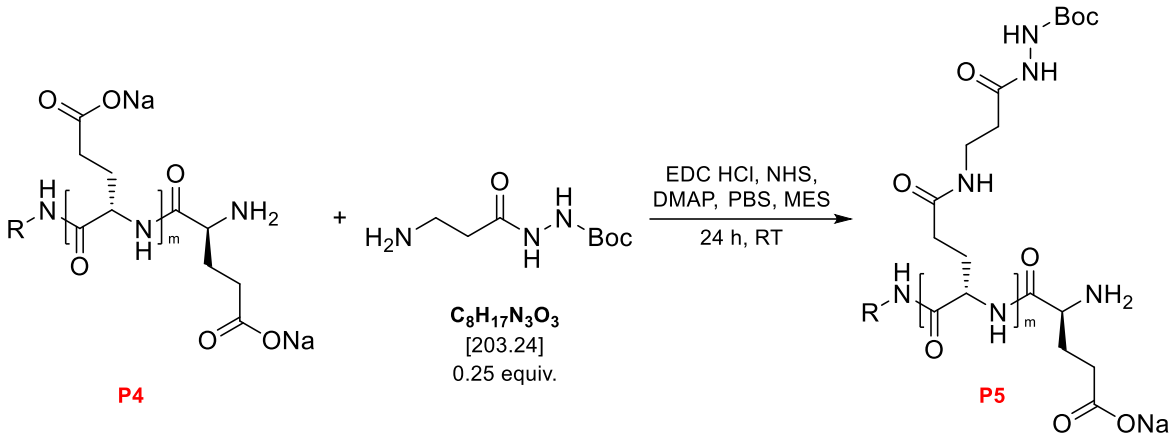


Bn-deprotected PPz-PGA (147.2 mg, 0.974 mmol with respect to glutamic acid residues, 1.0 equiv.) was dissolved in 15.6 mL of deionized water in a 100 mL round-bottom flask. The following solutions were added sequentially under stirring at room temperature (RT): EDC·HCl (2065 µL, 100 mg/mL in water, 1.077 mmol, 1.1 equiv.), NHS (1235 µL, 100 mg/mL in water, 1.073 mmol, 1.1 equiv.), and MES buffer (1915 µL, 1.0 M, 10x).

After stirring for 15 minutes, additional reagents were added: DMAP (646 µL, 50 mg/mL in DMF, 0.264 mmol, 0.27 equiv.), β-Ala-Boc-hydrazide linker (5329 µL, 10 mg/mL in DMF, 0.262 mmol, 0.27 equiv.), and PBS (2503 µL, 10x). The reaction mixture was stirred for 24 hours at RT, then purified by ultrafiltration using *Vivaspin 6* centrifugal concentrators (30 kDa MWCO) with a solution of 20% ethanol in Milli-Q water. Approximately 300 mL of wash solution went through, followed by three cycles with pure Milli-Q water. Freeze-drying yielded 150.1 mg (0.782 mmol, 80% yield) of a white, fluffy solid. The purified material was characterized by NMR ($D_2O$), ESI-MS, DLS, and GPC (aqueous).

$^{1}$H NMR (500 MHz, D2O, 298K): δ=1.45 (s, 9H), 2.01 (d, J=48.3 Hz, 10H), 2.37 (s, 10H), 2.53 (s, 2H), 3.50 (s, 2H), 4.35 ppm (s, 5H)

$^{13}$C NMR (125 MHz, D2O, 298K): δ=25.0, 27.3, 27.5, 32.6, 33.1, 35.5, 53.5, 82.9, 173.5, 174.5, 180.1

$^{31}$P NMR (202 MHz, $D_2O$, 298K): δ=4.93, 12.43, 20.13 ppm.

### 4.3 Conjugation procedure

#### 4.3.1 Boc-deprotection of β-Ala-Boc-hydrazide linked PPz-PGA

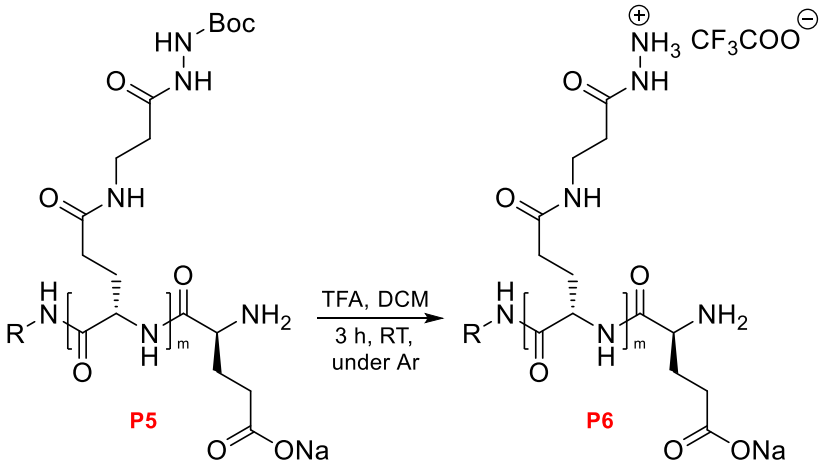


39.8 mg of P5 was placed in a two-necked 25 mL round-bottom flask, and 6 mL of anhydrous DCM was added. The mixture was stirred for several minutes until a homogeneous suspension formed. Subsequently, 3 mL of a TFA solution (3:1 DCM:TFA) was added slowly. The reaction was stirred under an Ar atmosphere for 3 hours. The solvent was then rapidly evaporated under reduced pressure, and the flask was kept under vacuum for 1 hour. The product was characterized by NMR spectroscopy and used without further purification in the next step. The yield for this step was not quantified.

#### 4.3.2 Conjugation of β-Ala-hydrazide linked PPz-PGA with SA-401

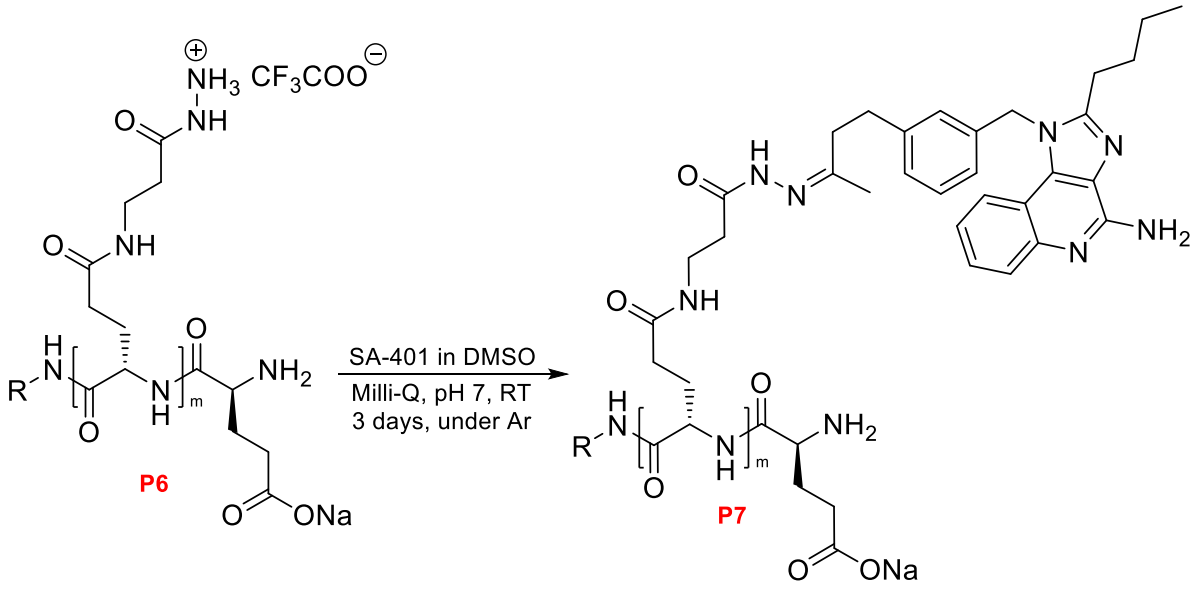


The deprotected polymer P6 from the previous step, which was in a 25-mL two-necked round-bottom flask, was dissolved in 4 mL of Milli-Q water. A turbid solution was obtained, with a pH of approximately 1-2. Several drops of saturated sodium carbonate solution were added to neutralize the mixture, resulting in the formation of a white precipitate. Next, a solution of

13.3 mg SA-401 in 3 mL of DMSO was added to the reaction mixture, which was stirred for 3 days at room temperature under an Ar atmosphere. The solvent was removed by freeze-drying.

The resulting product was then resuspended in 15 mL of 0.1 M sodium carbonate solution and distributed into two 15 mL centrifuge tubes. The product was washed six times with 6 mL of DCM (3 mL for each tube per wash). Residual DCM was removed under reduced pressure, and the product was diluted by a factor of five. Further purification was performed via ultrafiltration in *Vivaspin 6* tubes with a MWCO of 30 kDa. After loading the sample into four tubes, it was washed through with 30 mL of Milli-Q water, then three times with 30 mL of 20% EtOH in Milli-Q, and finally once more with 30 mL of Milli-Q water. The sample was transferred to a separating funnel in a total volume of 50 mL and washed again three times with 10 mL of DCM. Freeze-drying yielded 35 mg of the conjugate. Characterization was performed using NMR ($D_2O$), GPC (aqueous), DLS, HPLC-MS, and UV-Vis spectroscopy.

$^{1}H$ NMR (500 MHz, $D_2O$, 298K): δ=0.80 (br), 1.22 (br), 1.45 (br), 1.90 (d, J=50.3 Hz), 2.20 (br), 2.80 (br), 3.35 (br), 4.25 (br) ppm.

$^{31}P$ NMR (202 MHz, $D_2O$, 298K): δ=-2.90, 4.19, 12.37 ppm.

### 4.3.3 Drug loading quantification

To quantify drug loading, we identified a suitable solvent system: DMSO:PBS (1.5:2.5). This system effectively dissolves both the conjugate and the ligand, at least at concentrations below 50 µg/mL. A calibration curve was then prepared using concentrations ranging from 0 to 50 µg/mL, measured at five distinct wavelengths: 241, 243, 247, 265, and 322 nm.

Note on stock solution preparation: To achieve a 50 µg/mL stock, 1 mg of SA-401 was dissolved in 1.5 mL of DMSO, followed by the slow, portionwise addition of 2.5 mL of PBS. Vortexing was avoided to prevent precipitation. This stock concentration is not stable; therefore, the solution was immediately diluted to 50 µg/mL for stability.

# 5 Experimental part: *in vitro* cell culture assays

## 5.1 Materials and methods

**Isolation of the bone marrow:**

- RPMI medium: RPMI 1640 (Gibco, cat. number 11875093) + 1% L-Glutamine + 1% antibiotic solution (Sigma Aldrich, cat. number A5955) + 0.1% 2-mercaptoethanol
- FBS (Biosera, cat. number FB-1001/500)

**Flow cytometry:**

- Anti-Mouse F4/80 PE-Cy7, clone BM8, cat. number 25-4801-82
- FlowFacs buffer: 1x PBS + 1% BSA

**Seeding and activation of cells:**

- Resiquimod R848 (Tocris, cat. number 4536)
- LPS (Thermo Fisher Scientific, cat. number L23352)
- SA-401 (synthesized)
- Trypsin: 0.02% trypsin + 0.02% EDTA

**Lysis and measurement of protein concentration**

- Lysis buffer: 1% SDS, 25 mM Tris, 1x protease inhibitor cocktail, pH 9.5
- SDS (Sigma Aldrich, cat. number 436143-100G)
- Tris base (Sigma Aldrich, cat. number 10708976001)
- Protease inhibitor cocktail (Thermo Fisher Scientific, cat. number 78429)
- BCA (Pierce BCA Protein Assay Kit, cat. number 23225)

**SDS PAGE:**

- Separation gel 12% (2x): 4 mL of 30% acrylamide, 2.5 mL of 4x separation buffer, 3.4 mL of $dH_2O$, 4 uL of TEMED, 100 uL of 10% APS
- Stacking gel (2x): 330 uL of 30% acrylamide, 0.5 mL of 4x stacking buffer, 1.15 mL of $dH_2O$, 2 uL of TEMED, 20 uL of 10% APS
- 4x separation buffer: 153.9 g Tris base, 36.9 g Tris-HCl, 4 g SDS, 800 mL of $dH_2O$, adjust pH to 8.8, fill up to 1 L
- 4x stacking buffer: 78.5 g Tris-HCl, 2 g SDS, 400 mL of $dH_2O$, adjust pH to 6.8, fill up to 500 mL
- 10x running buffer: 30.2 g Tris base, 144 g glycine, 10 g SDS, fill up to 1 L
- 5x reducing loading buffer: 50% glycerol, 10% SDS, 0.313M Tris, pH 6.8, 0.05% bromophenol blue, 50 mM DTT

**Coomassie Blue Silver staining solution:**
To 100 mL of water, add phosphoric acid to achieve a final concentration of 10% (v/v) in the 1 L solution, add 100 g of ammonium sulfate, add 1.2 g of Coomassie Blue G-250, add water to bring the volume to 800 mL, add 200 mL of 100% methanol. Don't filter the solution!

### 5.2 Isolation of the bone marrow

The mouse was sacrificed by cervical dislocation and sprayed with 70% ethanol (EtOH) to minimize hair contamination during dissection and for disinfection. The upper legs were pinned to the dissection mat.

The skin was incised along the back and peeled away from the legs. The legs were then separated from the pelvis. All subsequent steps were performed in a flow box. Bones were thoroughly cleaned of muscle and other tissues, using gauze soaked in 70% EtOH for improved cleaning. If necessary, tools were cleaned with PBS and isopropanol. Hands could be wiped with paper tissues moistened with 70% EtOH. Clean bones were briefly dipped in 100% isopropanol, then transferred to a Petri dish containing RPMI medium.

An 18G needle was used to make a hole in a sterile 0.5 mL microtube, which was then placed inside a 2 mL microtube. From this point onward, all work was performed under sterile conditions. Bones were carefully cut at one end with scissors and placed into the 0.5 mL tube (with the cut end facing down). The smaller tube was closed, while the larger (2 mL) tube remained open. The assembly was centrifuged at 14 000 g for 30 seconds at 4°C (fixed angle rotor). The red bone marrow should now be collected in the larger microtube. The small tube containing the bones was discarded, and 1 mL of RPMI medium was added to the bone marrow. The bone marrow was resuspended in the medium using a pipette.

A BD filter/cell strainer was placed on a 50 mL centrifuge tube and pre-wetted with 2 mL of RPMI. The bone marrow suspension was pipetted onto the filter, which was then washed with an additional 3 mL of RPMI medium. The filter was discarded, and the volume was adjusted to 5 mL. The tube was centrifuged in a swinging bucket rotor for 8 minutes at 250 g, 4°C. After centrifugation, the supernatant was discarded, and 2 mL of 0.84% $NH_4Cl$ solution (pre-warmed to 37°C) was added to lyse erythrocytes. The cells were mixed thoroughly with a pipette. Lysis was stopped after 3 minutes by adding 10 mL of RPMI medium.

The cell suspension was mixed well, and 20 µL of cells were combined with 20 µL of trypan blue solution in a 0.5 mL tube. Then, 10 µL of this mixture was loaded into a Bürker chamber for cell counting (note: blue cells are dead and should not be counted). The average of three counts (each representing the number of cells in 25 fields) was multiplied by 10 000,

then by 2 (dilution factor), and finally by the total solution volume (12 mL). A total of 45 million cells was obtained.

The remaining cells (in the 50 mL tube) were centrifuged again (8 min, 250 g, 4°C, swinging bucket rotor), the supernatant was discarded, and 15 mL of RPMI medium supplemented with 10% FBS was added. The cells were resuspended and were then ready for further processing.

### 5.3 Differentiation of bone marrow derived macrophages

**Day 0:** Cells obtained from the previous step were seeded into TPP tissue culture dishes (87 mm diameter). For each dish, 1 mL of cell suspension (approximately 3 million cells) was added, followed by 9 mL of RPMI medium (with 10% FBS) supplemented with LCCM to achieve a final concentration of 30% LCCM after mixing. Images were taken at 100x and 400x magnification. The cells were incubated at 37°C with 5% $CO_2$.

**Day 3:** An additional 10 mL of RPMI medium (with 10% FBS) supplemented with 30% LCCM was added to each tissue culture dish. Images were again taken at 100x and 400x magnification.

**Day 7:** Images were taken at 100x and 400x magnification. The supernatant was discarded, and the cells were washed once with PBS (3 x 2 mL). Next, 1.5 mL of trypsin-EDTA solution was added to each dish. After incubating for 5 minutes at 37°C, the trypsinization reaction was stopped by adding 2 mL of medium. Cells should appear round after trypsinization. To facilitate detachment, gentle pipetting can be used. Tilting the dish at approximately 30° and using light can help visualize and detach the cells more easily.

All cells were collected and equally distributed into two 50 mL centrifuge tubes. The cells were centrifuged in a swinging bucket rotor for 8 minutes at 250 g, 4°C. Supernatants were discarded, and 10 mL of RPMI medium (with 10% FBS) was added to each tube. The cells were resuspended and combined into a single tube, and an additional 5 mL of medium was added. Cells were counted as previously described, yielding a total of 240 million cells. The cells were then analyzed by flow cytometry.

### 5.4 Flow cytometry

31.2 µL of the cell solution (approximately 300 000 cells) was taken and added to 2 mL of FacsFlow (FF) buffer (1x PBS + 1% BSA) in a specialized flow cytometry tube. The sample was then centrifuged at 250 g for 5 minutes at 4°C. After centrifugation, the supernatant was

discarded, and 1 mL of FF buffer was added. The sample was centrifuged again under the same conditions, and the supernatant was discarded.

Next, 1 µL of antibody (Anti-mouse F4/80 conjugated with PE-Cy7, 0.2 mg/mL, 100x) was added to approximately 100 µL of the remaining solution (after discarding the supernatant, approximately 100 µL of liquid remains in the tube). The sample was incubated for 20 minutes in the refrigerator, protected from light. After incubation, 2 mL of FF buffer was added, and the sample was centrifuged again. The supernatant was removed, and the cells were resuspended in 300 µL of FF buffer. The sample was then prepared for flow cytometry analysis.

The following parameters were used for measurement: dye = PE-Cy7, 30 000 events collected, sample volume of 50 µL, and a flow rate of 14 µL/min.

### 5.5 Cell seeding for the activation with ligands

Cells obtained in the previous step 5.3 (25 mL of cells in a 50 mL centrifuge tube) were equally distributed into two 50 mL centrifuge tubes (12.5 mL in each). One tube was centrifuged at 250 g for 8 minutes at 4°C (swinging bucket rotor), after which the supernatant was discarded and the cells were resuspended in 12.5 mL of RPMI medium pre-warmed to room temperature (without FBS). The cells were then distributed into new TPP tissue culture dishes (87 mm diameter).

Cells resuspended in FBS-containing medium (from the first centrifuge tube) were seeded in RPMI medium with FBS, while cells resuspended in FBS-free medium (from the second centrifuge tube) were seeded in RPMI medium without FBS. For seeding, 620 µL of cell suspension (containing approximately 6 million cells) was resuspended in 10 mL of the corresponding medium. In total, 20 dishes were seeded with FBS-containing medium and 20 dishes with FBS-free medium. The cells were incubated at 37°C with 5% $CO_2$ for 24 hours.

### 5.6 Activation of cells with ligands

24 hours after seeding (day 8), cells were observed under the microscope and activated with ligands according to the scheme below. The following stock solutions were prepared:

- **SA-401**: a 1 mg/mL stock solution was prepared by dissolving 1 mg of SA-401 in 1 mL of Milli-Q water, with 5 µL of 3.5% HCl added to assist dissolution. Vortexing and incubation at 37°C were used to further aid dissolution.

- **R848:** a 1 mg/mL stock solution was prepared by dissolving 1 mg of R848 in 1 mL of Milli-Q water, with 6.5 µL of 3.5% HCl added to assist dissolution. Vortexing and incubation at 37°C were used to ensure complete dissolution.
- **LPS:** a 1 mg/mL stock solution was prepared by dissolving 1 mg of LPS in 1 mL of Milli-Q water, with 13 µL of 3.5% HCl added. Vortexing and incubation at 37°C were applied to aid dissolution.
- **Negative control (NC):** Prepared by mixing 1 mL of Milli-Q water with 13 µL of 3.5% HCl.

Stock solutions were subjected to a 10-fold dilution, incubated at 37°C for 10-15 minutes, and then applied to each cell culture dish (containing 10620 µL of medium) according to the table below. Cells were then incubated for 24 hours at 37 °C, 5% $CO_2$.

| | SA-401 | R848 | LPS | HCl (NC) |
|---|---|---|---|---|
| Stock solutions | 1.0 mg/mL | 1.0 mg/mL | 1.0 mg/mL | 0.0449% |
| 10-fold diluted solutions | 0.1 mg/mL | 0.1 mg/mL | 0.1 mg/mL | 0.00449% |
| Applied volume of diluted solution | 138 uL | 106 uL | 53 uL | 53 uL |
| Final ligand concentration | 1.28 ug/mL | 0.99 ug/mL | 0.50 ug/mL | - |
| Final HCl concentration | 0.000022% | 0.000022% | 0.000022% | 0.000022% |

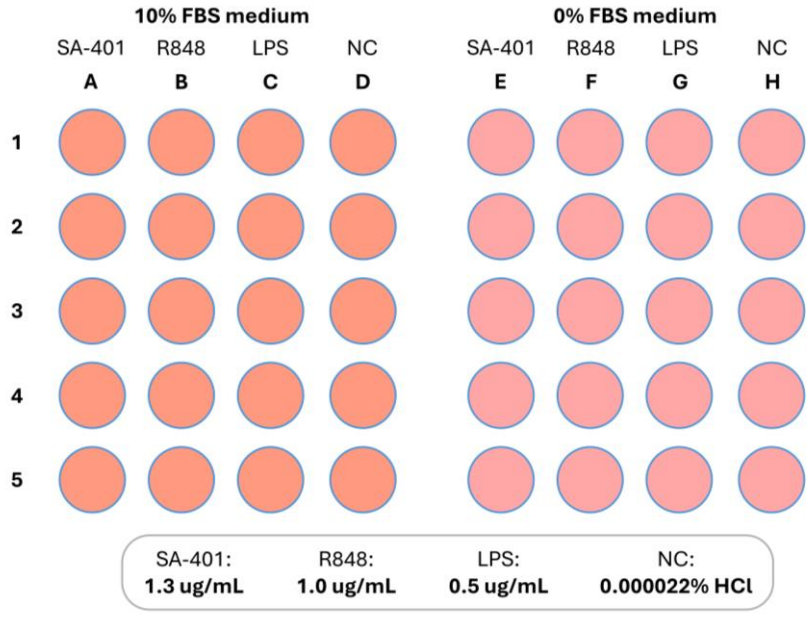

### 5.7 Cell harvesting and counting

24 hours after activation, cells were observed under the microscope and then processed for downstream procedures. First, 2 mL of supernatant from each dish was transferred to separate 2 mL microtubes and stored at -20 °C. For cells incubated with FBS, the remaining supernatant was discarded, and the cells were washed three times with 2 mL of PBS. It is recommended to tilt the dish and carefully add PBS from one lower edge, then gently swirl to wash the cells.

Next, cells were trypsinized with 1 mL of trypsin-EDTA solution for 5 minutes at 37 °C. Trypsinization was stopped by adding 2 mL of FBS-containing medium (RPMI with 10% FBS). It is important not to expose the cells to trypsin for too long, as this can cleave surface proteins and reduce cell viability. Cells were then detached from the surface by gentle pipetting as described earlier. The cell suspension was transferred to a 15 mL centrifuge tube. To ensure maximum cell recovery, 1-2 mL of medium was added to the culture dish, and the dish was washed by pipetting over any remaining cell clusters. It is best to process each dish individually to prevent cells from re-adhering after trypsinization, which would complicate detachment and transfer.

After collection, cells were centrifuged in a swinging bucket rotor at 250 g for 8 minutes at 4 °C. The supernatant was discarded, and 2 mL of fresh 1x PBS was added. The cells were centrifuged again under the same conditions, and the supernatant was discarded. This wash step with 2 mL of PBS, followed by centrifugation and supernatant removal, was repeated once more. After the third centrifugation, cells were resuspended in 0.5 mL of 1x PBS and transferred to 2 mL microtubes. One sample from each of the 4 groups was used for cell counting as described previously. Then, 1 additional mL of PBS was added to each tube, and cells were centrifuged again using a bench centrifuge at 3000 g for 4 minutes at room temperature. The supernatant was carefully removed with a 1 mL pipette, and the cell pellets were immediately frozen at -20 °C.

The following cell counts were obtained:

- A5: 2.9 million cells
- B5: 1.7 million cells
- C5: 2.3 million cells
- D5: 2.7 million cells

In the case of FBS-free conditions, trypsinization failed even after prolonged incubation. Instead, cells were washed three times with 2 mL of PBS, then 1 mL of PBS was added, and cells were detached using a cell scraper. The cell suspension was transferred to a 2 mL microtube. Another 1 mL of PBS was added to the dish, and scraping was repeated; the suspension was combined with the first. The combined suspension was centrifuged using a

bench centrifuge at 3000 g for 4 minutes at room temperature. After discarding the supernatant with a 1 mL pipette, the samples were immediately frozen and stored at -20 °C. Cell counting was unsuccessful due to high cell death caused by scraping.

**5.8 Lysis of the cells, measurement of the protein concentration**

Cell pellets were thawed, and 50 µL of lysis buffer (1% SDS, 25 mM Tris, 1x protease inhibitor cocktail, pH 9.5) was added to each microtube. Lysis was initiated using an ultrasonic bath for 30 seconds, followed by a 10-minute incubation on ice. This sonication-incubation cycle was repeated five times. Since the pellet remained visible, we conducted two freeze-thaw cycles (-78°C) to further disrupt the cells.

Next, an ultrasonication probe (60% amplitude, 0.4 cycle) was used. Samples were kept on ice during probe ultrasonication, and five sonication pulses were applied. To prevent foaming and protein degradation, the probe tip was positioned to touch the microtube's bottom. Samples were then incubated on ice for 10 minutes, and this sonication-incubation cycle was repeated twice more.

For protein quantification, a BCA assay was performed in a microplate following the manufacturer's protocol. Each sample was diluted 10-fold in a PCR tube, and 25 µL of the diluted sample was transferred to a microplate well. The plate was kept on ice during pipetting to maintain sample integrity. A working solution (50:1 Reagent A:B) was prepared, and 200 µL was added to each well within an 11-minute window to ensure uniform color development. The solution was mixed immediately by pipetting. The plate was then incubated at 37°C for 30 minutes, and absorbance was measured at 562 nm using a plate reader.

**5.9 SDS PAGE quality control**

Samples were prepared as follows: samples from groups A–D were diluted 4-fold, while samples from groups E–H were used without dilution. Each sample was loaded twice, with amounts of 3 µg and 6 µg. The protein marker used was the Broad Range Pre-stained Protein Marker from Proteintech. Gels were prepared as described in the Materials section and run at 120 V.

After electrophoresis, staining with Coomassie Blue Silver was performed. Gels were rinsed in distilled water ($dH_2O$) and fixed for 20 minutes in 50% ethanol containing 2% phosphoric acid. The gels were then washed twice for 20 minutes each with $dH_2O$. Following this, the staining solution was added, and the gels were stained overnight. Finally, the gels were washed three times with $dH_2O$ for 15 minutes each and visualized using the Syngene G:BOX visualization system, using the standard CBB protocol.

# 6 Experimental part: *in silico* modeling, MD simulations on TLR7/8, comparison of SA-401 and R848

## 6.1 Identification of residues involved in the interaction

PDB structures 5GMH (Monkey TLR7 with R848) and 3W3N (Human TLR8 with resiquimod) were loaded into Discovery Studio 2024 Visualizer. Interactions were visualized using the 2D interaction map feature.

## 6.2 Multiple sequence alignment (MSA)

Sequences were downloaded from UniProt and loaded into Jalview, where multiple sequence alignment was performed using the Muscle algorithm with default settings. The alignment results were then visualized using the ESPript 3.0 server.

## 6.3 Molecular dynamics simulations

Simulations were performed using GROMACS v2023.2 software. First, structures of apo proteins were prepared. We used the previously mentioned structures 5GMH and 3W3N. All ligands and water molecules were removed. Missing regions were restored using the AlphaFold 3.0 server. The H++ server was used to prepare the structures for simulation, assuming pH 7.4 and 5.0; missing hydrogens were added.

Ligands were prepared as follows: structures were drawn in Chem3D 20.0 and saved in mol format. Then, the Avogadro program was used to prepare Gaussian input files. Gaussian 16 was used to optimize geometry first, and then to assign ESP charges. The following commands were run in Gaussian:

```
%nprocshared=16
%mem=4GB
#n B3LYP/6-31G(d) Opt


%nprocshared=16
%mem=4GB
#HF/6-31G* pop=mk iop(6/33=2,6/41=10,6/42=17)
```

Then, AmberTools were further used to prepare ligands for the MD simulation and to prepare the GAFF force field. First, we generated .mol2 files:

```
conda activate AmberTools25

antechamber -i LIG.com.log -fi gout -o LIG.mol2 -fo mol2 -c resp -s 2
```

The command parmchk2 was used to generate missing parameters:

```
parmchk2 -i LIG.mol2 -f mol2 -o LIG.frcmod
```

Then, the tleap command was to generate coordinates and topology files:

```
tleap -f leap.in
```

Contents of the leap.in file:

```
source leaprc.gaff

LIG = loadmol2 LIG.mol2
loadamberparams LIG.frcmod

saveamberparm LIG LIG.prmtop LIG.inpcrd
quit
```

After that, acpype was run to generate files compatible with GROMACS:

```
acpype -p LIG.prmtop -x LIG.inpcrd
```

This generated a folder named MOL.amb2gmx, which includes MOL_GMX.gro (GROMACS coordinate file) and MOL_GMX.top (GROMACS topology file). Use the .top file to create the MOL.itp file by taking the first line and then the part from [atomtypes] to [dihedrals], followed by adding the lines:

```
#ifdef POSRES
#include "posre_MOL.itp"
#endif
```

Ligated structures (apo + ligand) were prepared using PyMol by manual docking of the ligand MOL_GMX.gro based on the original ligand position and combining it with the prepared apo protein structure. It is important to keep the original atom order. In the resulting file complex.pdb, the protein part must come first, followed by the ligands. Because two ligands were used, one was assigned residue number 1 and the other residue number 2.

Then the system was simulated in GROMACS with a simulation length of 200 ns. The force field used was *AMBER99SB-ILDN protein, nucleic AMBER94 (Lindorff-Larsen et al., Proteins 78, 1950-58, 2010).*

```
gmx pdb2gmx -f protein.pdb -o protein.gro -p protein.top -ignh

gmx editconf -f complex.pdb -o complex.gro
```

The topology file should be modified when the complex is simulated, after the force field description, add:

```
; Include ligand topology
#include "MOL.itp"
```

In the end it should be:

```
; Compound        #mols
Protein_chain_A     1
Protein_chain_B     1
MOL                 2
```

Create the simulation box:

```
gmx editconf -f complex.gro -o boxed.gro -c -d 1.0 -bt cubic
```

Solvate the system:

```
gmx solvate -cp boxed.gro -cs spc216.gro -o solvated.gro -p
protein.top
```

Add ions:

```
gmx grompp -f ions.mdp -c solvated.gro -p protein.top -o ions.tpr

gmx genion -s ions.tpr -o solvated_ions.gro -p protein.top -pname NA
-nname CL -neutral
```

Energy minimization:

```
gmx grompp -f em.mdp -c solvated_ions.gro -p protein.top -o em.tpr

gmx mdrun -v -deffnm em
```

Create an index if needed (for thermocoupling it might be needed to have PROTEIN_MOL index group):

```
gmx make_ndx -f em.gro -o index.ndx
```

NVT equilibration:

```
gmx grompp -f nvt.mdp -c em.gro -r em.gro -p protein.top -o nvt.tpr -
n index.ndx

gmx mdrun -deffnm nvt -nt 20
```

NPT equilibration:

```
gmx grompp -f npt.mdp -c nvt.gro -t nvt.cpt -r nvt.gro -p protein.top
-o npt.tpr -n index.ndx -maxwarn 1

gmx mdrun -deffnm npt -nt 20
```

Production MD run:

```
gmx grompp -f md.mdp -c npt.gro -t npt.cpt -p protein.top -o
md_0_200.tpr -n index.ndx

nohup gmx mdrun -deffnm md_0_200 -nt 20 > md_0_200.out 2>&1 &
```

### 6.4 Overview of the simulated systems

| System | Receptor | Ligand | pH | length / ns | Replicates |
|---|---|---|---|---|---|
| apo_1 | full TLR7 | - | 5.0 | 200 | 2 |
| apo_2 | full TLR7 | | 7.4 | 200 | 2 |
| apo_3 | 434-458 TLR7 | | 5.0 | 200 | 2 |
| apo_4 | full TLR8 | | 5.0 | 200 | 1 |
| apo_5 | 434-458 TLR8 | | 5.0 | 200 | 1 |
| R848_1 | full TLR7 | R848 | 5.0 | 200 | 2 |
| R848_2 | full TLR7 | | 7.4 | 200 | 2 |
| R848_3 | 434-458 TLR7 | | 5.0 | 200 | 2 |
| R848_4 | full TLR7 | R848 H+ | 5.0 | 200 | 2 |
| R848_5 | full TLR7 | | 7.4 | 200 | 2 |
| R848_6 | 434-458 TLR7 | | 5.0 | 200 | 2 |
| R848_7 | full TLR8 | | 5.0 | 200 | 1 |
| R848_8 | 434-458 TLR8 | | 5.0 | 200 | 1 |
| R837_1 | full TLR7 | R837 H+ | 5.0 | 200 | 1 |
| R837_2 | 434-458 TLR7 | | 5.0 | 200 | 1 |
| R837_3 | full TLR8 | | 5.0 | 200 | 1 |
| R837_4 | 434-458 TLR8 | | 5.0 | 200 | 1 |
| SA-401_1 | full TLR7 | SA-401 H+ | 5.0 | 200 | 1 |
| SA-401_2 | 434-458 TLR7 | | 5.0 | 200 | 1 |

### 6.5 Analysis of MD simulation runs

First trajectories should be extracted (choose group protein_MOL for centering and output):

```
gmx trjconv -s md_0_200.tpr -f md_0_200.xtc -o md_nojump.xtc -pbc
nojump -n index.ndx

gmx trjconv -s md_0_200.tpr -f md_nojump.xtc -o md_centered.xtc -
center -pbc mol -ur compact -n index.ndx

gmx trjconv -s md_0_200.tpr -f md_centered.xtc -o start.pdb -dump 0 -
n index.ndx

gmx trjconv -s md_0_200.tpr -f md_centered.xtc -o last.pdb -dump
10000 -n index.ndx

gmx trjconv -s md_0_200.tpr -f md_centered.xtc -o
md_centered_10_reduced.xtc -skip 10 -n index.ndx
```

**RMSD and RMSF analysis:**

```
gmx rms -s md_0_200.tpr -f md_centered_10_reduced.xtc -o
rmsd_backbone.xvg -n index.ndx
```

NB: use backbone for least squares fit and RMSD calculation

```
gmx rms -s md_0_200.tpr -f md_centered_10_reduced.xtc -o
rmsd_lig_1.xvg -n index.ndx
```

```
gmx rms -s md_0_200.tpr -f md_centered_10_reduced.xtc -o
rmsd_lig_2.xvg -n index.ndx

gmx rmsf -s md_0_200.tpr -f md_centered_10_reduced.xtc -o
rmsf_res.xvg -res -n index.ndx
```

NB: use backbone for root mean square calculation

**GBSA and PBSA calculations:**

```
conda activate gmxmmpbsa_env

nohup gmx_MMPBSA -O -i mmpbsa.in -cs md_0_200.tpr -ci index.ndx -cg 1
21 -ct md_centered.xtc -cp protein.top -o
FINAL_RESULTS_LIG1_MMPBSA_5000_10000.dat -eo
DECOMP_LIG1_5000_10000.csv &

nohup gmx_MMPBSA -O -i mmpbsa.in -cs md_0_200.tpr -ci index.ndx -cg 1
22 -ct md_centered.xtc -cp protein.top -o
FINAL_RESULTS_LIG2_MMPBSA_5000_10000.dat -eo
DECOMP_LIG2_5000_10000.csv &

nohup gmx_MMPBSA -O -i mmgbsa.in -cs md_0_200.tpr -ci index.ndx -cg 1
21 -ct md_centered.xtc -cp protein.top -o
FINAL_RESULTS_LIG1_MMGBSA_5000_10000.dat -eo
DECOMP_LIG1_GB_5000_10000.csv &

nohup gmx_MMPBSA -O -i mmgbsa.in -cs md_0_200.tpr -ci index.ndx -cg 1
22 -ct md_centered.xtc -cp protein.top -o
FINAL_RESULTS_LIG2_MMGBSA_5000_10000.dat -eo
DECOMP_LIG2_GB_5000_10000.csv &
```

mmpbsa.in contains:

```
&general
   sys_name = "Prot-Lig-ST",
   startframe = 5000,
   endframe = 10000,
   interval = 100,
   forcefields = "leaprc.protein.ff14SB",
   PBRadii = 2,
/
&pb
   istrng = 0.15,
   inp = 1,
/
```

mmgbsa.in contains:

```
&general
   sys_name = "Prot-Lig-ST",
   startframe = 5000,
   endframe = 10000,
   interval = 100,
   forcefields = "leaprc.protein.ff14SB",
```

```
   PBRadii = 2,
/

&gb
   igb = 5,
   saltcon = 0.15,
/
```

# 7 Results and discussion

## 7.1 Synthesis of SA-401

### 7.1.1 Synthesis of S1 and S2

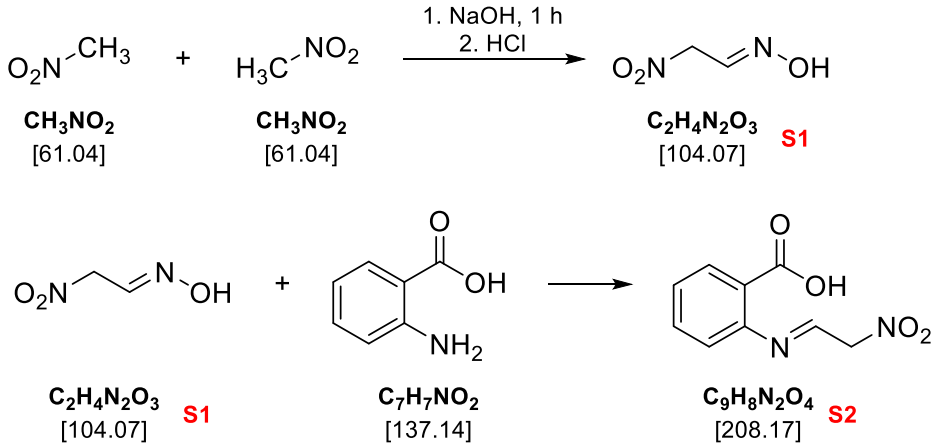


Product S2 was synthesized according to the procedure reported by Bachman, Welton et al.[155] Methazonic acid was first generated by reacting nitromethane with sodium hydroxide and was used directly, without further purification, in the subsequent reaction with anthranilic acid. Although the exact mechanism of this second reaction has not been fully elucidated, it is likely to proceed via a pathway analogous to nucleophilic substitution at a carbonyl center, involving the loss of iminic nitrogen, as illustrated in the figure below. The reaction afforded product S2 in a yield of 86%, consistent with the values previously reported in the literature.

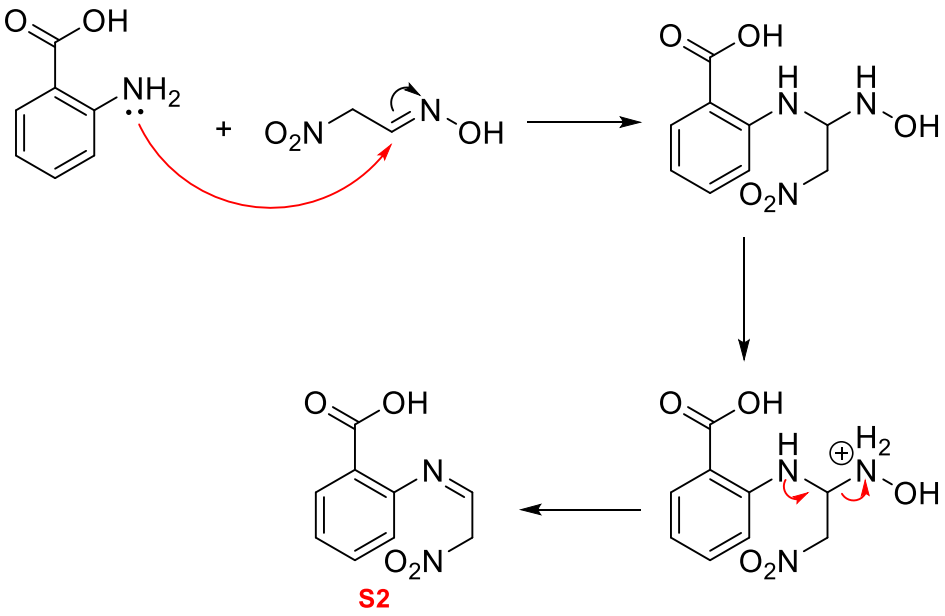


**Figure 25**: Proposed mechanism for the synthesis of product S2

### 7.1.2 Synthesis of S3


Previously, we synthesized product S3 using acetic anhydride; however, in this synthesis, all attempts to prepare S3 with acetic anhydride were unsuccessful. As an alternative strategy, product S3 was synthesized in a moderate yield of 59% via activation of the carboxyl group with thionyl chloride. Aluminum chloride acts as a Lewis acid in this reaction, facilitating the activation of the electrophilic carbon of the carbonyl group. The proposed mechanism is shown below.

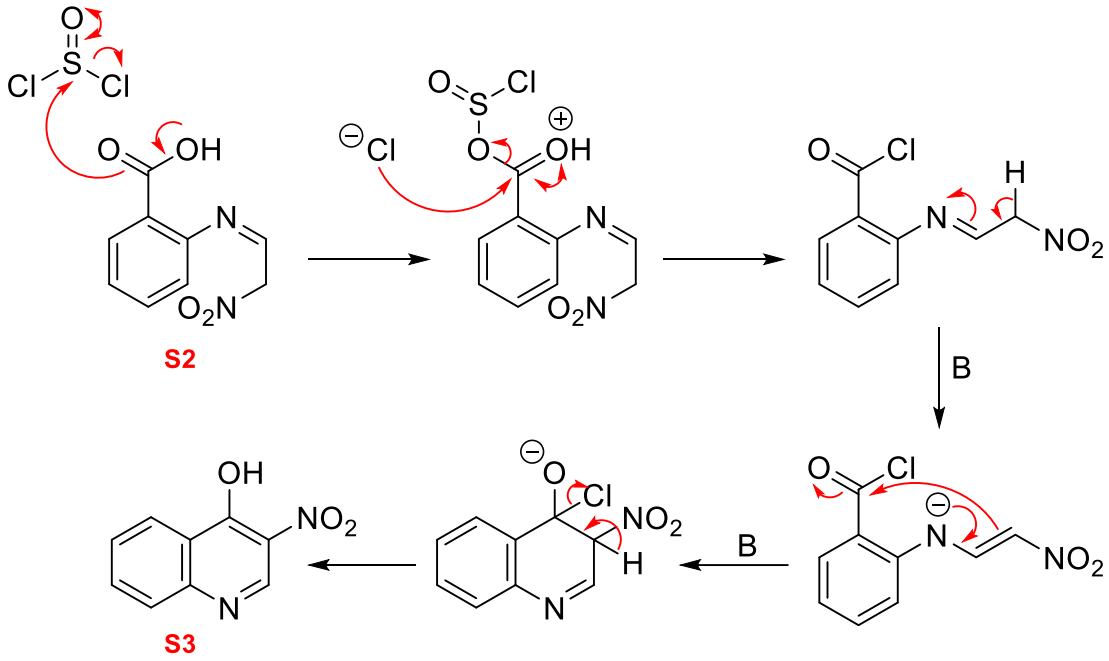


**Figure 26**: Proposed mechanism for the synthesis of product S3

### 7.1.3 Synthesis of S4

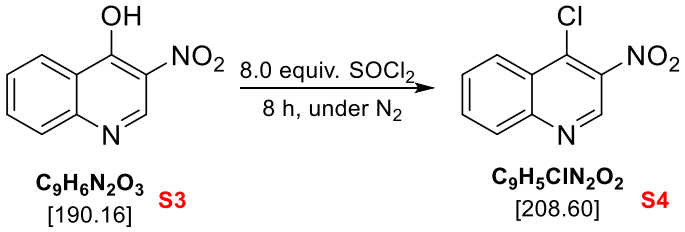


Product S4 was synthesized following the procedure reported by Stefan Aichhorn[156]. The reaction time appears to be critical, as attempts to extend the duration to 24 hours were unsuccessful. The transformation proceeds via a nucleophilic aromatic substitution

mechanism, likely involving an addition–elimination pathway[157]. The presence of a nitro group in the ortho position relative to the hydroxyl group facilitates the reaction by stabilizing the intermediate species. The isolated yield of 75% was slightly lower than that reported in the original procedure, but no other deviations were observed.

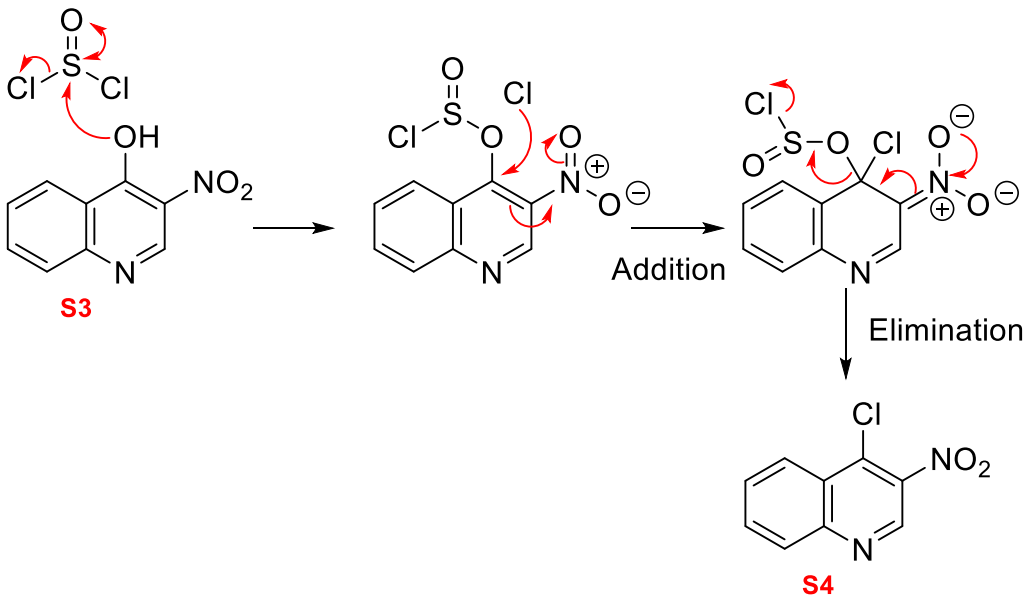


**Figure 27**: Proposed mechanism for the synthesis of product S4

### 7.1.4 Synthesis of S5

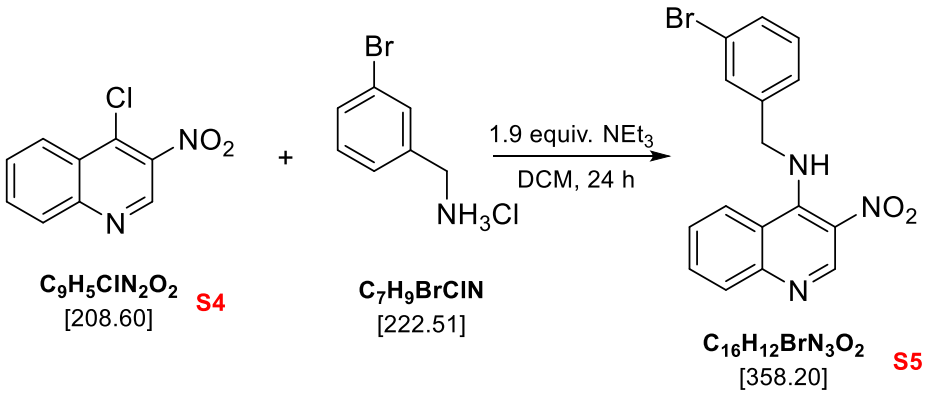


Product S5 was synthesized in 90% yield following the procedure reported by Stefan Aichhorn, with slight modifications[156]. Unlike the original procedure, 3-bromobenzylamine was used in the form of its hydrochloride salt, which required the use of 1.9 equivalents of triethylamine. The reaction proceeds via a nucleophilic aromatic substitution mechanism, as described below.

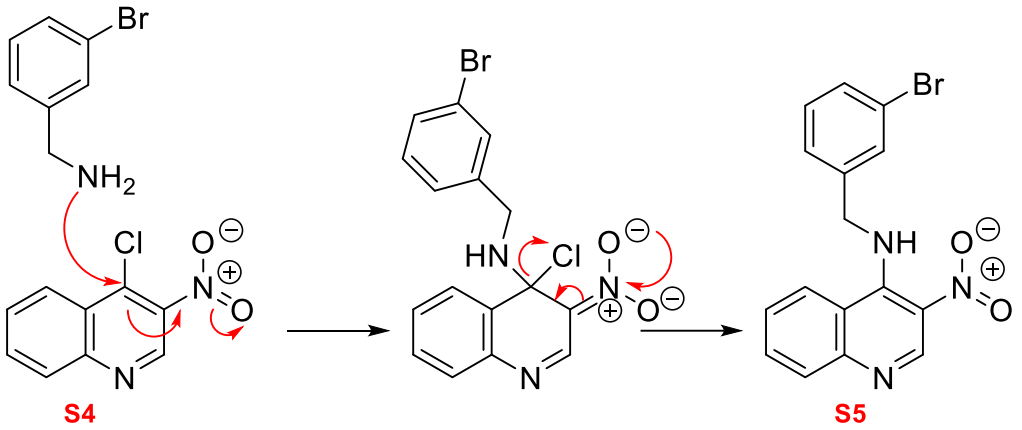


**Figure 28**: Proposed mechanism for the synthesis of product S5

### 7.1.5 Synthesis of S6

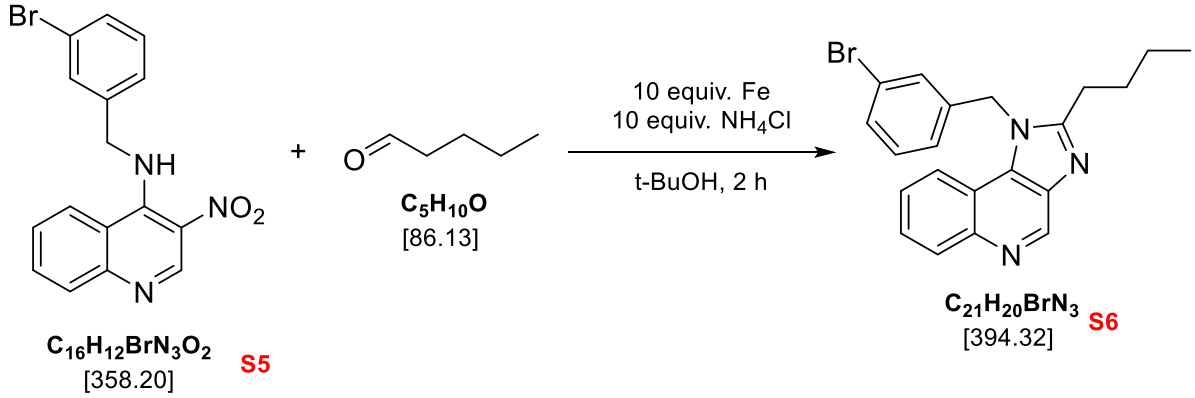


Product S6 was synthesized in a yield of 73% using a modified version of the procedure reported by Stefan Aichhorn[156]. In the first step, the nitro group is reduced with iron in the presence of ammonium chloride. In the second step, the resulting diamine undergoes a Phillips-Ladenburg reaction[158], in which pentanal serves as the methylene source[159]. It is essential to ensure that ethyl acetate is completely removed after extraction; therefore, the reaction residue should be kept under vacuum for a sufficient period. If this step is skipped, the desired precipitate will not form upon the addition of heptane.

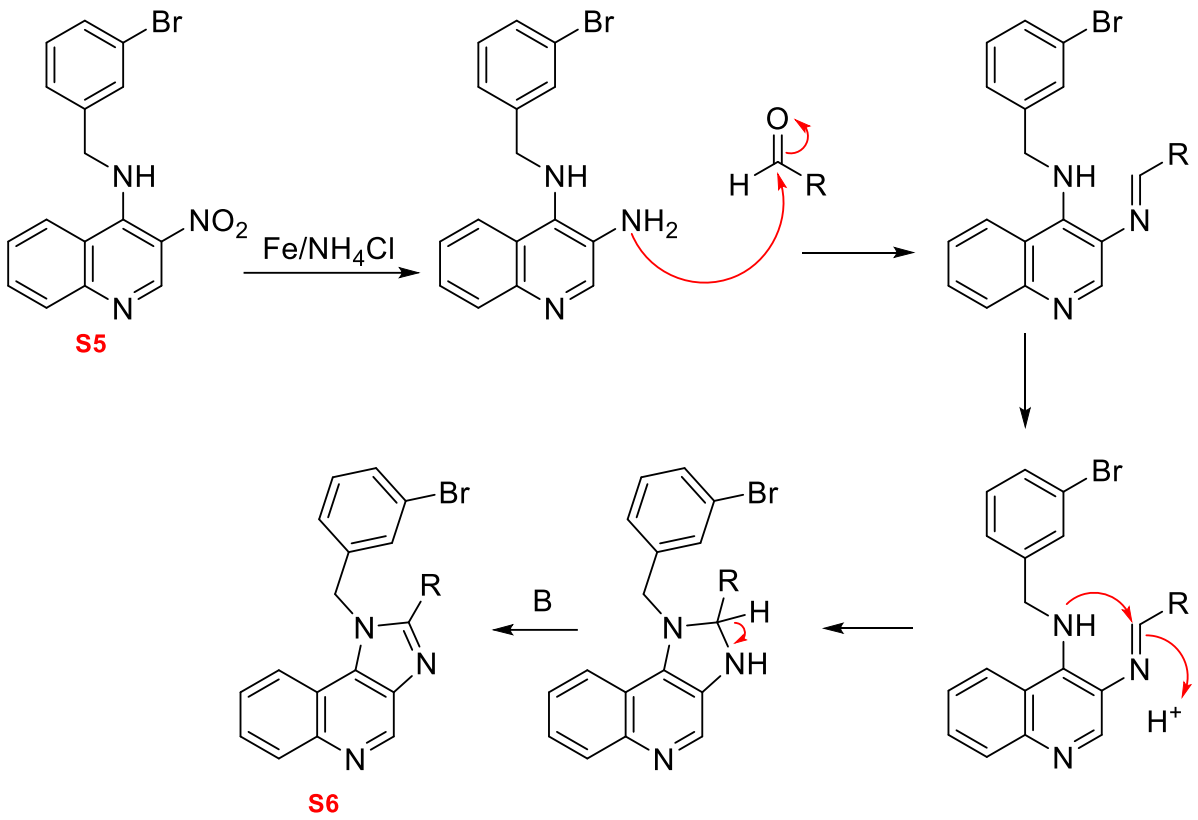


**Figure 29**: Proposed mechanism for the synthesis of product S6

### 7.1.6 Synthesis of S7

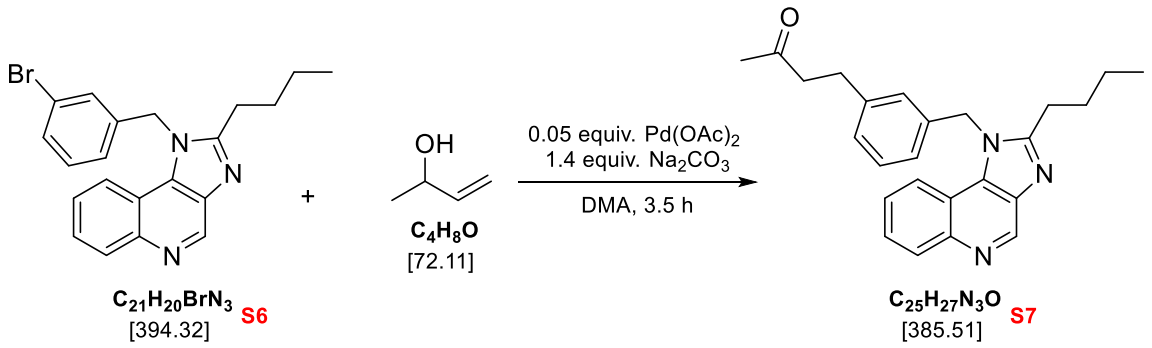


Product S7 was synthesized following a modified procedure reported by Stefan Aichhorn[156]. The reaction is an example of the Mizoroki–Heck reaction, a palladium-catalyzed cross-coupling of aryl or vinyl halides with alkenes. Initially, attempts to reproduce the reaction as described were unsuccessful, likely due to impurities in some of the reagents. In addition to the aryl halide and alkene, two important components of the Heck reaction are the catalyst and base. We tested different catalysts (e.g., $PdCl_2$ and $Pd(OAc)_2$) and varied the catalyst loading from 0.05 to 0.25 equivalents, but these modifications did not resolve the problem. Subsequently, we changed the base from triethylamine to sodium carbonate and were able to obtain the desired product.

Triphenylphosphine and its derivatives are frequently used in Heck reactions; however, in our case, the addition of triphenylphosphine was unnecessary and did not improve the yield. HPLC-MS analysis revealed that the product concentration was nearly the same after 1 hour and 3.5 hours of reaction, indicating that a 1-hour reaction time is sufficient. Furthermore, after 1 hour of reaction, no starting material (S6) remained. The corresponding HPLC chromatograms are provided in the supplementary section.

We also attempted to identify the reaction's side products. For this purpose, the EtOAc extract was analyzed using HPLC-MS. The UV chromatogram showed major impurities with m/z values of 316 and 476. The side product with m/z 316 likely arises from the debromination of the product S6. We hypothesized that debromination could be minimized by lowering the reaction temperature. The mixture was initially heated to 90 °C under nitrogen, but no product formation was observed after 4 hours. The temperature was then increased stepwise: to 100 °C for 15 hours, with no significant product, and finally to 120 °C for 2.5 hours, which also yielded little product. Only upon increasing the temperature to 130 °C did product formation occur.

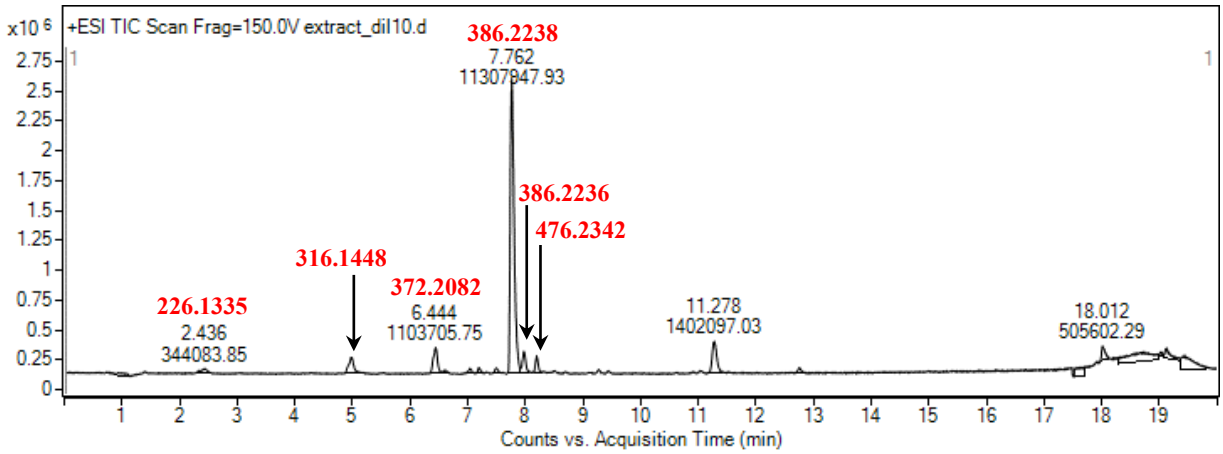


**Figure 30**: HPLC-MS chromatogram of EtOAc extract after the reaction; TIC

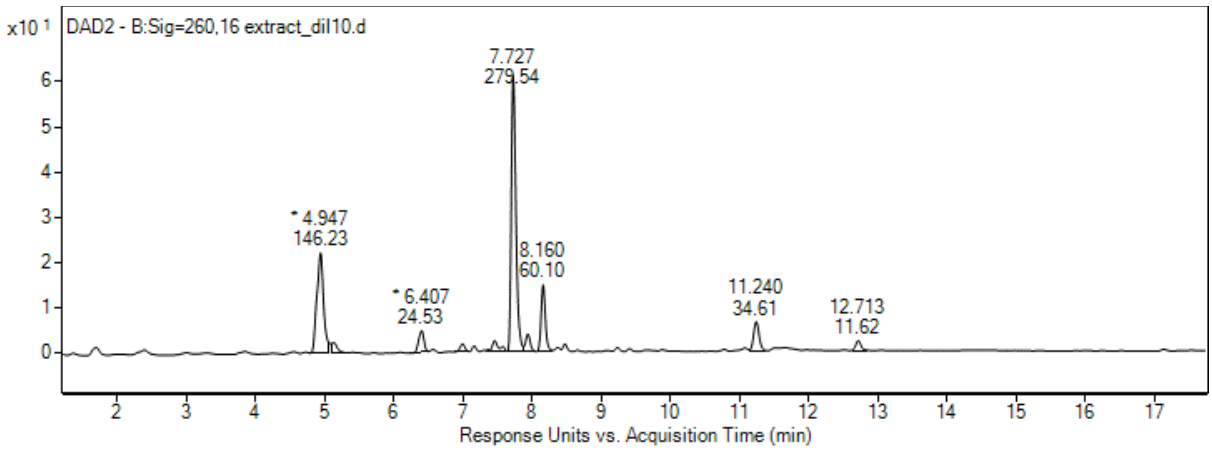


**Figure 31**: HPLC-MS chromatogram of EtOAc extract after the reaction; UV detector

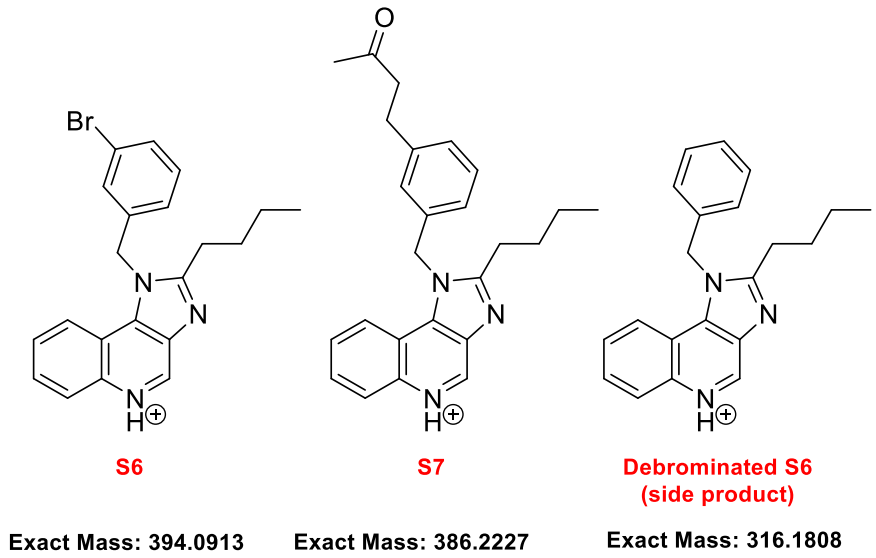


The mechanism of this reaction consists of four principal steps[160]. First, in situ formed Pd(0) undergoes oxidative addition. Next, it forms a π-complex with the alkene, followed by migratory insertion. The third step is β-hydride elimination – depending on the base used (e.g., $Et_3N$, $NaHCO_3$, $Na_2CO_3$), different double bond positions can result[161]. One of the possible products then undergoes tautomerization to form a ketone. The final step in the cycle is reductive elimination, which regenerates Pd(0) and closes the catalytic cycle.

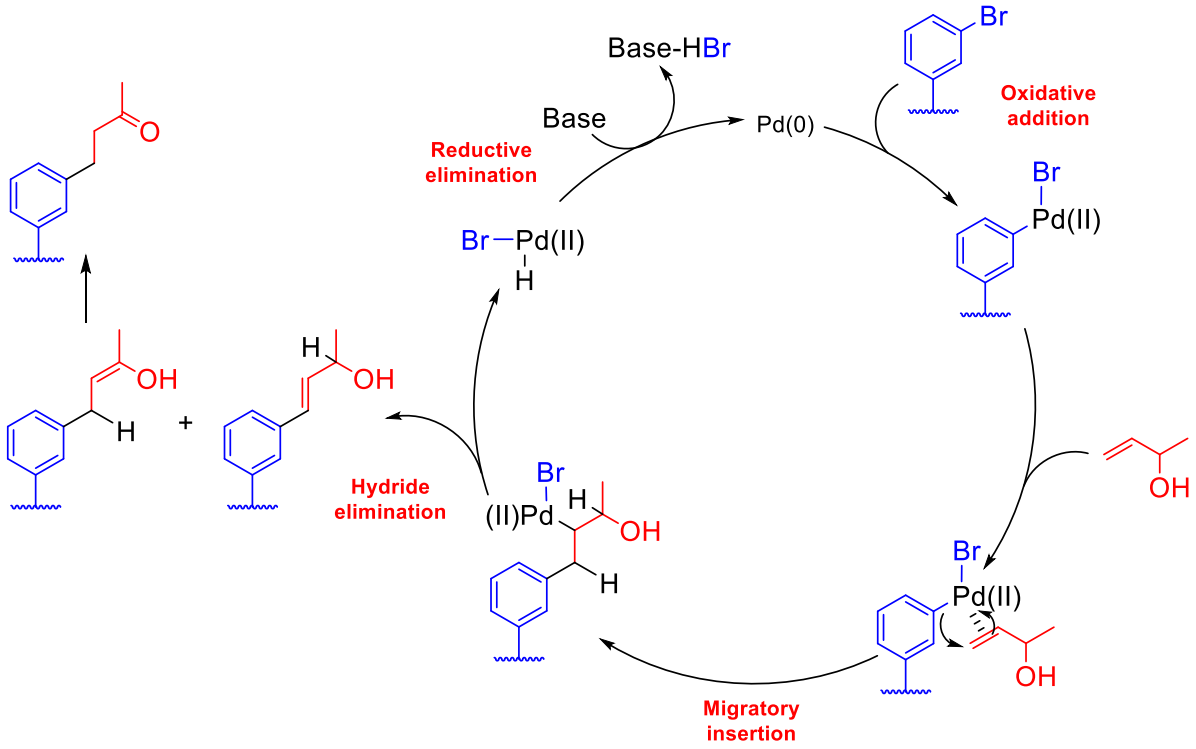


**Figure 32**: Proposed mechanism for the synthesis of product S7

### 7.1.7 Synthesis of S8

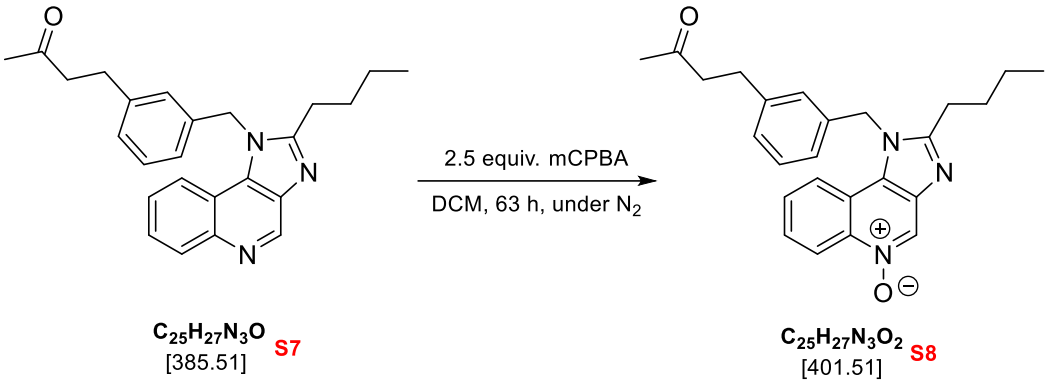


Product S8 was synthesized according to the procedure reported by Stefan Aichhorn. It was obtained as a brown oil in 115% yield, indicating the presence of certain impurities. However, these impurities do not interfere with the subsequent steps. Chemically, the reaction involves the formation of an N-oxide, typically introduced using peroxides, and is a common method for the functionalization of pyridines[162].

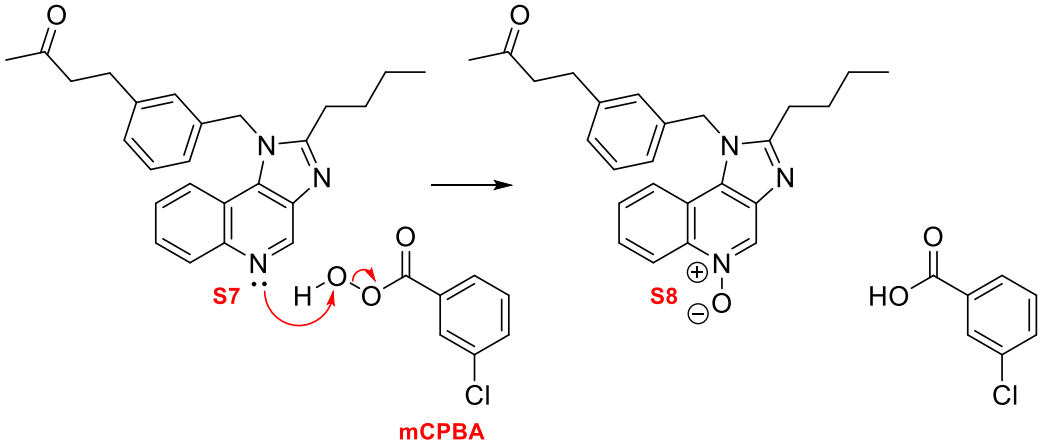


### 7.1.8 Synthesis of S9 (SA-401)

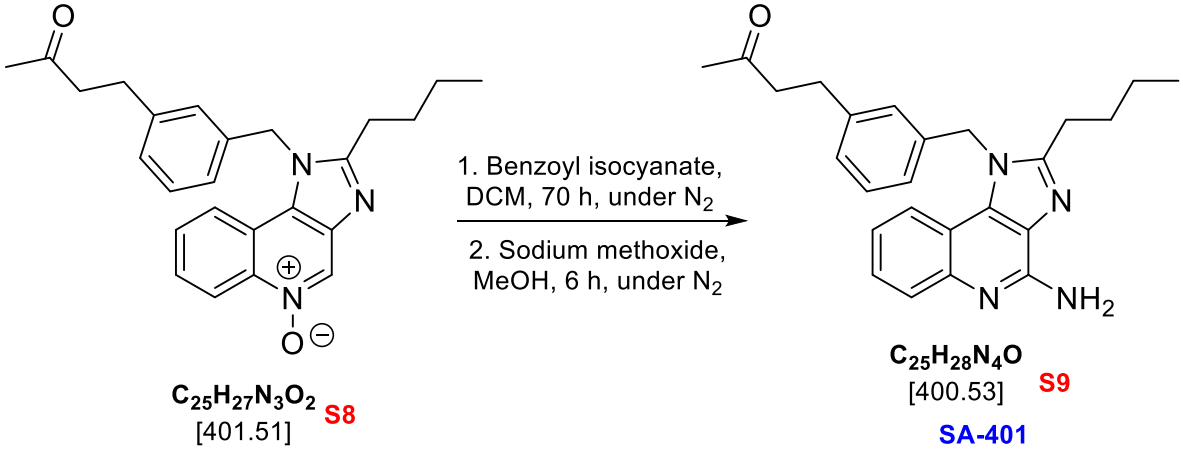


The product S9 (SA-401) was synthesized according to the procedure reported by Stefan Aichhorn[156], with slight modifications to the purification process. Purification was carried

out using two rounds of column chromatography followed by recrystallization. HPLC-MS analysis confirmed excellent purity, which is essential for a compound intended for medical applications.

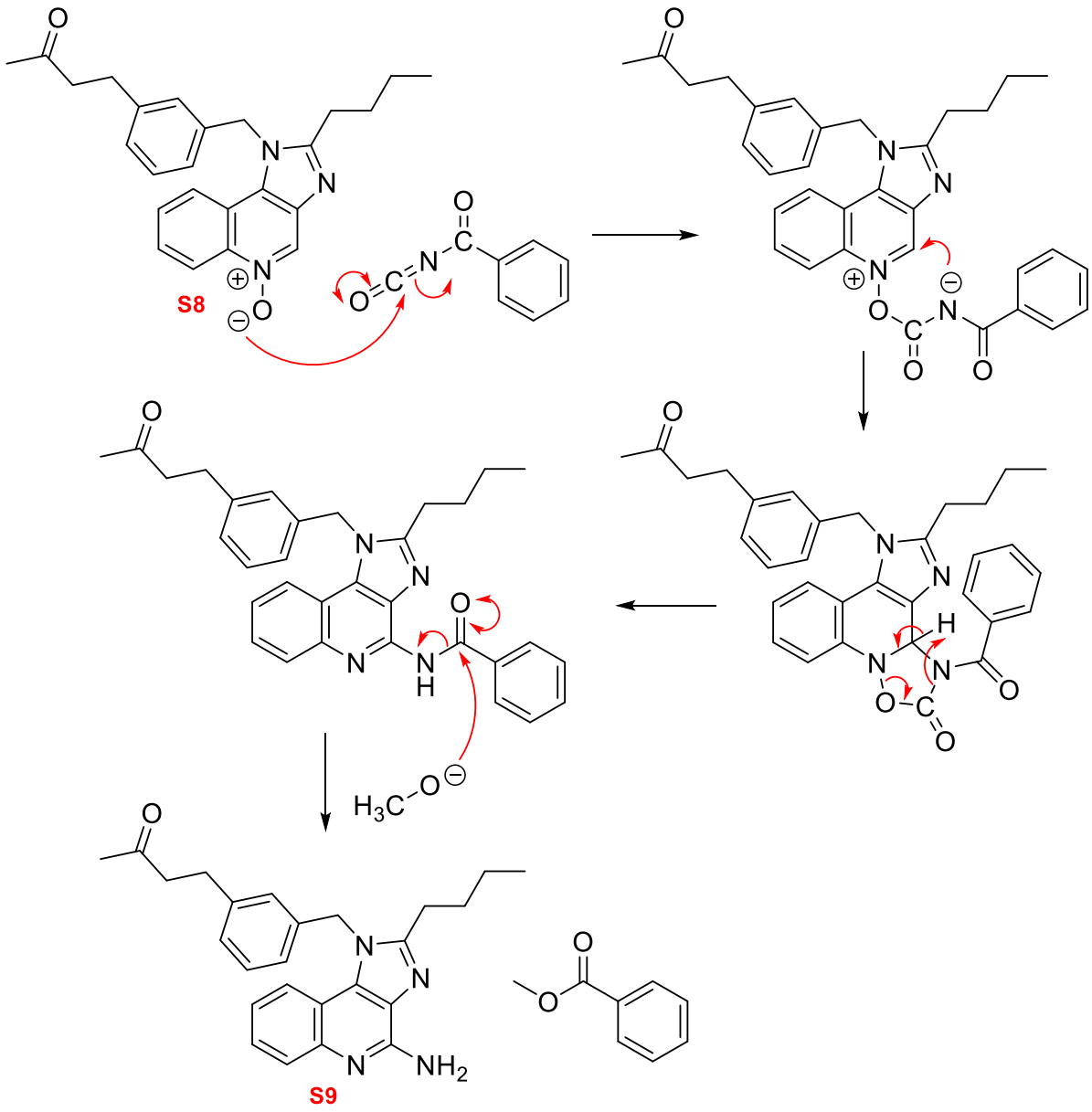


**Figure 33**: Proposed mechanism for the synthesis of product S9


**Figure 34**: Physical appearance of product S9 (SA-401) after purification

## 7.2 Synthesis of polyphosphazene polymer

### 7.2.1 Summary of results

| Polymer | M / kDa | $Mn^a$ / kDa | $Mn^b$ / kDa | Đ | Yield / % |
|---|---|---|---|---|---|
| P1 | 41 | 35 | 10 | 1.1 | 78 |
| P2 | 39 | 31 | - | - | 110 |
| P3 | 1669 | 625 | 254 | 1.3 | 33 |
| P4 | 1159 | 437 | 70 | 2.0 | 58 |
| P5 | 1464 | 550 | 85 | 2.7 | 80 |

**Table 1**: Summary of the main results from polymer synthesis. M represents the theoretical molecular weight, calculated based on the targeted number of repeat units (75 phosphazene repeat units and 100 glutamic acid units per phosphazene monomer). $Mn^a$ is the number-average molecular weight determined from NMR data (60 phosphazene repeat units and 46 glutamic acid units per phosphazene monomer), while $Mn^b$ is the number-average molecular weight obtained from GPC analysis.

### 7.2.2 Synthesis of tert-butyl (2-(2-(2-aminoethoxy)ethoxy)ethyl)carbamate

Tert-butyl (2-(2-(2-aminoethoxy)ethoxy)ethyl)carbamate was prepared with a yield of 107%, indicating that the product contained certain impurities. In the ESI-MS analysis, the desired product appeared as two signals: 249.20 m/z ($[M+H]^+$) and 271.05 m/z ($[M+Na]^+$). The following impurities were proposed based on the ESI-MS results: unreacted diamine at 149.20 m/z ($[M+H]^+$) and diprotected diamine at 371.25 m/z ($[M+Na]^+$). The presence of diprotected diamine poses no issue for the subsequent macrosubstitution, but it is critical to

minimize the amount of non-protected diamine, as it could lead to crosslinking of polyphosphazene chains.

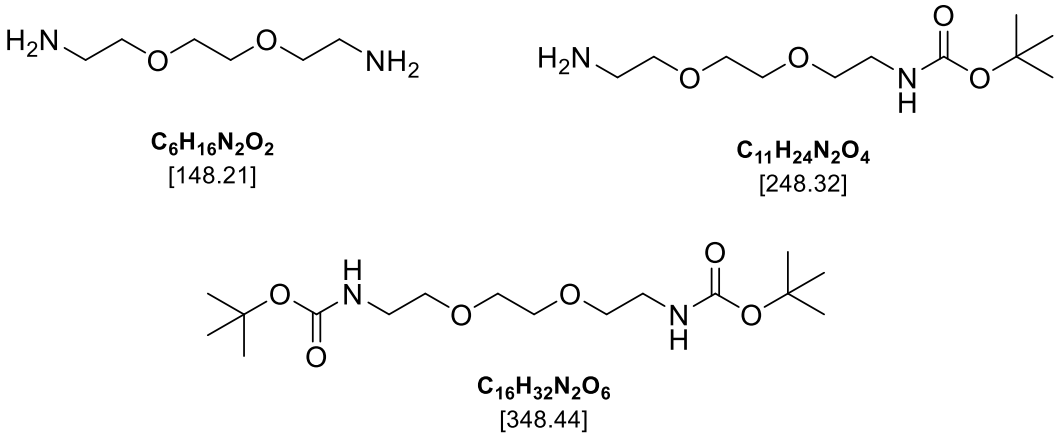


**Figure 35**: Potentially identified impurities during the characterization of tert-butyl (2-(2-(2-aminoethoxy)ethoxy)ethyl)carbamate

### 7.2.3 Synthesis of Boc-protected macrosubstituted polyphosphazene (PPz) (P1)

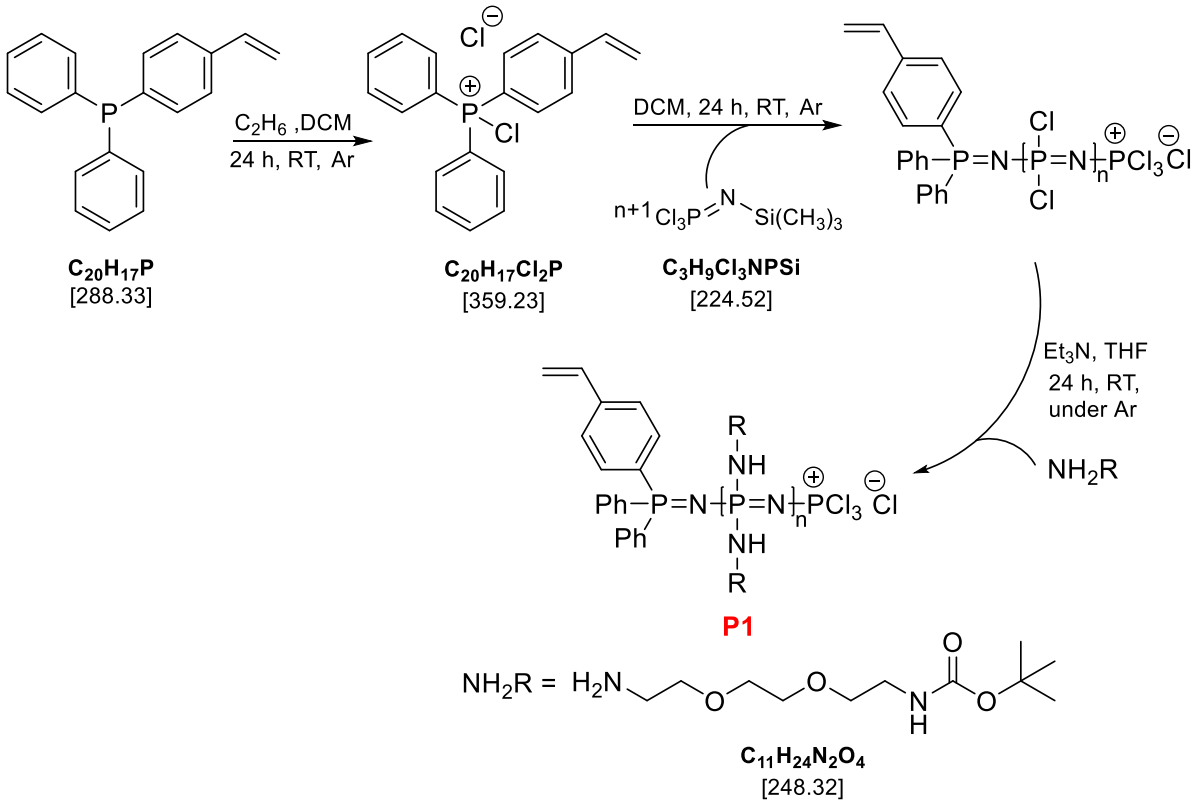


The polymer P1 was synthesized according to the procedure[154] reported by Strasser et al., yielding 78% as a clear, yellowish, viscous material. Characterization was performed using GPC (in DMF) and $^{1}H$ and $^{31}P$ NMR spectroscopy (in $CDCl_3$). The targeted chain length was 75 repeat units, corresponding to a theoretical molecular weight of approximately 40.5 kDa (the molecular weight of a single repeat unit is 539.61 Da). Based on $^{1}H$ NMR integration

(comparison of the aromatic signals at 7.42–7.78 ppm with the Boc-protons at 1.42 ppm), a chain length of 64 repeat units was determined, resulting in an estimated molecular weight of 34.5 kDa. GPC analysis using conventional calibration yielded a dispersity (Đ) of 1.1 and an Mn value of 10 kDa, which is significantly lower than the value calculated from the NMR data. This discrepancy can be explained by the fact that polystyrene, which is used for calibration, may behave and interact with the column differently from the analyzed polyphosphazene P1.

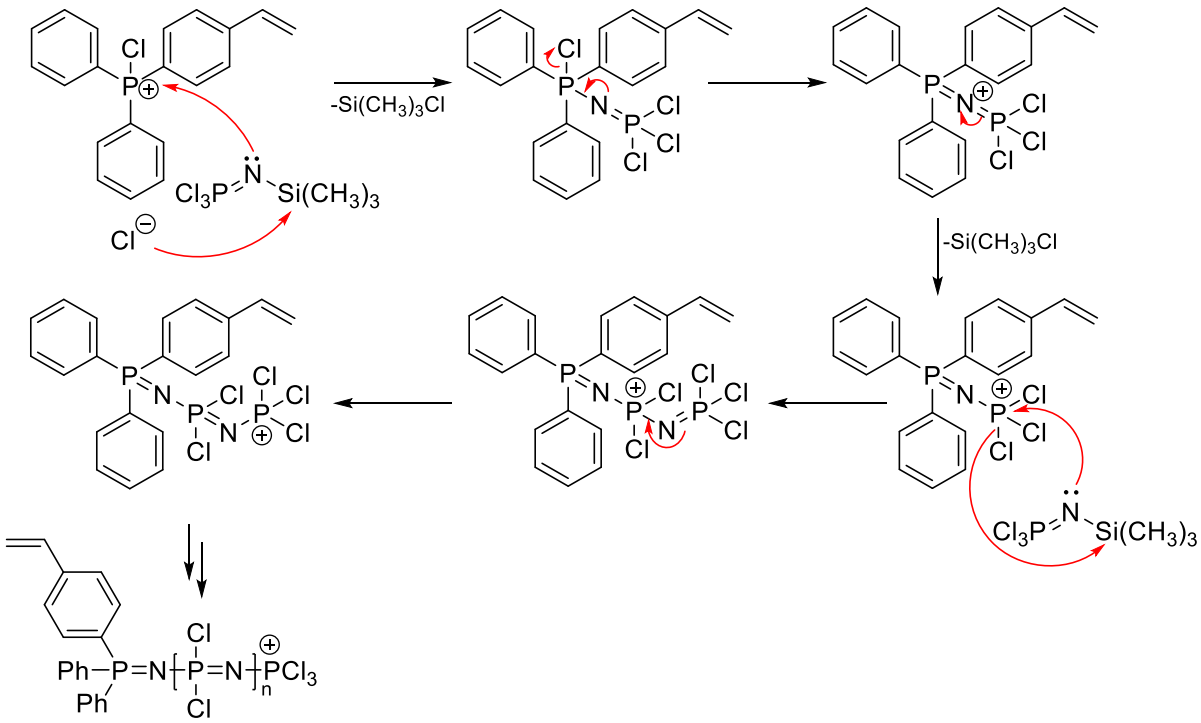


**Figure 36**: Proposed mechanism of polyphosphazene polymerization

### 7.2.4 Boc-deprotection of macrosubstituted PPz

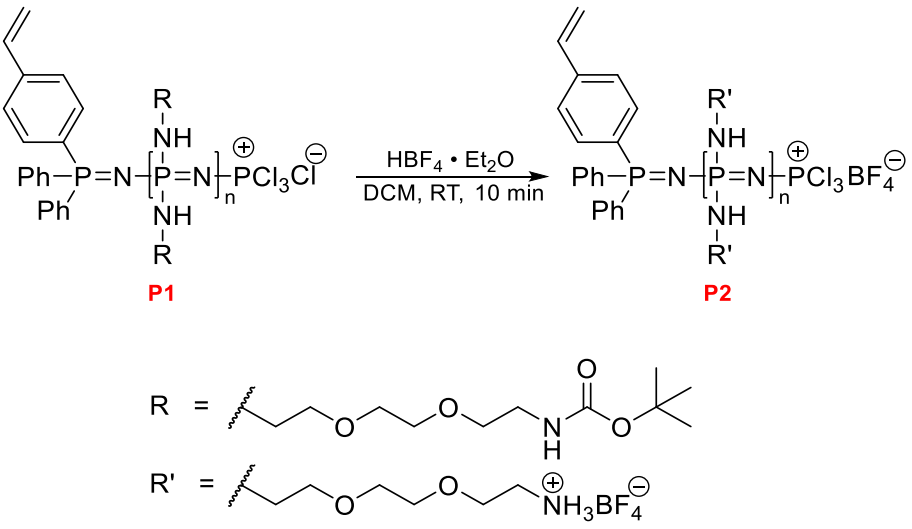

The polymer P2 was prepared according to the procedure reported by Strasser et al.[154], yielding 110% as a transparent viscous substance; this higher-than-100% yield likely arises from residual solvents due to incomplete drying. Characterization by $^{1}H$, $^{31}P$, and $^{19}F$ NMR ($D_2O$) spectroscopy confirmed the polymer structure, with $^{1}H$ NMR integration (aromatic protons at 7.57-7.91 ppm relative to four protons at 3.04-3.30 ppm) estimating a chain length of 60 phosphazene repeat units, corresponding to a molecular weight of 30.9 kDa, whereas the theoretical molecular weight calculated from targeted 75 repeat units (515.00 Da each) is 38.6 kDa.

### 7.2.5 Synthesis of Bn-protected PPz-PGA (P3)

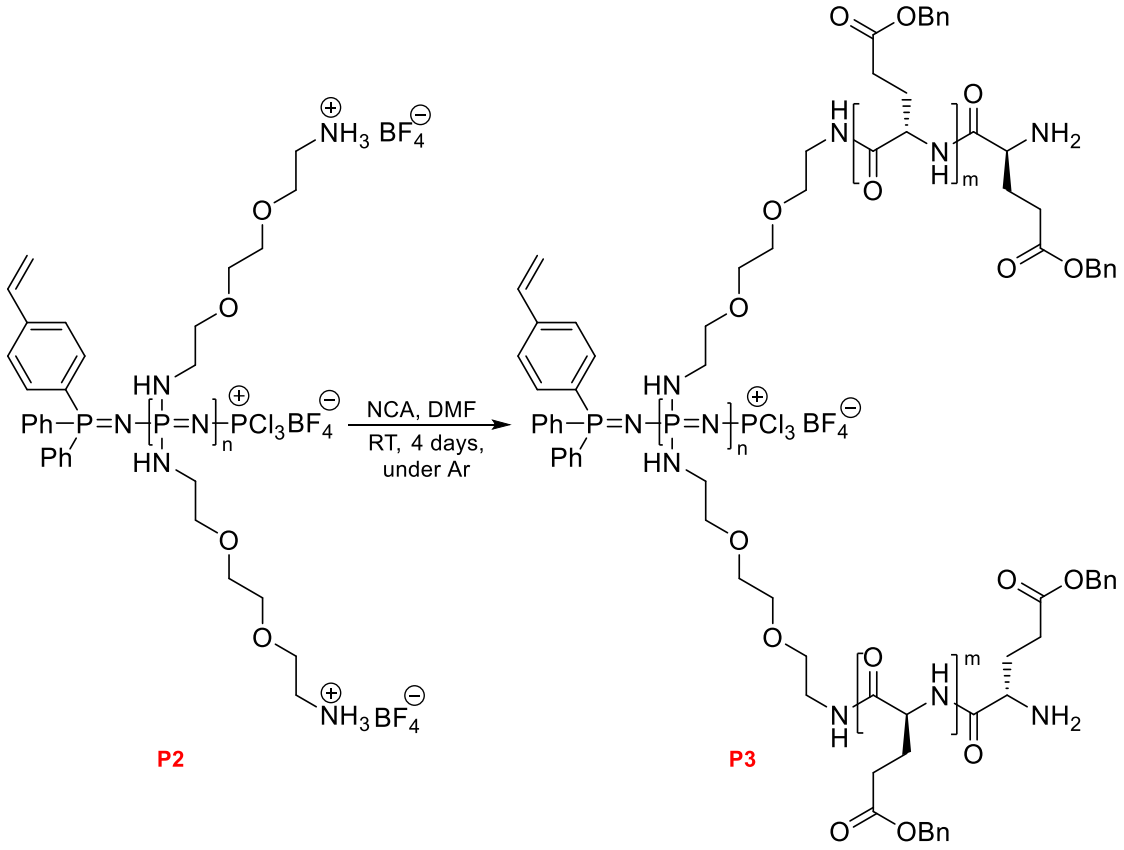


The polymer was prepared according to the procedure reported by Strasser et al.[154] with a yield of 33%, resulting in a transparent, rigid material. The product was characterized by NMR spectroscopy (in DMSO) and GPC (in DMF). In this polymer, we targeted 100 glutamic acid residues per phosphazene monomer. The predicted molecular weight—considering 75 PPz repeat units and 100 glutamic acid residues—is approximately 1.67 MDa (PPz unit without PGA: 337.37 Da; glutamic acid residue: 219.24 Da). However, due to spectral overlap and broad NMR signals, it was not possible to determine the actual number of glutamic acid units from the NMR data. The estimated number-average molecular weight (Mn) based on GPC data (using multiple detector calibration) is 254 kDa, with a dispersity value of 1.3.

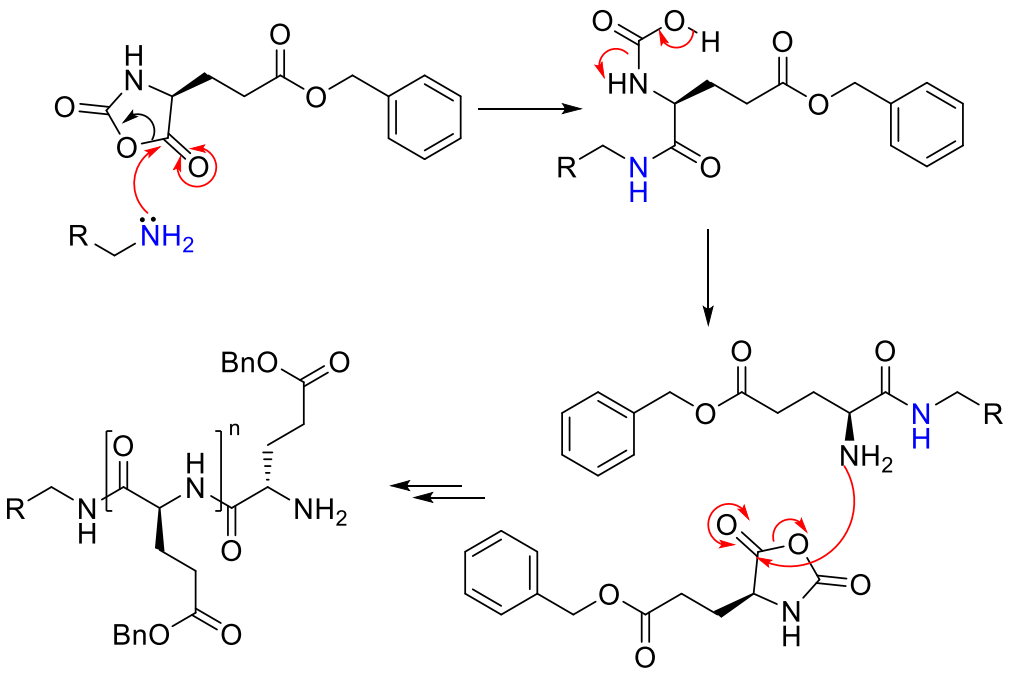

**Figure 37**: proposed mechanism of 5-benzyl L-glutamate NCA polymerization

### 7.2.6 Bn-deprotection of PPz-PGA

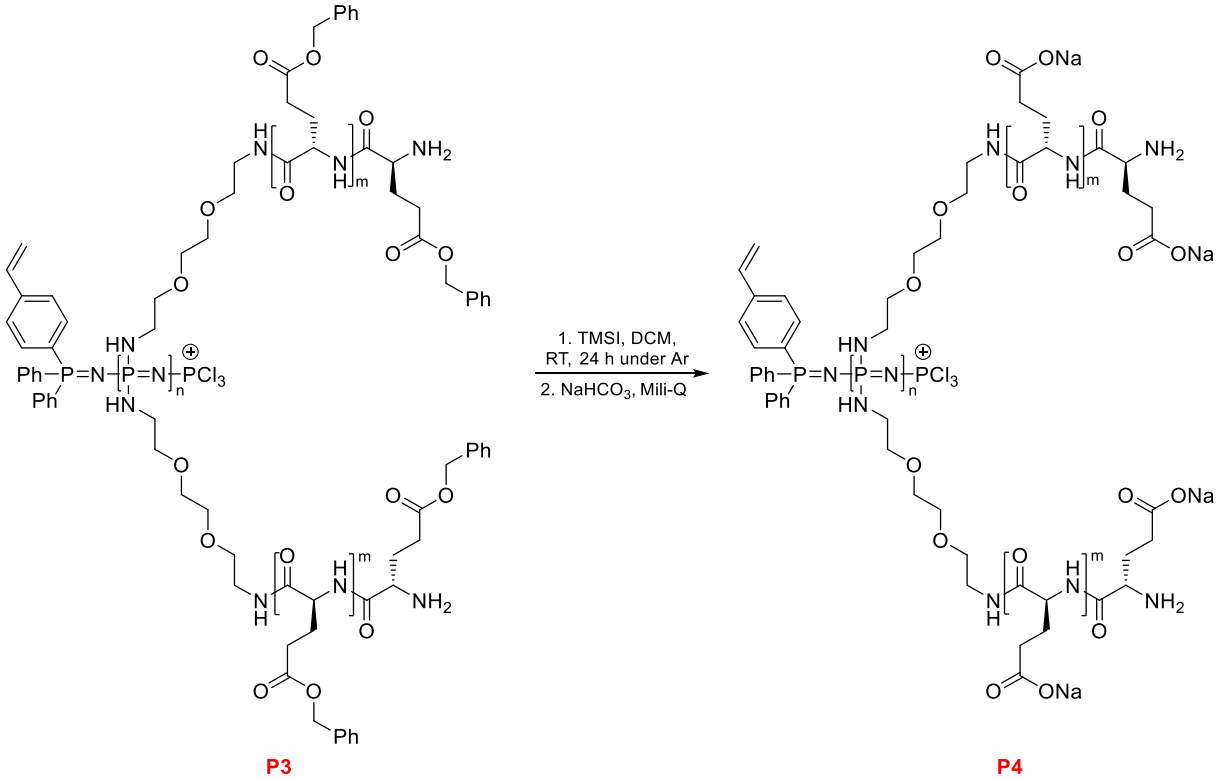


The deprotection was performed according to the procedure reported by Strasser et al[154]. The product was obtained as a white, fluffy substance with a yield of 58%. A dn/dc value of 0.1675 was used to evaluate the molecular weight from the GPC data. The results obtained were 70 kDa for Mn and 143 kDa for Mw, which are significantly lower than the theoretical value of 1.16 MDa (where the PPz unit without PGA is 337.37 Da and the glutamic acid residue is

151.10 Da). The dispersity value estimated from the GPC data was 2.0. Based on the NMR data and integration of the signals from the proton spectrum, we estimate 46 glutamic acid units per phosphazene monomer (integration of the peak at 3.44–3.83 ppm). Considering that previous NMR data indicated 60 phosphazene repeat units, the estimated molecular weight is 437 kDa.

### 7.2.7 Synthesis of Cbz-protected β-Ala-Boc-hydrazide linker

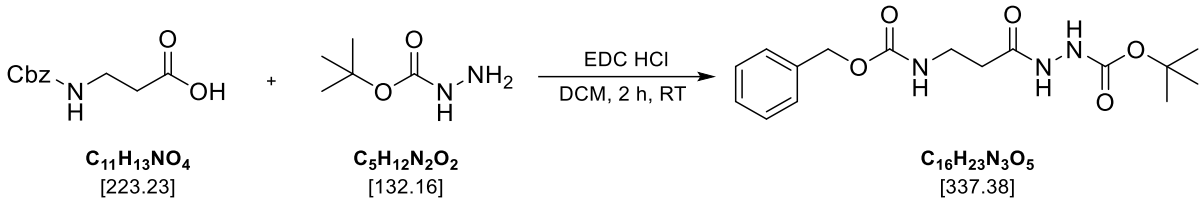


$C_{11}H_{13}NO_4$ [223.23] $C_5H_{12}N_2O_2$ [132.16] $C_{16}H_{23}N_3O_5$ [337.38]

The Cbz-protected β-Ala-Boc-hydrazide linker was prepared according to the procedure reported by Teasdale et al[163]. The product was obtained as a white solid in 89% yield and characterized by NMR spectroscopy and ESI-MS analysis. Observed NMR signals matched literature data, and the ESI-MS spectrum showed a sodium adduct peak at m/z 360.10, consistent with the target compound. While minor unidentified impurities were present, critical reactants and coupling byproducts (e.g., EDC urea) were absent, confirming that the acetic acid washing step effectively removed these residues.

### 7.2.8 Cbz-deprotection of β-Ala-Boc-hydrazide linker

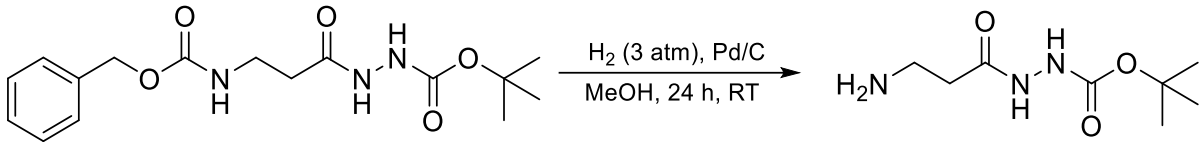


$C_{16}H_{23}N_3O_5$ [337.38] $C_8H_{17}N_3O_3$ [203.24]

The Cbz-deprotected β-Ala-Boc-hydrazide linker was obtained as a white foam in 82% yield following the procedure reported by Teasdale et al.[163] and characterized by NMR spectroscopy, ESI-MS, and IR spectroscopy. The NMR spectra matched literature data. ESI-MS analysis revealed four peaks of the target compound: 204.10 $[M+H]^+$, 226.10 $[M+Na]^+$, 407.25 $[2M+H]^+$, and 429.20 $[2M+Na]^+$ (m/z).

### 7.2.9 Synthesis of β-Ala-Boc-hydrazide linked PPz-PGA

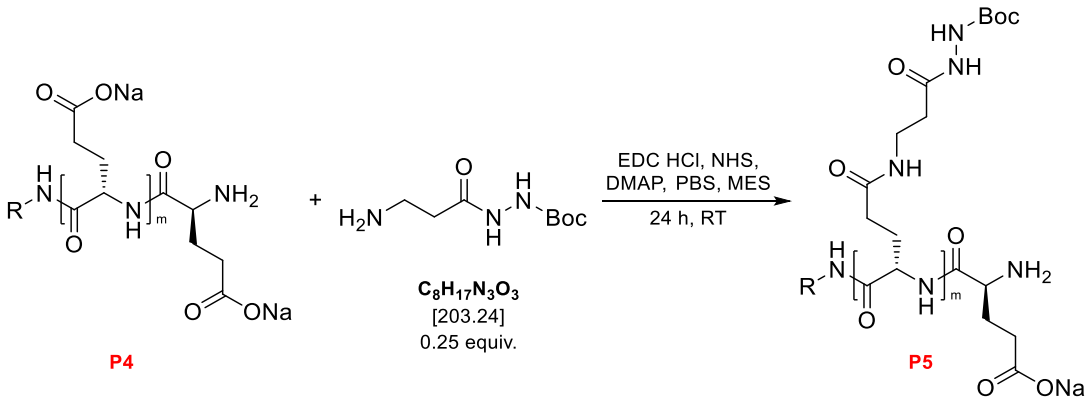


The polymer P5 was prepared following the procedure reported by Baumgartner et al.[164] yielding 80% of a white, fluffy solid. Characterization was performed using NMR ($D_2O$), dynamic light scattering (DLS), aqueous gel permeation chromatography (GPC), ESI-MS, and HPLC-MS. The target was a 25% loading of β-alanine-linker, with a predicted molecular weight of 1.46 MDa (the molecular weight of one PPz unit (without PGA) is 337.37 Da, and the average molecular weight of a PGA monomer substituted with β-alanine–linker is 191.91 Da). The dispersity value based on GPC data (assuming a dn/dc value of 0.1675) is 2.7, with a number-average molecular weight (Mn) of 85 kDa. Despite extensive purification, residual DMAP and EDC urea were detected in the final product, as confirmed by NMR, HPLC-MS, and ESI-MS. DLS measurements were carried out to determine the polydispersity index (PDI = 0.374) and hydrodynamic diameter (Dh = 34 nm).

## 7.3 Conjugation procedure

### 7.3.1 Boc-deprotection of of β-Ala-Boc-hydrazide linked PPz-PGA

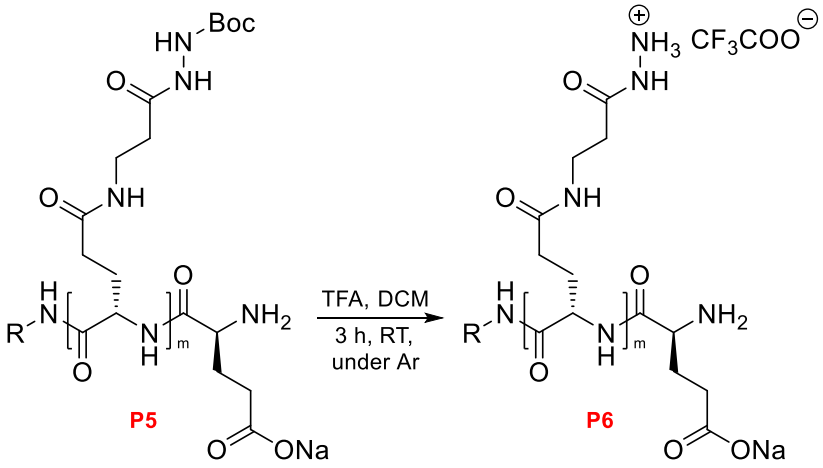


The deprotection procedure was optimized based on the method reported by Aichhorn, Linhardt et al[165]. We tested various reaction times and TFA concentrations and identified optimal conditions that efficiently remove the Boc group without damaging the sensitive

polymer backbone or PGA side chains. It is essential to note that the solvent evaporation should be completed relatively quickly. If evaporation is too slow, DCM may evaporate first, increasing the relative concentration of TFA and potentially leading to degradation. Therefore, minimizing the polymer's exposure to pure TFA is recommended. After evaporation, the sample should be kept under vacuum for a sufficient period (e.g., 3 hours) to remove residual TFA, which is crucial for the success of the next step.

### 7.3.2 Conjugation of β-Ala-hydrazide linked PPz-PGA with SA-401

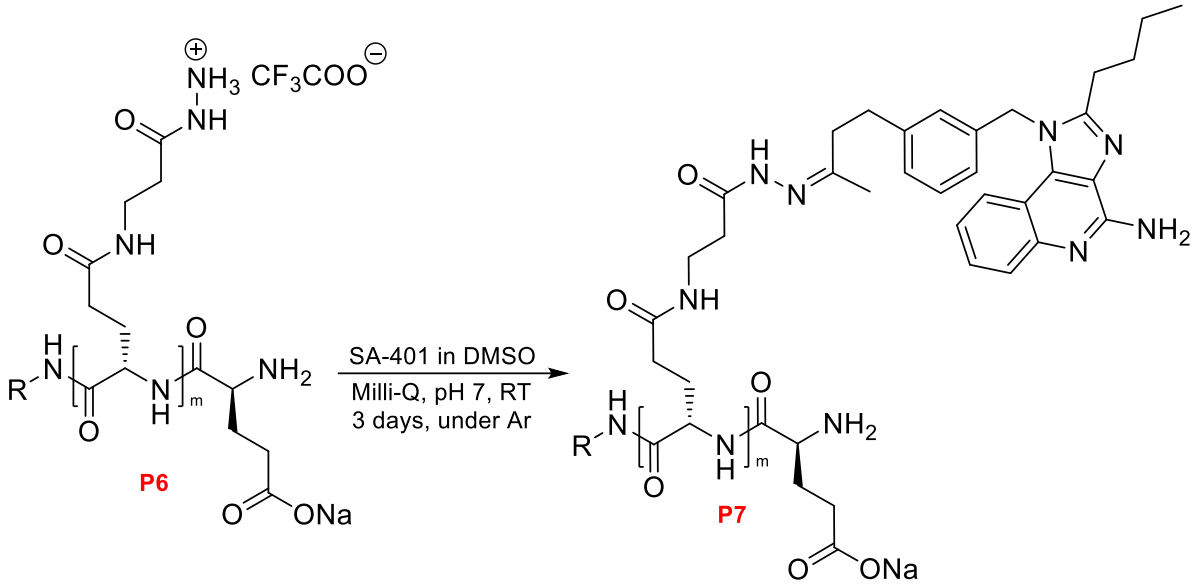


The final product P7 was prepared based on the optimized procedure reported by Aichhorn, Linhardt, et al. An attempt to follow the original method using methanol as the reaction solvent was unsuccessful, as the resulting product was insoluble in most common solvents, including water, methanol, DMF, DMSO, and acetone. We found that a water:DMSO mixture (4:3) provided optimal solubility for both the polymer and the ligand. The slightly acidic pH resulting from water addition is neutralized by the basic ligand, resulting in a pH of approximately 6; no further neutralization is required. Purification was achieved by washing with DCM to remove excess ligand, followed by ultrafiltration to eliminate remaining impurities. The final product was obtained as a fluffy white solid perfectly soluble in water (neutral pH).

The product was characterized by aqueous GPC, NMR ($D_2O$), and UV-Vis. The obtained dispersity value from GPC data is 2.8. Calculated Mn value (considering dn/dc is 0.1675) is 22.8 kDa.

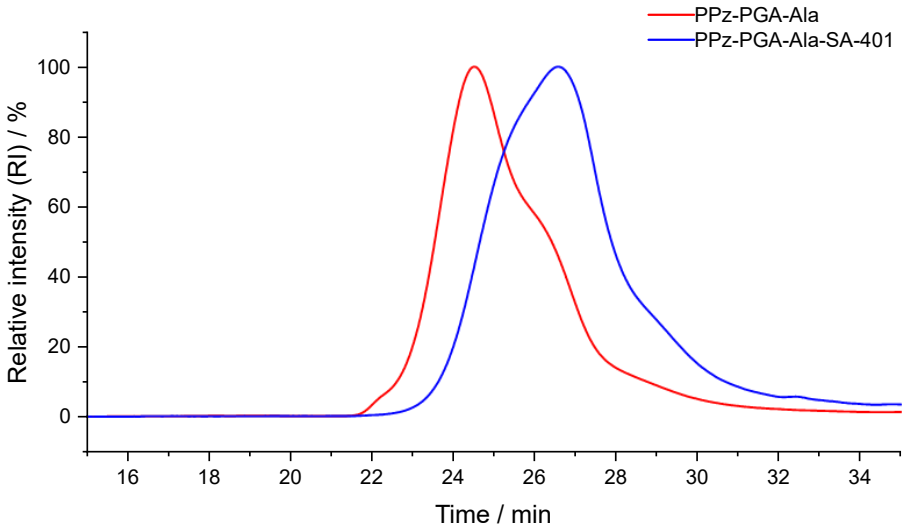


**Figure 38**: Normalized GPC chromatograms (refractive index) of PPz-PGA-Ala and PPz-PGA-Ala-SA-401 (conjugate)

### 7.3.3 Drug loading quantification

Of the five wavelengths measured, only two (322 nm and 265 nm) provided data that fit a linear calibration curve. At the other wavelengths, the sample concentration exceeded the detector's linear range. We prepared a sample by dissolving 1.3 mg of conjugate in 2.5 mL PBS and 1.5 mL DMSO, resulting in a final concentration of 325 µg/mL. Based on the calibration curve at 265 nm, the detected concentration was 23.9 µg/mL, while the 322 nm curve indicated 23.4 µg/mL. Thus, the calculated drug loading is approximately 7%.

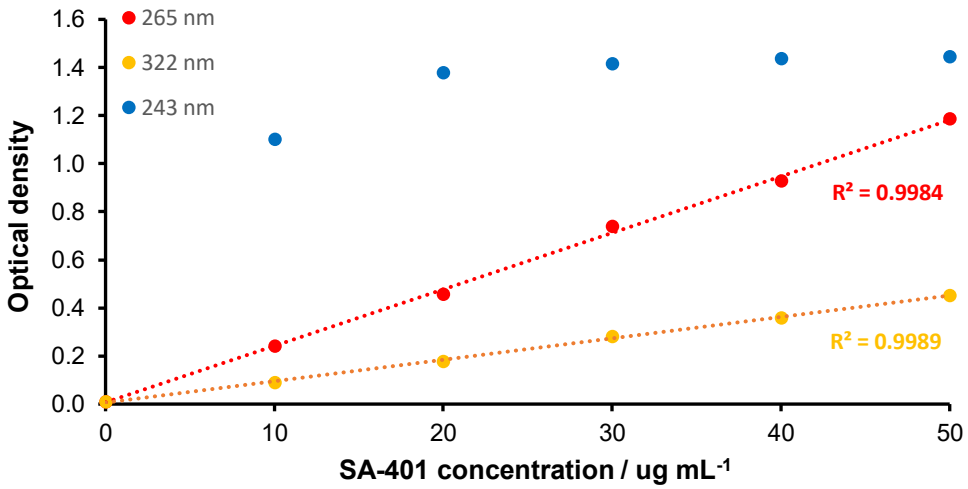


**Figure 39**: Calibration curves for SA-401, measured at 243, 265, and 322 nm. The x-axis represents SA-401 concentration (µg/mL), while the y-axis corresponds to optical density

### 7.4 Isolation of bone marrow and differentiation of BMMs

Flow cytometry analysis confirmed that the chosen differentiation strategy yielded a highly pure culture of macrophages expressing the F4/80 marker, with a purity of 97%. In this experiment, we used LCCM, which stands for L-cell conditioned medium — the supernatant collected from L929 fibroblast cell cultures. This medium is a widely used source of macrophage colony-stimulating factor (M-CSF).

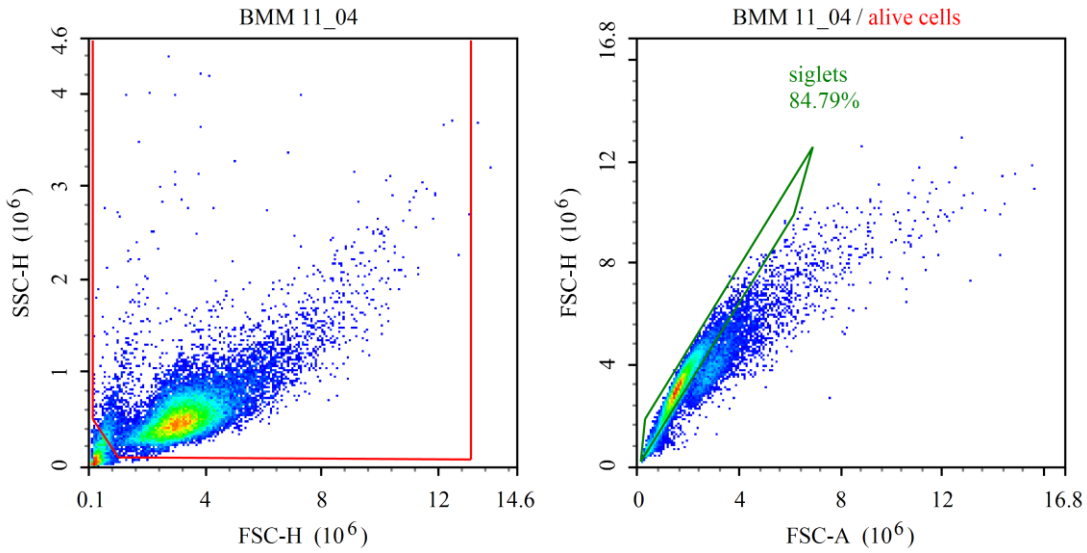


**Figure 40**: Flow cytometry analysis. Left: forward scatter-height (FSC-H) versus side scatter-height (SSC-H) dot plot showing cell size and granularity distribution. Right: Forward scatter-area (FSC-A) versus FSC-H dot plot for doublet discrimination. Cells were analyzed using a PE-Cy7-conjugated anti-mouse F4/80 antibody (clone BM8) to identify macrophages.

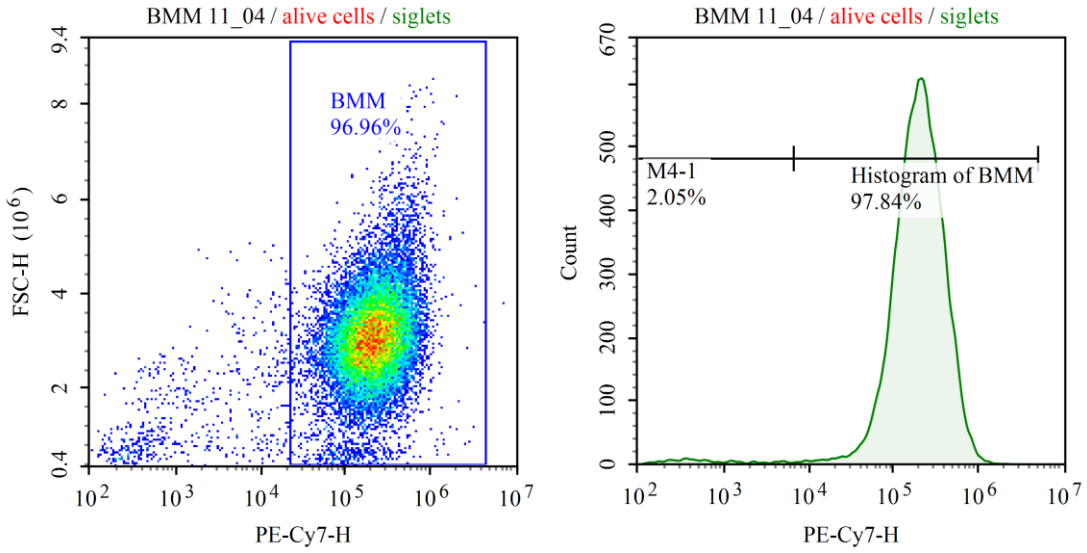


**Figure 41:** Flow cytometry analysis. Left: PE-Cy7-H fluorescence intensity versus FSC-H dot plot demonstrating F4/80 expression relative to cell size. Right: PE-Cy7-H histogram (fluorescence intensity versus count) quantifying F4/80 expression levels. Cells were analyzed using a PE-Cy7-conjugated anti-mouse F4/80 antibody (clone BM8) to identify macrophages.

By day 3 of differentiation, cells displaying macrophage-like morphology were observed in the microscopy images. At day 7, the cell population had expanded; however, their overall morphological characteristics remained consistent.

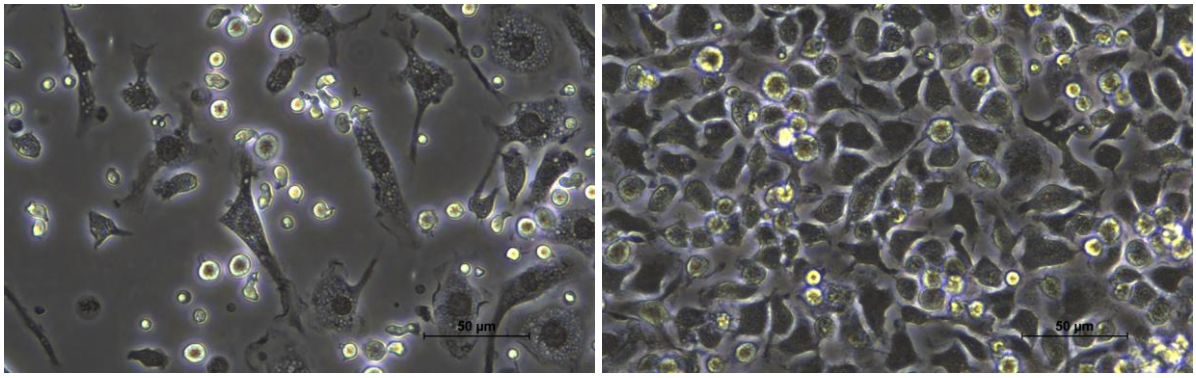


**Figure 42**: Microscopy images of cells on day 3 (left) and day 7 (right) of differentiation; imaged at 400x magnification

Prior to activation, the cells were divided into two groups: one cultured in a serum-containing medium and the other in a serum-free medium. At this stage, clear morphological differences were observed. Cells maintained with serum exhibited distinct elongated dendrites, whereas those cultured without serum retained a normal morphology.

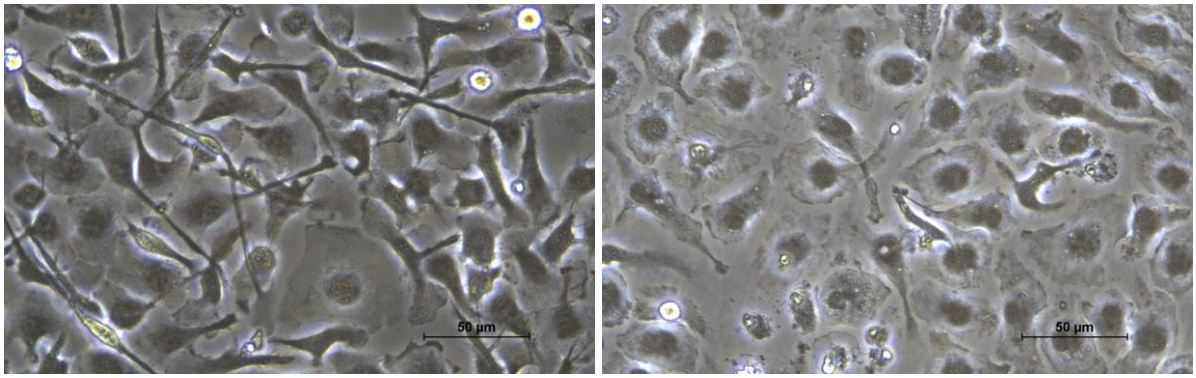


**Figure 43**: Microscopy images of cells on day 8 of differentiation, cultured with serum (left) or without serum (right). Imaged at 400x magnification

### 7.5 Cell lysis results

#### 7.5.1 BCA concentration measurement

| | A | B | C | D | E | F | G | H |
|---|---|---|---|---|---|---|---|---|
| **1** | 7071 | 10642 | 11813 | 5685 | 3773 | 3324 | 6436 | 3480 |
| **2** | 8866 | 10525 | 10994 | 7120 | 2582 | 3128 | 4016 | 2377 |
| **3** | 10115 | 10067 | 11560 | 7842 | 3431 | 3324 | 4319 | 3109 |
| **4** | 11540 | 10759 | 11501 | 5295 | 3548 | 2494 | 4173 | 4104 |
| **5** | 10955 | 11023 | 12555 | 5802 | 2816 | 2680 | 2114 | 3821 |

**Table 2**: Results from the BCA protein concentration measurements after cell lysis are shown for five samples from each group: A – SA-401 (10% FBS medium), B – R848 (10% FBS medium), C – LPS

(10% FBS medium), D – negative control (10% FBS medium), E – SA-401 (FBS-free medium), F – R848 (FBS-free medium), G – LPS (FBS-free medium), and H – negative control (FBS-free medium).

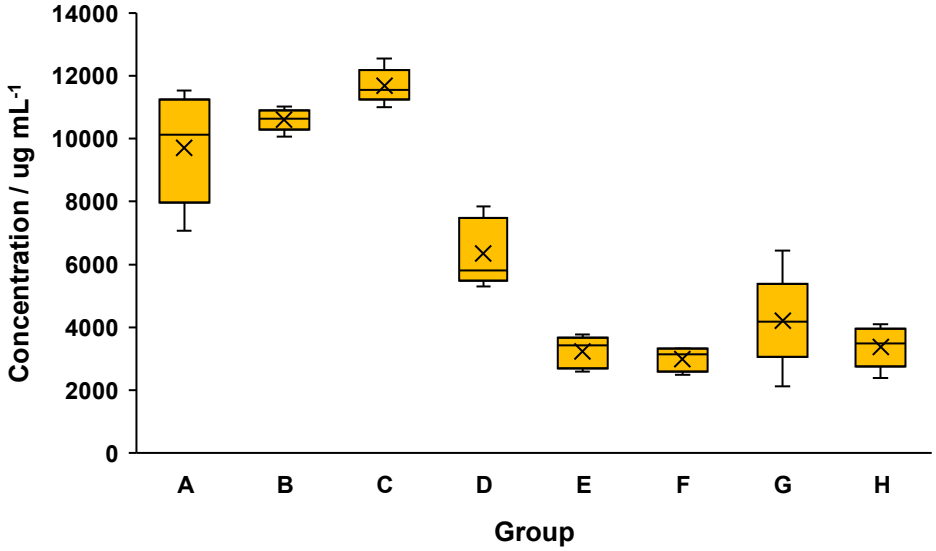


**Figure 44**: Boxplots demonstrating total protein concentrations quantified via BCA assay across experimental groups (n=5 per group): A – SA-401 (10% FBS medium), B – R848 (10% FBS medium), C – LPS (10% FBS medium), D – negative control (10% FBS medium), E – SA-401 (FBS-free medium), F – R848 (FBS-free medium), G – LPS (FBS-free medium), and H – negative control (FBS-free medium).

The measured protein concentration after cell lysis confirmed a high protein content in the samples. Although the calibration curve showed a good linear fit with an $R^2$ of 0.993, deviations may occur between the actual concentration and the measured values due to the absence of replicates during measurement. Nevertheless, we can conclude that the lysis protocol worked well.

Additionally, we observed that protein content was consistently higher in samples obtained from serum-containing medium (for example, group A vs. group E, or group D vs. group H). This can be explained by two factors. First, cell viability decreases when serum is removed from the medium due to the absence of essential growth factors. Second, the harvesting methods differed: cells grown in serum-containing medium were trypsinized and transferred intact to microtubes, whereas cells in serum-free medium were detached using a cell scraper, which caused cell damage and potentially led to protein loss.

Furthermore, when comparing serum-containing groups (A, B, C, and D), protein content was higher in activated cells. The control group D, where no ligand was applied, had the lowest protein concentration, confirming that TLR agonists activate cells and induce protein production. This results in higher protein content in groups A, B, and C compared to group D.

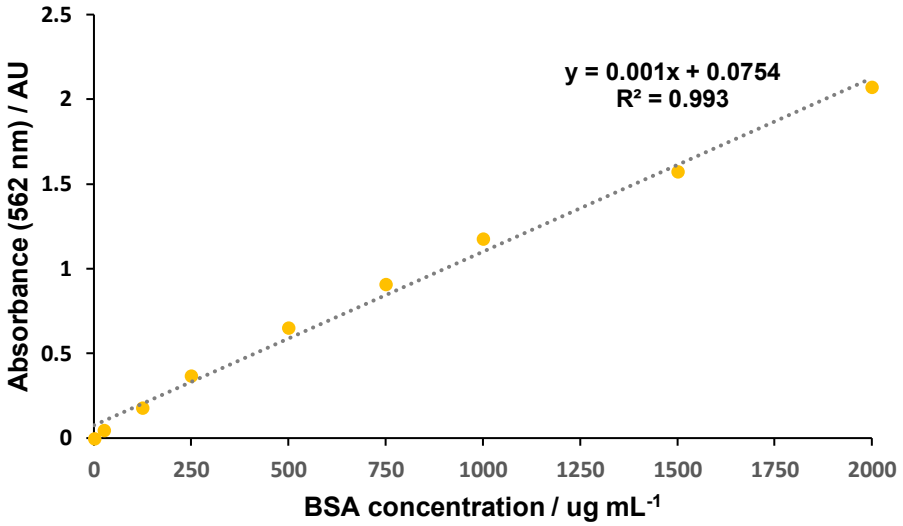


**Figure 45**: The BCA calibration curve was generated by plotting the average blank-corrected absorbance at 562 nm for each bovine serum albumin (BSA) standard against its known concentration (µg/mL);

### 7.5.2 SDS PAGE results

To perform quality control of the cell lysis stage, we conducted SDS-PAGE. As shown in the results below, the overall protein profiles are similar across different groups, although some small differences are noticeable. These differences confirm variations in the cellular response depending on the ligand applied. As previously described, even ligands targeting the same receptor type can trigger different responses.

We can also draw conclusions about protein concentration measurements. Since protein loading was performed using equal quantities (based on protein concentration, either 3 µg or 6 µg), the similar lane intensities – aside from a few exceptions – confirm the accuracy of the protein concentration evaluation.

In future experiments, we will need to repeat the SDS-PAGE and perform Western blotting to confirm macrophage activation. Upon activation, macrophages produce cytokines such as TNF, which can be detected using specific antibodies in Western blot analysis.

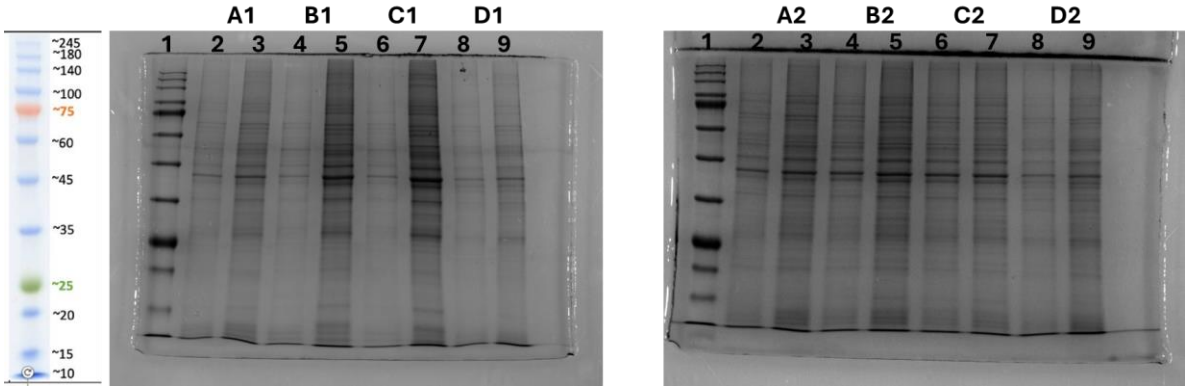


**Figure 46**: Left gel: lanes 1 – protein marker; 2 – A1 (3 µg); 3 – A1 (6 µg); 4 – B1 (3 µg); 5 – B1 (6 µg); 6 – C1 (3 µg); 7 – C1 (6 µg); 8 – D1 (3 µg); 9 – D1 (6 µg). Right gel: lanes 1 – protein marker; 2 – A2 (3 µg); 3 – A2 (6 µg); 4 – B2 (3 µg); 5 – B2 (6 µg); 6 – C2 (3 µg); 7 – C2 (6 µg); 8 – D2 (3 µg); 9 – D2 (6 µg).

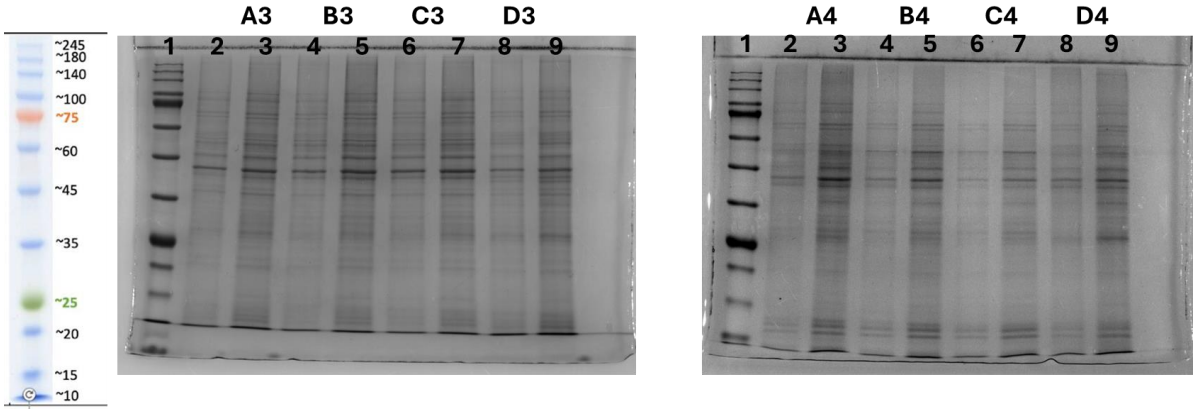


**Figure 47**: Left gel: lanes 1 – protein marker; 2 – A3 (3 µg); 3 – A3 (6 µg); 4 – B3 (3 µg); 5 – B3 (6 µg); 6 – C3 (3 µg); 7 – C3 (6 µg); 8 – D3 (3 µg); 9 – D3 (6 µg). Right gel: lanes 1 – protein marker; 2 – A4 (3 µg); 3 – A4 (6 µg); 4 – B4 (3 µg); 5 – B4 (6 µg); 6 – C4 (3 µg); 7 – C4 (6 µg); 8 – D4 (3 µg); 9 – D4 (6 µg).

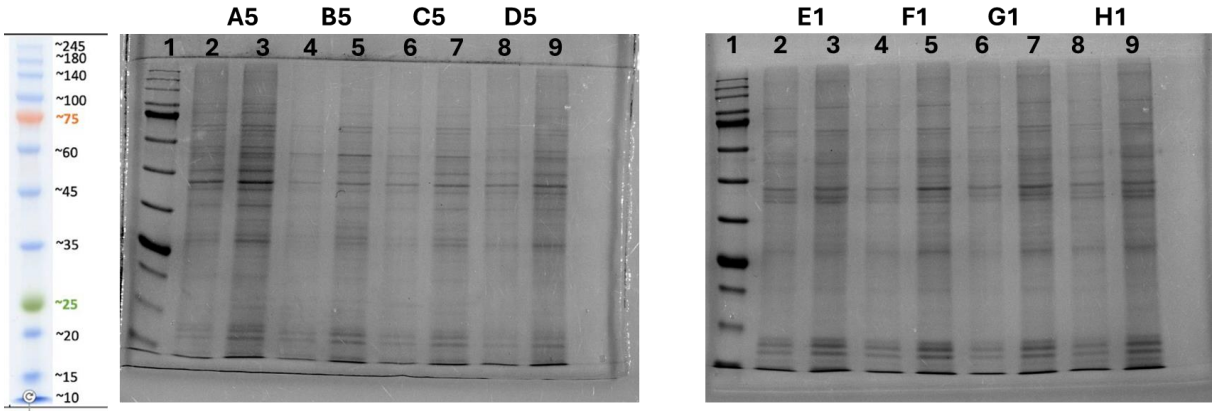


**Figure 48**: Left gel: lanes 1 – protein marker; 2 – A5 (3 µg); 3 – A5 (6 µg); 4 – B5 (3 µg); 5 – B5 (6 µg); 6 – C5 (3 µg); 7 – C5 (6 µg); 8 – D5 (3 µg); 9 – D5 (6 µg). Right gel: lanes 1 – protein marker; 2 – E1 (3 µg); 3 – E1 (6 µg); 4 – F1 (3 µg); 5 – F1 (6 µg); 6 – G1 (3 µg); 7 – G1 (6 µg); 8 – H1 (3 µg); 9 – H1 (6 µg).

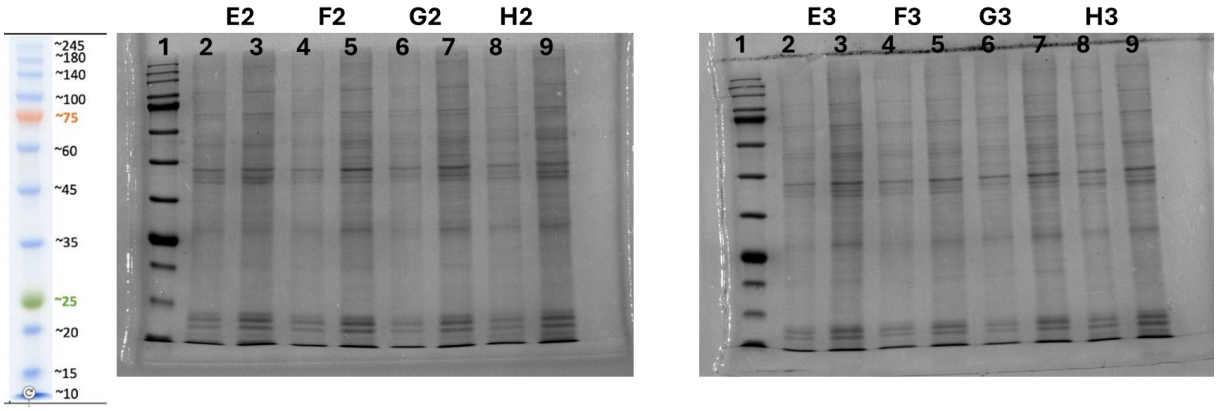


**Figure 49**: Left gel: lanes 1 – protein marker; 2 – E2 (3 µg); 3 – E2 (6 µg); 4 – F2 (3 µg); 5 – F2 (6 µg); 6 – G2 (3 µg); 7 – G2 (6 µg); 8 – H2 (3 µg); 9 – H2 (6 µg). Right gel: lanes 1 – protein marker; 2 – E3 (3 µg); 3 – E3 (6 µg); 4 – F3 (3 µg); 5 – F3 (6 µg); 6 – G3 (3 µg); 7 – G3 (6 µg); 8 – H3 (3 µg); 9 – H3 (6 µg).

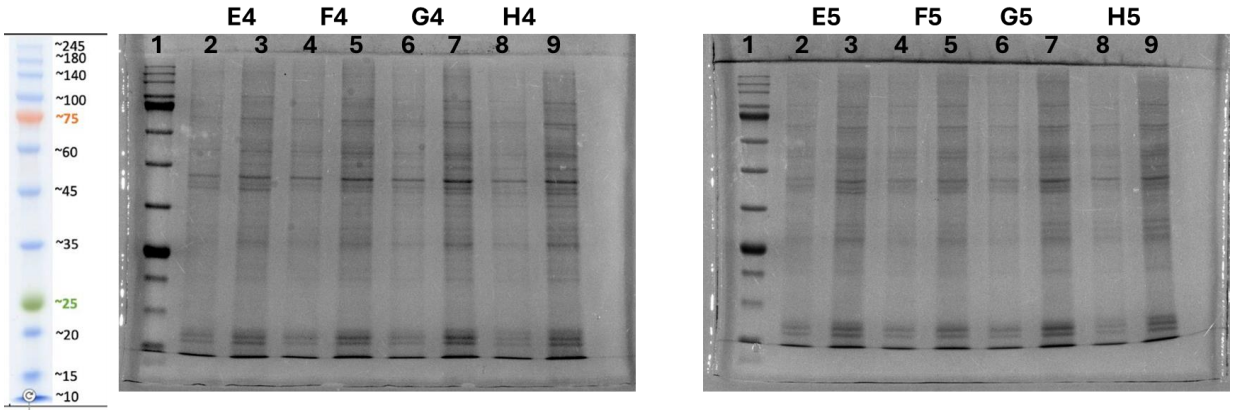


**Figure 50**: Left gel: lanes 1 – protein marker; 2 – E4 (3 µg); 3 – E4 (6 µg); 4 – F4 (3 µg); 5 – F4 (6 µg); 6 – G4 (3 µg); 7 – G4 (6 µg); 8 – H4 (3 µg); 9 – H4 (6 µg). Right gel: lanes 1 – protein marker; 2 – E5 (3 µg); 3 – E5 (6 µg); 4 – F5 (3 µg); 5 – F5 (6 µg); 6 – G5 (3 µg); 7 – G5 (6 µg); 8 – H5 (3 µg); 9 – H5 (6 µg).

## 7.6 Bioinformatics and MD simulations

### 7.6.1 Amino acid residues involved in receptor-ligand interactions

Analysis of the TLR7 receptor's interactions with the ligands revealed four main residues involved: Tyr356 and Phe408 (Tyr353 and Phe405 in TLR8), which participate in π-π stacking with the imidazoquinoline ring, and Asp555 and Thr586 (Asp543 and Thr574 in TLR8), which form hydrogen bonds with the ligand.

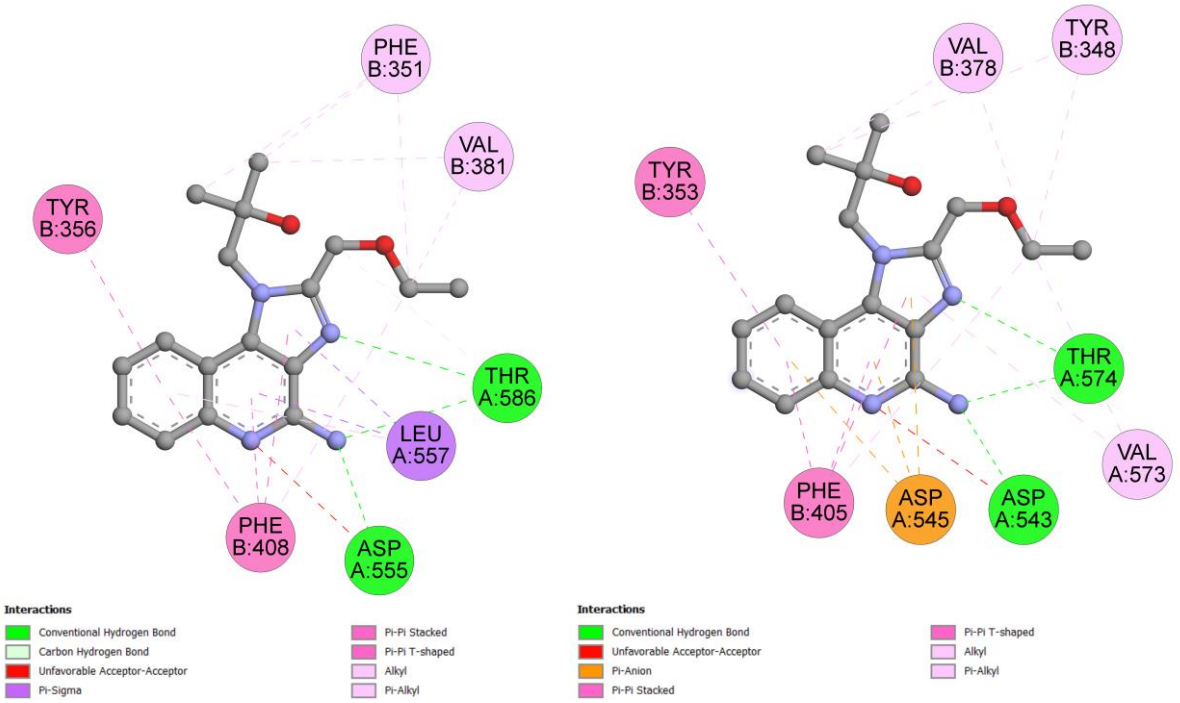


**Figure 51**: Key amino acid residues involved in the interaction of resiquimod with TLR7 (left) and TLR8 (right).

Furthermore, these residues are conserved between human and mouse TLR7 and TLR8, but are not found in most other TLRs.

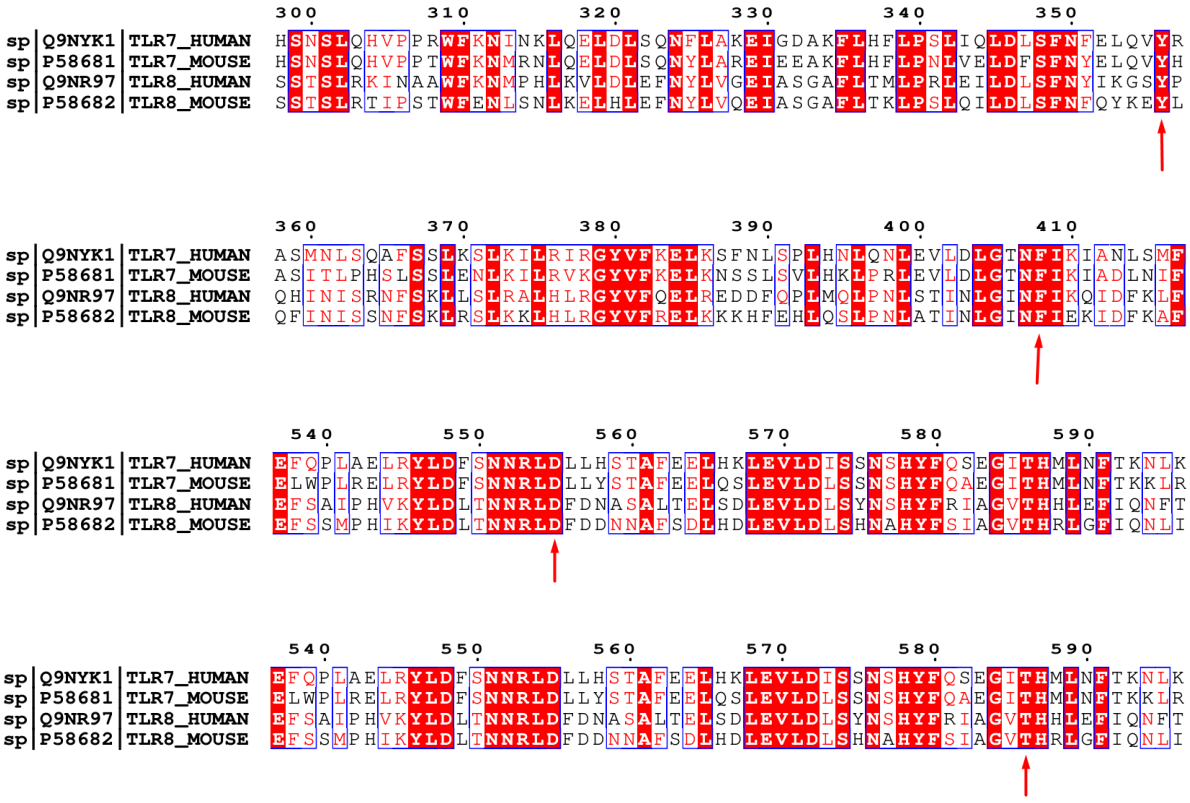


**Figure 52**: Multiple sequence alignment (MUSCLE) of human and mouse TLR7 and TLR8; red arrows show conserved residues in the binding site

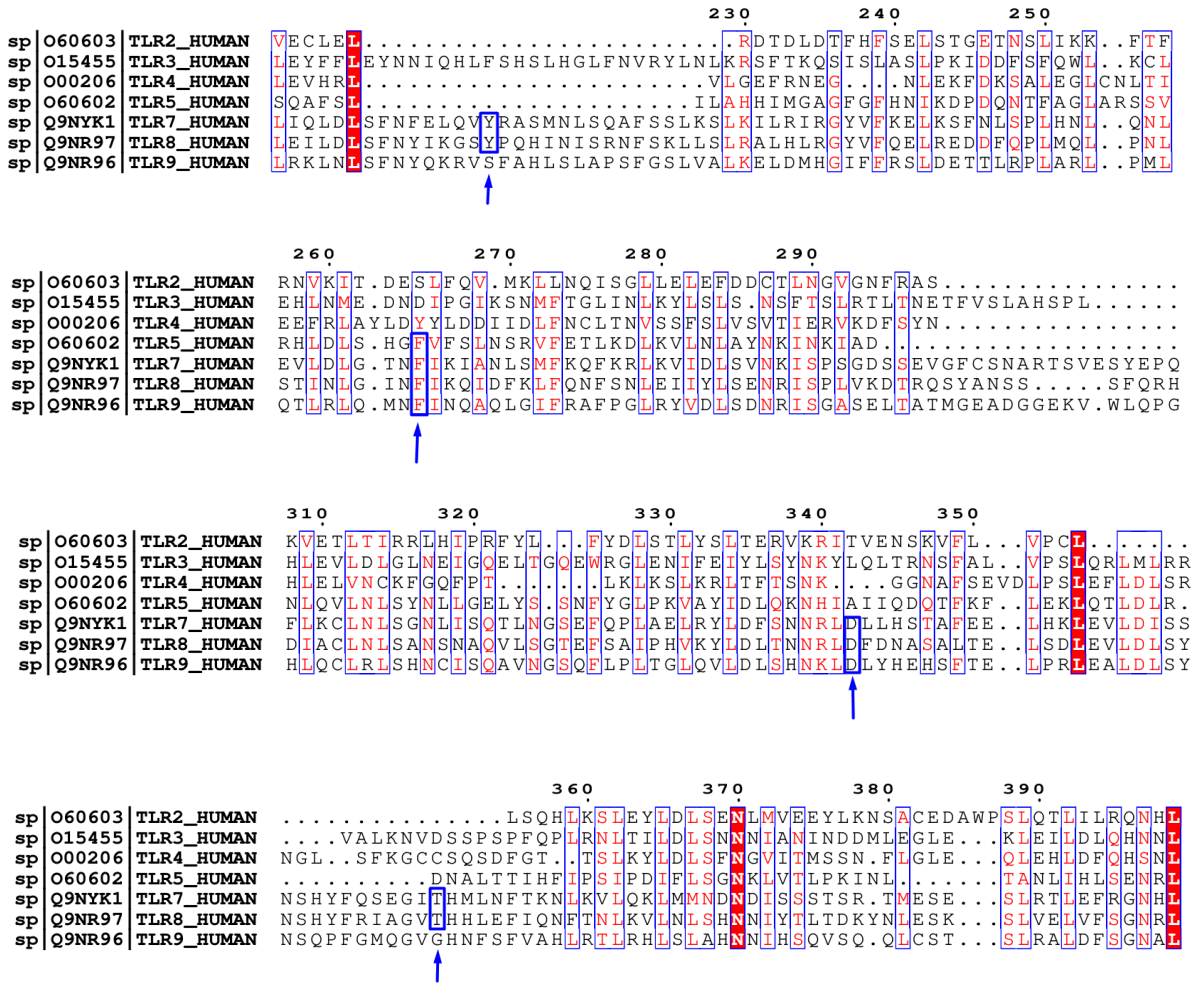


**Figure 53**: Multiple sequence alignment (MUSCLE) of human TLR2,3,4,5,7,8,9; blue arrows show conserved residues in the binding site

### 7.6.2 Analysis of MD simulation results: RMSD and RMSF graphs

We can observe that the ligated receptor (e.g., complexed with R848) is more stabilized than the apo protein, especially when residues 434–458 are removed. The ligand brings the two receptor subunits together, creating a binding site for adaptor proteins and ensuring downstream signaling. Analysis of all RMSD values for TLR7 (full) indicates that SA-401 resulted in the most stable complex. On the other hand, the complex formed with R837 appeared to be the most dynamic and even more dynamic than the non-ligated protein. In the case of TLR8, we can see a similar trend and even more pronounced stabilization with R848 and SA-401 and destabilization with R837.

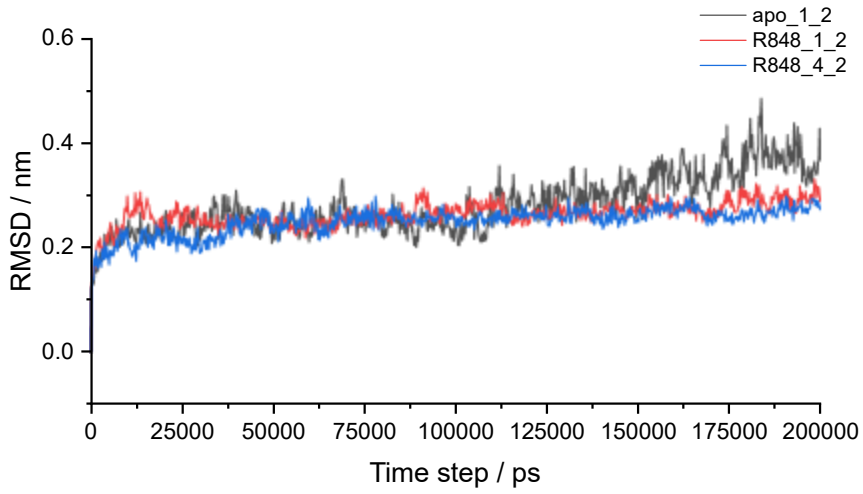


**Figure 54**: RMSD graph showing full TLR7 at pH 5.0 (apo_1_2), complex with non-protonated R848 (R848_1_2) and complex with protonated R848 (R848_4_2)

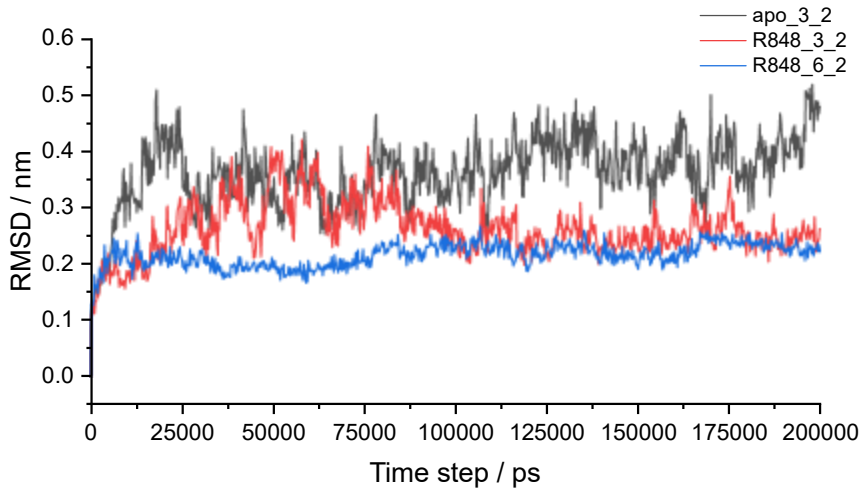


**Figure 55**: RMSD graph showing TLR7 at pH 5.0 with residues 434-458 removed (apo_3_2), complex with non-protonated R848 (R848_4_2) and complex with protonated R848 (R848_6_2)

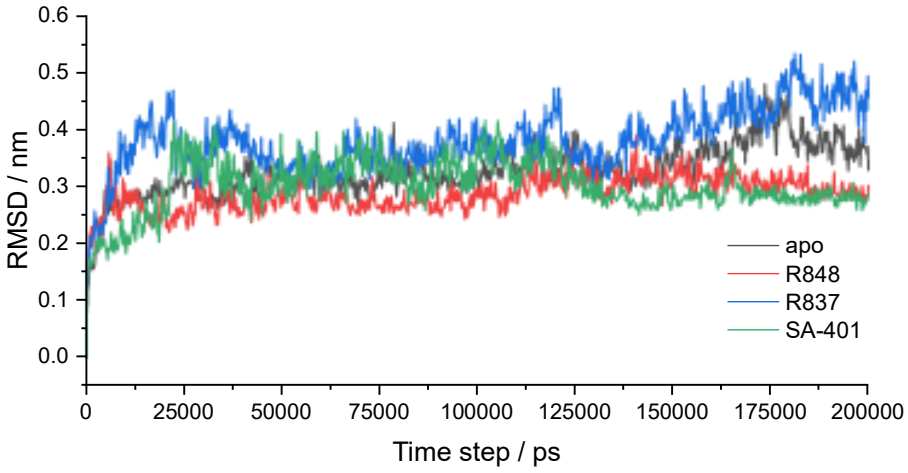


**Figure 56**: RMSD of TLR7: apo, ligated with R848, R837, and SA-401

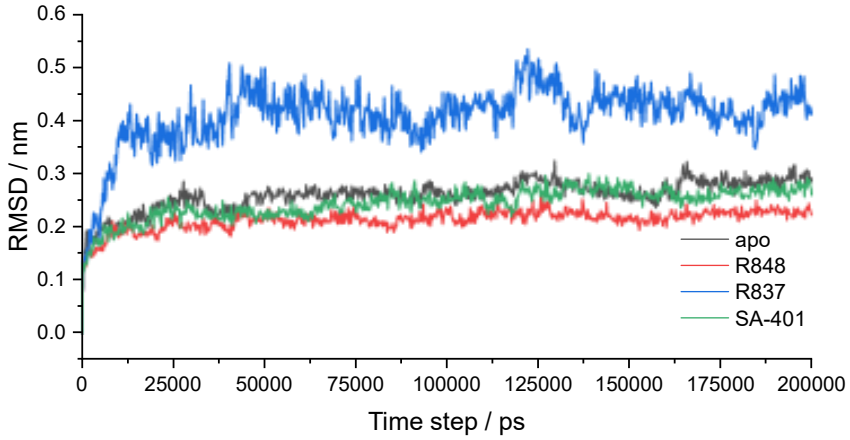


**Figure 57**: RMSD of TLR8: apo, ligated with R848, R837, and SA-401

In turn, when examining the RMSD graph of the ligand, we can identify several distinct states in which the ligand can be found within the binding site. Furthermore, although the binding sites are identical, molecular dynamics cause them to become asymmetric, leading to different ligand behaviors and potentially varying binding energies.

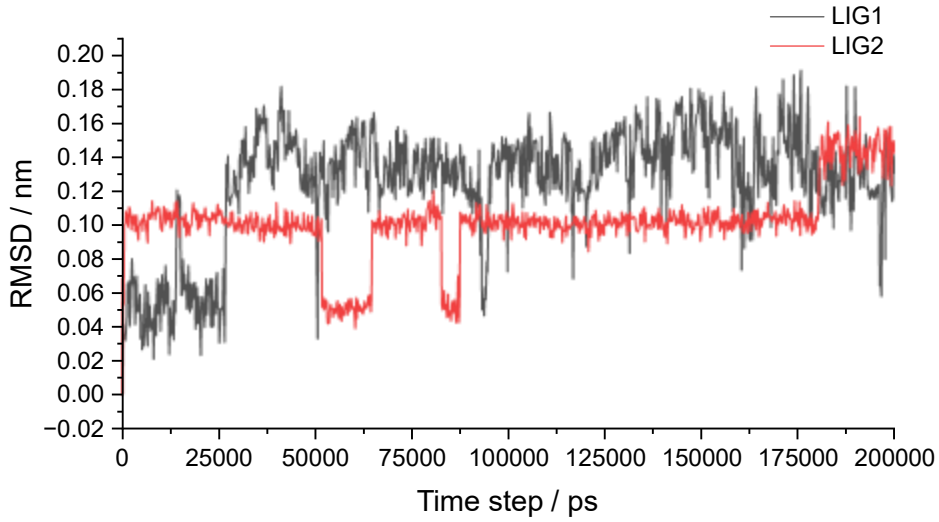


**Figure 58**: RMSD of both ligands in R848_4

We also performed RMSF analysis, which revealed notable differences between the ligand-bound and apo systems. As shown in the figure below, the smallest differences in fluctuation occur in the central region of the protein (residues 350–600), excluding the flexible segment that does not form stable secondary structure. In contrast, fluctuations are considerably higher at the N- and C-terminal regions. These findings suggest that ligand binding stabilizes not only the local ligand–protein interface but also the inter-chain interface of the receptor.

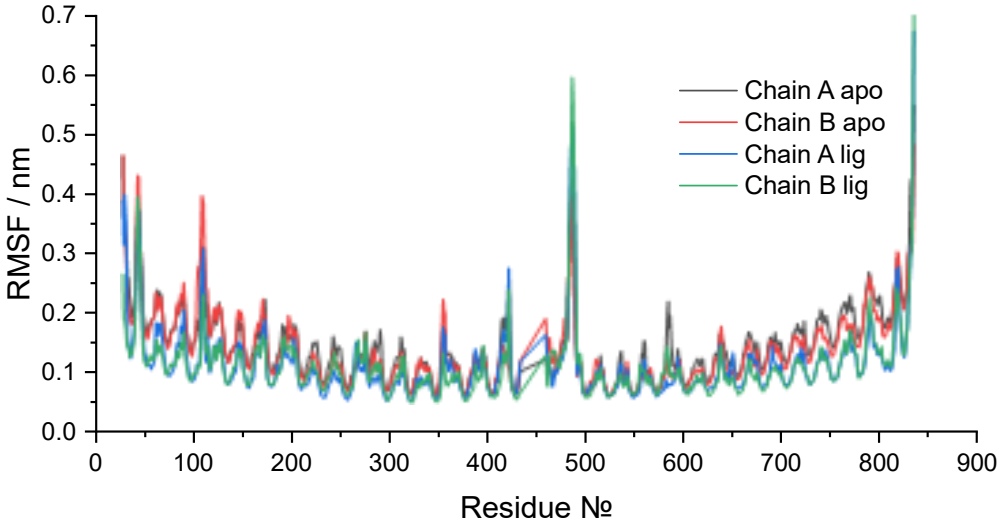


**Figure 59**: RMSF analysis of apo_3_2 and R848_6_2

### 7.6.3 MM/PBSA and MM/GBSA results

First, we analyzed the reproducibility of the obtained results. For this, simulations R848_1 to R848_6 were repeated twice, starting from the same initial complex. Solvation, ionization procedures, as well as energy minimization and equilibration steps, were repeated. It can be observed that, while reproducibility was quite good in some cases (e.g., R848_1), it was worse in others (e.g., R848_5), despite identical starting positions for the ligand and receptor. This variability is likely due to the random nature of the solvation and ionization steps, which can affect ligand-receptor interactions. Ideally, several replicates should be run to ensure a proper comparison.

**Table 3**: Binding energies (kcal/mol) for resiquimod complexed with TLR7. The normal form is represented as R848_1, R848_2, and R848_3, while the protonated form is represented as R848_4, R848_5, and R848_6. PBSA1 and PBSA2 correspond to the two resiquimod molecules within each complex

| | | | **Binding energy / kcal mol$^{-1}$** | | | |
|---|---|---|---|---|---|---|
| | | | **Replicate 1** | | **Replicate 2** | |
| **System** | **Receptor** | **pH** | **PBSA1** | **PBSA2** | **PBSA1** | **PBSA2** |
| R848_1 | full TLR7 | 5.0 | -19.40 | -21.84 | -17.55 | -23.12 |
| R848_2 | full TLR7 | 7.4 | -25.52 | -15.15 | -22.19 | -22.58 |
| R848_3 | 434-458 TLR7 | 5.0 | -20.19 | -20.78 | -16.25 | -17.89 |
| R848_4 | full TLR7 | 5.0 | -18.60 | -24.40 | -30.21 | -36.64 |
| R848_5 | full TLR7 | 7.4 | -32.98 | -32.89 | -25.51 | -12.75 |
| R848_6 | 434-458 TLR7 | 5.0 | -26.53 | -29.84 | -20.32 | -30.93 |

In this study, we also compared the MM/PBSA and MM/GBSA methods used for the quantitative description of ligand-receptor interactions. Both methods are widely used for

evaluating free energy calculations and are based on the following thermodynamic principles[166]:

$$\Delta G_{\text{bind}} = \Delta H - T\Delta S \approx \Delta E_{\text{MM}} + \Delta G_{\text{sol}} - T\Delta S$$

where $\Delta E_{\text{MM}}$ is the change of the gas-phase molecular mechanics (MM) energy, $\Delta G_{\text{sol}}$ is the solvation free energy, and $T\Delta S$ represents the conformational entropy.

The molecular mechanics energy $\Delta E_{\text{MM}}$ is a sum of internal contributions $\Delta E_{\text{internal}}$ (bonds, angles, dihedrals), electrostatic interactions, and van der Waals interactions. The solvation free energy is composed of a polar component (calculated via the Poisson-Boltzmann model $\Delta G_{\text{PB}}$ or the Generalized Born model $\Delta G_{\text{GB}}$) and a nonpolar component (calculated via solvent-accessible surface area $\Delta G_{\text{SA}}$)[166]:

$$\Delta E_{\text{MM}} = \Delta E_{\text{internal}} + \Delta E_{\text{electrostatic}} + \Delta E_{\text{vdw}}$$

$$\Delta G_{\text{sol}} = \Delta G_{\text{PB/GB}} + \Delta G_{\text{SA}}$$

It is worth mentioning that these calculations can be sensitive to the system being simulated and other conditions, such as the force field used, simulation length, and other molecular dynamics parameters. Hou et al.[166] found that the PBSA model is more accurate for calculating absolute free binding energies, while GBSA is generally more robust and can perform better in relative free energy calculations.

Among the various systems tested, we examined the effect of varying pH levels by preparing the receptor at pH 5.0 versus pH 7.4, as the endosomal environment is typically acidic, with pH depending on the type of endosome. Additionally, the receptor must be proteolytically cleaved prior to activation, as this is essential for its function. Therefore, we simulated the system at pH 5.0 with residues 434–458 removed, as previously described by Wang et al[167]. We also tested different ligand states; at pH 5.0, the nitrogen of the quinoline ring is expected to be protonated.

When the ligand is not protonated, the pH of receptor preparation does not affect the result (system R848_1 vs. R848_2). Similar results were obtained when comparing the full receptor to the one with residues removed. However, when the protonated ligand is docked, the difference between receptors prepared at pH 7.4 and pH 5.0 becomes significant (R848_4 vs. R848_5).

**Table 4**: Results obtained for the averaged MM/PBSA and MM/GBSA values for all simulated systems

| System | Receptor | Ligand | pH | PBSA aver. | GBSA aver. |
|---|---|---|---|---|---|
| R848_1 | full TLR7 | R848 | 5.0 | -20.62 | -29.76 |
| R848_2 | full TLR7 | | 7.4 | -20.34 | -25.04 |
| R848_3 | 434-458 TLR7 | | 5.0 | -20.49 | -31.48 |
| R848_4 | full TLR7 | R848 H+ | 5.0 | -21.50 | -17.00 |
| R848_5 | full TLR7 | | 7.4 | -32.94 | -33.81 |
| R848_6 | 434-458 TLR7 | | 5.0 | -28.19 | -26.64 |
| R848_7 | full TLR8 | R848 H+ | 5.0 | -42.52 | -50.33 |
| R848_8 | 434-458 TLR8 | | | -37.32 | -36.62 |
| R837_1 | full TLR7 | R837 H+ | 5.0 | -22.94 | -21.09 |
| R837_2 | 434-458 TLR7 | | | -22.17 | -26.08 |
| R837_3 | full TLR8 | R837 H+ | 5.0 | -42.56 | -41.97 |
| R837_4 | 434-458 TLR8 | | | -35.22 | -36.09 |
| SA-401_1 | full TLR7 | SA-401 H+ | 5.0 | -43.23 | -47.49 |
| SA-401_2 | 434-458 TLR7 | | | -27.51 | -35.41 |
| SA-401_3 | full TLR8 | SA-401 H+ | 5.0 | -49.88 | -55.22 |
| SA-401_4 | 434-458 TLR8 | | | -41.56 | -45.29 |

Next, we compared the binding energy of protonated resiquimod to TLR7 and TLR8 (e.g., R848_4 vs. R848_7). In both cases (full and cleaved receptor), a stronger binding affinity toward TLR8 was observed. A similar trend was seen when imiquimod was docked instead of resiquimod. This result is inconsistent with previously reported data by Wang et al[167], indicating that further optimization is needed to improve accuracy.

One important factor could be the initial ligand conformation. The ligand was manually docked based on the crystal structure of the complex, which may have introduced structural clashes. After energy minimization, ligand destabilization could occur. To improve this, it would be beneficial to use docking software and simulate several docking poses.

In this study, we compared resiquimod, imiquimod, and our ligand SA-401. For the TLR7 systems, SA-401 demonstrated the strongest binding, particularly in the case of full TLR7. The obtained value was approximately twice as high as that for R848. However, the difference between SA-401 and R848 became negligible when the processed TLR7 (with residues removed) was simulated. In the TLR8 systems, SA-401 also showed the highest binding energy, although the difference was not significant.

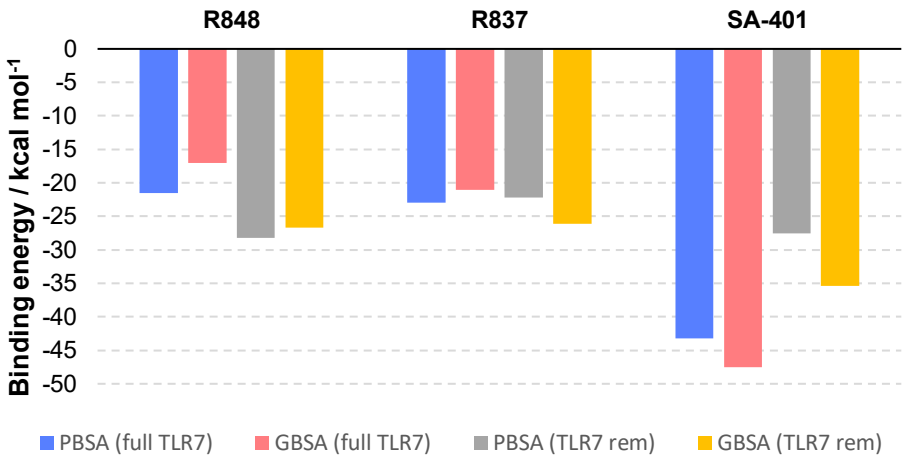


**Figure 60**: Bar chart of binding energy results for all systems with TLR7

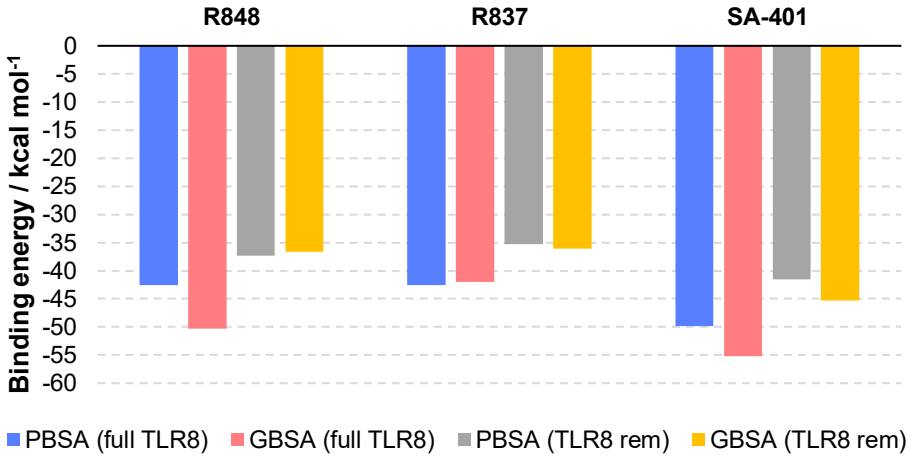


**Figure 61**: Bar chart of binding energy results for all systems with TLR8

# 8 Conclusion

Previously, we demonstrated that the TLR7/8 agonist SA-401 can effectively replace resiquimod in MBTA immunotherapy in vivo without compromising its therapeutic efficacy. In this study, we extended that work with several aims. First, SA-401 was successfully synthesized and characterized by NMR spectroscopy and HPLC/MS, confirming its high purity. Second, we synthesized a novel polyphosphazene polymer grafted with PGA chains for conjugation to SA-401 via a hydrazone bond; this polymer was characterized by NMR and GPC. We optimized the coupling protocol and quantified the drug loading using UV-Vis spectroscopy, which yielded 7% (weight percent) loading. The polymer conjugate has the potential for enhanced *in vivo* delivery by improving tumor selectivity and reducing side effects commonly associated with immune response modifiers, such as resiquimod. This should be tested in future experiments. Third, we aimed to compare resiquimod and SA-401 using a comprehensive proteomics assay in primary bone-marrow-derived macrophages, achieving 97% purity in macrophage cultures, as confirmed by flow cytometry. We optimized activation and lysis protocols and evaluated protein content using BCA assays and SDS-PAGE; however, full proteomics analysis remains a priority for future work due to time constraints. Finally, molecular dynamics simulations employing MM/GBSA and MM/PBSA methods were used to compare various TLR ligands, revealing that binding energy predictions are highly sensitive to simulation parameters, initial complex structures, ligand protonation states, and related variables. Among all ligands tested, SA-401 showed the highest binding energy for both TLR7 and TLR8, although for TLR8, the difference from the other ligands was not significant. We confirmed that ligand binding stabilizes the receptor, consistent with natural agonist function, but noted that further optimization is necessary for reliable binding energy predictions and ligand comparisons. Together, these findings advance the understanding of SA-401's therapeutic potential and identify key areas for future investigation.

## 9 List of abbreviations

| | |
|---|---|
| Abs | Antibodies |
| AID | Activation-induced cytidine deaminase |
| ALRs | AIM-2-like receptors |
| API | Active pharmaceutical ingredient |
| CDK | Cyclin-dependent kinase |
| CKI | Cyclin-dependent kinase inhibitor |
| CLRs | C-type-lectin receptors |
| COX | Cyclooxygenase |
| CRP | C-reactive protein |
| CRs | Complement receptors |
| CTLs | Cytotoxic T lymphocytes |
| DAMPs | Damage-associated molecular patterns |
| DD | Death domain |
| DISC | Death-inducing signaling complex |
| DTCs | Disseminated tumor cells |
| EGFR | Epidermal growth factor receptor |
| EMT | Epithelial-mesenchymal transition |
| ESL | E-selectin ligand |
| FGF | Fibroblast growth factor receptor |
| FGFR | Fibroblast growth factor receptor |
| GFs | Growth factors |
| GPCR | G-protein coupled receptor |
| HIF | Hypoxia-inducible factor |
| ICAD | Inhibitor of caspase-activated Dnase |
| IKK | IκB kinase |
| IL | Interleukin |
| IRAK | IL-1R-associated kinase |
| IRF | Interferon regulatory factor |
| ISGs | Interferon-stimulated genes |
| ISRE | Interferon-stimulated response elements |
| LTA | Lipoteichoic acid |
| MET | Mesenchymal-epithelial transition (MET) |
| miRNAs | microRNAs |
| MMP | Matrix metalloproteinase |
| MOMP | Membrane permeabilization |

| | |
|---|---|
| MyD88 | Myeloid differentiation primary response 88 |
| NEMO | NF-kB essential regulator |
| NF-kB | Nuclear factor-kB |
| NLRs | NOD-like receptors |
| NOD | Nucleotide-binding domain |
| PAMPs | Pathogen-associated molecular patterns |
| PDGF | Platelet-derived growth factor |
| PEG | Polyethylene glycol |
| PGA | Polyglutamic acid |
| POPZ | Poly(organo)phosphazenes |
| PRRs | Pathogen recognition receptors |
| PSGL | P-selectin glycoprotein ligand |
| RLRs | RIG-I-like receptors |
| ROS | Reactive oxygen species |
| RTK | Receptor tyrosine kinase |
| TAB | TAK1-binding protein |
| TAK | TGF-β-activated kinase |
| TCA | Tricarboxylic acid cycle |
| TFs | Transcription factors |
| TLRs | Toll-like receptors |
| TME | Tumor microenvironment |
| TNF | Tumor necrosis factor |
| TRAF | TNF receptor-associated factor |
| TSG | Tumor suppressor genes |
| Ubc | Ubiquitin-conjugating enzyme |
| VEGF | Vascular endothelial growth factor |

## 10 References


[1] I. B. Weinstein, K. Case, *Cancer research* **2008**, *68*, 6861–6862.
[2] F. Balkwill, A. Mantovani, *Lancet (London, England)* **2001**, *357*, 539–545.
[3] S. McAleer, *The Ulster Medical Journal* **2022**, *91*, 124–129.
[4] F. Bray, M. Laversanne, H. Sung, J. Ferlay, R. L. Siegel, I. Soerjomataram, A. Jemal, *CA: a cancer journal for clinicians* **2024**, *74*, 229–263.
[5] M. Arruebo, N. Vilaboa, B. Sáez-Gutierrez, J. Lambea, A. Tres, M. Valladares, A. González-Fernández, *Cancers* **2011**, *3*, 3279–3330.
[6] W. M. C. van den Boogaard, D. S. J. Komninos, W. P. Vermeij, *Cancers* **2022**, *14*.
[7] D. T. Debela, S. G. Muzazu, K. D. Heraro, M. T. Ndalama, B. W. Mesele, D. C. Haile, S. K. Kitui, T. Manyazewal, *SAGE open medicine* **2021**, *9*, 20503121211034366.
[8] E. F. McCarthy, *The Iowa orthopaedic journal* **2006**, *26*, 154–158.
[9] S. Tan, D. Li, X. Zhu, *Biomedicine & pharmacotherapy = Biomedecine & pharmacotherapie* **2020**, *124*, 109821.
[10] Y. Zhang, Z. Zhang, *Cellular & molecular immunology* **2020**, *17*, 807–821.
[11] J. S. Brown, S. R. Amend, R. H. Austin, R. A. Gatenby, E. U. Hammarlund, K. J. Pienta, *Molecular cancer research : MCR* **2023**, *21*, 1142–1147.
[12] A. Ottaiano, M. Ianniello, M. Santorsola, R. Ruggiero, R. Sirica, F. Sabbatino, F. Perri, M. Cascella, M. Di Marzo, M. Berretta, M. Caraglia, G. Nasti, G. Savarese, *Biology* **2023**, *12*.
[13] D. Hanahan, R. A. Weinberg, *Cell* **2011**, *144*, 646–674.
[14] D. Hanahan, R. A. Weinberg, *Cell* **2000**, *100*, 57–70.
[15] D. Hanahan, *Cancer discovery* **2022**, *12*, 31–46.
[16] Bruce Alberts, Alexander Johnson, Julian Lewis, David Morgan, Martin Raff, Keith Roberts, and Peter Walter, *Molecular Biology of the Cell*, **2014**.
[17] E. N. Kontomanolis, A. Koutras, A. Syllaios, D. Schizas, A. Mastoraki, N. Garmpis, M. Diakosavvas, K. Angelou, G. Tsatsaris, A. Pagkalos, T. Ntounis, Z. Fasoulakis, *Anticancer research* **2020**, *40*, 6009–6015.
[18] O. Bagci, S. Kurtgöz, *North American journal of medical sciences* **2015**, *7*, 341–346.
[19] A. Fernández-Medarde, E. Santos, *Genes & cancer* **2011**, *2*, 344–358.
[20] Robert A. Weinberg, *The Biology of Cancer*, **2014**.
[21] E. Spehalski, A. L. Kovalchuk, J. T. Collins, G. Liang, W. Dubois, H. C. Morse, D. O. Ferguson, R. Casellas, W. A. Dunnick, *Proceedings of the National Academy of Sciences of the United States of America* **2012**, *109*, 13728–13732.
[22] J. Zheng, *Oncology reports* **2013**, *30*, 2011–2019.
[23] E. Witsch, M. Sela, Y. Yarden, *Physiology (Bethesda, Md.)* **2010**, *25*, 85–101.
[24] C. Tomuleasa, A.-B. Tigu, R. Munteanu, C.-S. Moldovan, D. Kegyes, A. Onaciu, D. Gulei, G. Ghiaur, H. Einsele, C. M. Croce, *Signal transduction and targeted therapy* **2024**, *9*, 201.
[25] S. Tiash, E. Chowdhury, *J Cancer Metastasis Treat* **2015**, *1*, 190.
[26] H. Wang, M. Guo, H. Wei, Y. Chen, *Signal transduction and targeted therapy* **2023**, *8*, 92.
[27] T. C. Dakal, B. Dhabhai, A. Pant, K. Moar, K. Chaudhary, V. Yadav, V. Ranga, N. K. Sharma, A. Kumar, P. K. Maurya, J. Maciaczyk, I. G. H. Schmidt-Wolf, A. Sharma, *MedComm* **2024**, *5*, e582.
[28] A. D. Choudhury, H. Beltran, *Clinical cancer research : an official journal of the American Association for Cancer Research* **2019**, *25*, 4199–4201.

[29] P. Bhateja, M. Chiu, G. Wildey, M. B. Lipka, P. Fu, M. C. L. Yang, F. Ardeshir-Larijani, N. Sharma, A. Dowlati, *Cancer medicine* **2019**, *8*, 1459–1466.
[30] D. L. Burkhart, J. Sage, *Nature reviews. Cancer* **2008**, *8*, 671–682.
[31] J. Huang, *Pharmacology & therapeutics* **2021**, *220*, 107720.
[32] F. Mantovani, L. Collavin, G. Del Sal, *Cell death and differentiation* **2019**, *26*, 199–212.
[33] F. Pentimalli, *Cell death and differentiation* **2018**, *25*, 7–9.
[34] S. Fulda, *International journal of cancer* **2009**, *124*, 511–515.
[35] B. Salaun, P. Romero, S. Lebecque, *European journal of immunology* **2007**, *37*, 3311–3318.
[36] B. A. Carneiro, W. S. El-Deiry, *Nature reviews. Clinical oncology* **2020**, *17*, 395–417.
[37] Y. Shi, *Molecular cell* **2002**, *9*, 459–470.
[38] J. C. de Bardet, C. R. Cardentey, B. L. González, D. Patrone, I. L. Mulet, D. Siniscalco, M. d. L. A. Robinson-Agramonte, *Biotech (Basel (Switzerland))* **2023**, *12*.
[39] M. S. Waitkus, E. N. Erman, Z. J. Reitman, D. M. Ashley, *Neuro-oncology* **2024**, *26*, 1012–1024.
[40] J. K. Soo, A. D. Mackenzie Ross, D. M. Kallenberg, C. Milagre, W. Heung Chong, J. Chow, L. Hill, S. Hoare, R. S. Collinson, M. Hossain, W. N. Keith, R. Marais, D. C. Bennett, *Pigment cell & melanoma research* **2011**, *24*, 490–503.
[41] U. Herbig, J. M. Sedivy, *Mechanisms of ageing and development* **2006**, *127*, 16–24.
[42] I. Pellarin, A. Dall'Acqua, A. Favero, I. Segatto, V. Rossi, N. Crestan, J. Karimbayli, B. Belletti, G. Baldassarre, *Signal transduction and targeted therapy* **2025**, *10*, 11.
[43] D. Aguilar-Cazares, R. Chavez-Dominguez, A. Carlos-Reyes, C. Lopez-Camarillo, O. N. La Hernadez de Cruz, J. S. Lopez-Gonzalez, *Frontiers in oncology* **2019**, *9*, 1399.
[44] C. S. Melincovici, A. B. Boşca, S. Şuşman, M. Mărginean, C. Mihu, M. Istrate, I. M. Moldovan, A. L. Roman, C. M. Mihu, *Romanian journal of morphology and embryology = Revue roumaine de morphologie et embryologie* **2018**, *59*, 455–467.
[45] R. Zhang, Y. Yao, H. Gao, X. Hu, *Frontiers in oncology* **2024**, *14*, 1359069.
[46] K. Masłowska, P. K. Halik, D. Tymecka, A. Misicka, E. Gniazdowska, *Cancers* **2021**, *13*.
[47] P. Mabeta, V. Steenkamp, *International journal of molecular sciences* **2022**, *23*.
[48] X. Wang, A. M. Bove, G. Simone, B. Ma, *Frontiers in cell and developmental biology* **2020**, *8*, 599281.
[49] Z. Chen, F. Han, Y. Du, H. Shi, W. Zhou, *Signal transduction and targeted therapy* **2023**, *8*, 70.
[50] G. L. Semenza, *Nature reviews. Cancer* **2003**, *3*, 721–732.
[51] K. Ganesh, J. Massagué, *Nature medicine* **2021**, *27*, 34–44.
[52] P. S. Steeg, D. Theodorescu, *Nature clinical practice. Oncology* **2008**, *5*, 206–219.
[53] S. Gerstberger, Q. Jiang, K. Ganesh, *Cell* **2023**, *186*, 1564–1579.
[54] E. Risson, A. R. Nobre, V. Maguer-Satta, J. A. Aguirre-Ghiso, *Nature cancer* **2020**, *1*, 672–680.
[55] D. H. Kim, T. Xing, Z. Yang, R. Dudek, Q. Lu, Y.-H. Chen, *Journal of clinical medicine* **2017**, *7*.
[56] T.-T. Liao, M.-H. Yang, *Molecular oncology* **2017**, *11*, 792–804.
[57] J. Yang, R. A. Weinberg, *Developmental cell* **2008**, *14*, 818–829.
[58] C. Liao, Q. Wang, J. An, Q. Long, H. Wang, M. Xiang, M. Xiang, Y. Zhao, Y. Liu, J. Liu, X. Guan, *International journal of biological sciences* **2021**, *17*, 3036–3047.
[59] Y. Huang, W. Hong, X. Wei, *Journal of Hematology & Oncology* **2022**, *15*.

[60] G. Assani, Y. Zhou, *Oncology letters* **2019**, *17*, 23–30.
[61] D. G. Hardie, *Endocrine-related cancer* **2022**, *29*, T1-T13.
[62] M. Potter, E. Newport, K. J. Morten, *Biochemical Society Transactions* **2016**, *44*, 1499–1505.
[63] X. Chen, Y. Qian, S. Wu, *Free radical biology & medicine* **2014**, *0*, 253–263.
[64] I. Barba, L. Carrillo-Bosch, J. Seoane, *International journal of molecular sciences* **2024**, *25*.
[65] J. D. Gordan, C. B. Thompson, M. C. Simon, *Cancer cell* **2007**, *12*, 108–113.
[66] J. S. Burns, G. Manda, *International journal of molecular sciences* **2017**, *18*.
[67] J. Liu, C. Zhang, W. Hu, Z. Feng, *Journal of molecular cell biology* **2019**, *11*, 284–292.
[68] D. C. Wallace, *Nature reviews. Cancer* **2012**, *12*, 685–698.
[69] R. Shiratori, K. Furuichi, M. Yamaguchi, N. Miyazaki, H. Aoki, H. Chibana, K. Ito, S. Aoki, *Scientific reports* **2019**, *9*, 18699.
[70] S. Y. Lunt, M. G. Vander Heiden, *Annual review of cell and developmental biology* **2011**, *27*, 441–464.
[71] J. Zheng, *Oncology letters* **2012**, *4*, 1151–1157.
[72] N. C. Denko, *Nature reviews. Cancer* **2008**, *8*, 705–713.
[73] Q. A. Obaid, A. M. Al-Shammari, K. K. Khudair, *Frontiers in molecular biosciences* **2022**, *9*, 816510.
[74] R. Zagozdzon, M. Winiarska, M. Firczuk, *Cancers* **2022**, *14*.
[75] S. K. Kim, S. W. Cho, *Frontiers in pharmacology* **2022**, *13*, 868695.
[76] Judith A. Owen, Jenni Punt, Sharon A. Stranford, Patricia P. Jones, *Kuby Immunology*, **2013**.
[77] I. T. Myszor, G. H. Gudmundsson, *Frontiers in immunology* **2023**, *14*, 1197908.
[78] H. Schulenburg, C. L. Kurz, J. J. Ewbank, *Immunological reviews* **2004**, *198*, 36–58.
[79] R. Wang, C. Lan, K. Benlagha, N. O. S. Camara, H. Miller, M. Kubo, S. Heegaard, P. Lee, L. Yang, H. Forsman, X. Li, Z. Zhai, C. Liu, *MedComm* **2024**, *5*, e714.
[80] E. R. Sherwood, K. R. Burelbach, M. A. McBride, C. L. Stothers, A. M. Owen, A. Hernandez, N. K. Patil, D. L. Williams, J. K. Bohannon, *Journal of immunology (Baltimore, Md. : 1950)* **2022**, *208*, 785–792.
[81] T. Lazarov, S. Juarez-Carreño, N. Cox, F. Geissmann, *Nature* **2023**, *618*, 698–707.
[82] M. Jaeger, M. H. T. Stappers, L. A. B. Joosten, I. C. Gyssens, M. G. Netea, *Future microbiology* **2015**, *10*, 989–1008.
[83] K. Sheu, S. Luecke, A. Hoffmann, *Current opinion in systems biology* **2019**, *18*, 53–61.
[84] P. J. Murray, T. A. Wynn, *Nature reviews. Immunology* **2011**, *11*, 723–737.
[85] E. Uribe-Querol, C. Rosales, *Frontiers in immunology* **2020**, *11*, 1066.
[86] J. Moretti, J. M. Blander, *Current opinion in immunology* **2014**, *26*, 100–110.
[87] L. Franchi, N. Warner, K. Viani, G. Nuñez, *Immunological reviews* **2009**, *227*, 106–128.
[88] L. Chen, H. Deng, H. Cui, J. Fang, Z. Zuo, J. Deng, Y. Li, X. Wang, L. Zhao, *Oncotarget* **2018**, *9*, 7204–7218.
[89] T. H. Mogensen, *Clinical microbiology reviews* **2009**, *22*, 240-73, Table of Contents.
[90] L. Zhao, J. Y. Lee, D. H. Hwang, *Nutrition reviews* **2011**, *69*, 310–320.
[91] D. Salvemini, S. F. Kim, V. Mollace, *American journal of physiology. Regulatory, integrative and comparative physiology* **2013**, *304*, R473-87.

[92] A. C. C. C. Branco, F. S. Y. Yoshikawa, A. J. Pietrobon, M. N. Sato, *Mediators of inflammation* **2018**, *2018*, 9524075.
[93] F. Wu, L. Liu, H. Zhou, *Journal of leukocyte biology* **2017**, *101*, 1119–1132.
[94] E. Chavakis, E. Y. Choi, T. Chavakis, *Thrombosis and haemostasis* **2009**, *102*, 191–197.
[95] D. Vestweber, *Nature reviews. Immunology* **2015**, *15*, 692–704.
[96] O. Takeuchi, S. Akira, *Cell* **2010**, *140*, 805–820.
[97] M. K. Vidya, V. G. Kumar, V. Sejian, M. Bagath, G. Krishnan, R. Bhatta, *International reviews of immunology* **2018**, *37*, 20–36.
[98] S. Akira, K. Takeda, *Nature reviews. Immunology* **2004**, *4*, 499–511.
[99] J. Deguine, G. M. Barton, *F1000prime reports* **2014**, *6*, 97.
[100] G. W. Rhyasen, D. T. Starczynowski, *British journal of cancer* **2015**, *112*, 232–237.
[101] J. Wang, X. Wu, M. Jiang, G. Tai, *BioMed research international* **2020**, *2020*, 4607197.
[102] D. B. Conze, C.-J. Wu, J. A. Thomas, A. Landstrom, J. D. Ashwell, *Molecular and cellular biology* **2008**, *28*, 3538–3547.
[103] A. Kanayama, R. B. Seth, L. Sun, C.-K. Ea, M. Hong, A. Shaito, Y.-H. Chiu, L. Deng, Z. J. Chen, *Molecular cell* **2004**, *15*, 535–548.
[104] Y.-R. Xu, C.-Q. Lei, *Frontiers in immunology* **2020**, *11*, 608976.
[105] M. C. Mulero, T. Huxford, G. Ghosh, *Advances in experimental medicine and biology* **2019**, *1172*, 207–226.
[106] K. Taniguchi, M. Karin, *Nature reviews. Immunology* **2018**, *18*, 309–324.
[107] H. Zhao, L. Wu, G. Yan, Y. Chen, M. Zhou, Y. Wu, Y. Li, *Signal transduction and targeted therapy* **2021**, *6*, 263.
[108] Y. Endo, H. Marusawa, K. Kinoshita, T. Morisawa, T. Sakurai, I.-M. Okazaki, K. Watashi, K. Shimotohno, T. Honjo, T. Chiba, *Oncogene* **2007**, *26*, 5587–5595.
[109] A. Oh, M. Pardo, A. Rodriguez, C. Yu, L. Nguyen, O. Liang, A. Chorzalska, P. M. Dubielecka, *Cell communication and signaling : CCS* **2023**, *21*, 291.
[110] K. Augoff, A. Hryniewicz-Jankowska, R. Tabola, K. Stach, *Cancers* **2022**, *14*.
[111] P. Pandey, S. Lakhanpal, D. Mahmood, H. N. Kang, B. Kim, S. Kang, J. Choi, M. Choi, S. Pandey, M. Bhat, S. Sharma, F. Khan, M. N. Park, B. Kim, *Frontiers in pharmacology* **2024**, *15*, 1513422.
[112] H. Yu, L. Lin, Z. Zhang, H. Zhang, H. Hu, *Signal transduction and targeted therapy* **2020**, *5*, 209.
[113] A. T. Bender, E. Tzvetkov, A. Pereira, Y. Wu, S. Kasar, M. M. Przetak, J. Vlach, T. B. Niewold, M. A. Jensen, S. L. Okitsu, *ImmunoHorizons* **2020**, *4*, 93–107.
[114] A. Schoenemeyer, B. J. Barnes, M. E. Mancl, E. Latz, N. Goutagny, P. M. Pitha, K. A. Fitzgerald, D. T. Golenbock, *The Journal of biological chemistry* **2005**, *280*, 17005–17012.
[115] X. Yu, A. U. Rehman, L. Dang, X. Zhang, J. Liu, X. Xiong, G. Chen, Z. Jian, *Frontiers in immunology* **2025**, *16*, 1535823.
[116] H. Almuttaqi, I. A. Udalova, *The FEBS journal* **2019**, *286*, 1624–1637.
[117] J. Ren, X. Chen, Z. J. Chen, *Proceedings of the National Academy of Sciences of the United States of America* **2014**, *111*, 17438–17443.
[118] D. H. Kim, W.-W. Lee, *Immune network* **2024**, *24*, e21.
[119] A. Malik, T.-D. Kanneganti, *Immunological reviews* **2018**, *281*, 124–137.
[120] D. Boraschi, *Frontiers in immunology* **2022**, *13*, 872155.
[121] E. Grebenciucova, S. VanHaerents, *Frontiers in immunology* **2023**, *14*, 1255533.

[122] X. Wang, Y. Lin, *Acta pharmacologica Sinica* **2008**, *29*, 1275–1288.
[123] V. Carlini, D. M. Noonan, E. Abdalalem, D. Goletti, C. Sansone, L. Calabrone, A. Albini, *Frontiers in immunology* **2023**, *14*, 1161067.
[124] C. A. Dinarello, D. Novick, S. Kim, G. Kaplanski, *Frontiers in immunology* **2013**, *4*, 289.
[125] C. E. Hughes, R. J. B. Nibbs, *The FEBS journal* **2018**, *285*, 2944–2971.
[126] C. M. López de Padilla, T. B. Niewold, *Gene* **2016**, *576*, 14–21.
[127] S. L. Pogue, B. T. Preston, J. Stalder, C. R. Bebbington, P. M. Cardarelli, *Journal of interferon & cytokine research : the official journal of the International Society for Interferon and Cytokine Research* **2004**, *24*, 131–139.
[128] J. W. Schoggins, C. M. Rice, *Current opinion in virology* **2011**, *1*, 519–525.
[129] N. Singh, D. Baby, J. P. Rajguru, P. B. Patil, S. S. Thakkannavar, V. B. Pujari, *Annals of African medicine* **2019**, *18*, 121–126.
[130] K. Park, M. S. Veena, D. S. Shin, *Frontiers in cell and developmental biology* **2022**, *10*, 830208.
[131] S. Tambunlertchai, S. M. Geary, A. K. Salem, *Pharmaceutics* **2022**, *14*.
[132] F. Palamara, S. Meindl, M. Holcmann, P. Lührs, G. Stingl, M. Sibilia, *Journal of immunology (Baltimore, Md. : 1950)* **2004**, *173*, 3051–3061.
[133] X. Zhang, Y. Xie, L. Wang, *Dermatology and therapy* **2023**, *13*, 1909–1934.
[134] H. Hackstein, A. Knoche, A. Nockher, J. Poeling, T. Kubin, M. Jurk, J. Vollmer, G. Bein, *Cellular immunology* **2011**, *271*, 401–412.
[135] F. Brugnolo, S. Sampognaro, F. Liotta, L. Cosmi, F. Annunziato, C. Manuelli, P. Campi, E. Maggi, S. Romagnani, P. Parronchi, *The Journal of allergy and clinical immunology* **2003**, *111*, 380–388.
[136] D. N. Sauder, M. H. Smith, T. Senta-McMillian, I. Soria, T.-C. Meng, *Antimicrobial agents and chemotherapy* **2003**, *47*, 3846–3852.
[137] C. Anfray, F. Mainini, E. Digifico, A. Maeda, M. Sironi, M. Erreni, A. Anselmo, A. Ummarino, S. Gandoy, F. Expósito, M. Redrado, D. Serrano, A. Calvo, M. Martens, S. Bravo, A. Mantovani, P. Allavena, F. T. Andón, *Journal for immunotherapy of cancer* **2021**, *9*.
[138] S. Stier, C. Maletzki, U. Klier, M. Linnebacher, *Clinical & developmental immunology* **2013**, *2013*, 271246.
[139] V. Caisová, O. Uher, P. Nedbalová, I. Jochmanová, K. Kvardová, K. Masáková, G. Krejčová, L. Paďouková, J. Chmelař, J. Kopecký, J. Ženka, *International immunopharmacology* **2018**, *59*, 86–96.
[140] T. Meyer, C. Surber, L. E. French, E. Stockfleth, *Expert opinion on investigational drugs* **2013**, *22*, 149–159.
[141] R.-M. Szeimies, J. Bichel, J.-P. Ortonne, E. Stockfleth, J. Lee, T.-C. Meng, *The British journal of dermatology* **2008**, *159*, 205–210.
[142] P. J. Pockros, D. Guyader, H. Patton, M. J. Tong, T. Wright, J. G. McHutchison, T.-C. Meng, *Journal of hepatology* **2007**, *47*, 174–182.
[143] C. Li, J. Wang, Y. Wang, H. Gao, G. Wei, Y. Huang, H. Yu, Y. Gan, Y. Wang, L. Mei, H. Chen, H. Hu, Z. Zhang, Y. Jin, *Acta pharmaceutica Sinica. B* **2019**, *9*, 1145–1162.
[144] M. Ikeda-Imafuku, L. L.-W. Wang, D. Rodrigues, S. Shaha, Z. Zhao, S. Mitragotri, *Journal of controlled release : official journal of the Controlled Release Society* **2022**, *345*, 512–536.

[145] Y. Nakamura, A. Mochida, P. L. Choyke, H. Kobayashi, *Bioconjugate chemistry* **2016**, *27*, 2225–2238.
[146] Y. Ali, A. Alqudah, S. Ahmad, S. Abd Hamid, U. Farooq, *Designed monomers and polymers* **2019**, *22*, 91–97.
[147] K. Ulbrich, K. Holá, V. Šubr, A. Bakandritsos, J. Tuček, R. Zbořil, *Chemical reviews* **2016**, *116*, 5338–5431.
[148] Y. Gao, M. Joshi, Z. Zhao, S. Mitragotri, *Bioengineering & translational medicine* **2023**, *9*, e10600.
[149] W. B. Liechty, D. R. Kryscio, B. V. Slaughter, N. A. Peppas, *Annual review of chemical and biomolecular engineering* **2010**, *1*, 149–173.
[150] E. A. Simone, T. D. Dziubla, V. R. Muzykantov, *Expert opinion on drug delivery* **2008**, *5*, 1283–1300.
[151] P. Ilayaperumal, P. Chelladurai, K. Vairan, P. Anilkumar, B. Balagurusamy, *Macro Materials & Eng* **2023**, *308*.
[152] K. S. Ogueri, K. S. Ogueri, H. R. Allcock, C. T. Laurencin, *Journal of vacuum science and technology. B, Nanotechnology & microelectronics : materials, processing, measurement, & phenomena : JVST B* **2020**, *38*, 30801.
[153] S. Rothemund, I. Teasdale, *Chemical Society reviews* **2016**, *45*, 5200–5215.
[154] P. Strasser, B. Montsch, S. Weiss, H. Sami, C. Kugler, S. Hager, H. Schueffl, R. Mader, O. Brüggemann, C. R. Kowol, M. Ogris, P. Heffeter, I. Teasdale, *Small (Weinheim an der Bergstrasse, Germany)* **2023**, *19*, e2300767.
[155] G. B. BACHMAN, D. E. WELTON, *Journal of the American Chemical Society* **1947**, *69*, 365–371.
[156] Stefan Aichhorn, PhD thesis, JKU, **2016**.
[157] J. Clayden, N. Greeves, S. G. Warren, *Organic chemistry;* Oxford University Press, **2012**.
[158] Z. Wang, Ed, *Comprehensive Organic Name Reactions and Reagents;* Wiley, **2010**.
[159] E. Hanan, B. Chan, A. Estrada, D. Shore, J. Lyssikatos, *Synlett* **2010**, *2010*, 2759–2764.
[160] A. Koranne, S. Turakhia, V. K. Jha, S. Gupta, R. Ravi, A. Mishra, A. K. Aggarwal, C. K. Jha, N. Dheer, A. K. Jha, *RSC advances* **2023**, *13*, 22512–22528.
[161] D. W. Tay, H. Jong, Y. H. Lim, W. Wu, X. Chew, E. G. Robins, C. W. Johannes, *The Journal of organic chemistry* **2015**, *80*, 4054–4063.
[162] M. Kobus, T. Friedrich, E. Zorn, N. Burmeister, W. Maison, *Journal of medicinal chemistry* **2024**, *67*, 5168–5184.
[163] I. Teasdale, S. Wilfert, I. Nischang, O. Brüggemann, *Polym. Chem.* **2011**, *2*, 828–834.
[164] R. Baumgartner, D. Kuai, J. Cheng, *Biomaterials science* **2017**, *5*, 1836–1844.
[165] S. Aichhorn, A. Linhardt, A. Halfmann, M. Nadlinger, S. Kirchberger, M. Stadler, B. Dillinger, M. Distel, A. Dohnal, I. Teasdale, W. Schöfberger, *Chemistry (Weinheim an der Bergstrasse, Germany)* **2017**, *23*, 17721–17726.
[166] T. Hou, J. Wang, Y. Li, W. Wang, *Journal of chemical information and modeling* **2011**, *51*, 69–82.
[167] X. Wang, Y. Chen, S. Zhang, J. N. Deng, *PloS one* **2022**, *17*, e0260565.

# 11 Appendix

## Synthesis of SA-401

### Characterization of S2

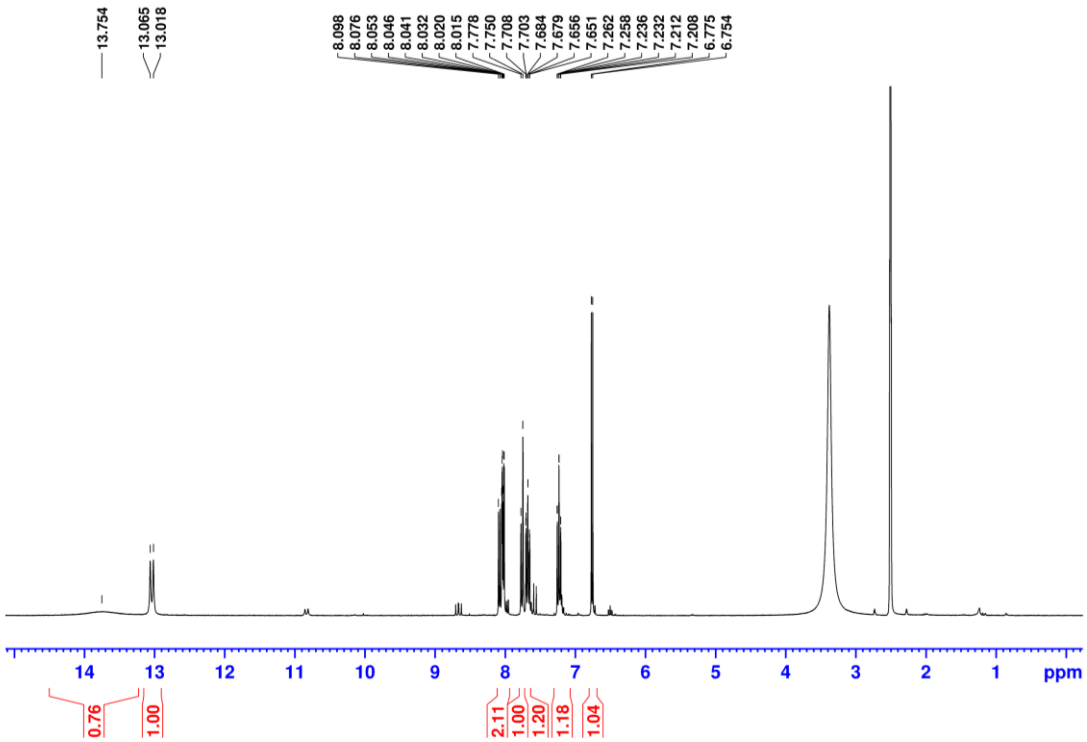


**Figure 62**: $^{1}$H NMR of S2, 300 MHz, DMSO

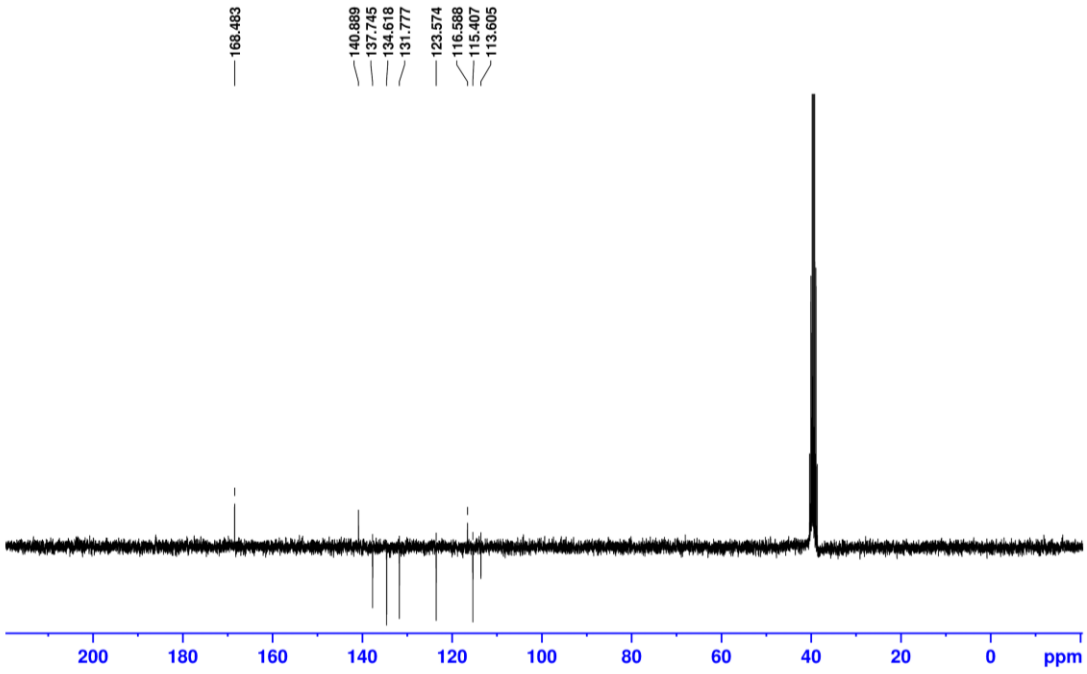


**Figure 63**: $^{13}$C NMR of S2, C13APT, 75 MHz, DMSO

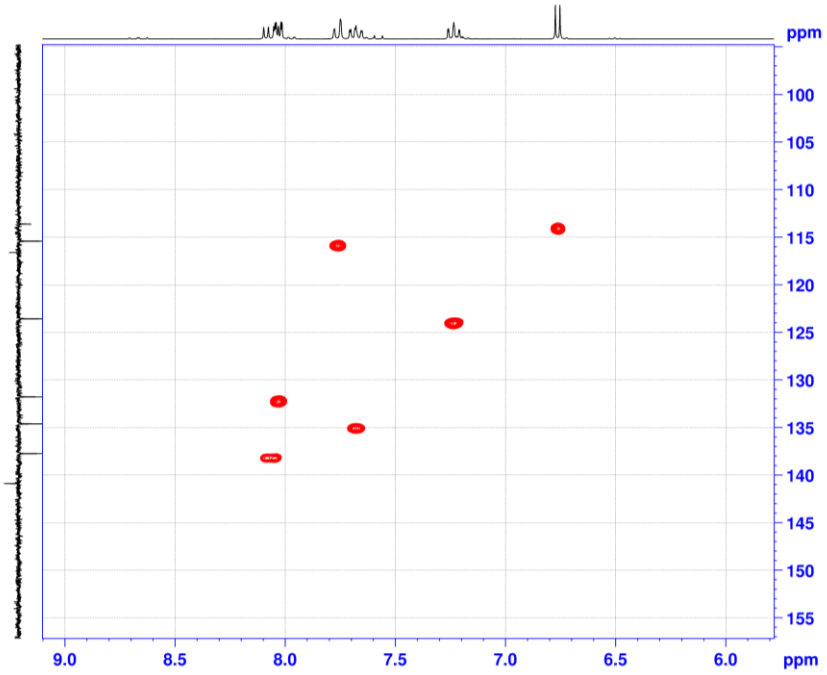


**Figure 64**: HSQC NMR of S2, HSQCGP, 300 and 75 MHz, DMSO

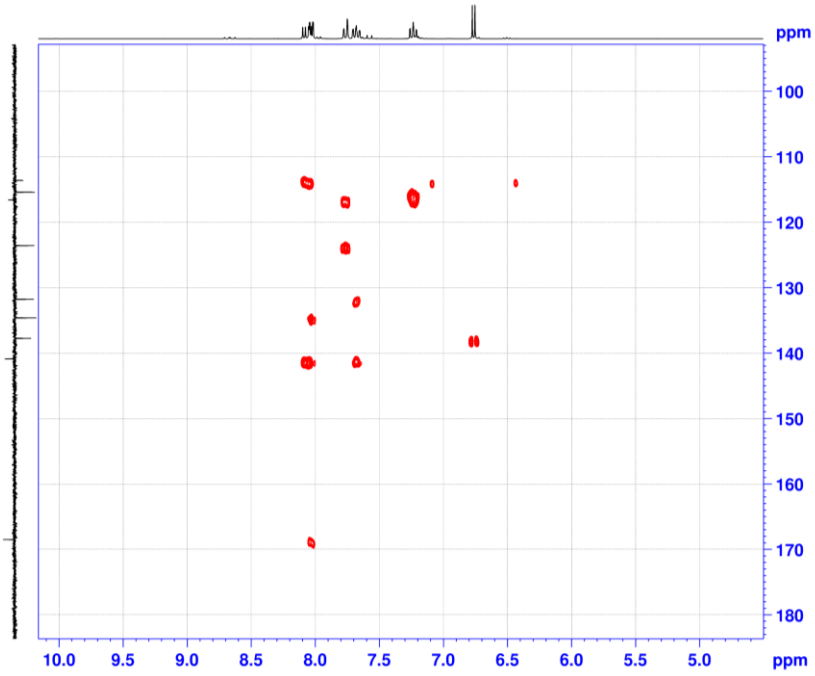


**Figure 65**: HMBC NMR of S2, HMBCGP, 300 and 75 MHz, DMSO

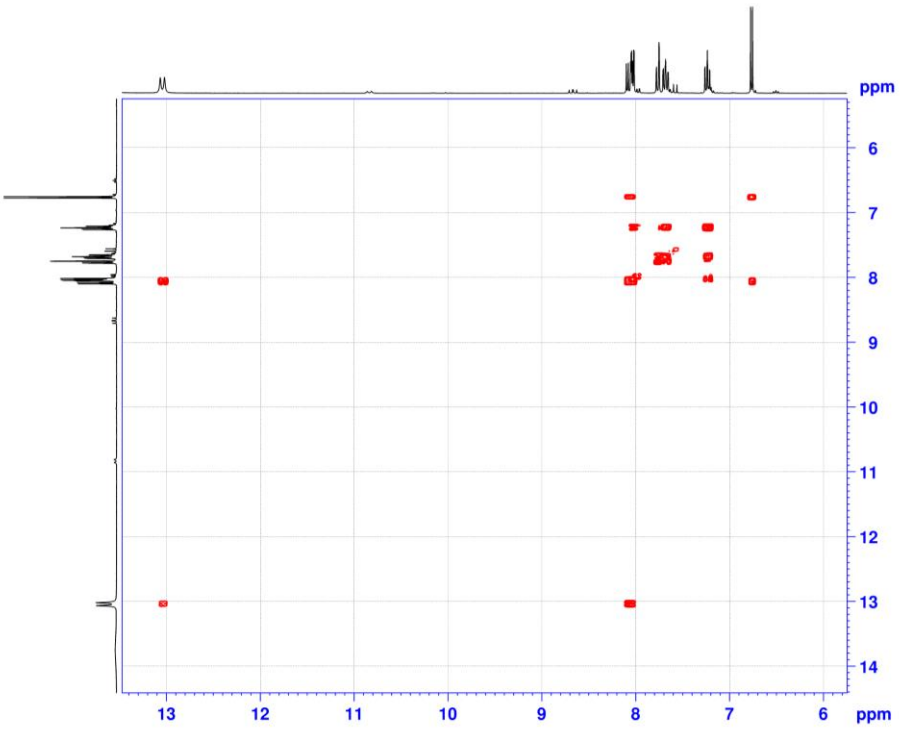


**Figure 66**: COSY NMR of S2, COSYGPSW, 300 MHz, DMSO

## Characterization of S3

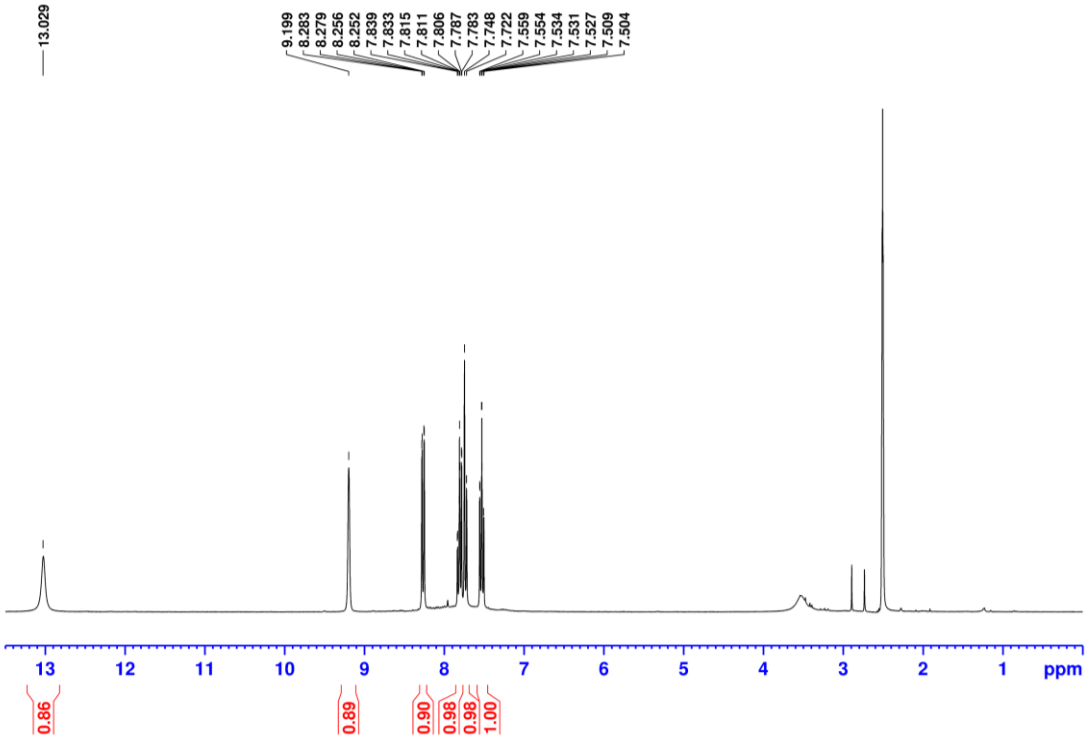


**Figure 67**: $^{1}$H NMR of S3, 300 MHz, DMSO

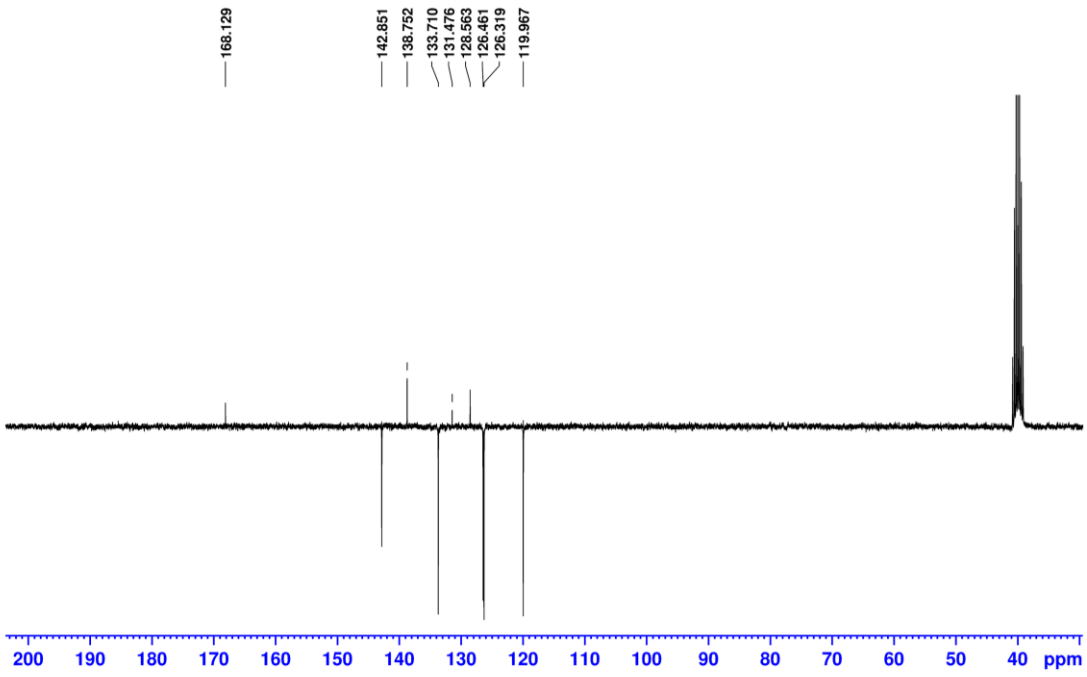


**Figure 68**: $^{13}C$ NMR of S3, C13APT, 75 MHz, DMSO

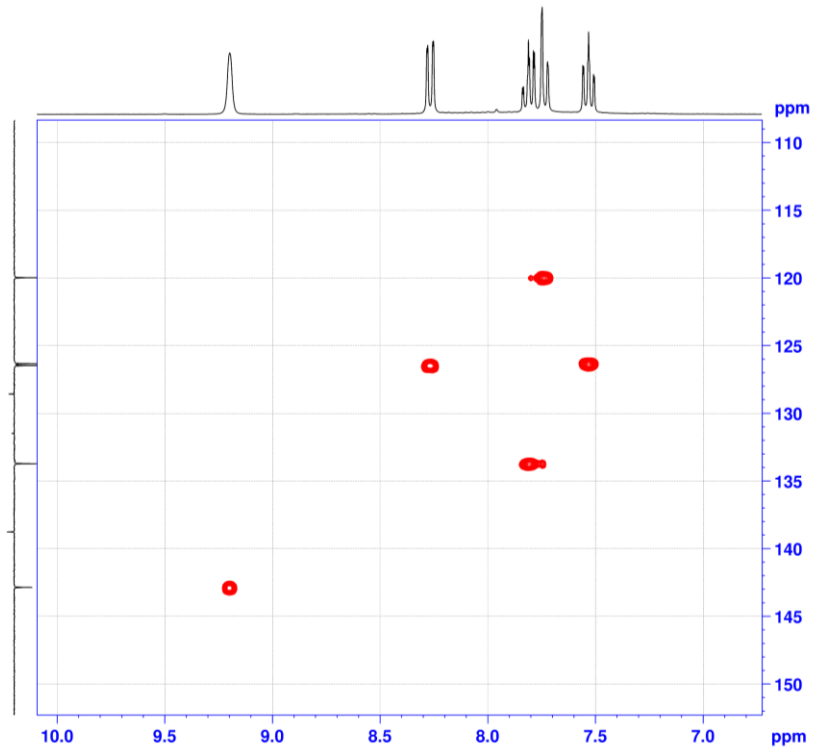


**Figure 69**: HSQC NMR of S3, HSQCGP, 300 and 75 MHz, DMSO

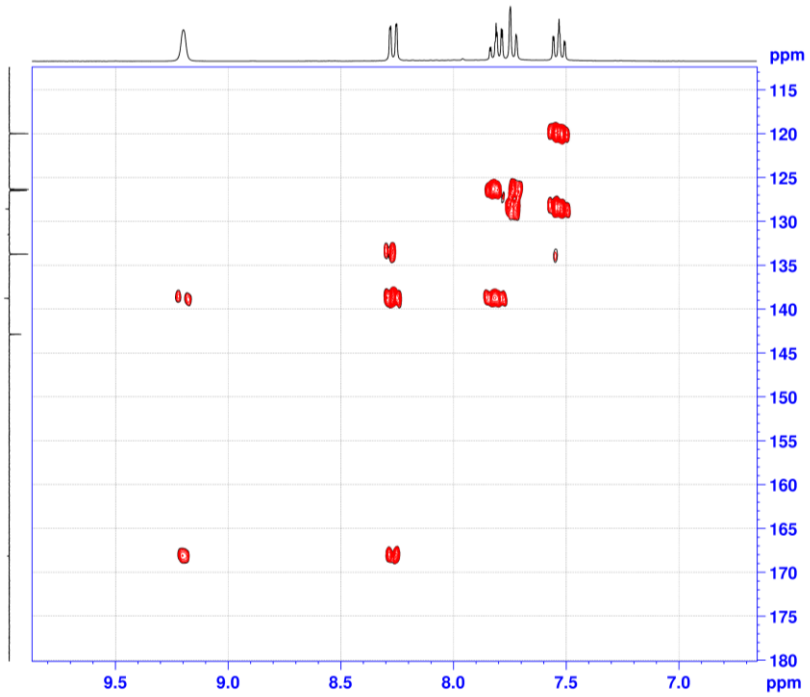


**Figure 70**: HMBC NMR of S3, HMBCGP, 300 and 75 MHz, DMSO

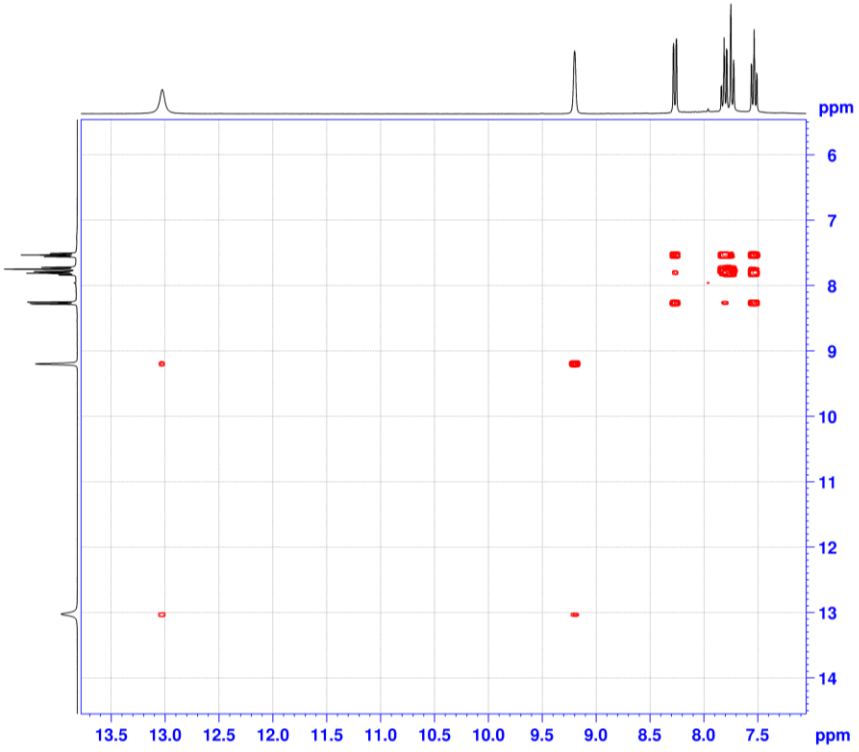


**Figure 71**: COSY NMR of S3, COSYGPSW, 300 MHz, DMSO

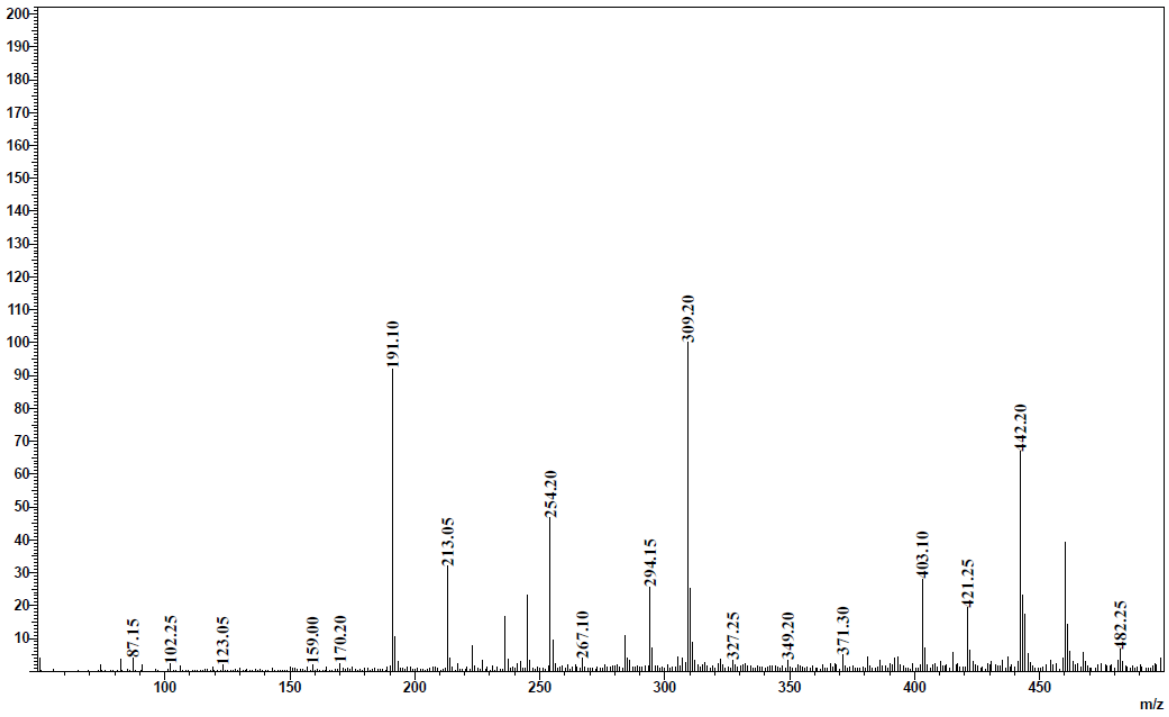


**Figure 72**: ESI-MS of S3; Shimadzu LCMS-2020, positive mode

## Characterization of S4

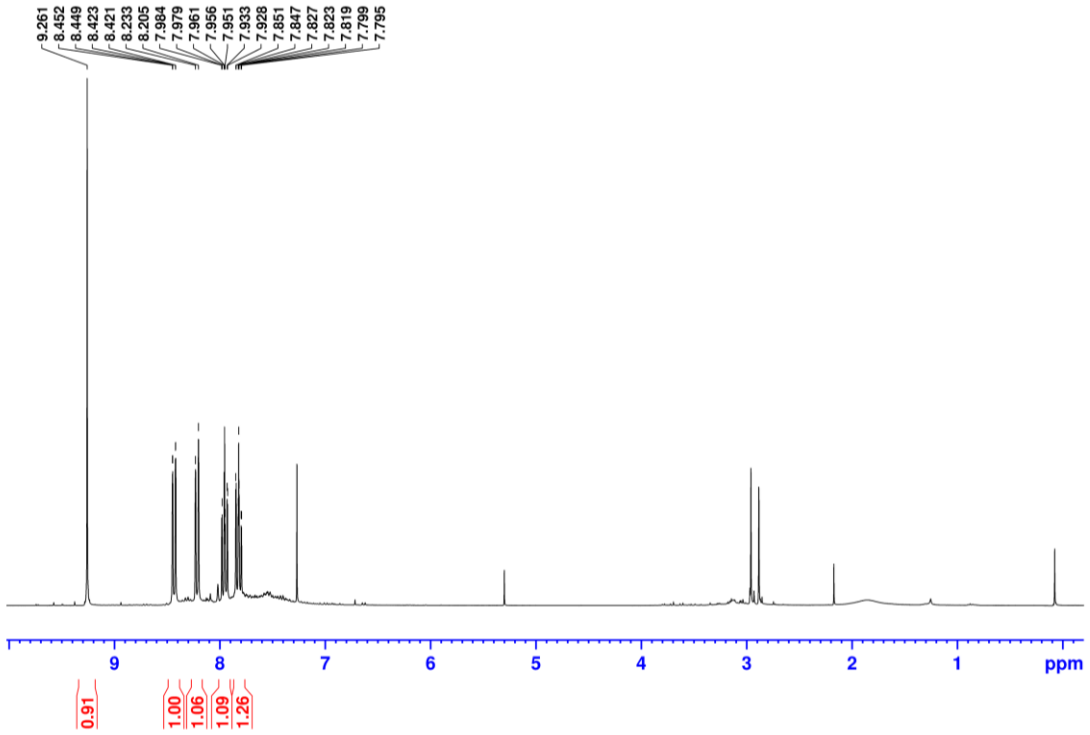


**Figure 73**: $^{1}$H NMR of S4, 300 MHz, $CDCl_3$

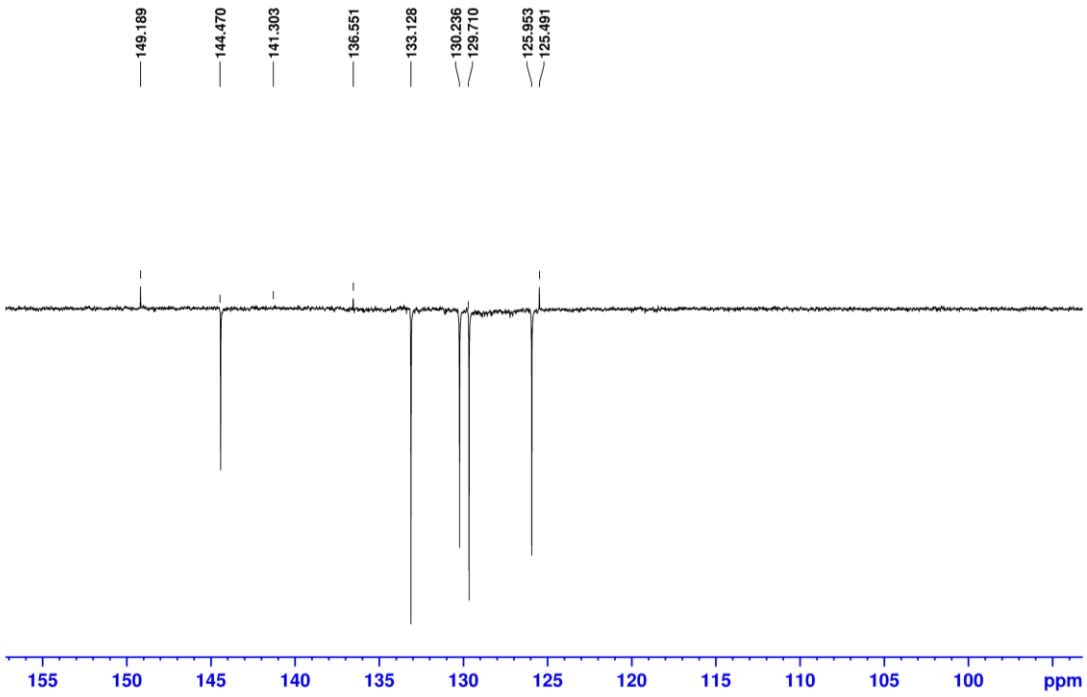


**Figure 74**: $^{13}C$ NMR of S4, C13APT, 75 MHz, $CDCl_3$

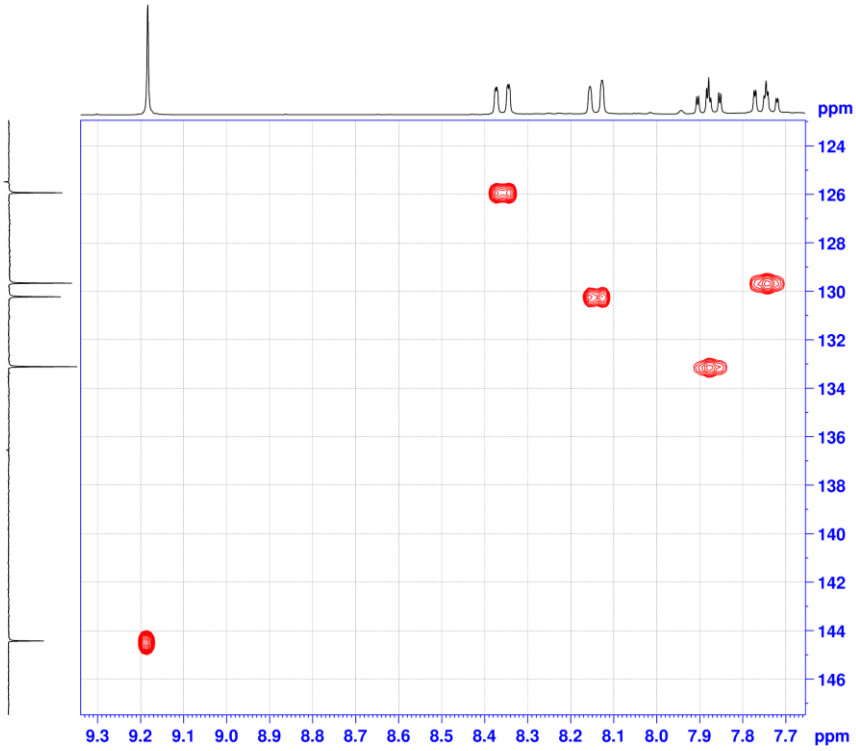


**Figure 75**: HSQC NMR of S4, HSQCGP, 300 and 75 MHz, $CDCl_3$

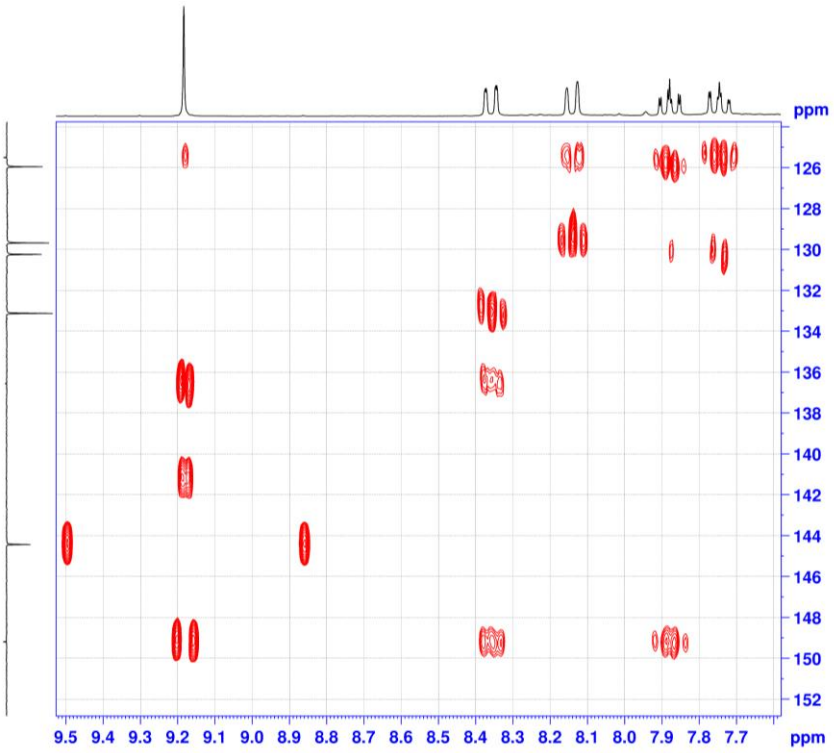


**Figure 76**: HMBC NMR of S4, HMBCGP, 300 and 75 MHz, $CDCl_3$

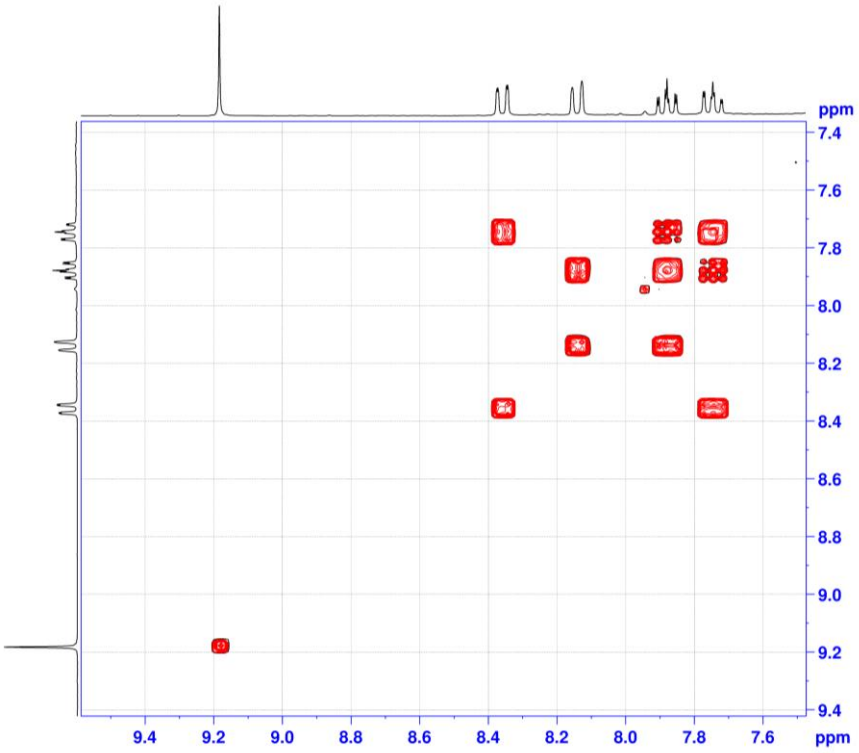


**Figure 77**: COSY NMR of S4, COSYGPSW, 300 MHz, $CDCl_3$

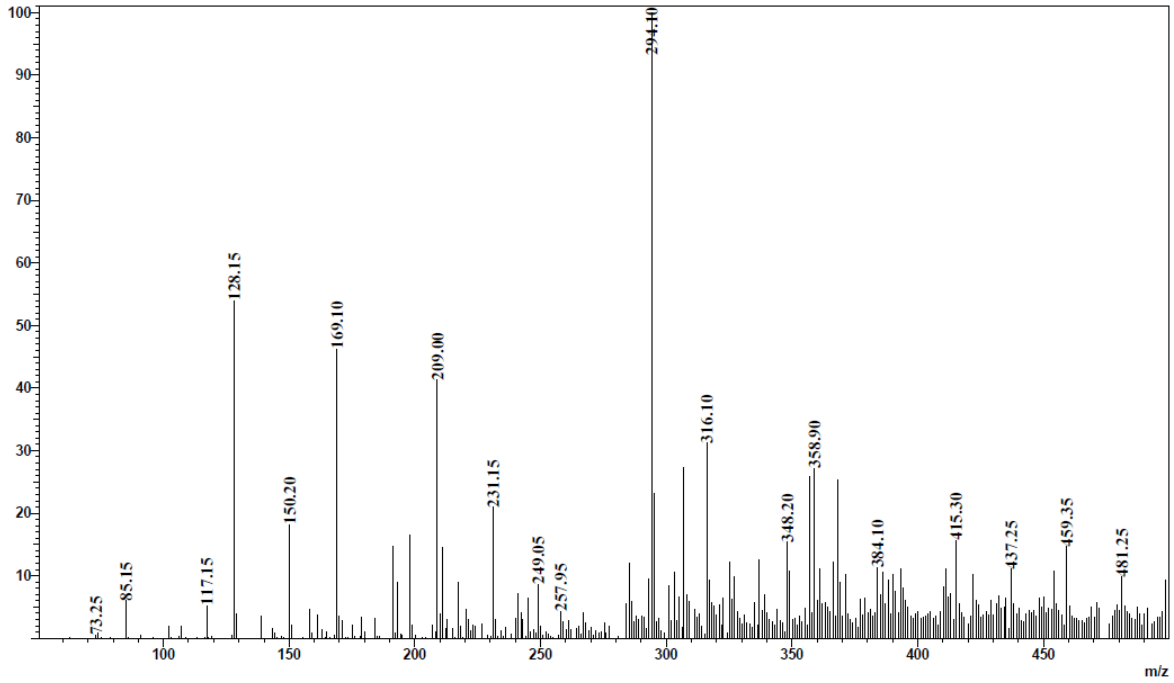


**Figure 78:** ESI-MS of S4; Shimadzu LCMS-2020, positive mode

## Characterization of S5

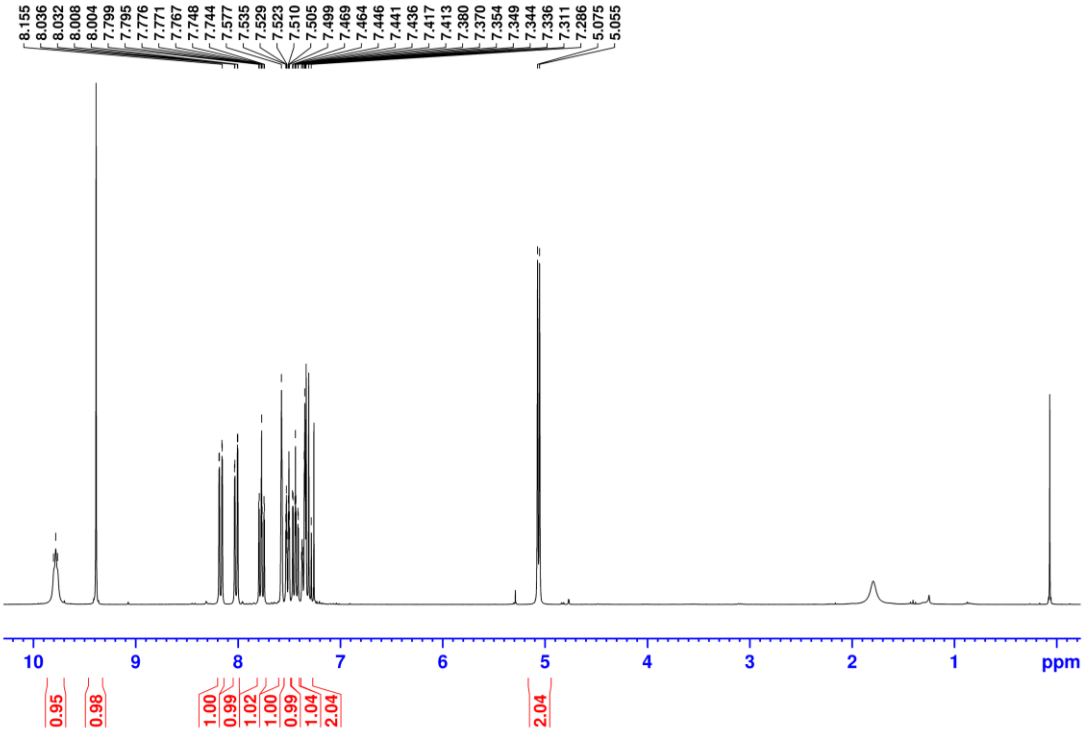


**Figure 79:** $^{1}$H NMR of S5, 300 MHz, $CDCl_3$

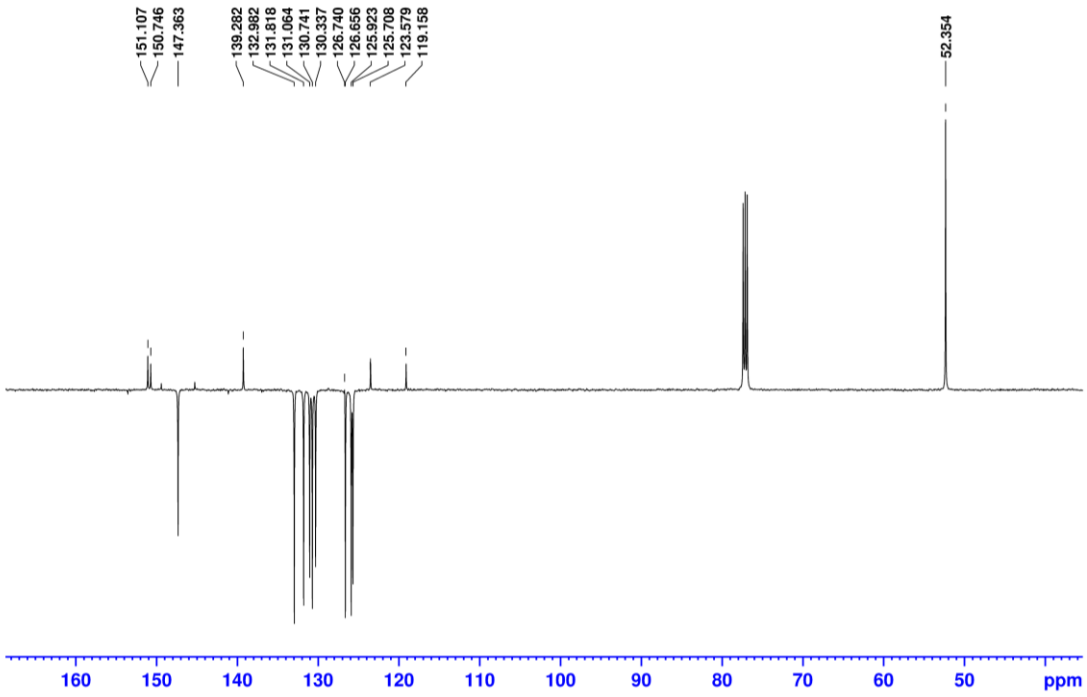


**Figure 80**: $^{13}C$ NMR of S5, C13APT, 126 MHz, $CDCl_3$

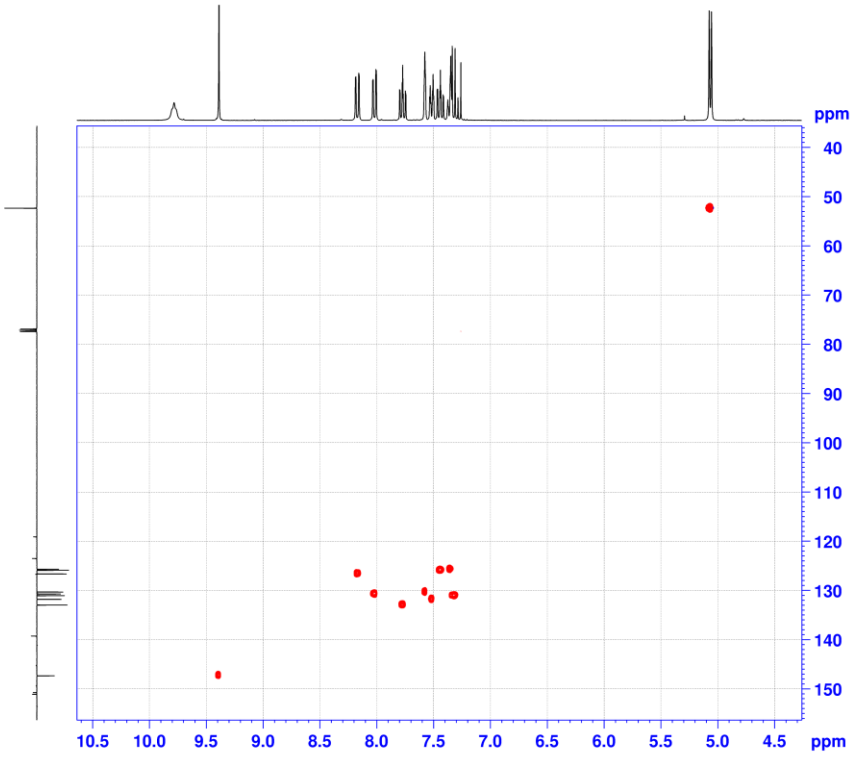


**Figure 81**: HSQC NMR of S5, HSQCGP, 500 and 126 MHz, $CDCl_3$

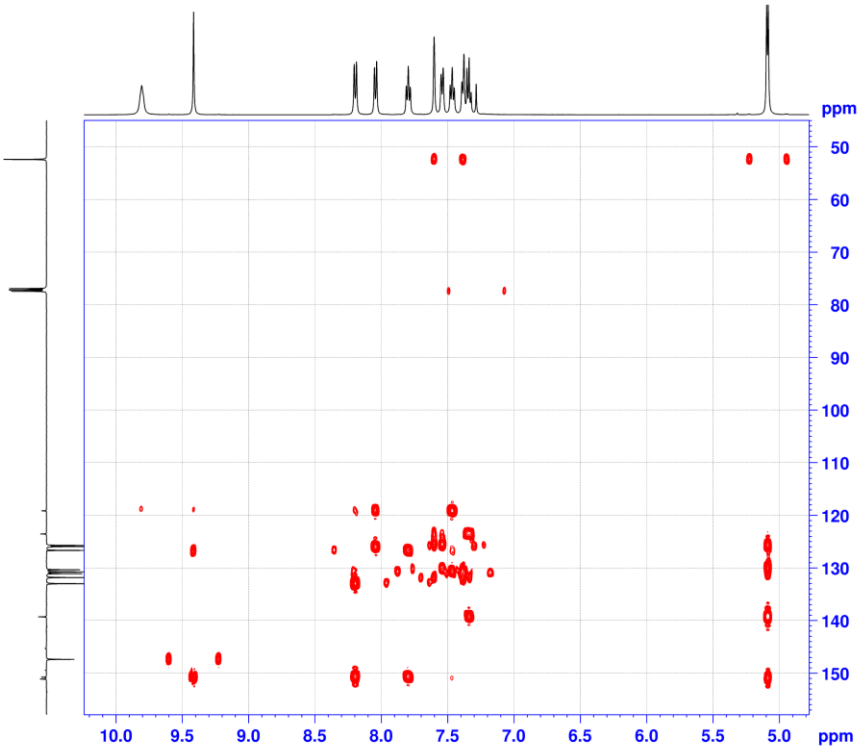


**Figure 82**: HMBC NMR of S5, HMBCGP, 500 and 126 MHz, $CDCl_3$

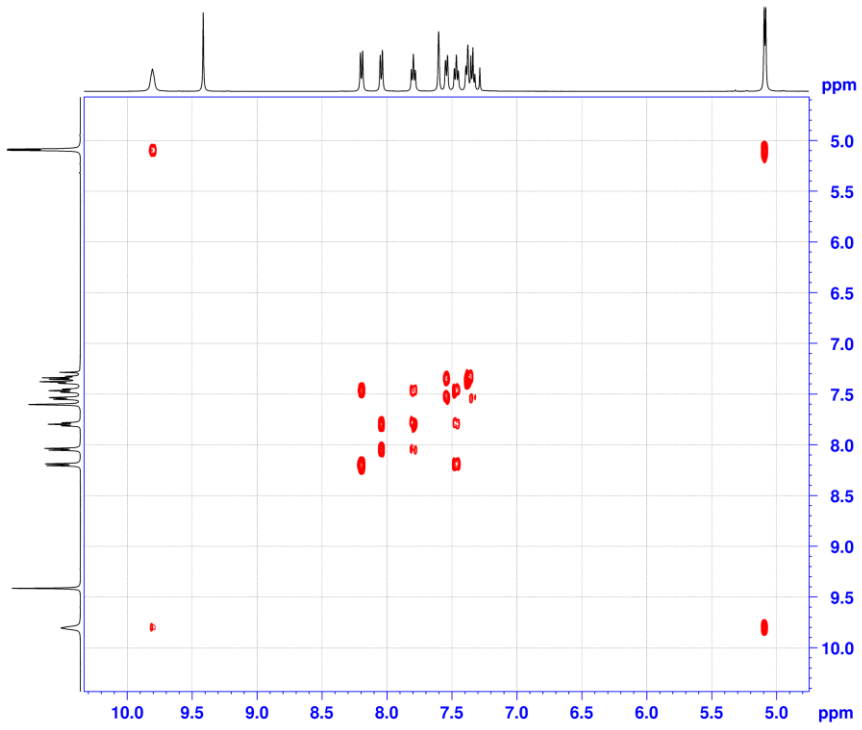


**Figure 83**: COSY NMR of S5, COSYGPMFSW, 500 MHz, $CDCl_3$

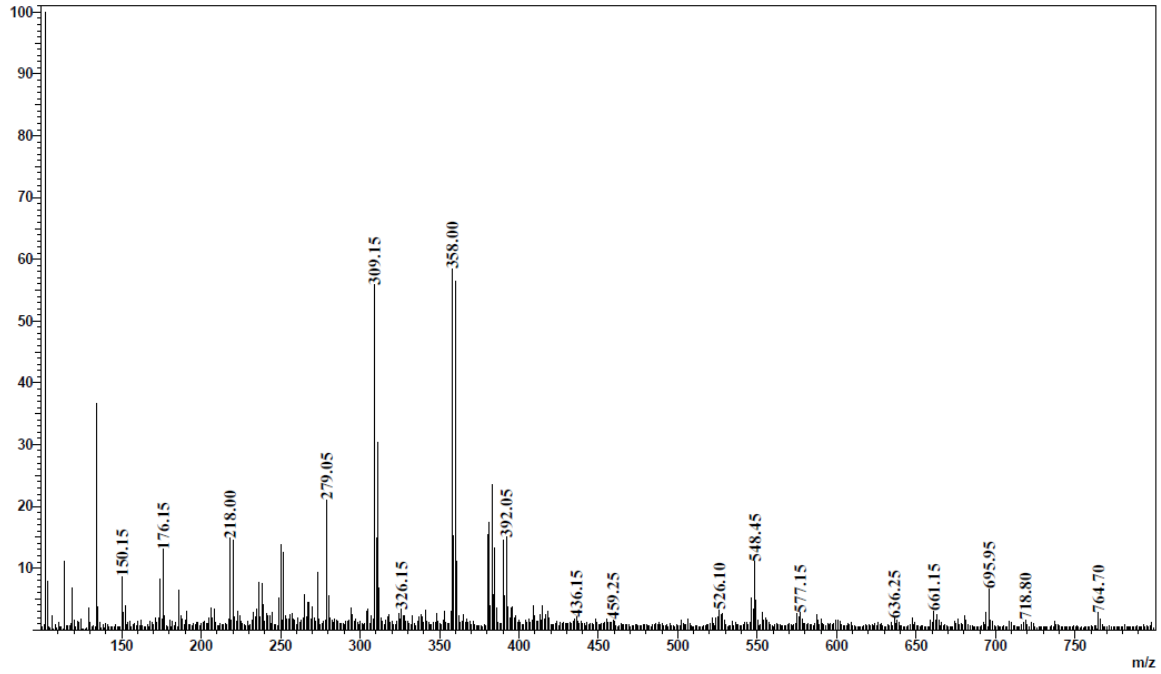


**Figure 84**: ESI-MS of S5; Shimadzu LCMS-2020, positive mode

## Characterization of S6

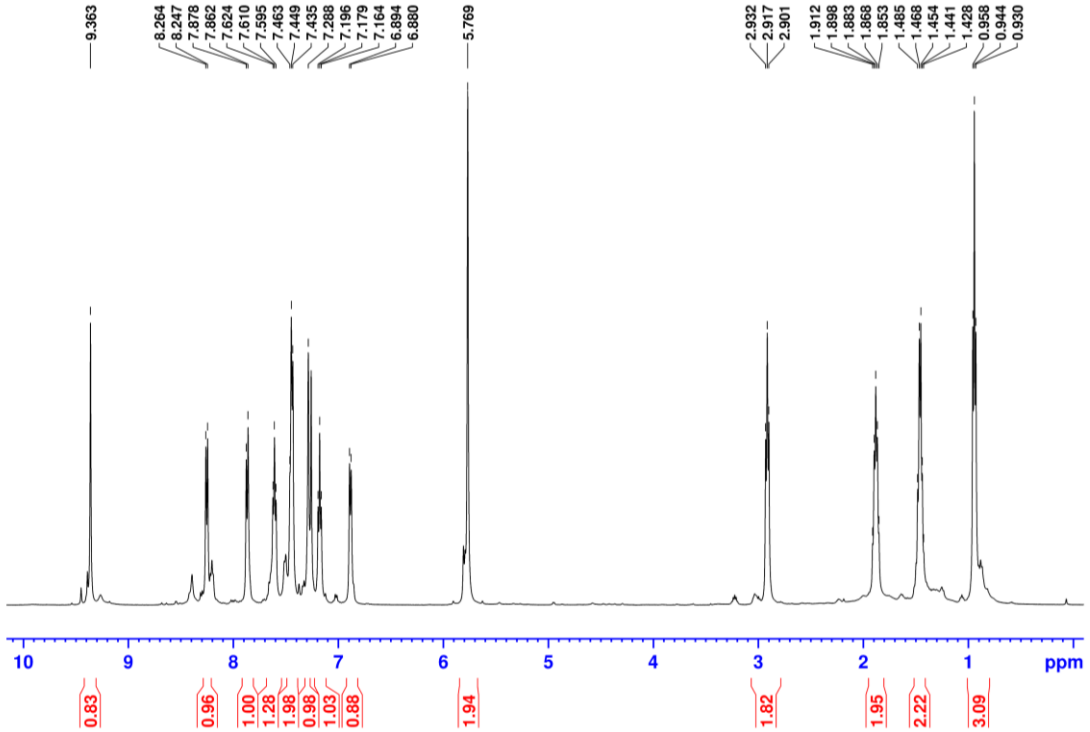


**Figure 85**: $^{1}H$ NMR of S6, 500 MHz, $CDCl_3$

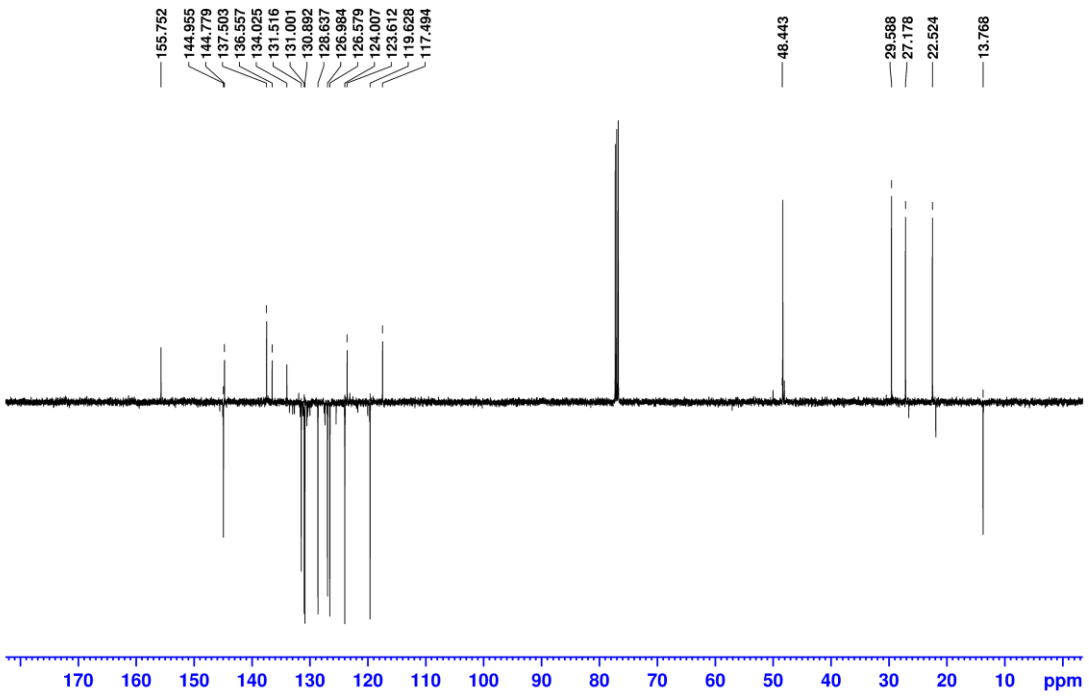


**Figure 86**: $^{13}C$ NMR of S6, C13APT, 126 MHz, $CDCl_3$

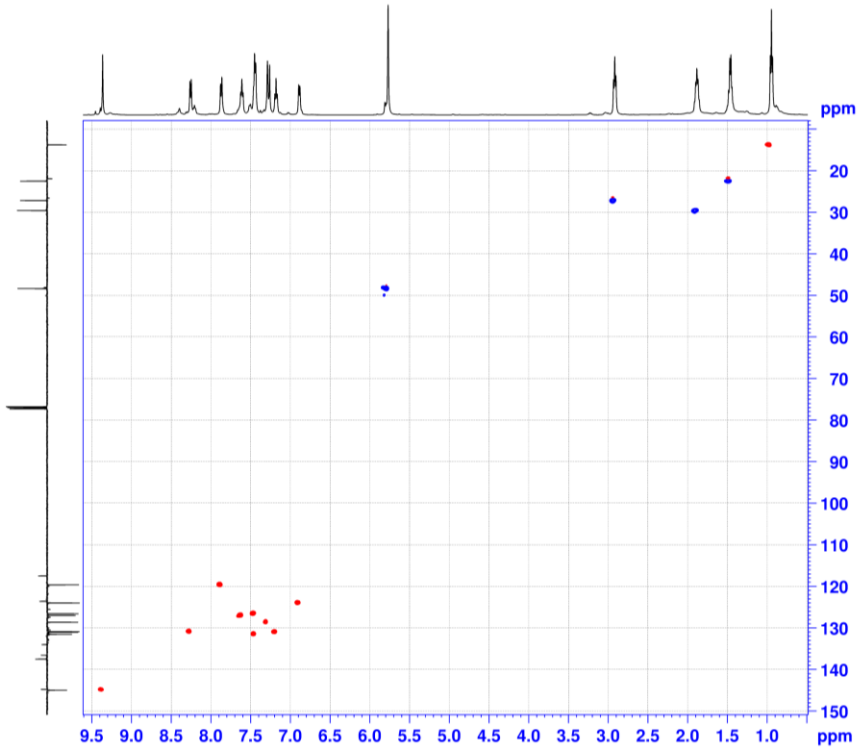


**Figure 87**: HSQC NMR of S6, HSQCEDETGP, 500 and 126 MHz, $CDCl_3$

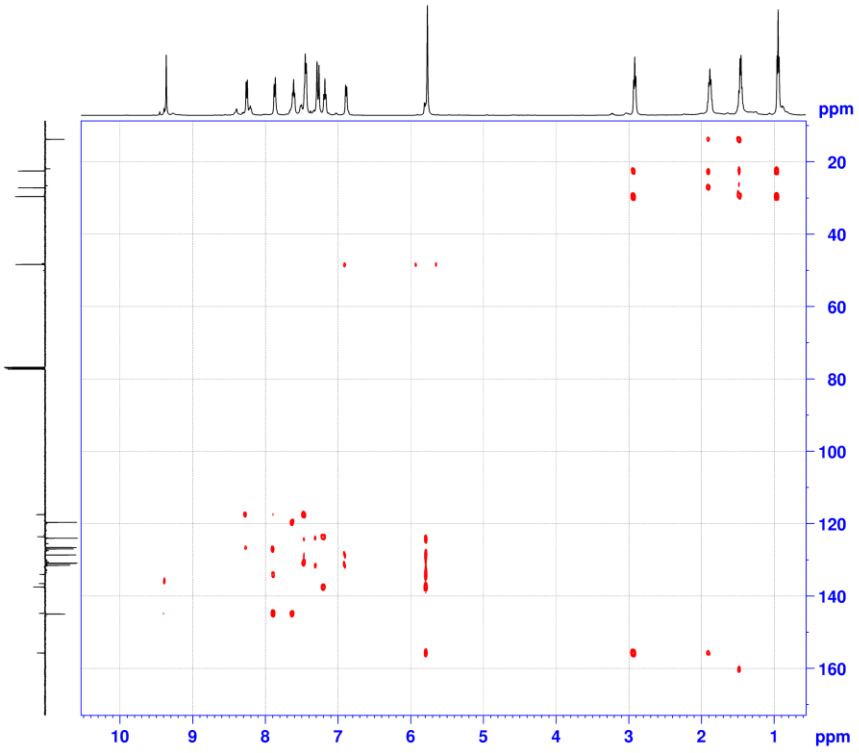


**Figure 88**: HMBC NMR of S6, HMBCGP, 500 and 126 MHz, $CDCl_3$

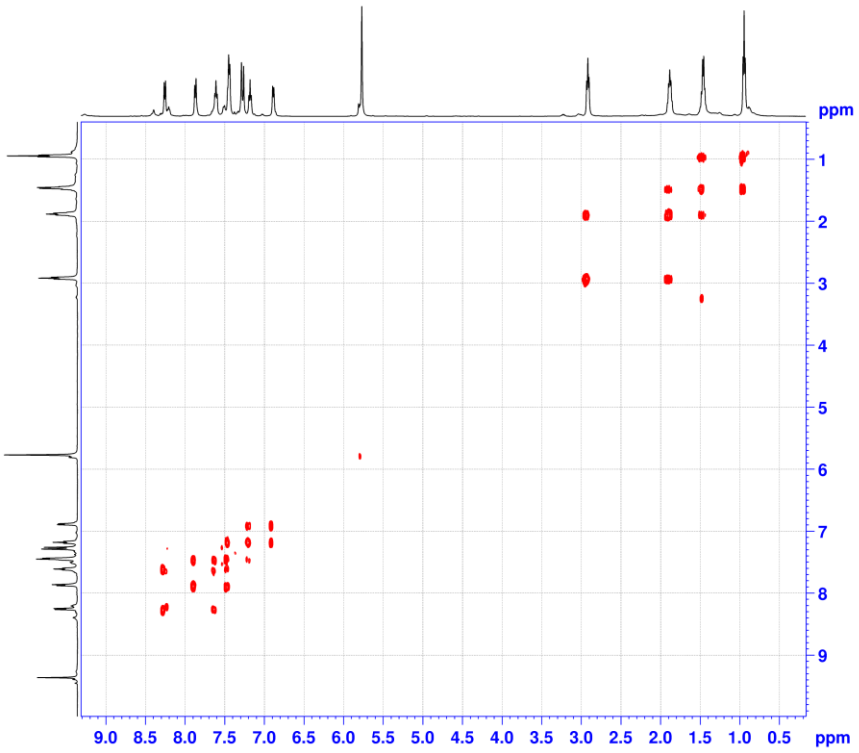


**Figure 89**: COSY NMR of S6, COSYGPMFSW, 500 MHz, $CDCl_3$

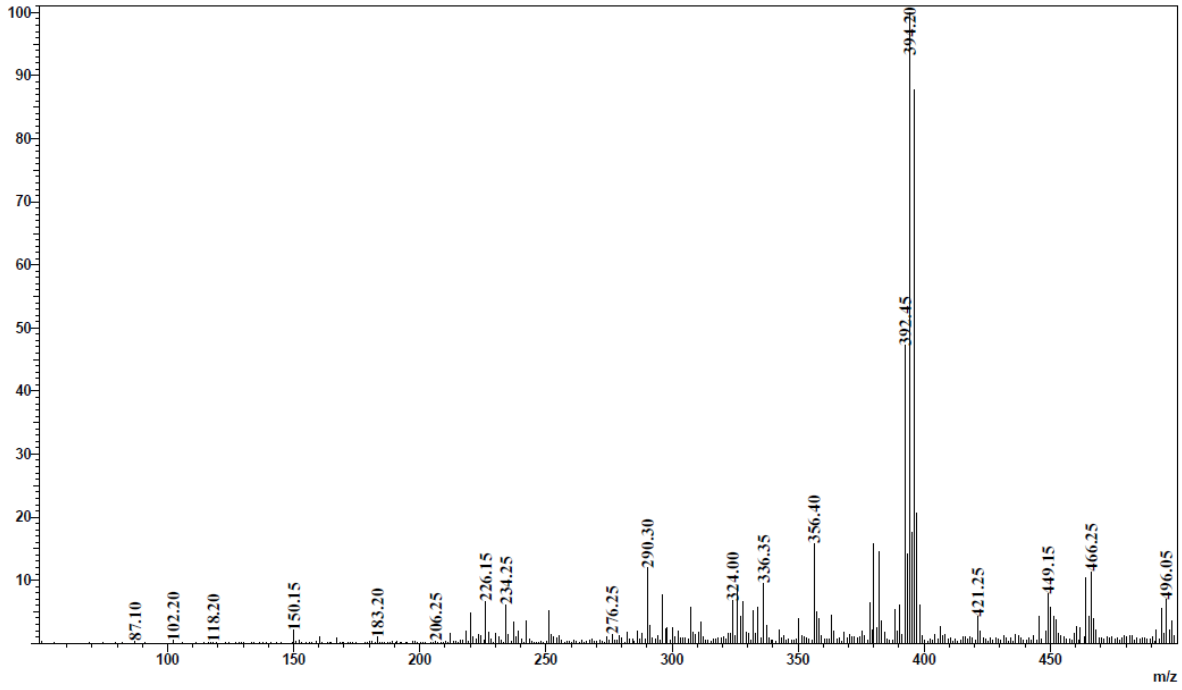


**Figure 90**: ESI-MS of S6; Shimadzu LCMS-2020, positive mode

## Characterization of S7

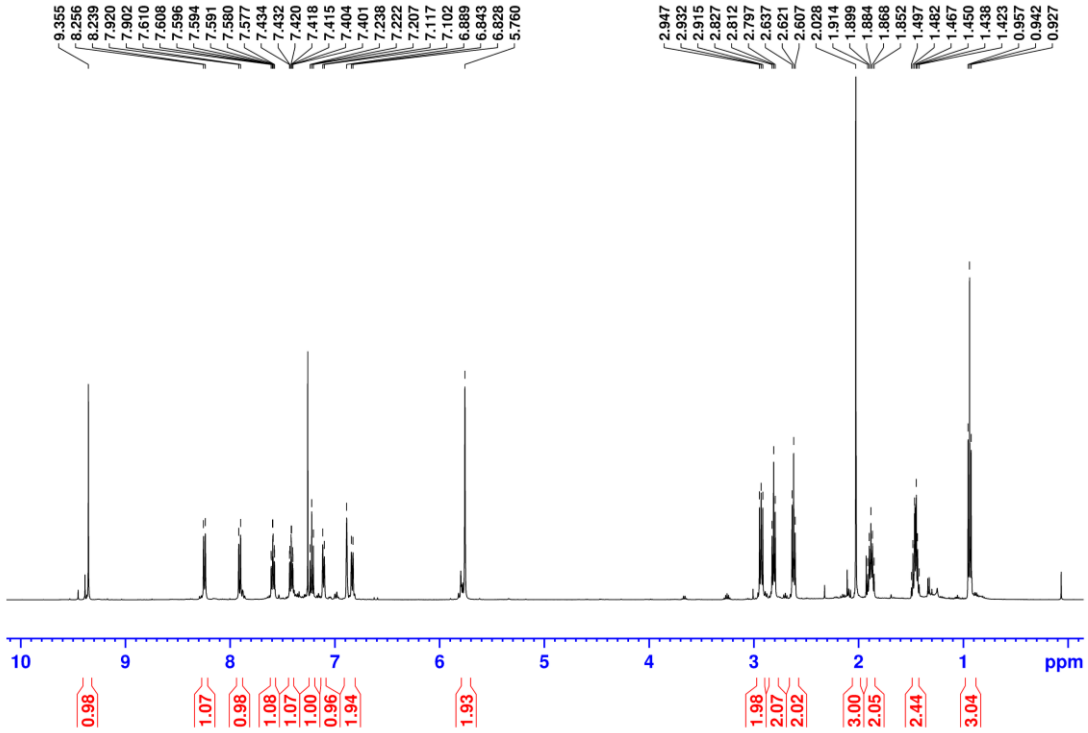


**Figure 91**: $^{1}$H NMR of S7, 500 MHz, $CDCl_3$

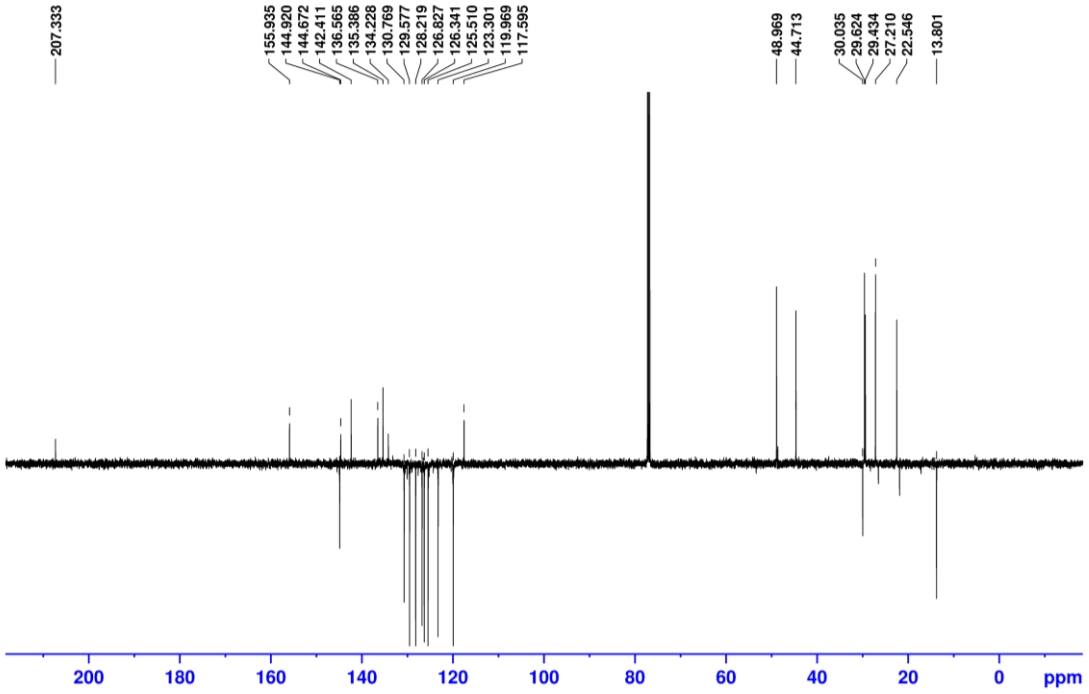


**Figure 92**: $^{13}C$ NMR of S7, C13APT, 500 MHz, $CDCl_3$

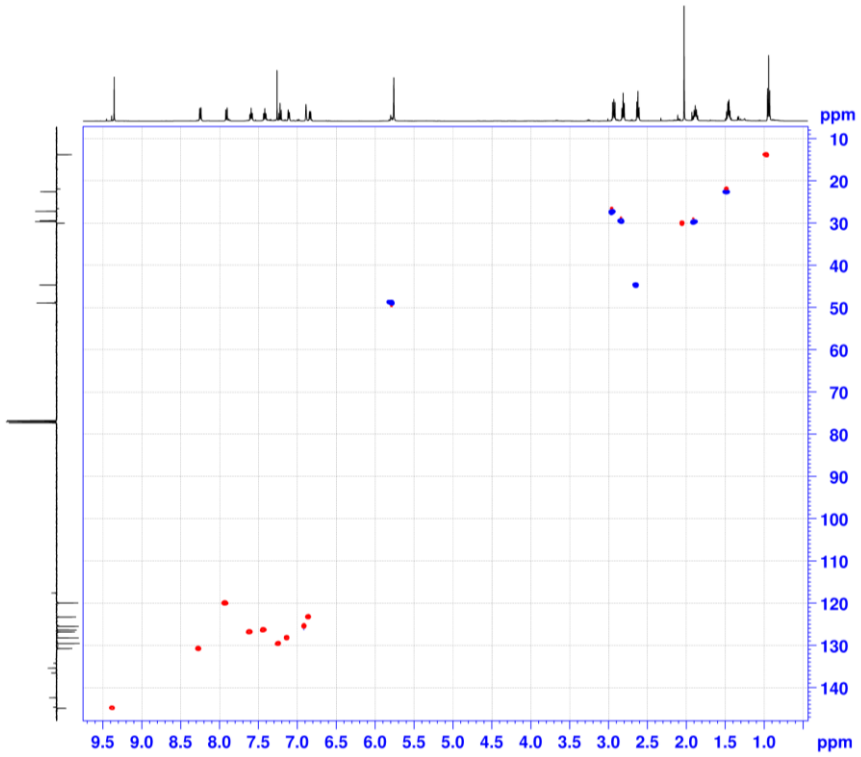


**Figure 93**: HSQC NMR of S7, HSQCEDETGP, 500 and 126 MHz, $CDCl_3$

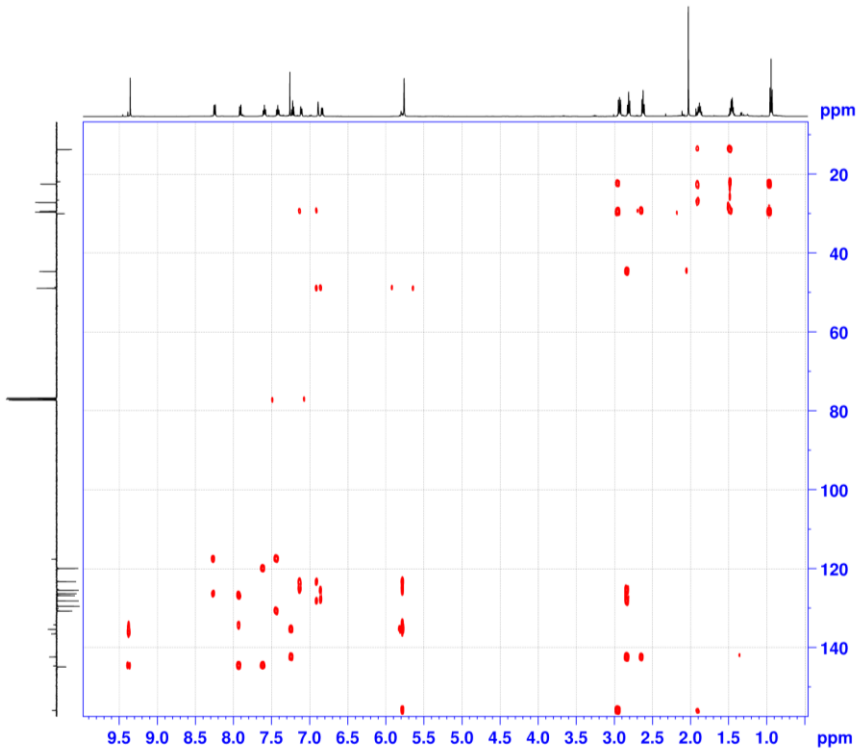


**Figure 94**: HMBC NMR of S7, HMBCGP, 500 and 126 MHz, $CDCl_3$

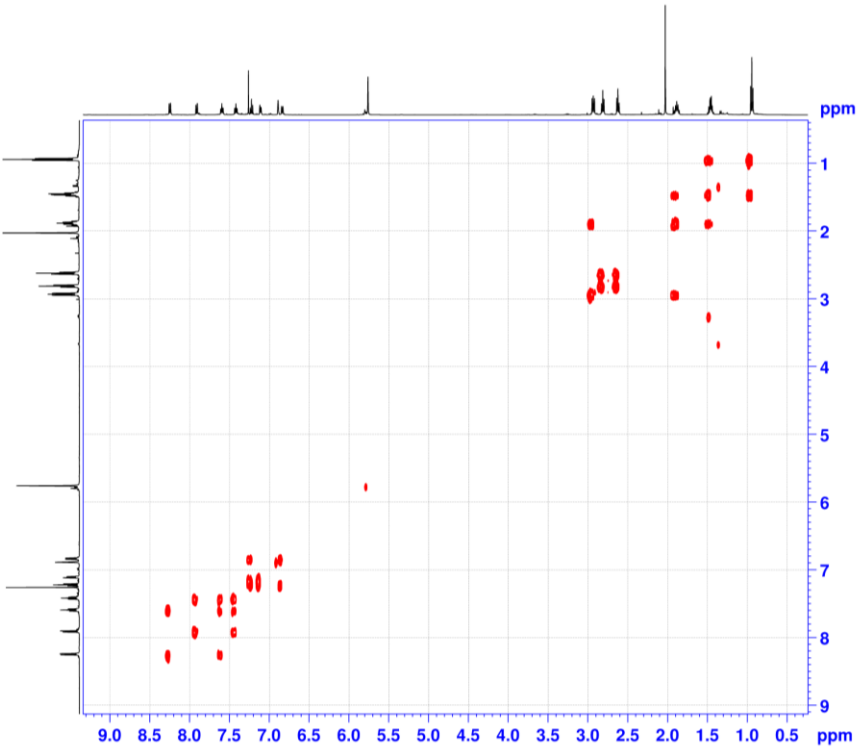


**Figure 95**: COSY NMR of S7, COSYGPMFSW, 500 MHz, $CDCl_3$

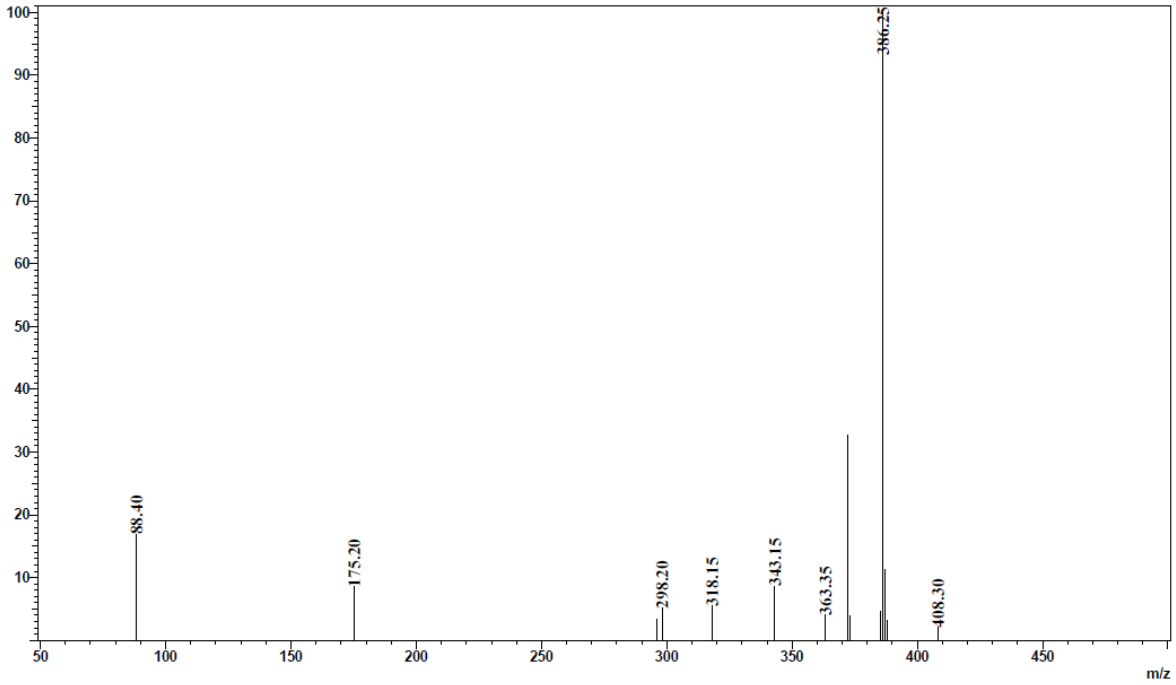


**Figure 96**: ESI-MS of S7; Shimadzu LCMS-2020, positive mode

## Characterization of S8

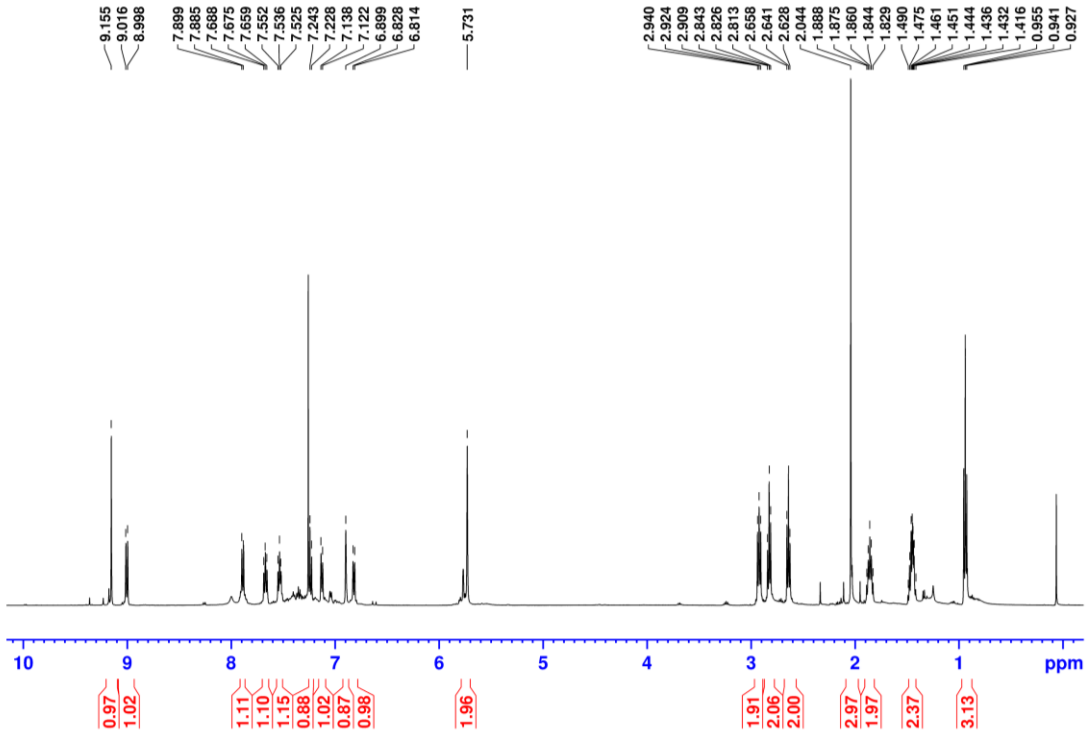


**Figure 97**: $^{1}H$ NMR of S8, 500 MHz, $CDCl_3$

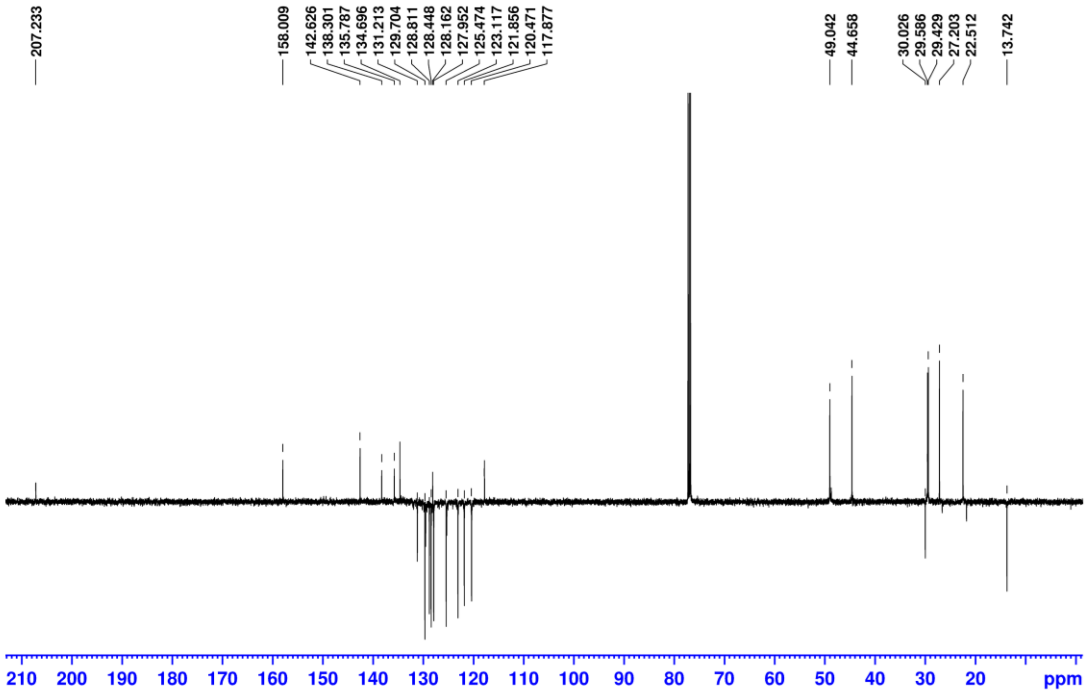


**Figure 98**: $^{13}C$ NMR of S8, C13APT, 500 MHz, $CDCl_3$

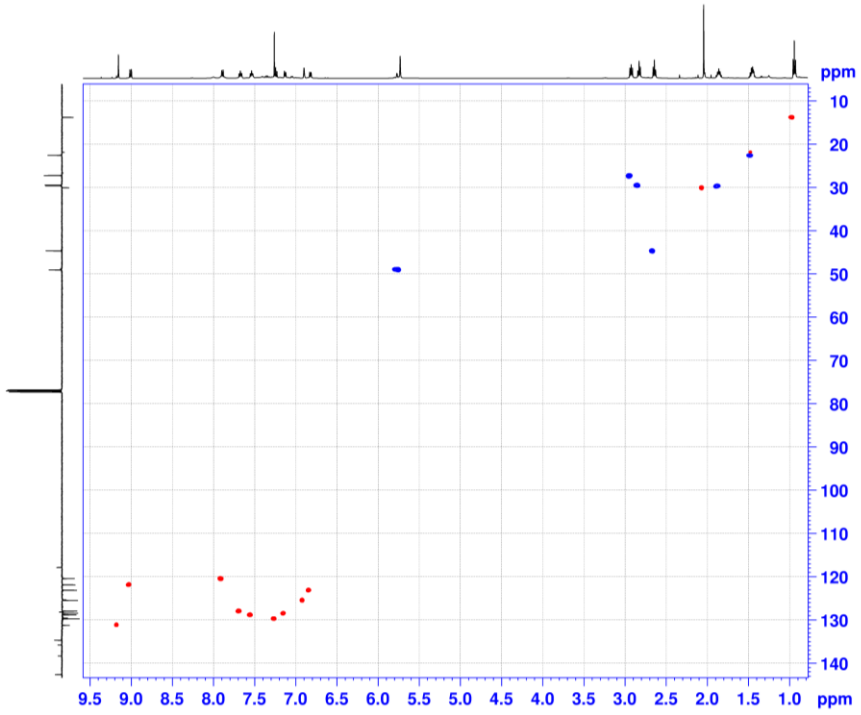


**Figure 99**: HSQC NMR of S8, HSQCEDETGP, 500 and 126 MHz, $CDCl_3$

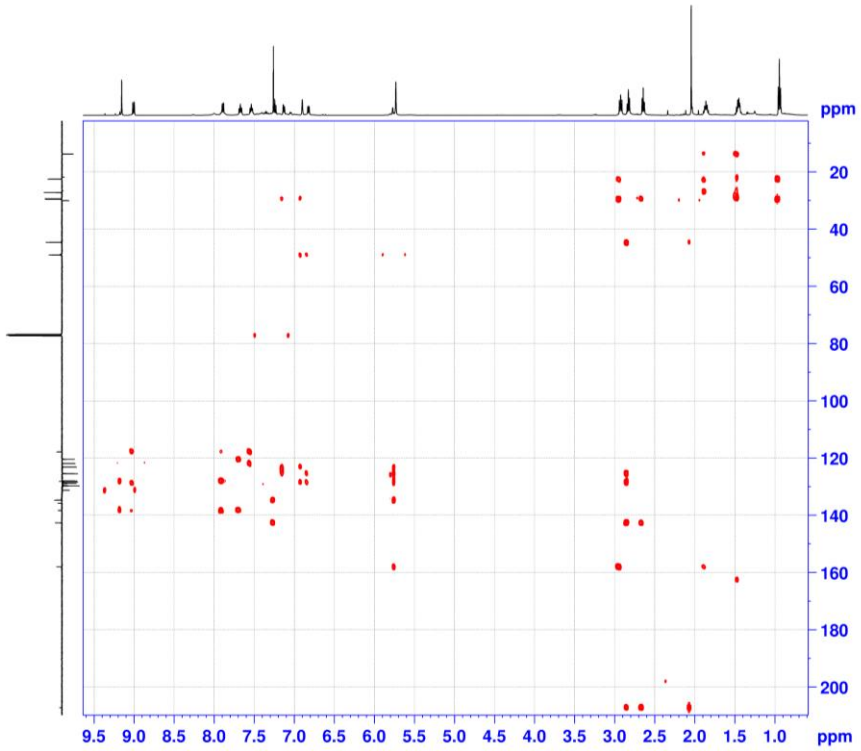


**Figure 100**: HMBC NMR of S8, HMBCGP, 500 and 126 MHz, $CDCl_3$

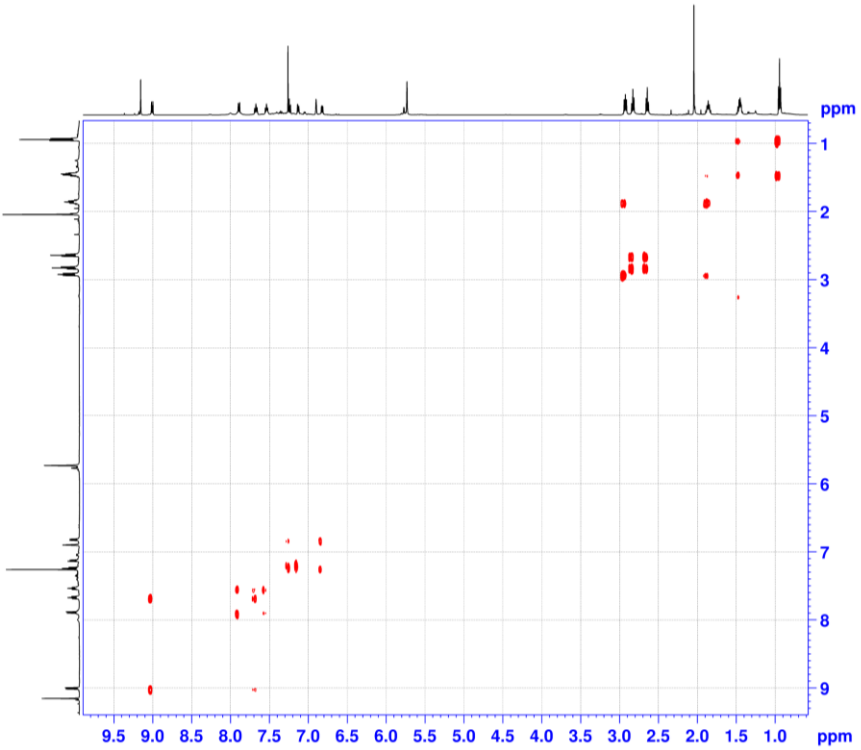


**Figure 101**: COSY NMR of S8, COSYGPMFSW, 500 MHz, $CDCl_3$

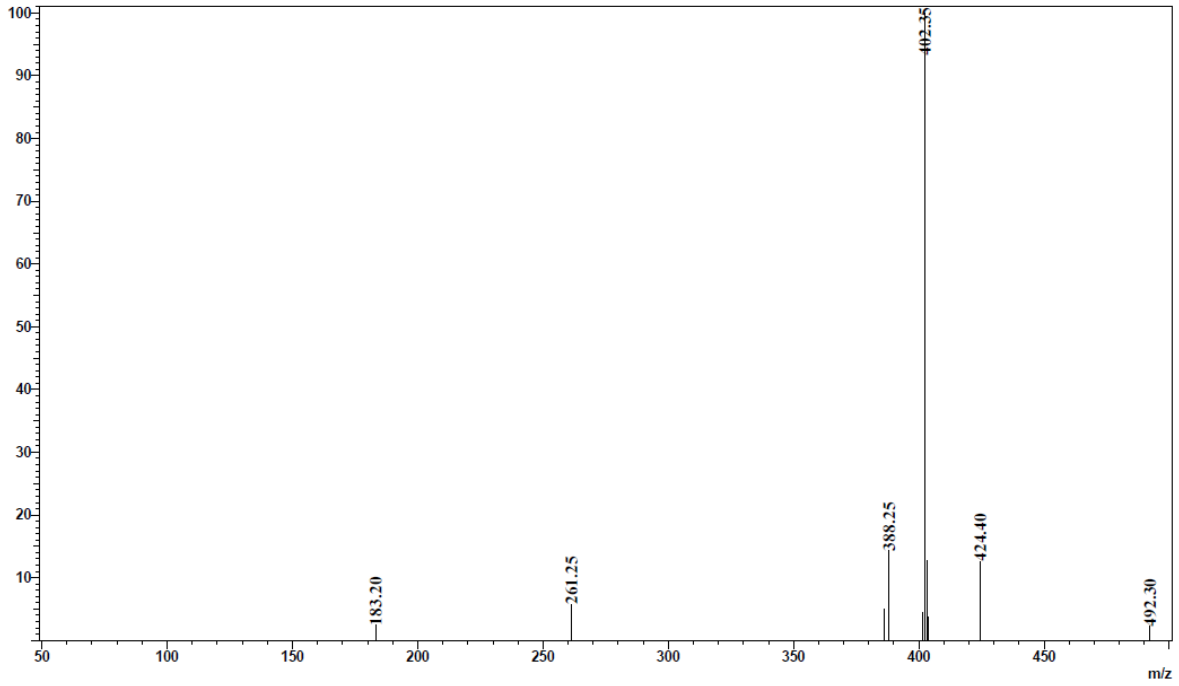


**Figure 102**: ESI-MS of S8; Shimadzu LCMS-2020, positive mode

## Characterization of S9

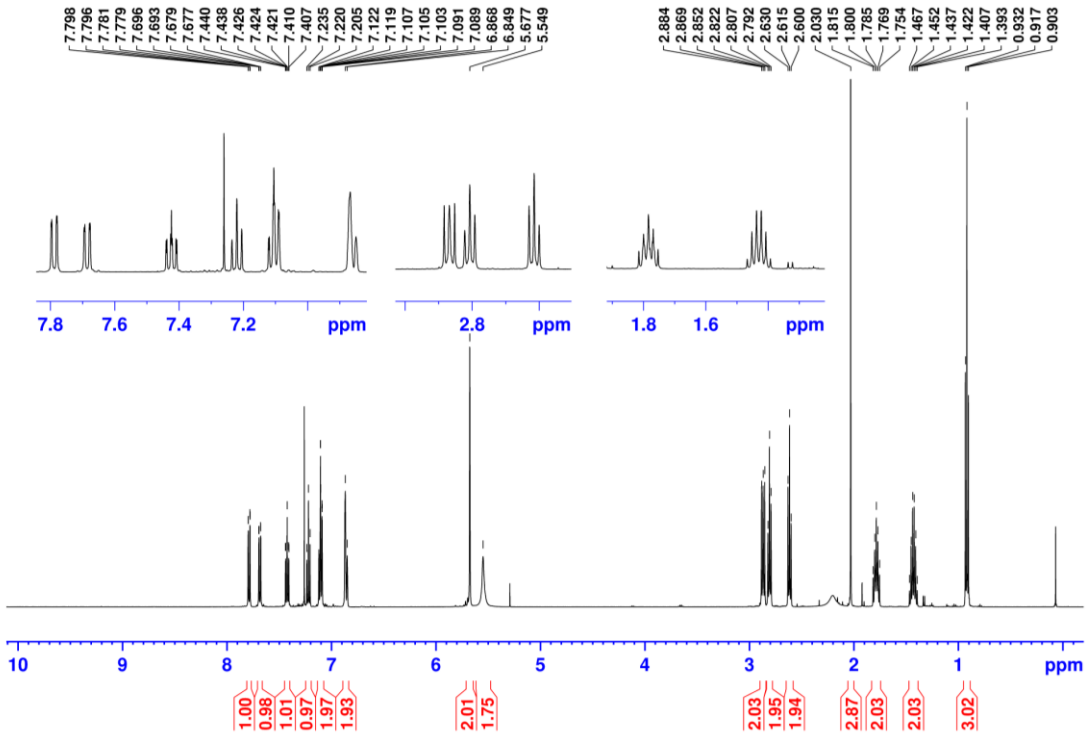


**Figure 103**: $^{1}H$ NMR of S9, 500 MHz, $CDCl_3$

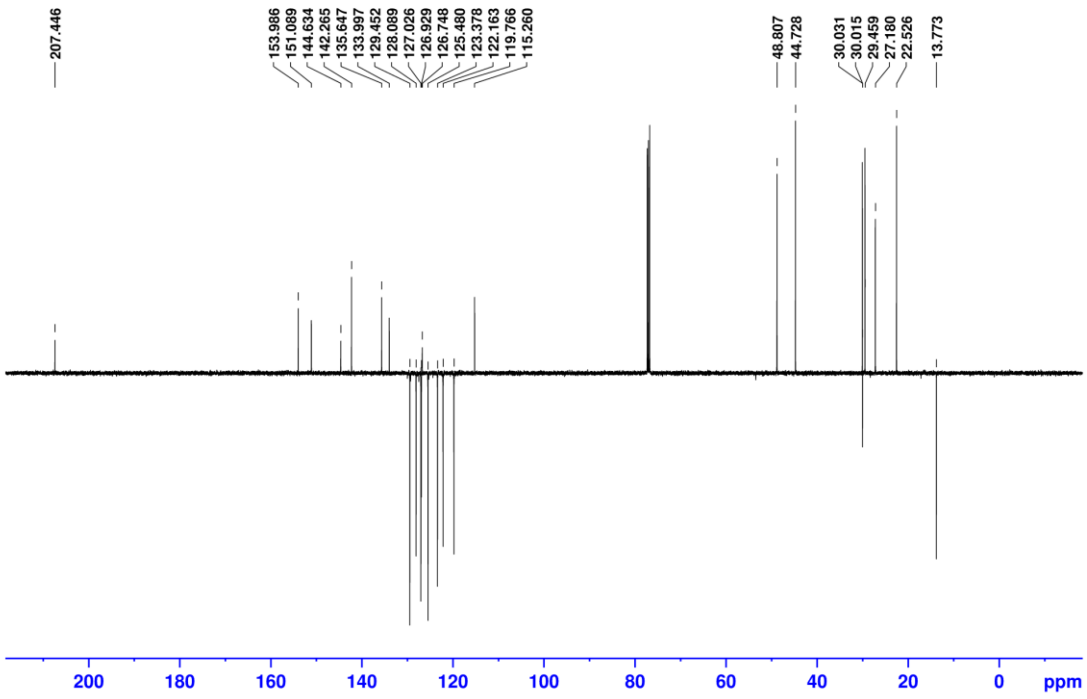


**Figure 104**: $^{13}C$ NMR of S9, C13APT, 500 MHz, $CDCl_3$

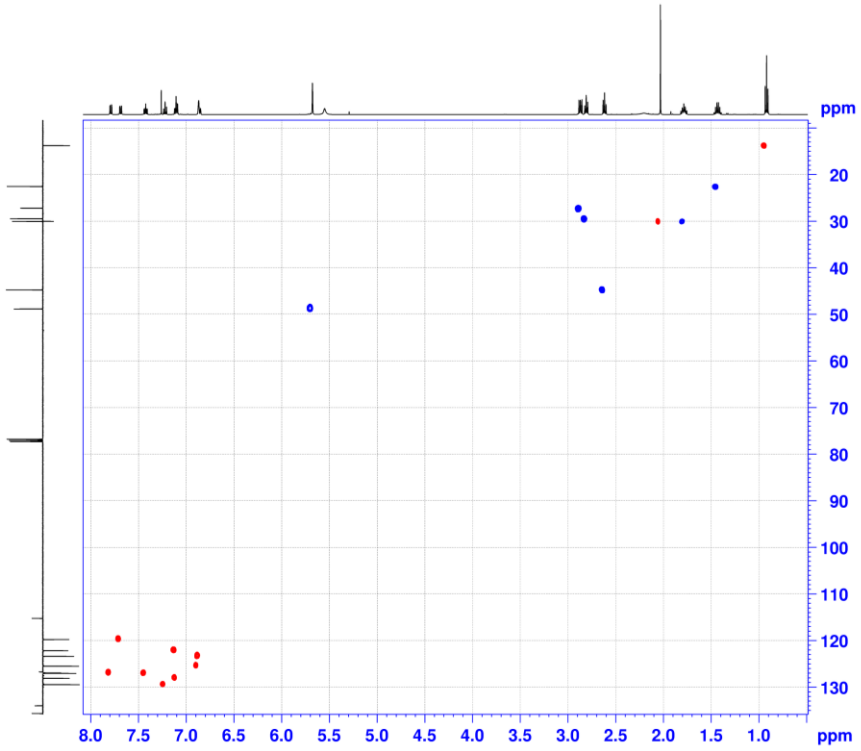


**Figure 105**: HSQC NMR of S9, HSQCEDETGP, 500 and 126 MHz, $CDCl_3$

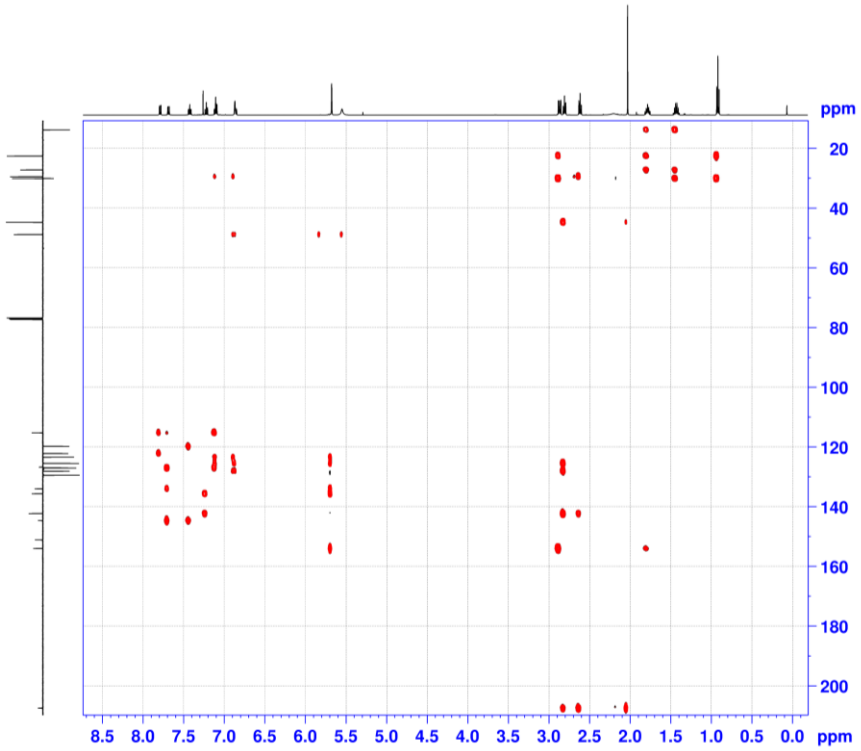


**Figure 106**: HMBC NMR of S9, HMBCGP, 500 and 126 MHz, $CDCl_3$

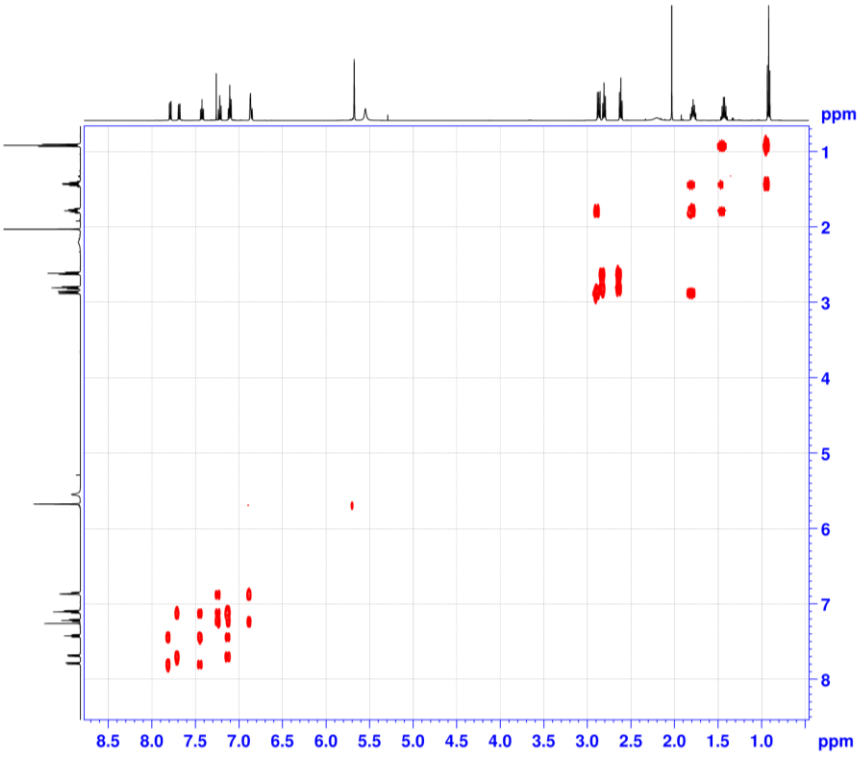


**Figure 107**: COSY NMR of S9, COSYGPMFSW, 500 MHz, $CDCl_3$

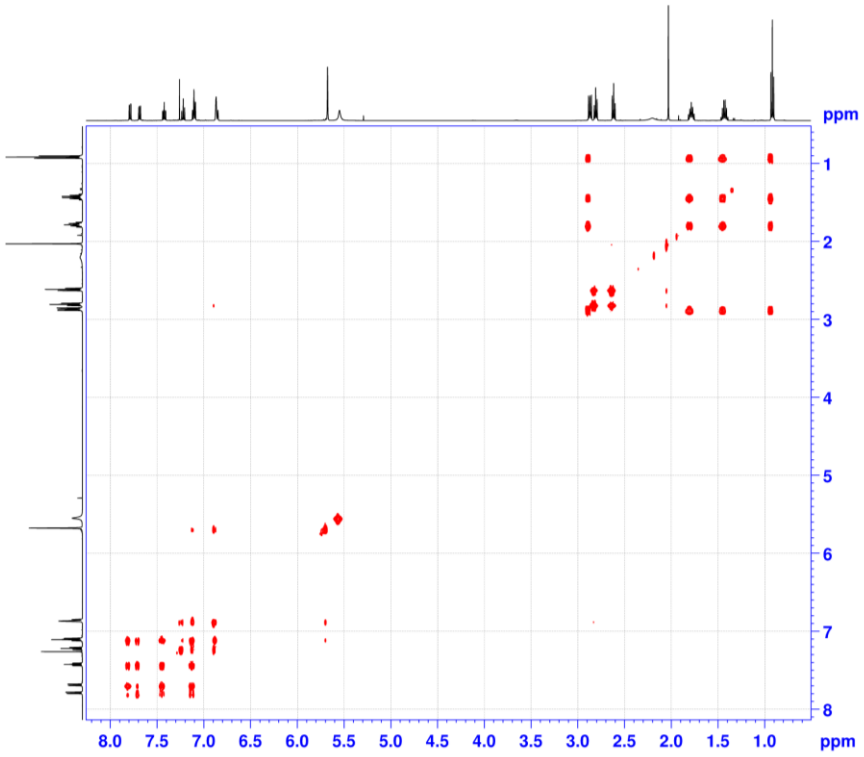


**Figure 108**: TOCSY NMR of S9, MLEVPHSW, 500 MHz, $CDCl_3$

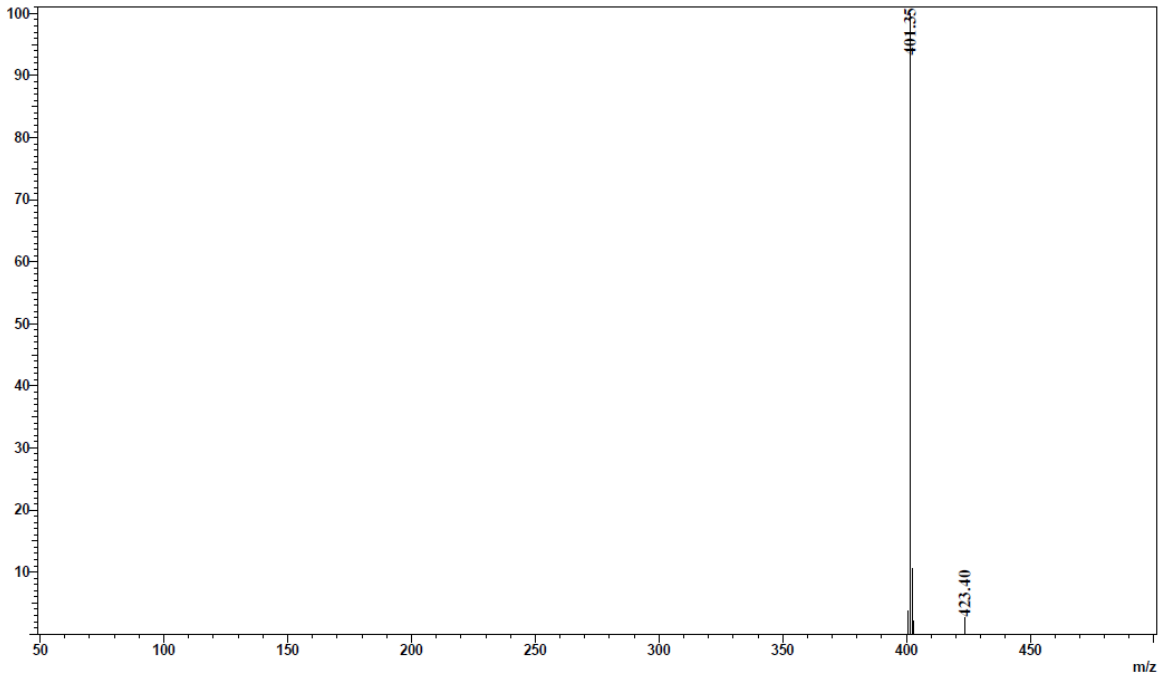


**Figure 109**: ESI-MS of S9 after recrystallization; Shimadzu LCMS-2020, positive mode

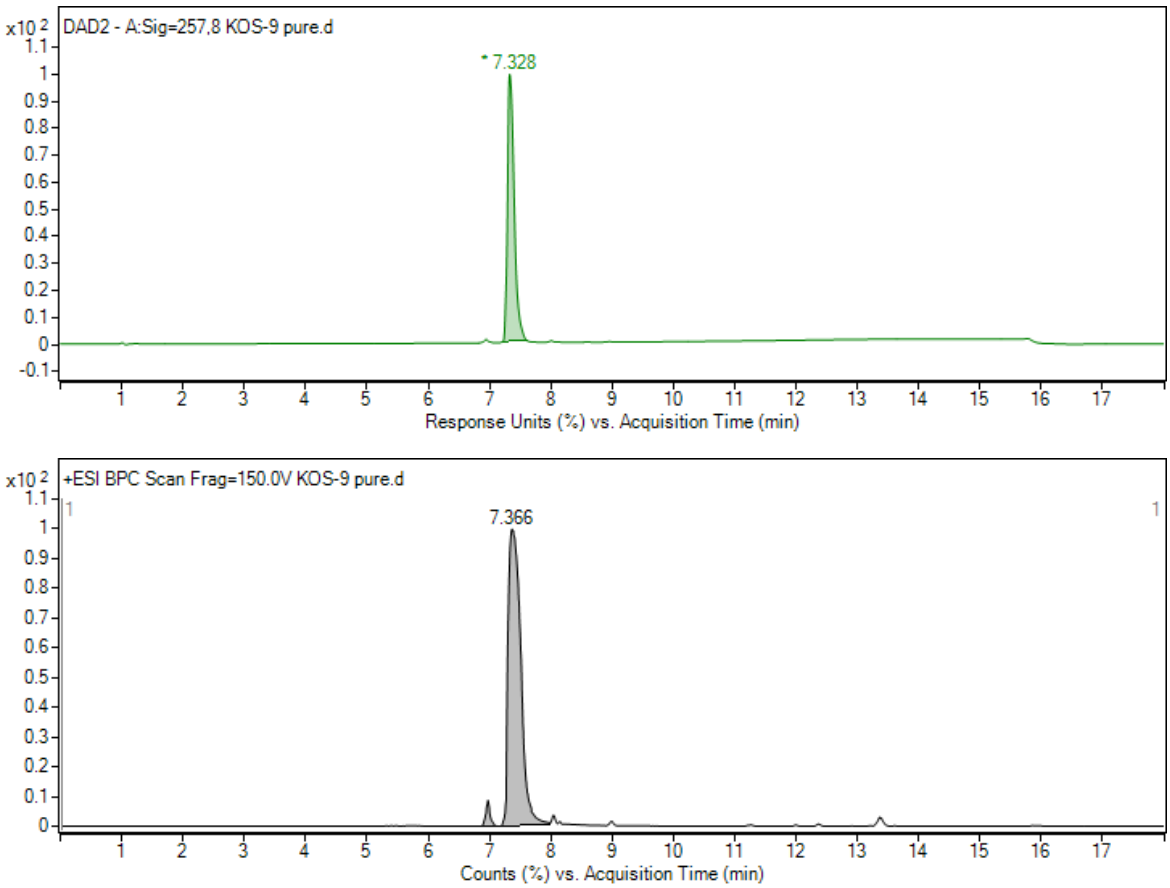


**Figure 110**: HPLC chromatogram of purified SA-401; UV detection (257 nm, upper) and ESI-MS (positive mode, lower)

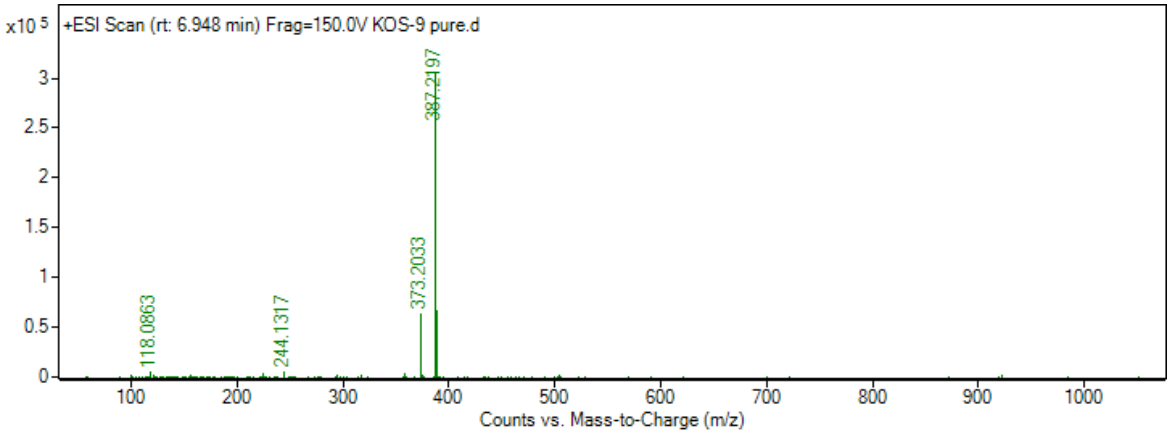


**Figure 111**: ESI scan, HPLC-MS analysis of SA-401, positive mode, 6.948 min retention time

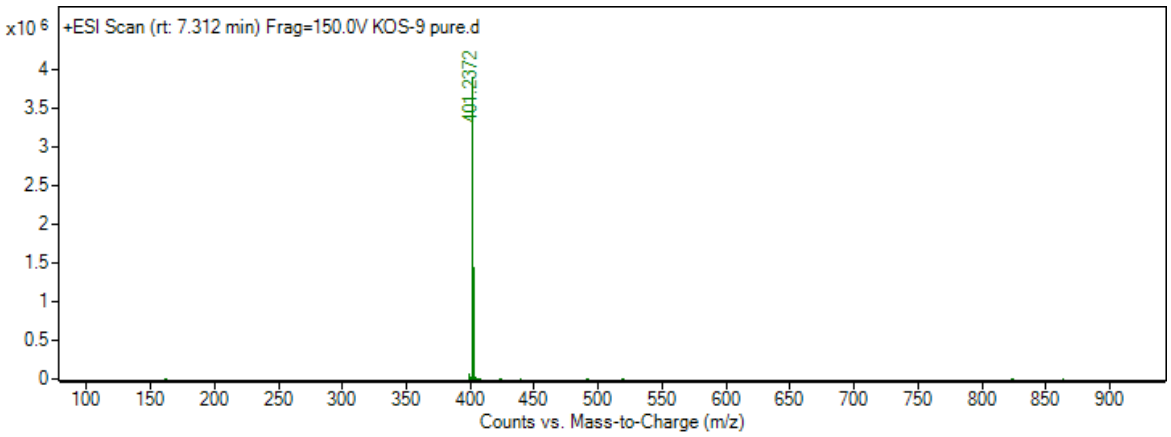


**Figure 112**: ESI scan, HPLC-MS analysis of SA-401, positive mode, 7.312 min retention time

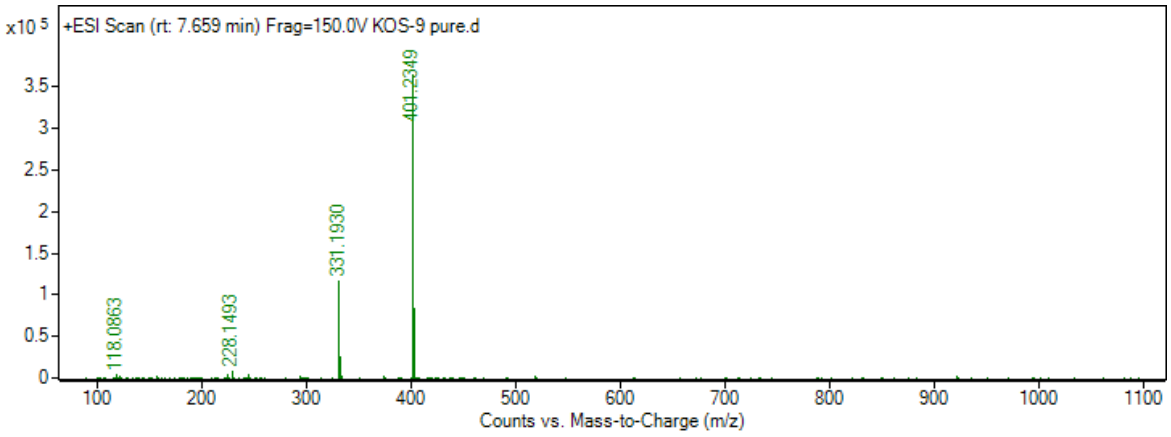


**Figure 113**: ESI scan, HPLC-MS analysis of SA-401, positive mode, 7.659 min retention time

**HPLC-MS analysis of the synthesis of product S7**

For the analysis, standards of products S6 and S7 were prepared in methanol at a concentration of 1 mg/mL. To analyze the extract, 20 µL was taken and diluted with 980 µL of methanol. Similarly, 20 µL aliquots of the reaction mixture were collected after 1 hour and 3.5 hours of reaction time. All samples were then further diluted 10-fold prior to HPLC-MS analysis.

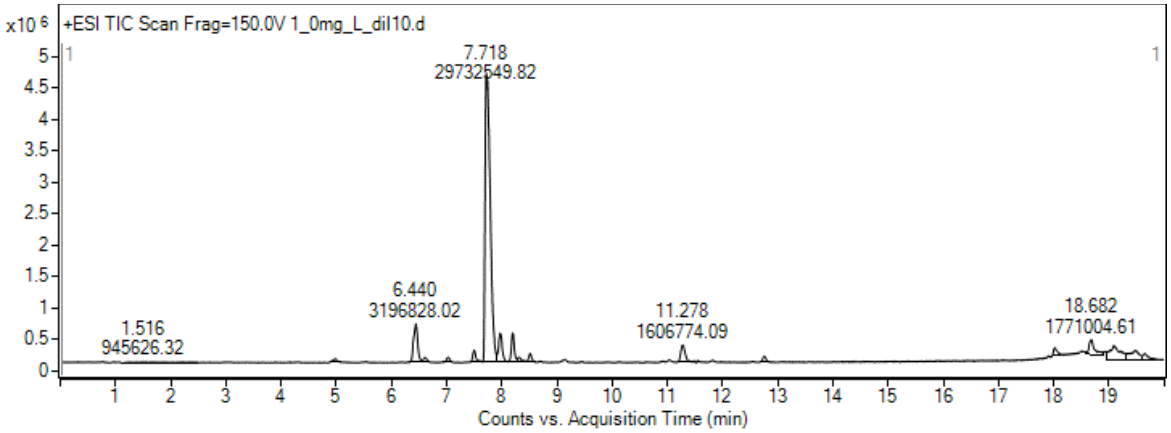


**Figure 114**: HPLC-MS chromatogram of product S7 (0.1 mg/mL); TIC

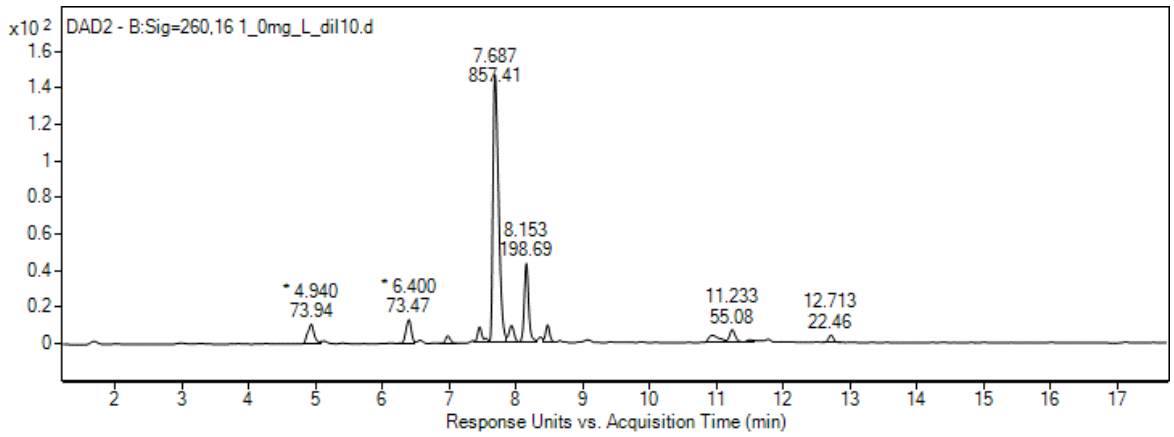


**Figure 115**: HPLC-MS chromatogram of product S7 (0.1 mg/mL); UV detection (260 nm)

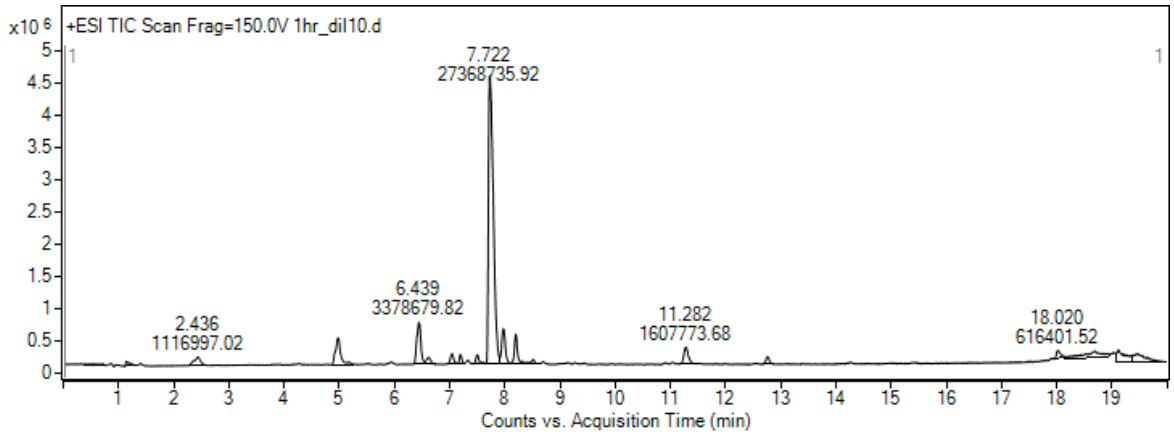


**Figure 116**: HPLC-MS chromatogram of reaction mixture (1 hour); TIC

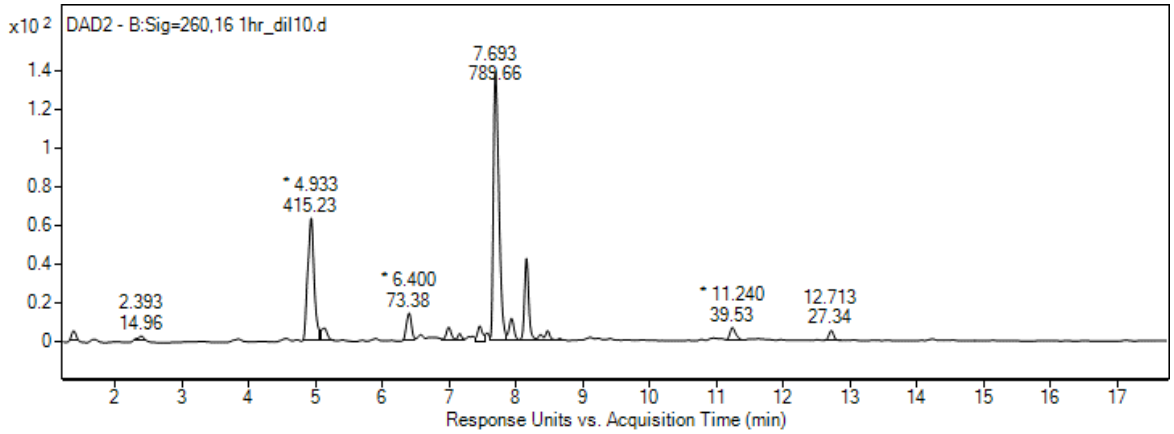


**Figure 117**: HPLC-MS chromatogram of reaction mixture (1 hour); UV detection (260 nm)

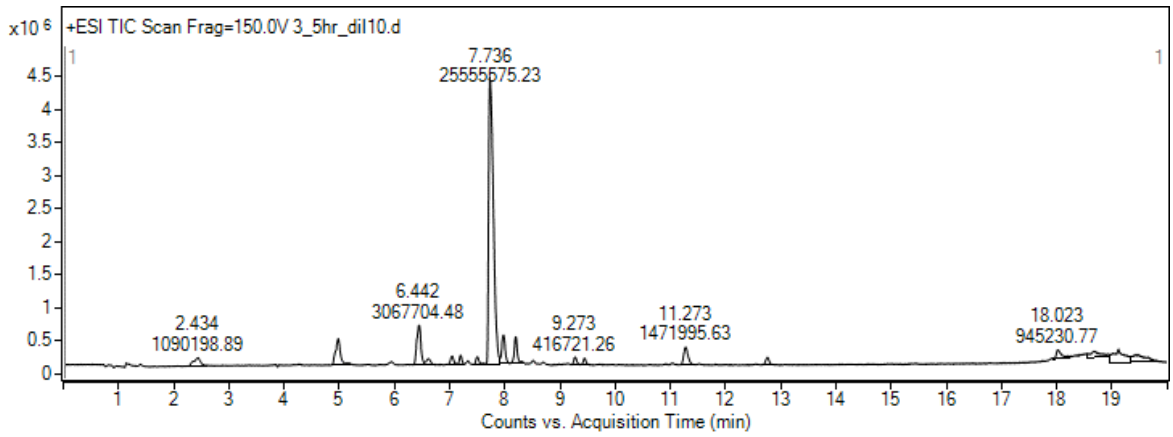


**Figure 118**: HPLC-MS chromatogram of reaction mixture (3.5 hours); TIC

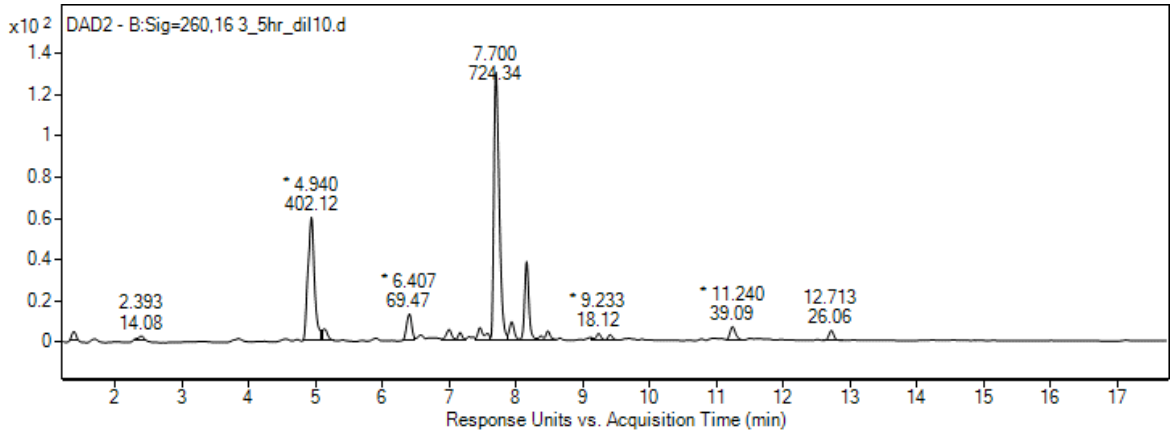


**Figure 119**: HPLC-MS chromatogram of reaction mixture (3.5 hours); UV detection (260 nm)

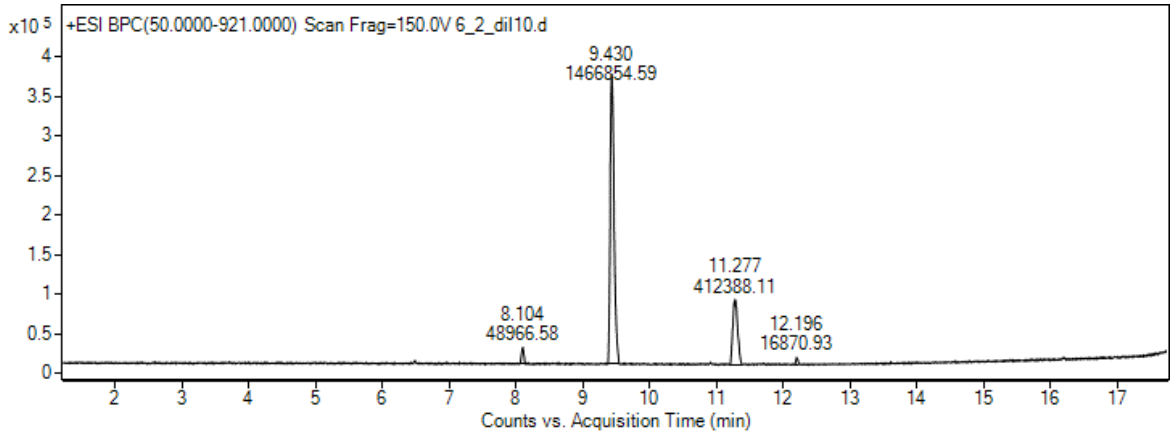


**Figure 120**: HPLC-MS chromatogram of product S6 (reagent, 0.1 mg/mL); TIC

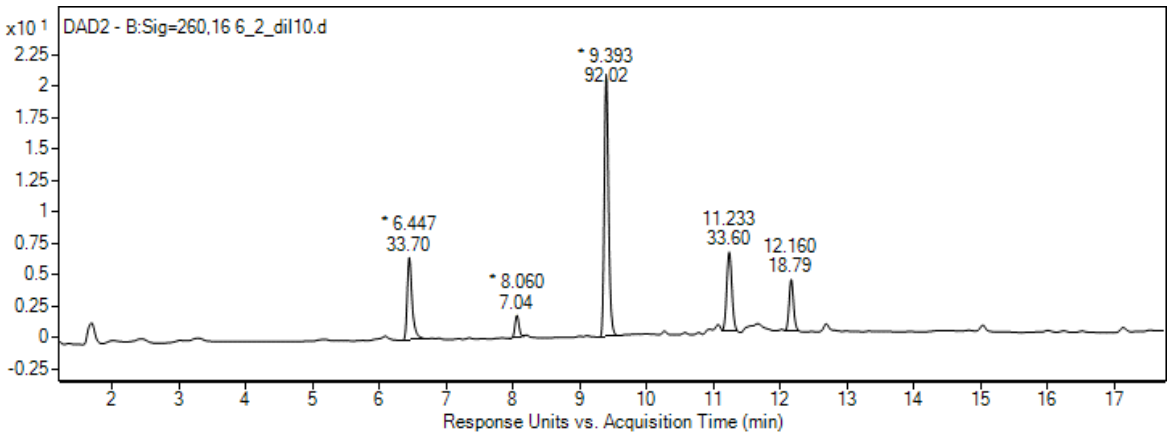


**Figure 121**: HPLC-MS chromatogram of product S6 (reagent, 0.1 mg/mL); UV detection (260 nm)

## Synthesis of polyphosphazene polymer

### Characterization of tert-butyl (2-(2-(2-aminoethoxy)ethoxy)ethyl)carbamate

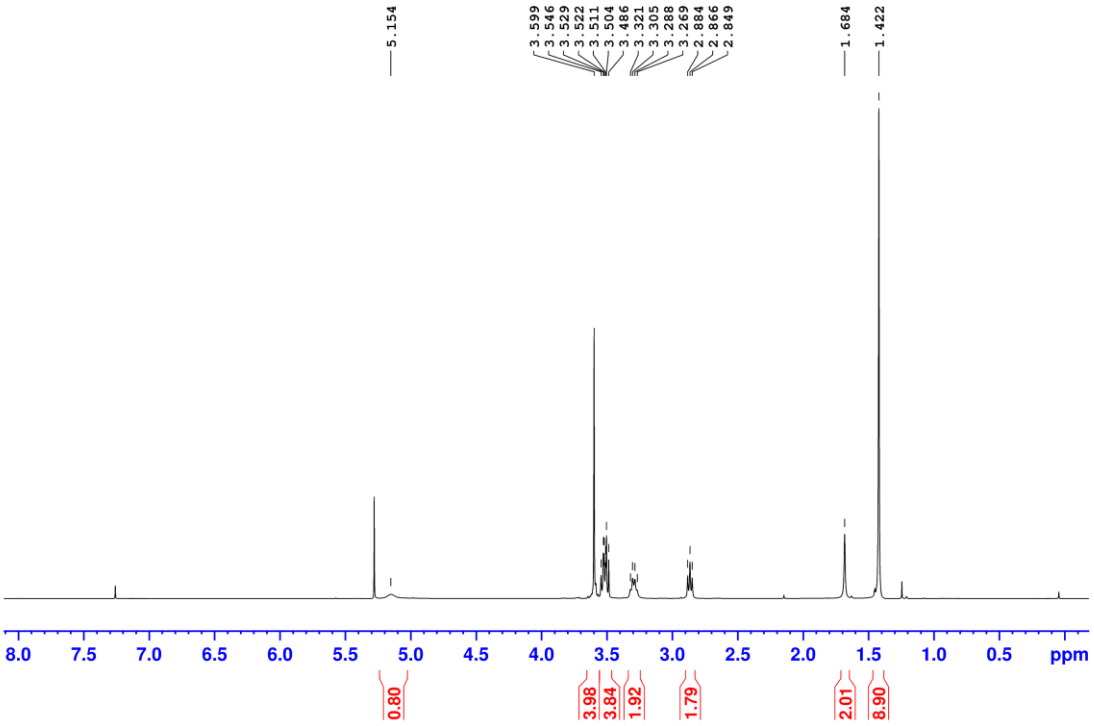


**Figure 122**: $^{1}$H NMR of tert-butyl (2-(2-(2-aminoethoxy)ethoxy)ethyl)carbamate, 300 MHz, $CDCl_3$

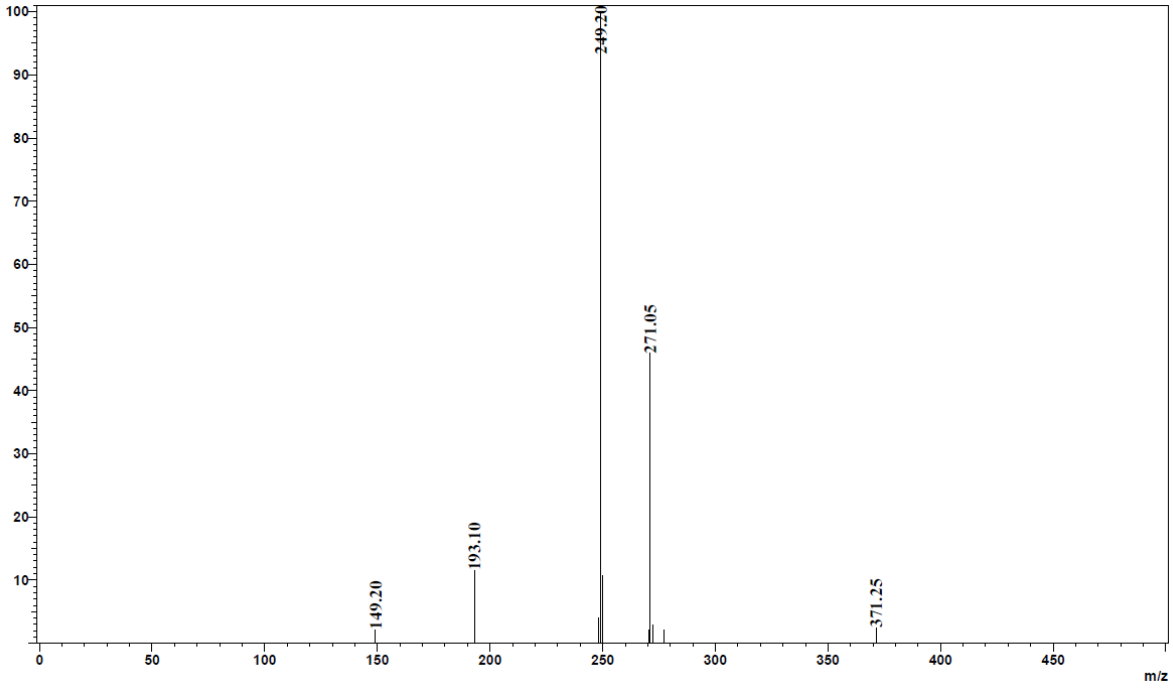


**Figure 123**: ESI-MS of tert-butyl (2-(2-(2-aminoethoxy)ethoxy)ethyl)carbamate; Shimadzu LCMS-2020, positive mode

## Characterization of Boc-protected macrosubstituted PPz

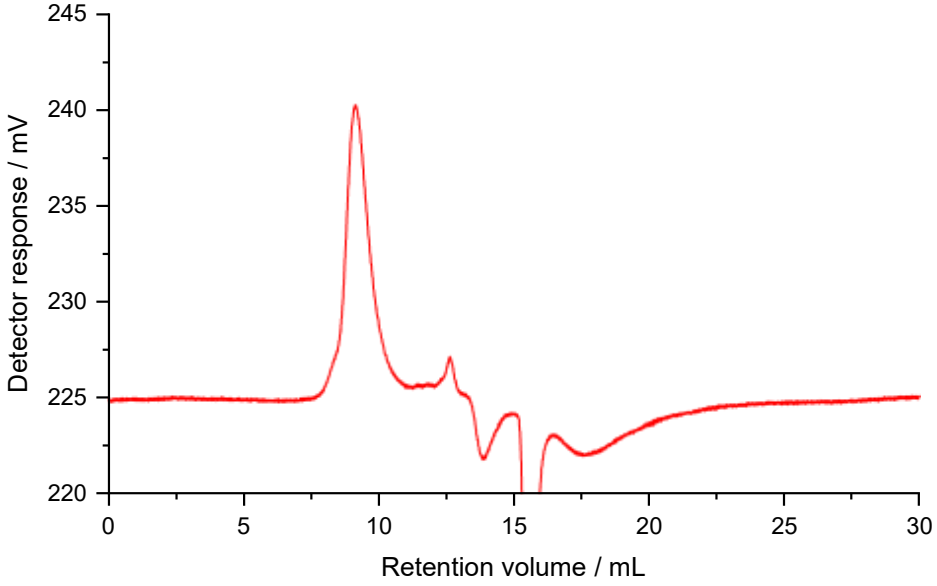


**Figure 124**: GPC chromatogram of Boc-protected macrosubstituted PPz; DMF, refractive index detector

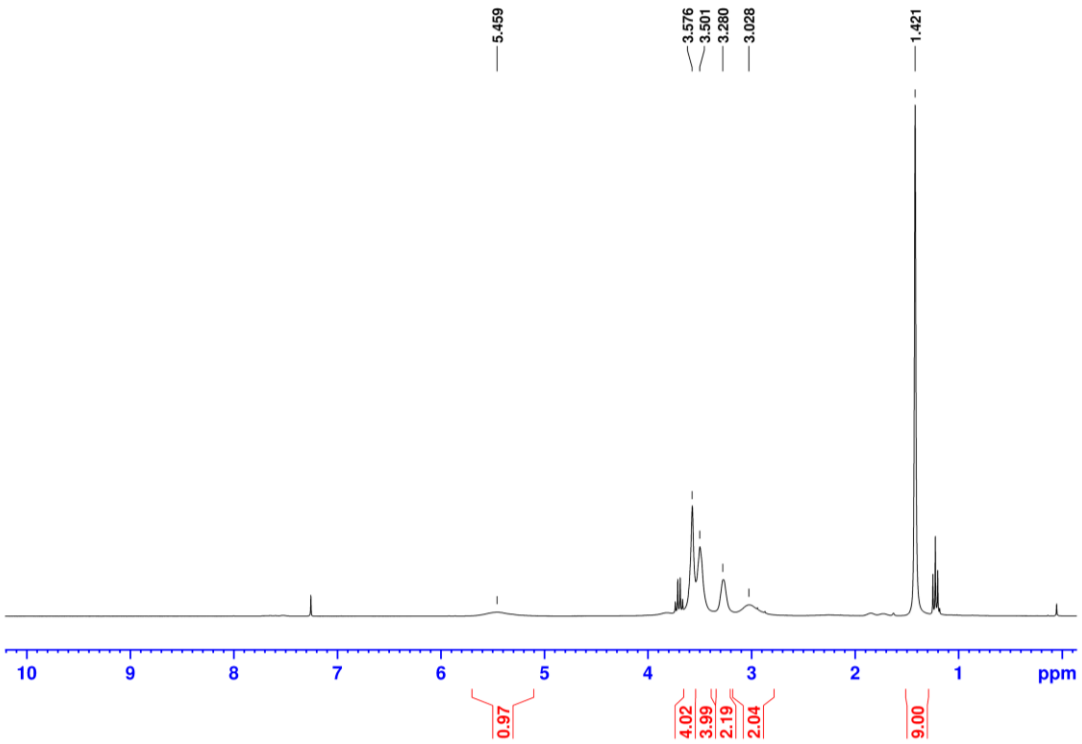


**Figure 125**: $^{1}H$ NMR of Boc-protected macrosubstituted PPz; 300 MHz, $CDCl_3$

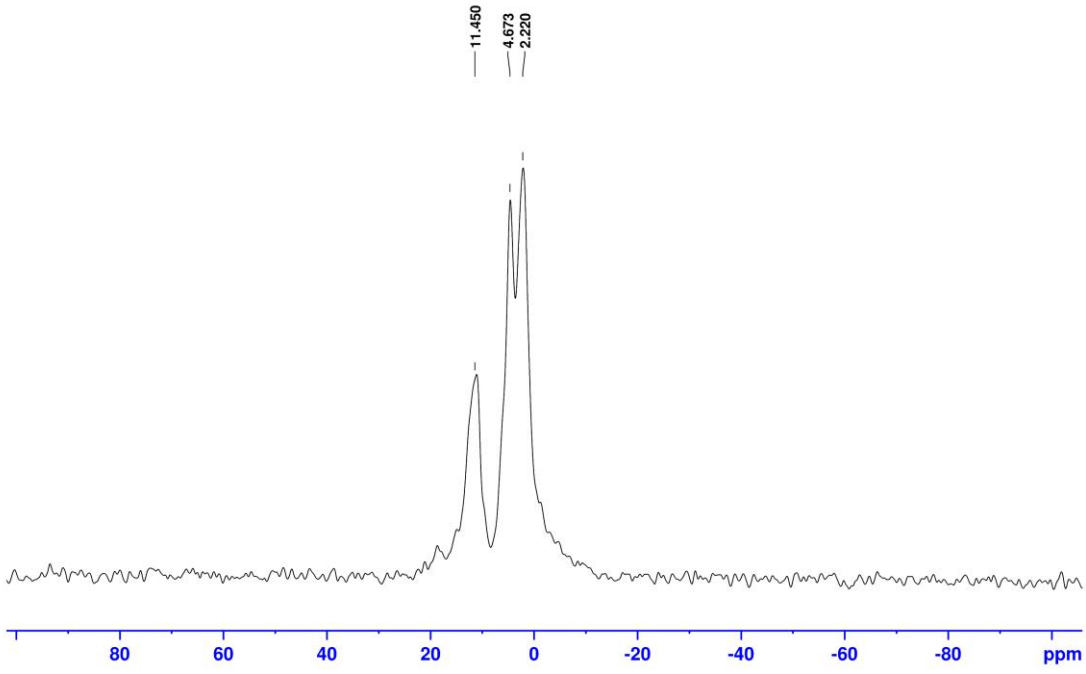


**Figure 126**: $^{31}P$ NMR of Boc-protected macrosubstituted PPz; P31CPD, 512 scans, 122 MHz, $CDCl_3$

## Characterization of Boc-deprotected macrosubstituted PPz

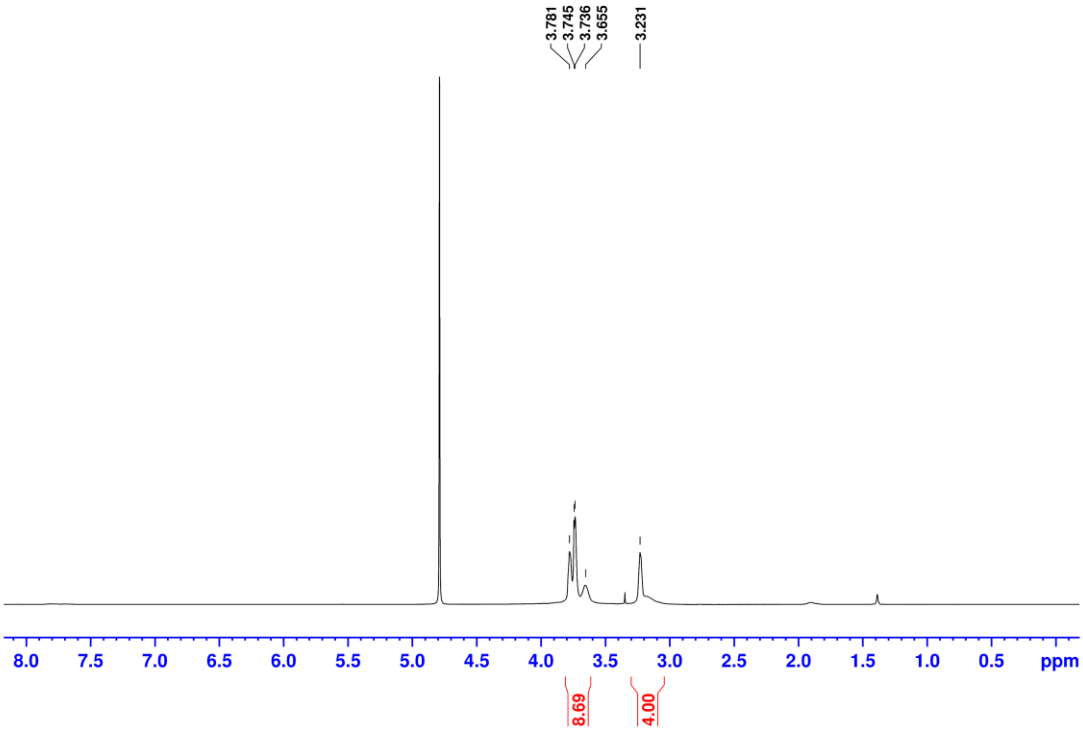


**Figure 127:** $^{1}H$ NMR of Boc-deprotected macrosubstituted PPz; 500 MHz, $D_2O$

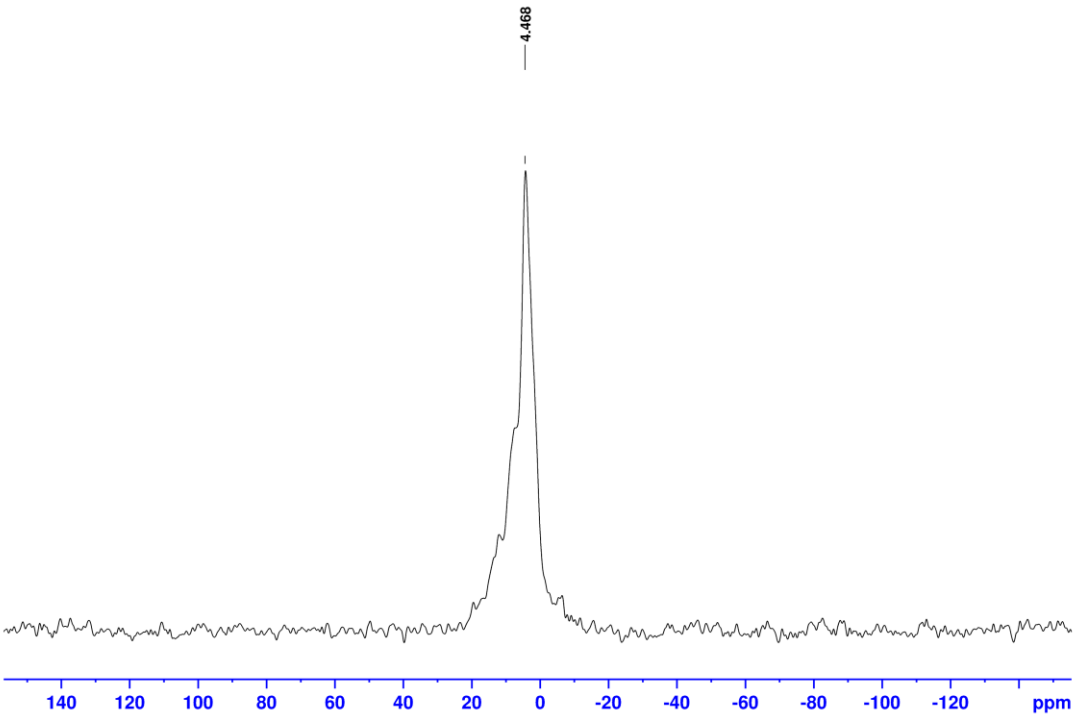


**Figure 128**: $^{31}P$ NMR of Boc-deprotected macrosubstituted PPz; P31IG, 1184 scans, 202 MHz, $D_2O$

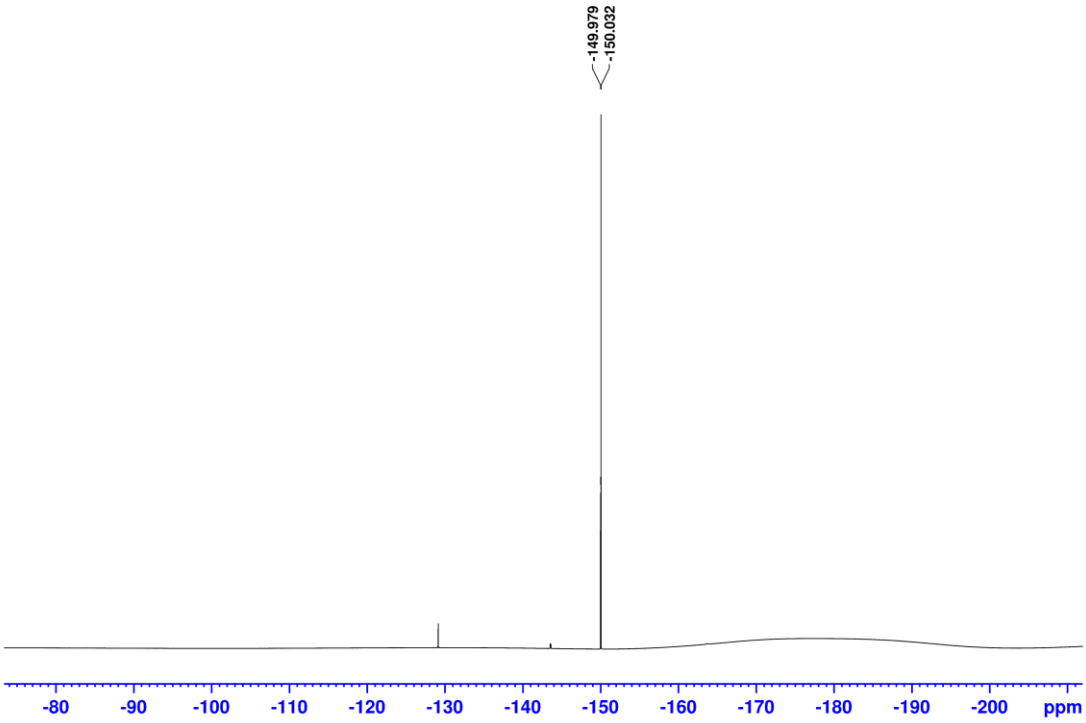


**Figure 129**: $^{19}F$ NMR of Boc-deprotected macrosubstituted PPz; 256 scans, 471 MHz, $D_2O$

## Characterization of Bn-protected PPz-PGA

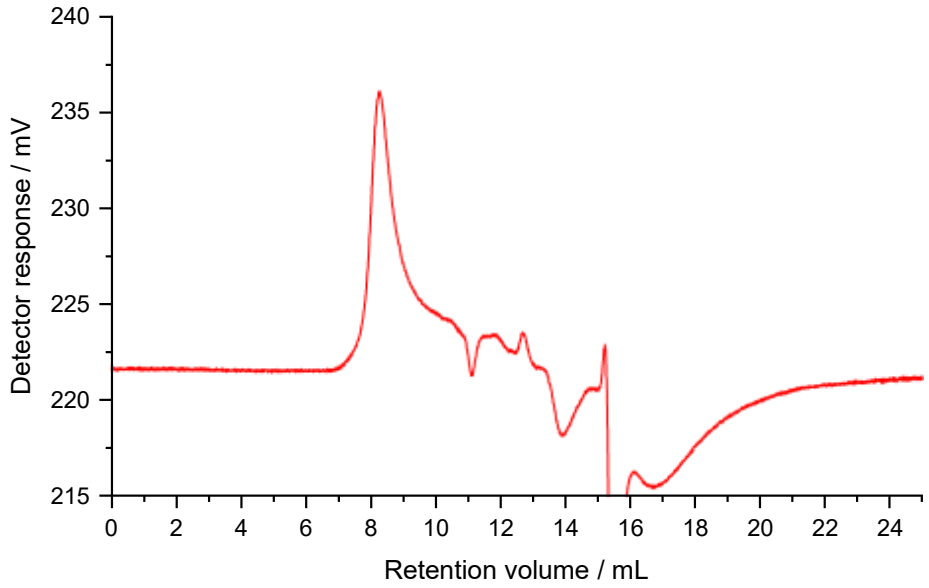


**Figure 130**: GPC chromatogram of Bn-protected PPz-PGA; DMF, refractive index detector

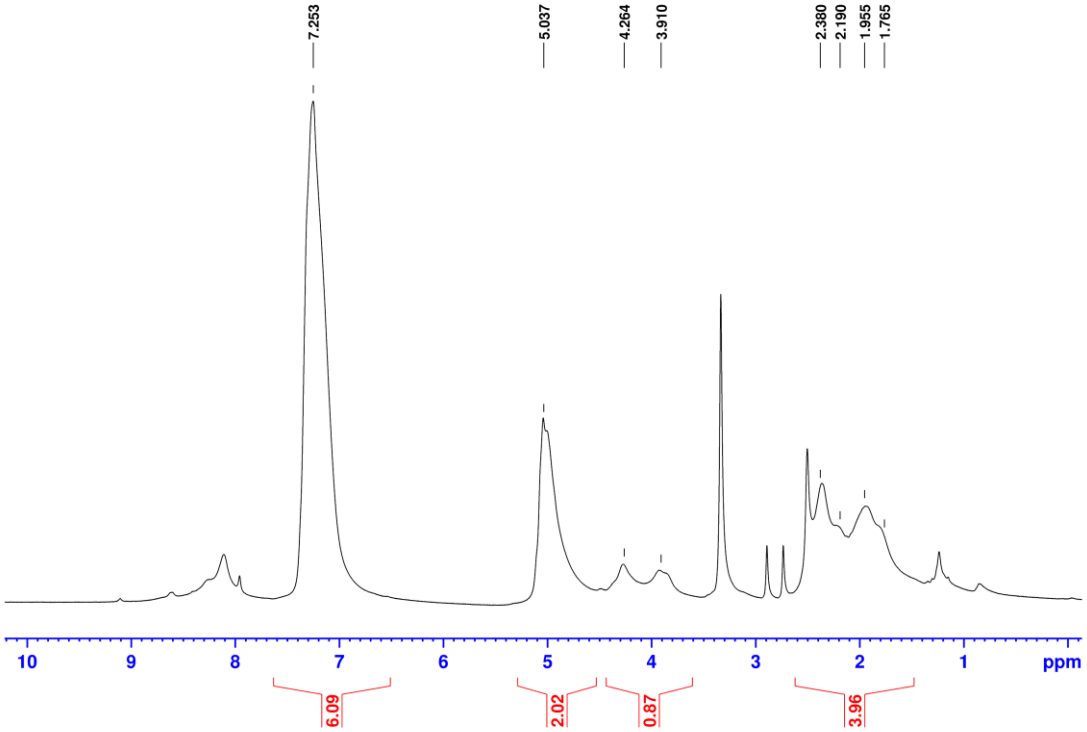


**Figure 131**: $^{1}H$ NMR of Bn-protected PGA-PPz; 300 MHz, DMSO

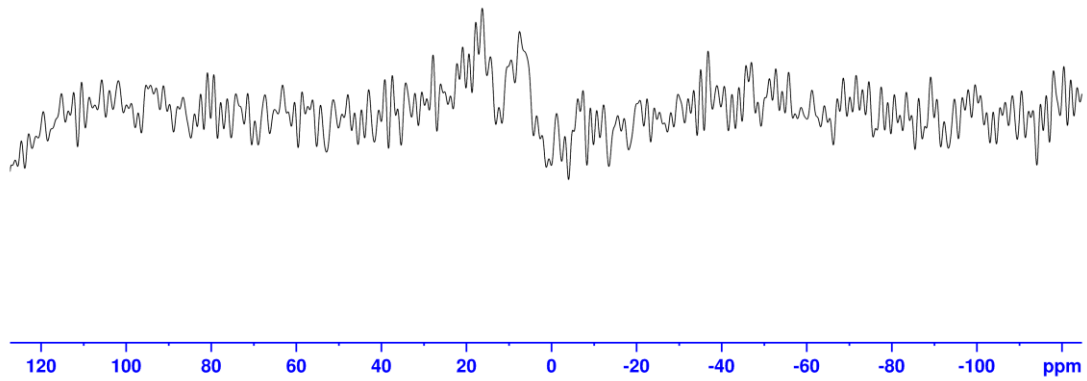


**Figure 132**: $^{31}P$ NMR of Bn-protected PGA-PPz; P31 (no decoupling, no NOE), 45 000 scans, 202 MHz, DMSO

## Characterization of Bn-deprotected PPz-PGA

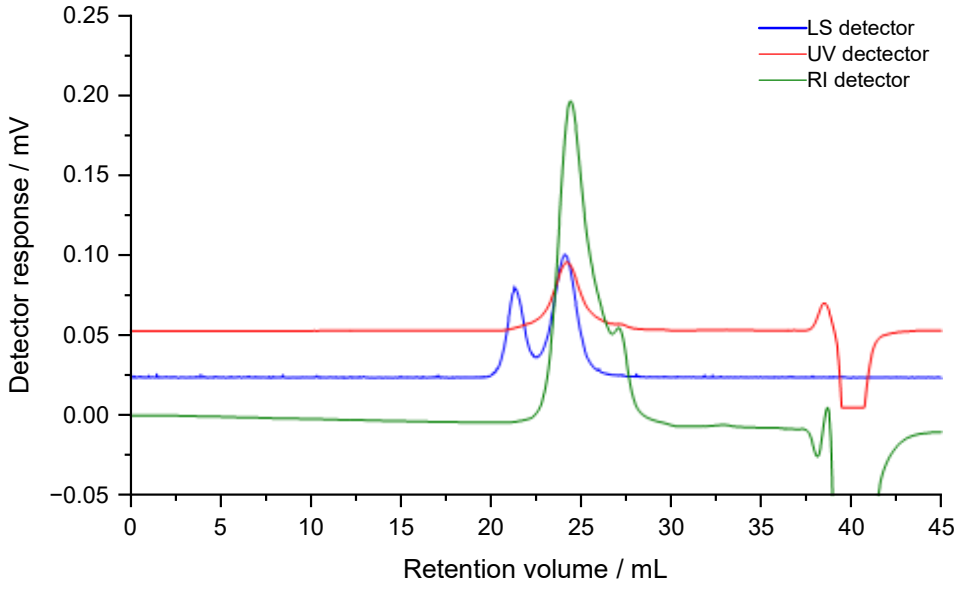


**Figure 133:** GPC chromatogram of Bn-deprotected PPz-PGA; aqueous, light scattering (LS), refractive index (RI), and UV detection

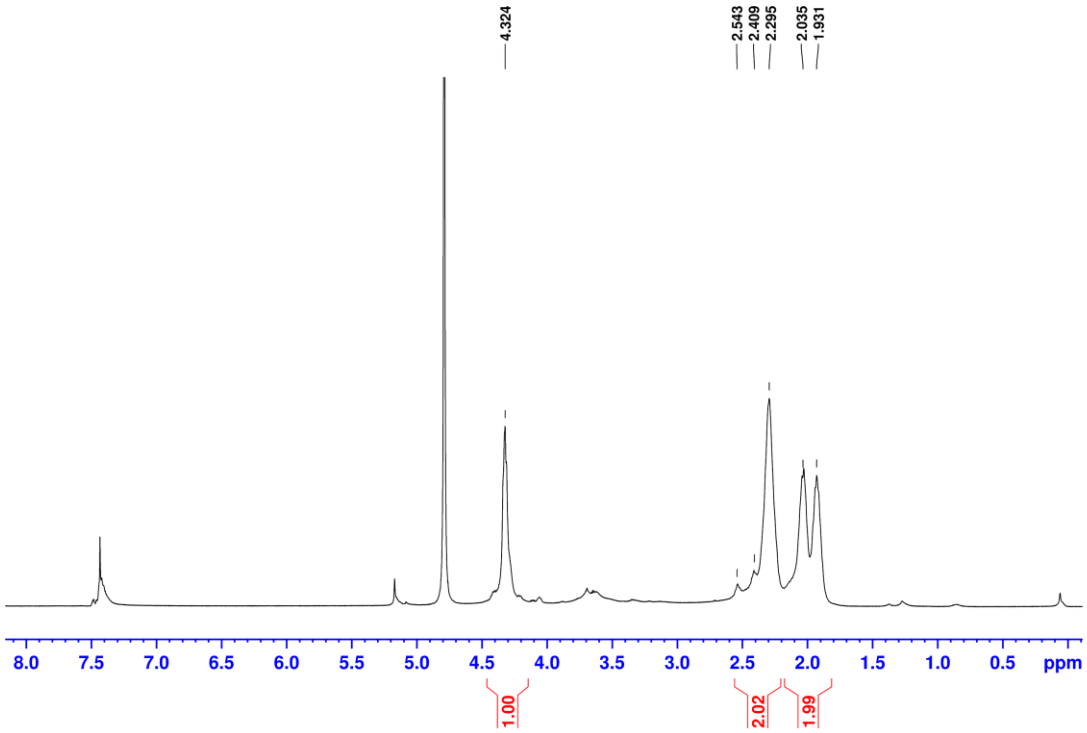


**Figure 134**: $^{1}H$ NMR of Bn-deprotected PPz-PGA; 500 MHz, $D_2O$

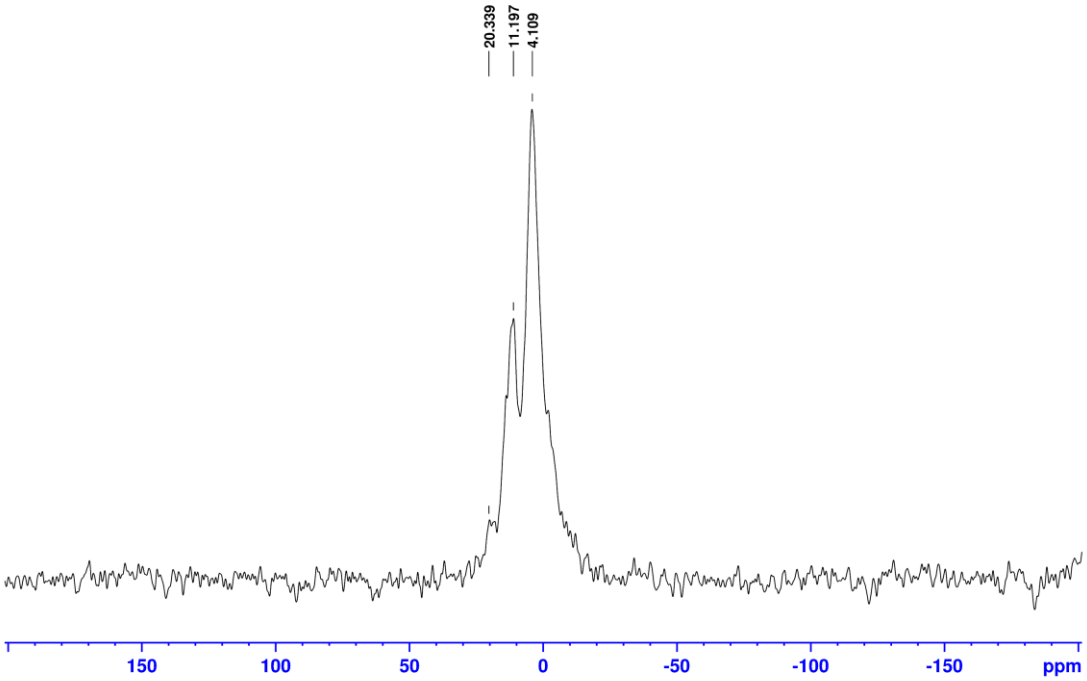


**Figure 135:** $^{31}P$ NMR of Bn-deprotected PPz-PGA; P31IG, 53033 scans, 202 MHz, $D_2O$

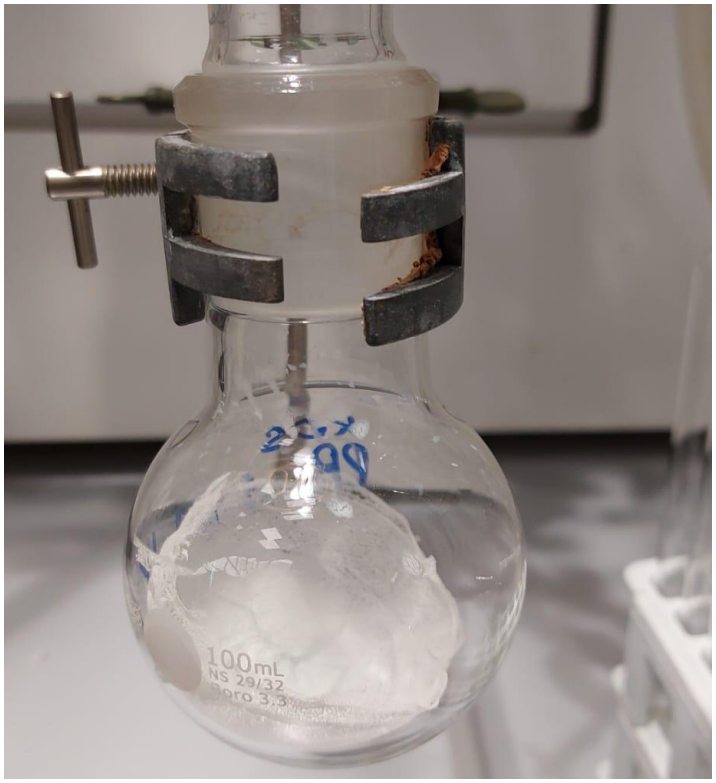


**Figure 136**: Appearance of Bn-deprotected PPz-PGA

**Characterization of Cbz-protected β-Ala-Boc-hydrazide linker**

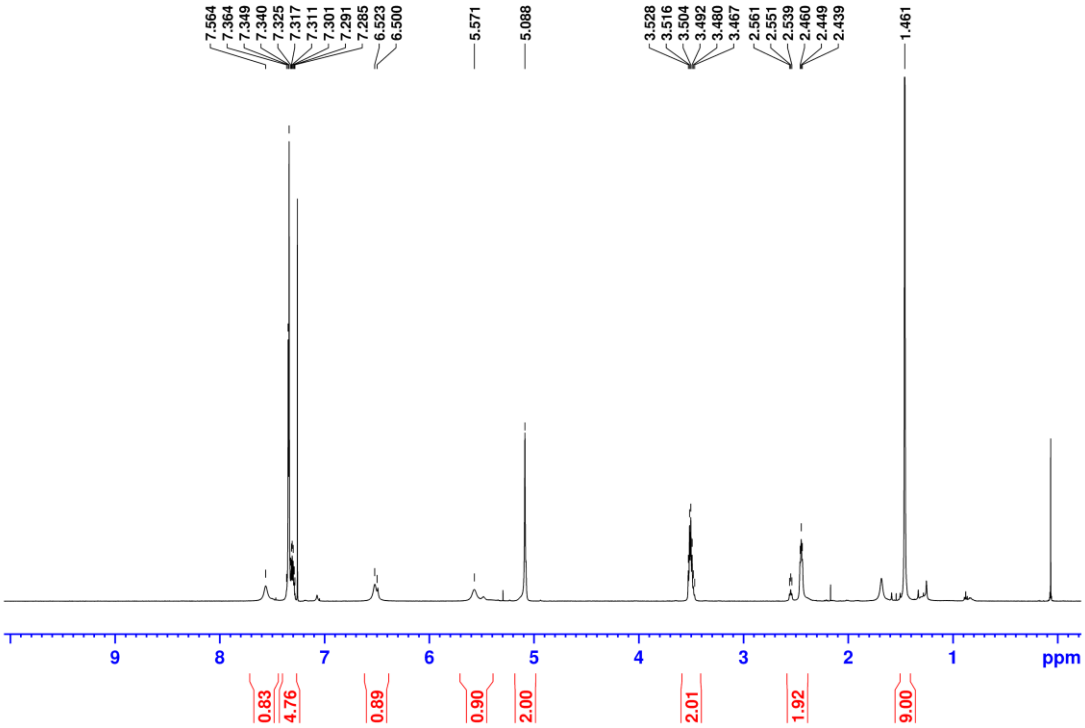


**Figure 137**: $^{1}$H NMR of Cbz-protected β-Ala-Boc-hydrazide linker; 500 MHz, $CDCl_3$

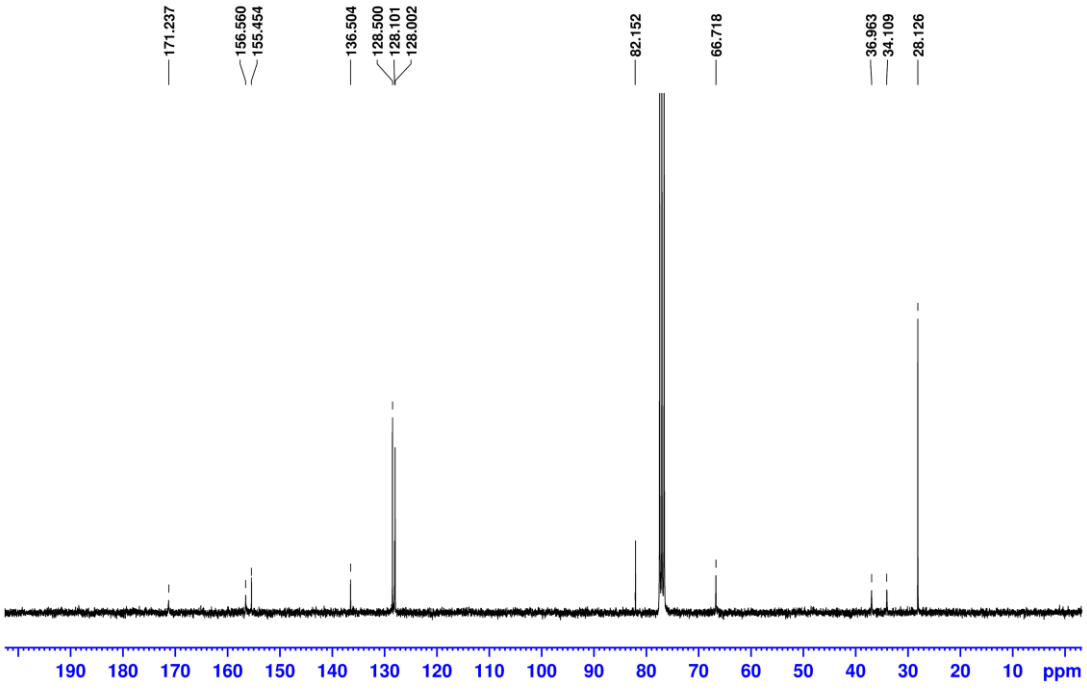


**Figure 138**: $^{13}$C NMR of Cbz-protected β-Ala-Boc-hydrazide linker; C13CPD, 4096 scans, 75 MHz, $CDCl_3$

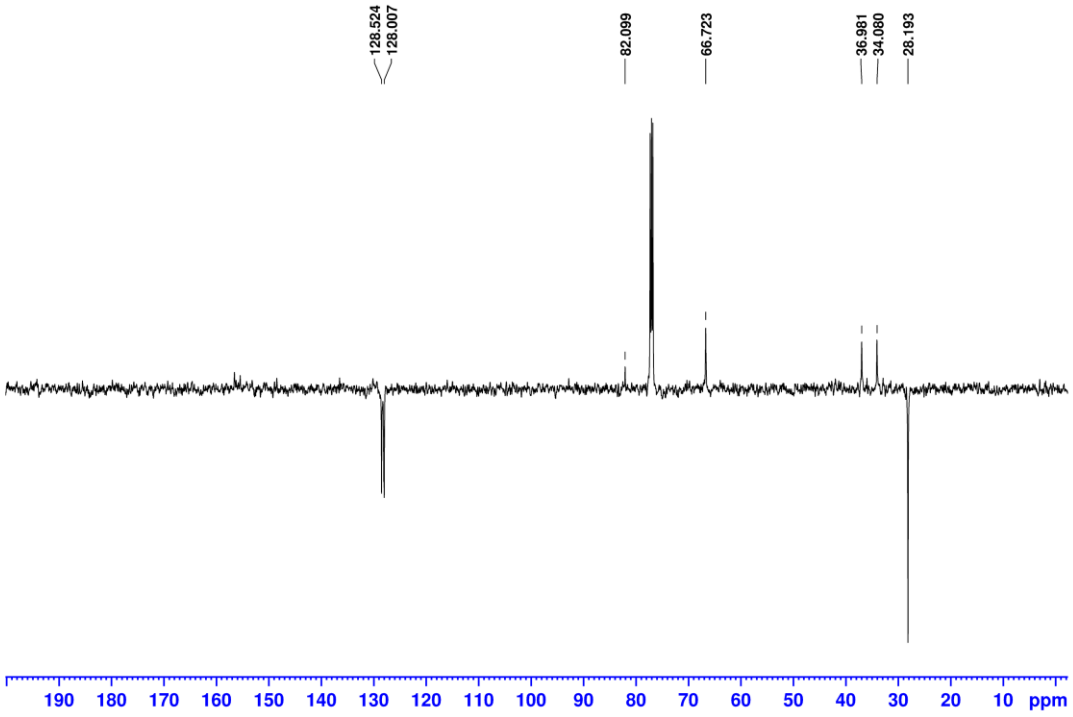


**Figure 139**: $^{13}C$ NMR of Cbz-protected β-Ala-Boc-hydrazide linker; C13APT, 512 scans, 125 MHz, $CDCl_3$

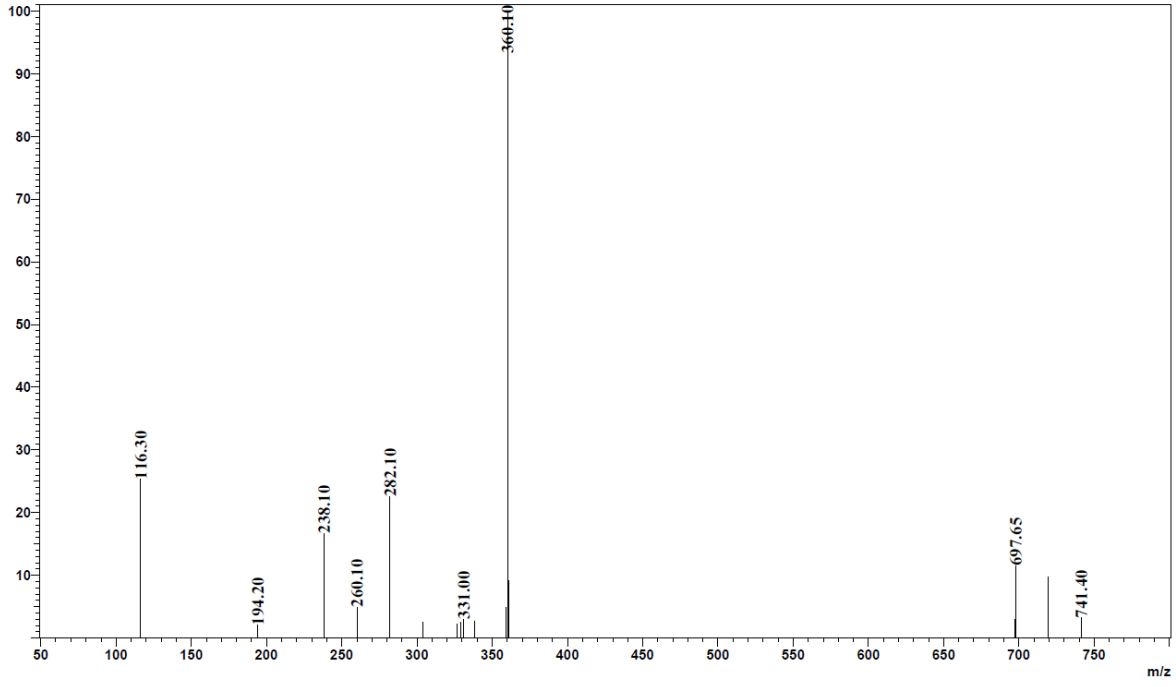


**Figure 140:** ESI-MS of Cbz-protected β-Ala-Boc-hydrazide linker; Shimadzu LCMS-2020, positive mode

**Characterization of Cbz-deprotected β-Ala-Boc hydrazide linker**

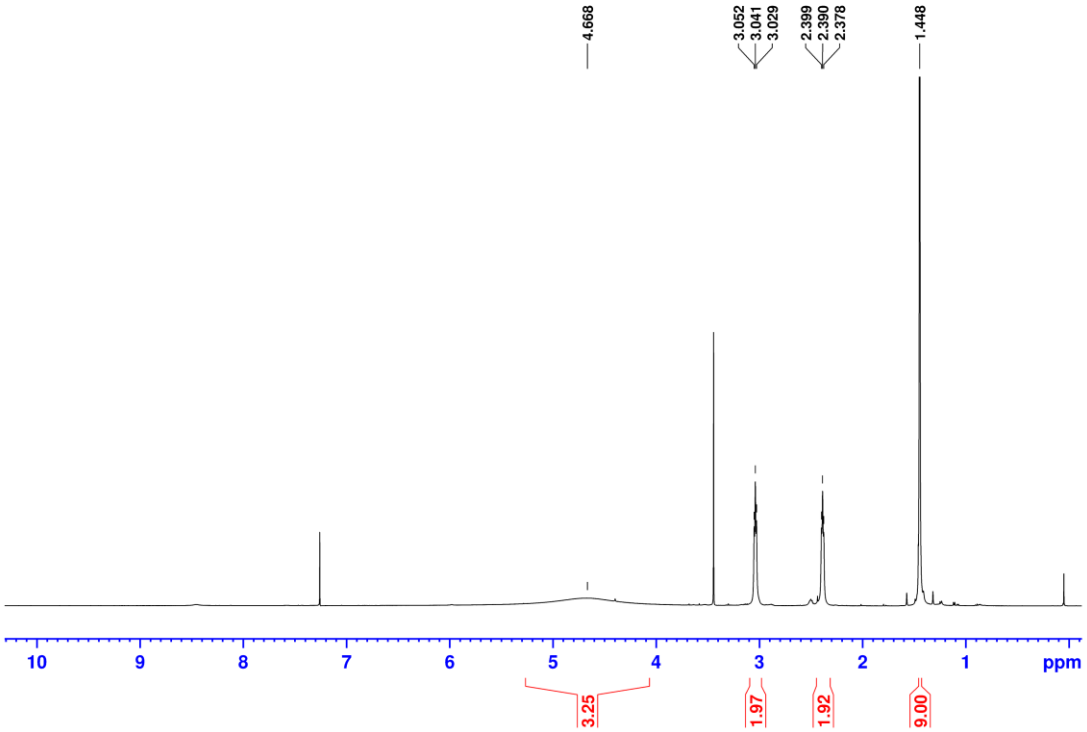


**Figure 141**: $^{1}H$ NMR of Cbz-deprotected β-Ala-Boc-hydrazide linker; 500 MHz, $CDCl_3$

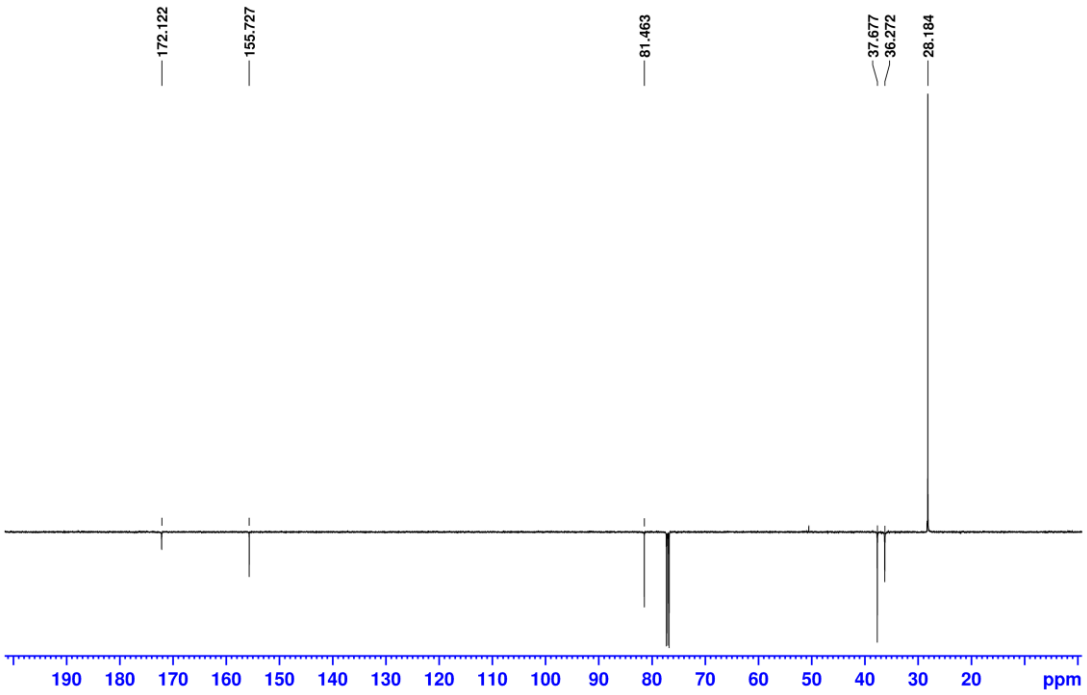


**Figure 142**: $^{13}C$ NMR of Cbz-deprotected β-Ala-Boc-hydrazide linker; C13APT, 4096 scans, 125 MHz, $CDCl_3$

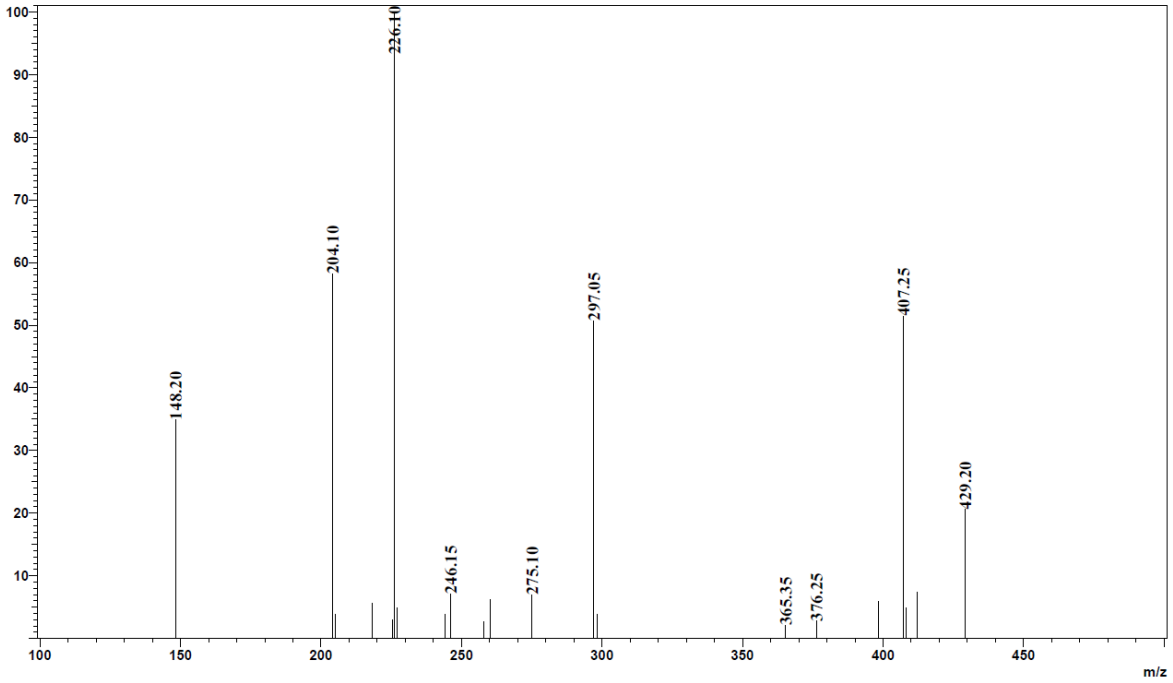


**Figure 143**: ESI-MS of Cbz-deprotected β-Ala-Boc-hydrazide linker; Shimadzu LCMS-2020, positive mode

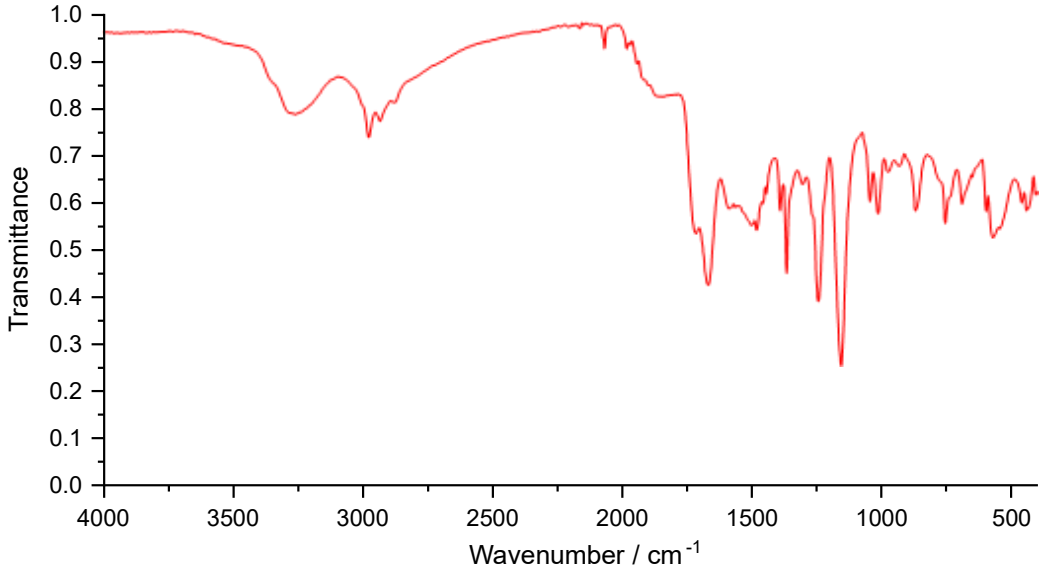


**Figure 144**: IR spectrum of Cbz-deprotected β-Ala-Boc-hydrazide linker; Bruker Alpha II FT-IR spectrometer

**Characterization of β-Ala-Boc-hydrazide-linked PPz-PGA**

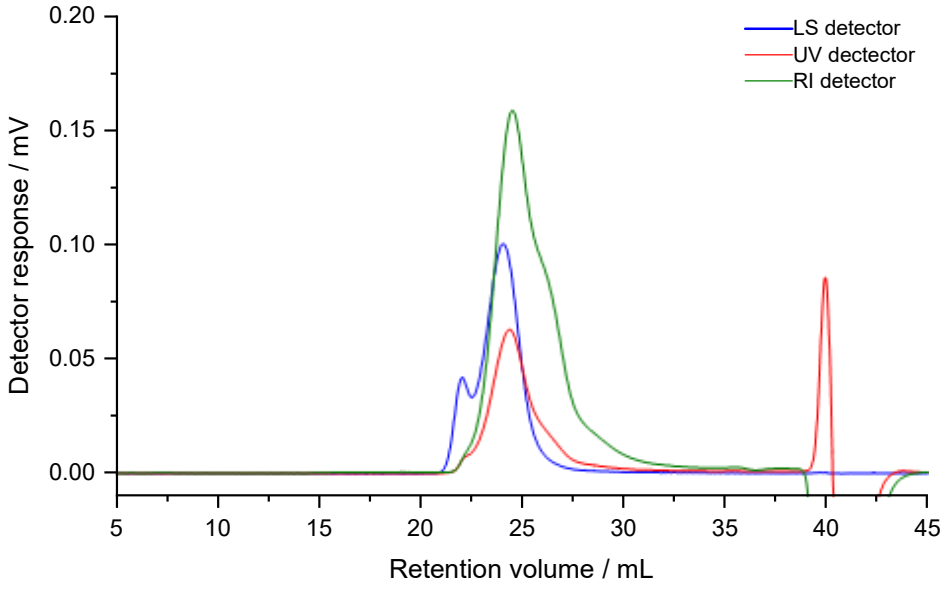


**Figure 145**: GPC chromatogram of β-Ala-Boc-hydrazide-linked PPz-PGA; aqueous, light scattering (LS), refractive index (RI), and UV detection

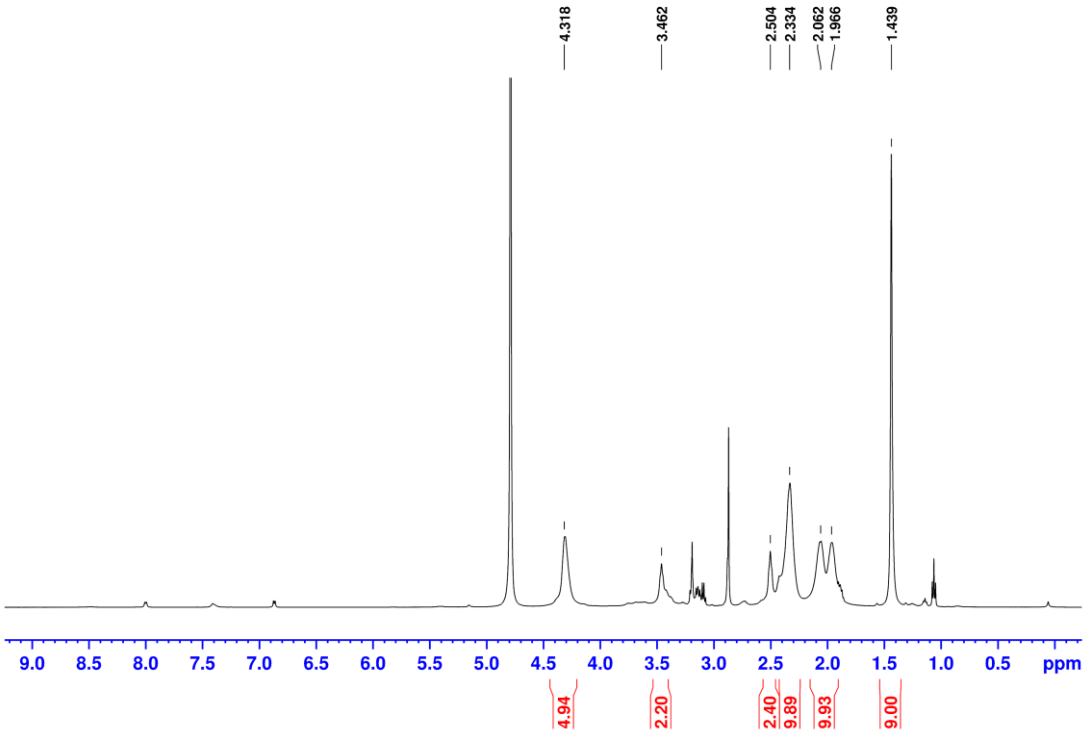


**Figure 146**: $^{1}H$ NMR of β-Ala-Boc-hydrazide-linked PPz-PGA; 500 MHz, $D_2O$

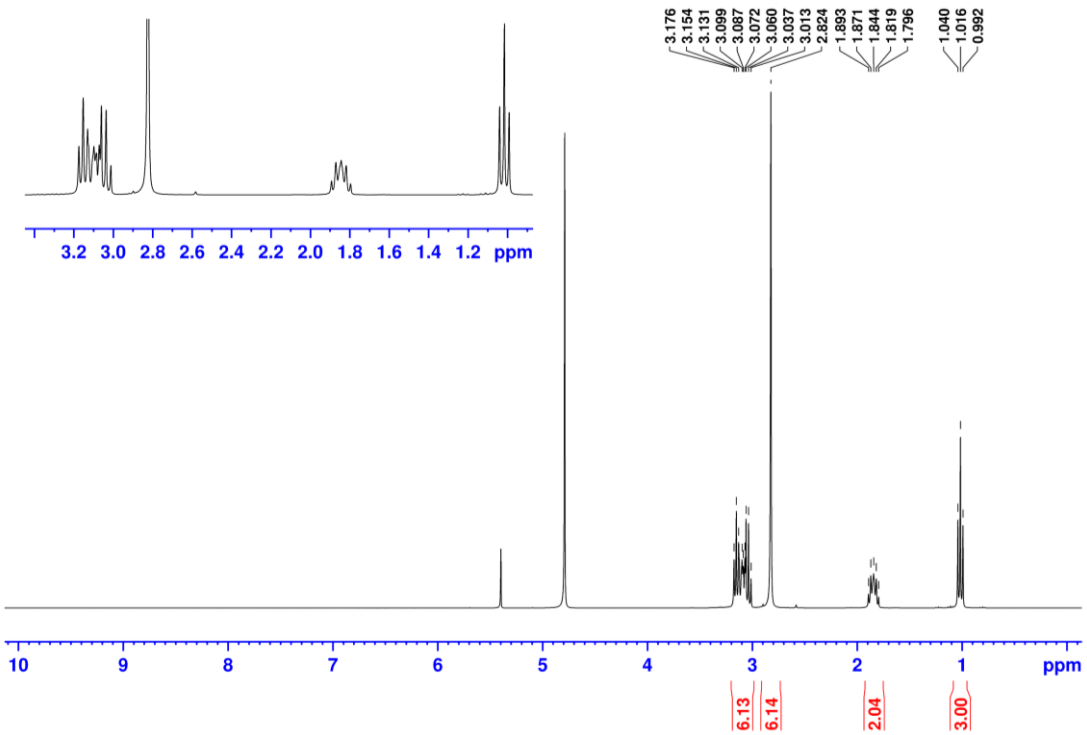


**Figure 147**: $^{1}$H NMR of EDC urea (coupling side product), obtained by hydrolysis of EDC HCl in water (pH 4-5) for 2 hours; 500 MHz, $D_2O$

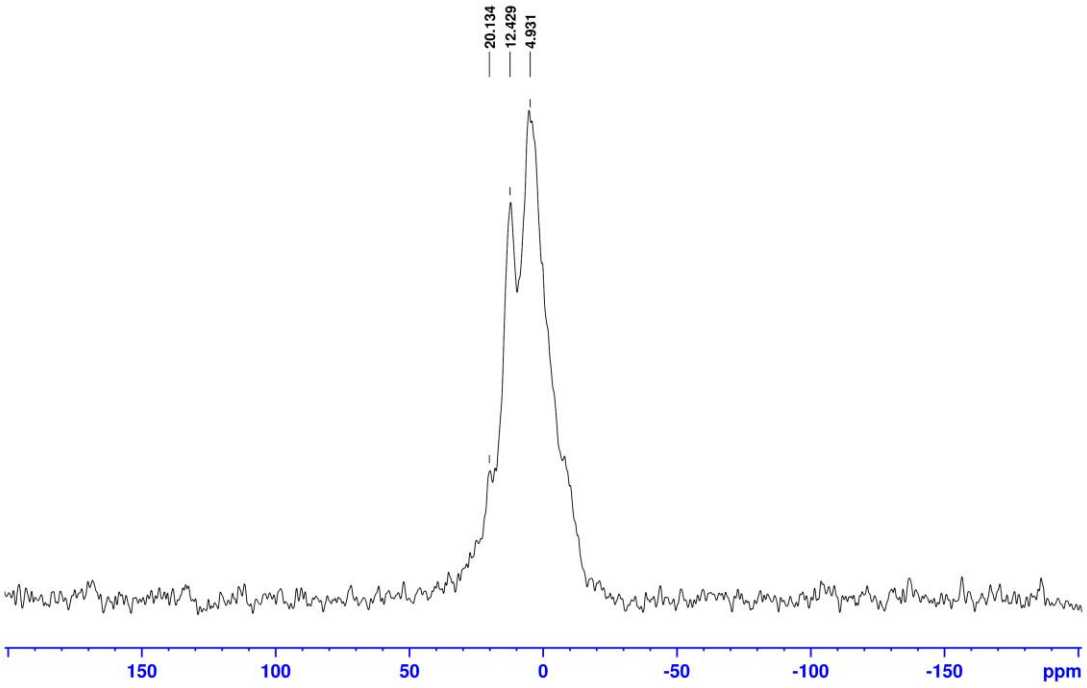


**Figure 148**: $^{31}$P NMR of β-Ala-Boc-hydrazide linked PPz-PGA; P31IG, 47246 scans, 202 MHz, $D_2O$

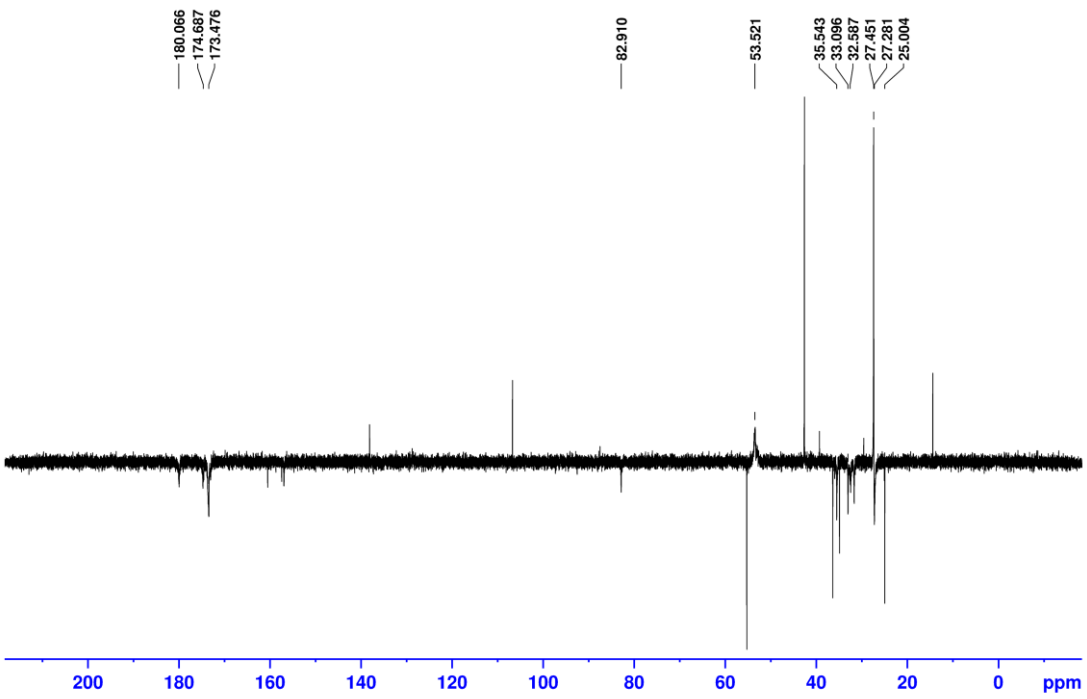


**Figure 149**: $^{13}C$ NMR of β-Ala-Boc-hydrazide linked PPz-PGA; C13APT, 4096 scans, 125 MHz, $D_2O$

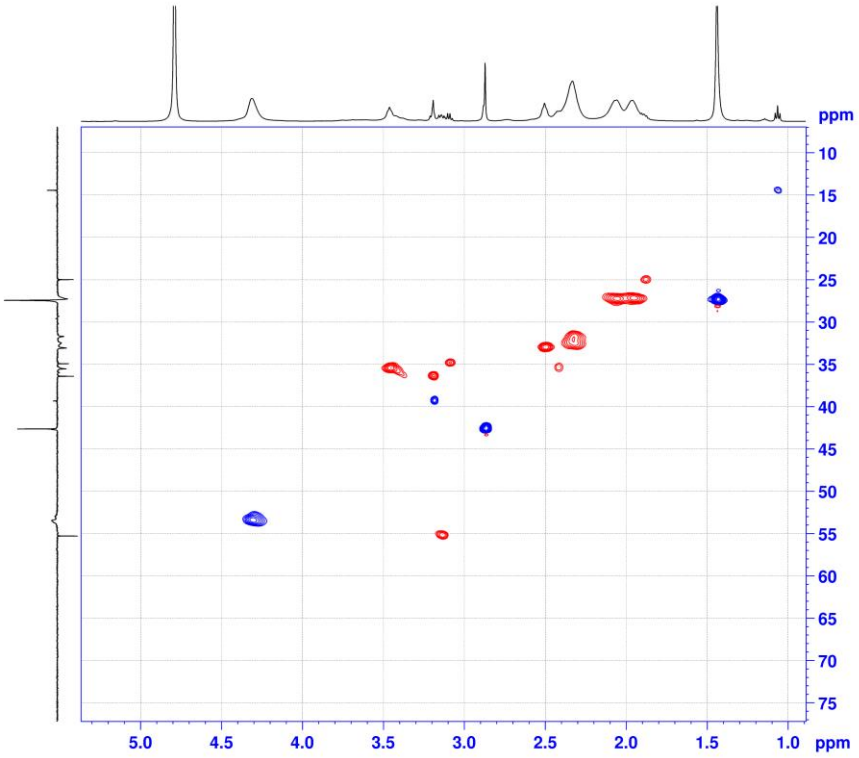


**Figure 150**: HSQC NMR of β-Ala-Boc-hydrazide linked PPz-PGA; HSQCEDETGP, 32 scans, 500 MHz ($^1H$) and 125 MHz ($^{13}C$), $D_2O$

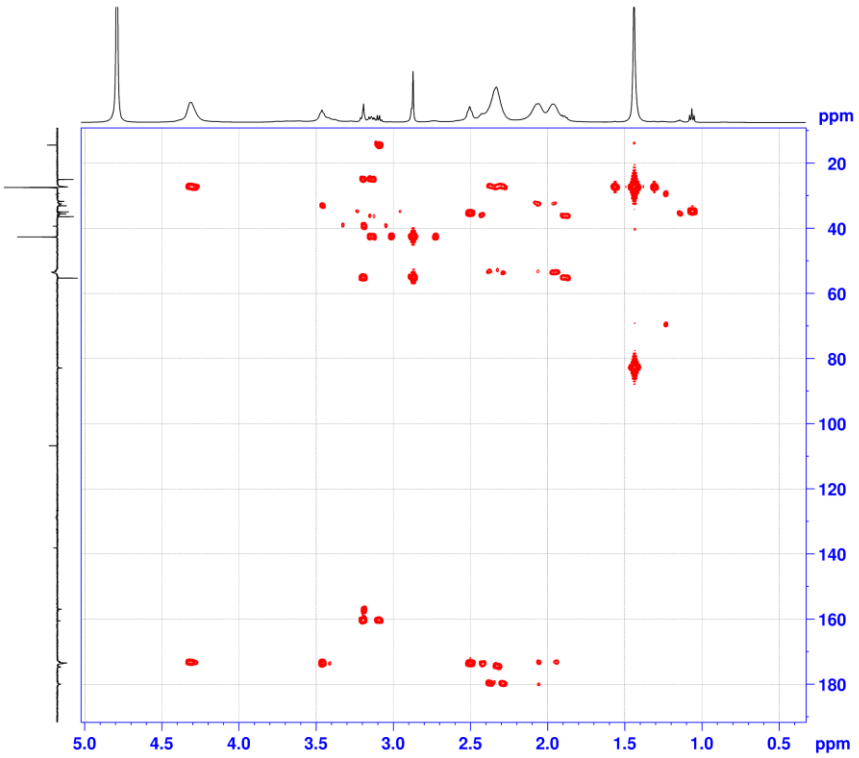


**Figure 151**: HMBC NMR of β-Ala-Boc-hydrazide linked PPz-PGA; HMBCGP, 64 scans, 500 MHz ($^{1}H$) and 125 MHz ($^{13}C$), $D_2O$

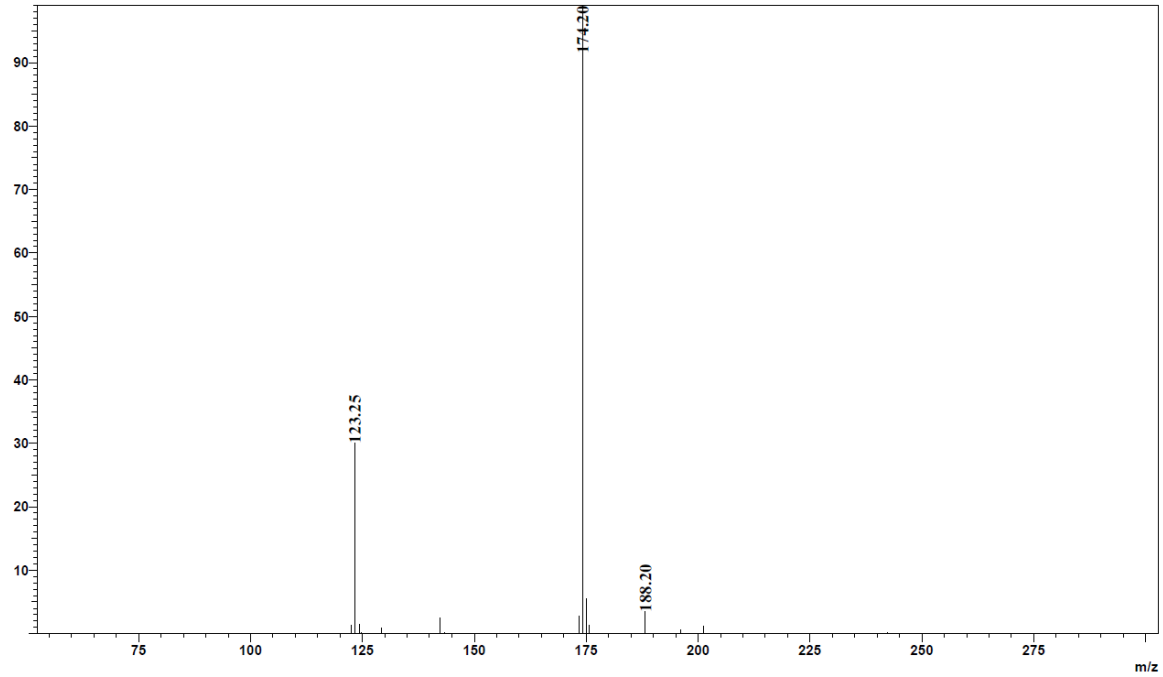


**Figure 152**: ESI-MS of β-Ala-Boc-hydrazide linked PPz-PGA; Shimadzu LCMS-2020, positive mode

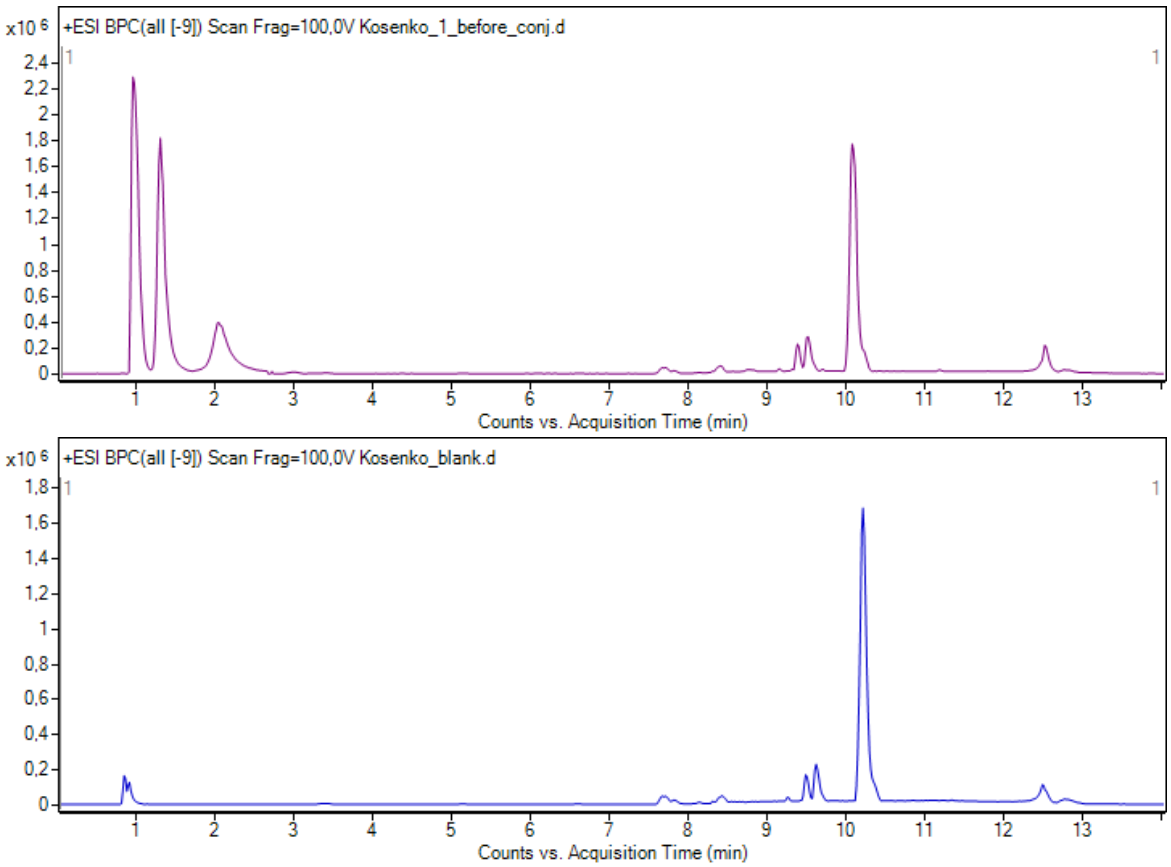


**Figure 153**: Base peak chromatograms (BPC) from HPLC-MS analysis of β-Ala-Boc-hydrazide-linked PPz-PGA (1 mg/mL in methanol, filtered through a 0.2 µm PTFE filter) compared with a blank (methanol filtered through a 0.2 µm PTFE filter).

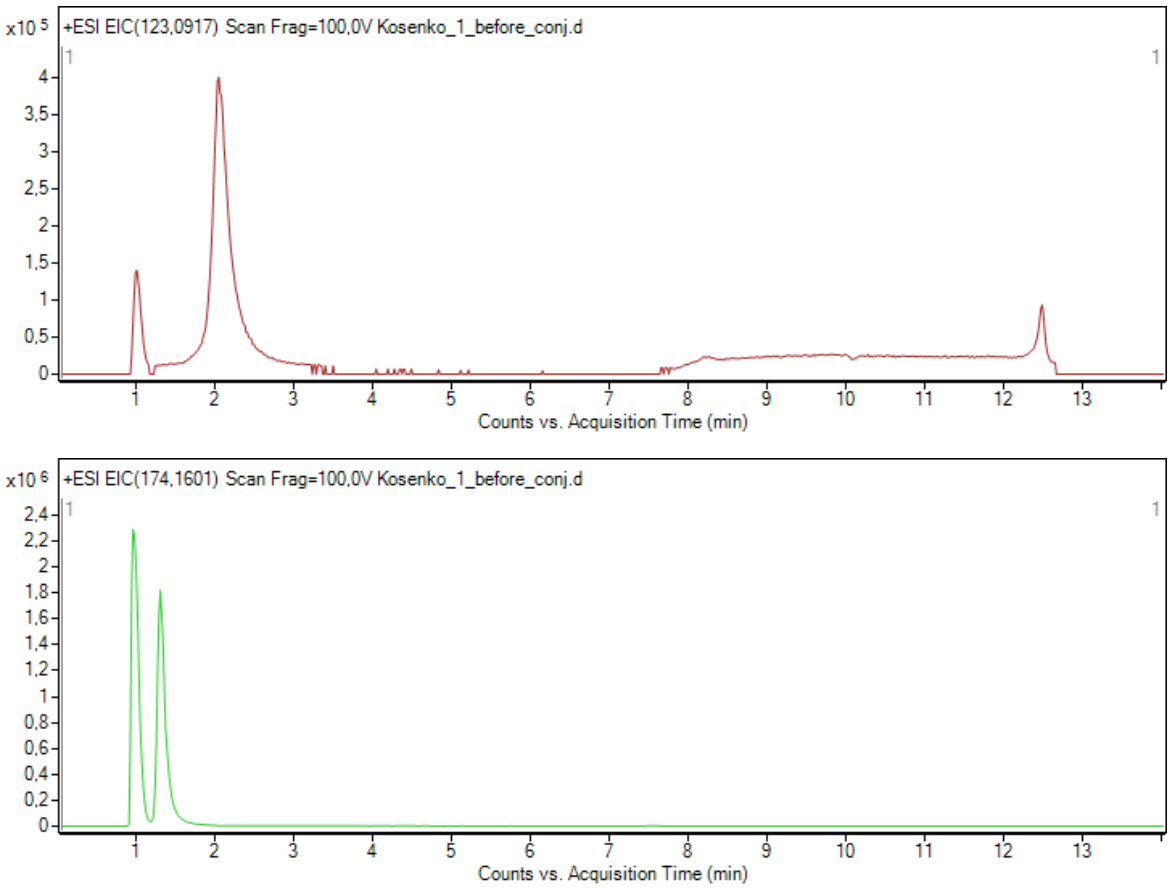


**Figure 154**: Extracted ion chromatograms (EIC) from HPLC-MS analysis of β-Ala-Boc-hydrazide-linked PPz-PGA (1 mg/mL in methanol, filtered through a 0.2 µm PTFE filter)

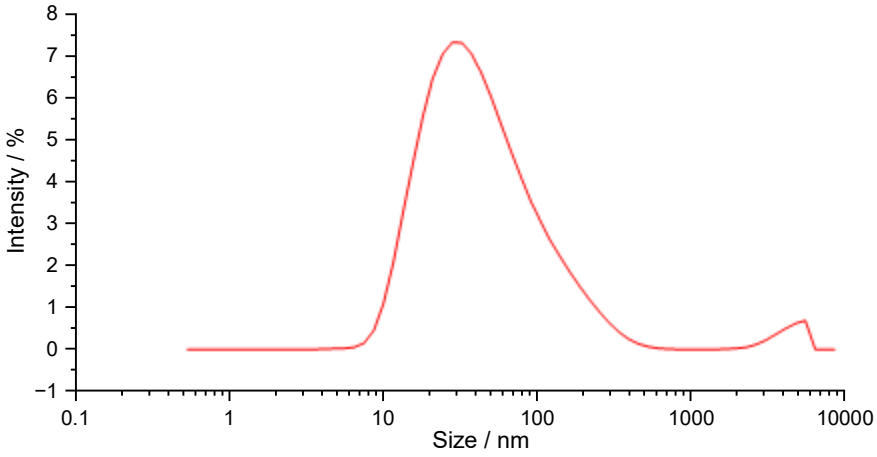


**Figure 155**: Size distribution (d.nm, by intensity) of β-Ala-Boc-hydrazide-linked PPz-PGA determined by DLS measurements; 1xPBS

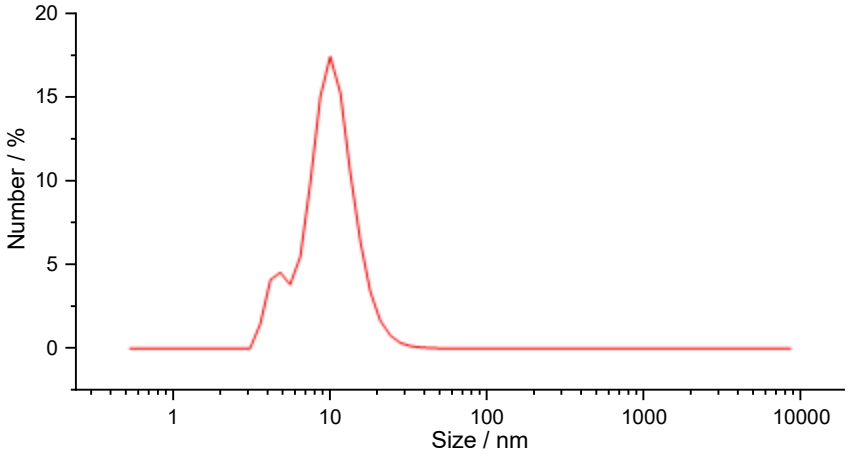


**Figure 156**: Size distribution (d.nm, by number) of β-Ala-Boc-hydrazide-linked PPz-PGA determined by DLS measurements; 1xPBS

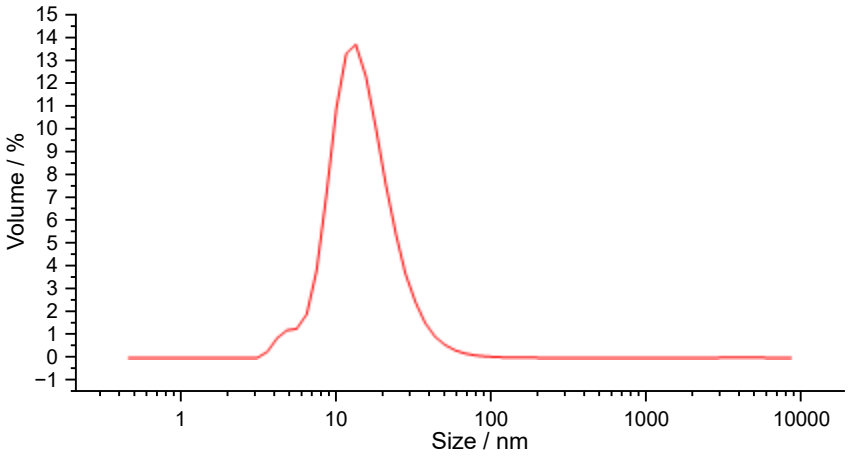


**Figure 157**: Size distribution (d.nm, by volume) of β-Ala-Boc-hydrazide-linked PPz-PGA determined by DLS measurements; 1xPBS

**Figure 158**: Appearance of β-Ala-Boc-hydrazide linked PPz-PGA

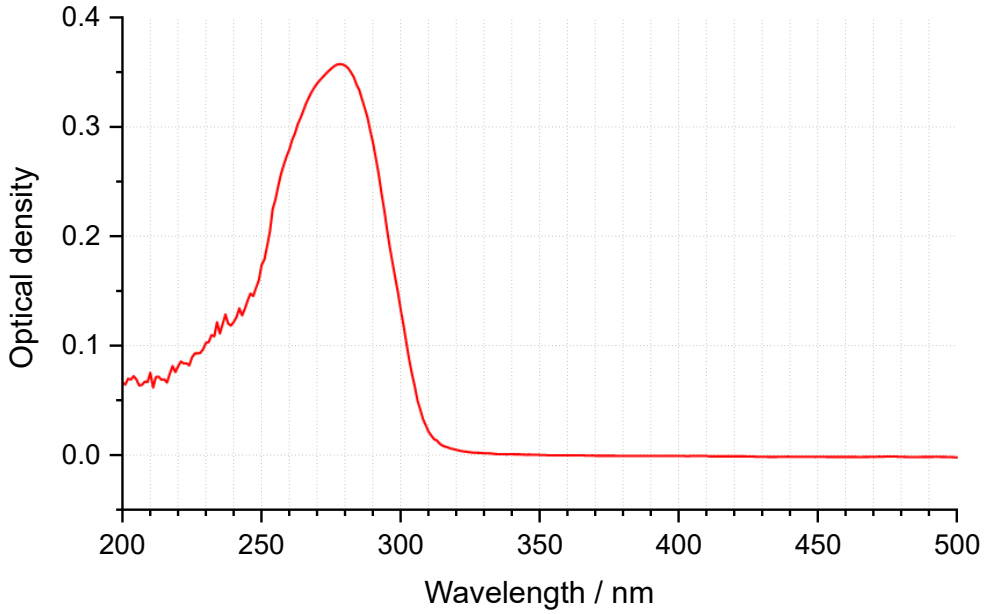


**Figure 159**: UV-Vis spectrum of β-Ala-Boc-hydrazide-linked PPz-PGA; 0.175 mg/mL, 1.5:2.5 DMSO:1xPBS

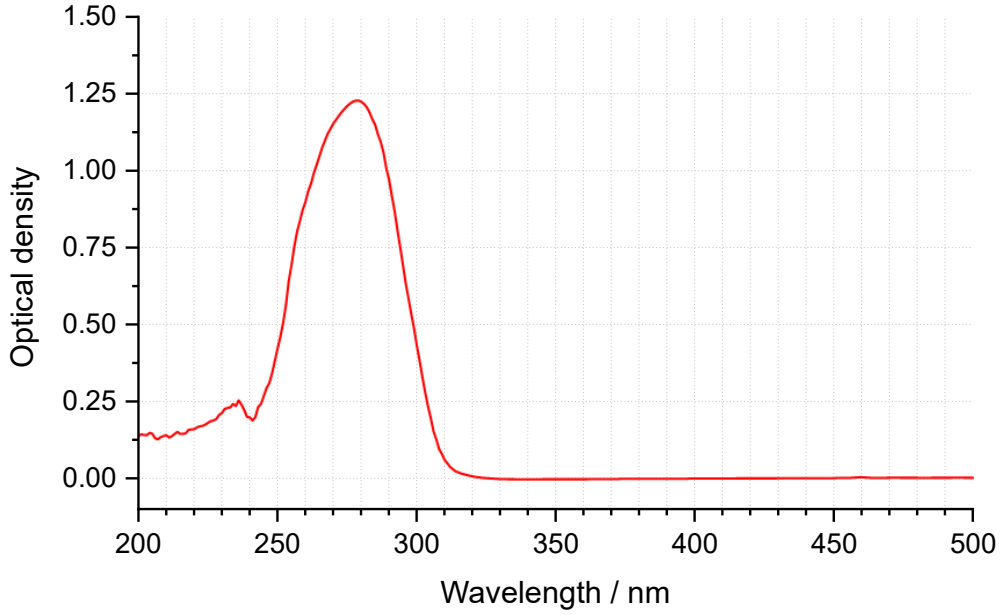


**Figure 160**: UV-Vis spectrum of β-Ala-Boc-hydrazide-linked PPz-PGA; 0.011 mg/mL, 1.5:2.5 DMSO:1xPBS

## Conjugation with SA-401

### Characterization of Boc-deprotected of β-Ala-Boc-hydrazide linked PPz-PGA

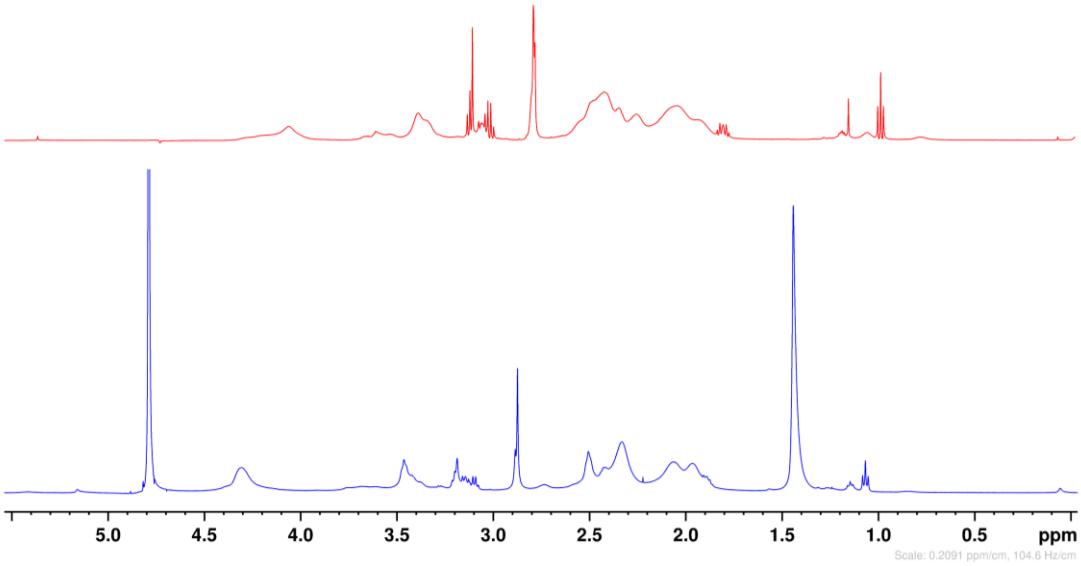


**Figure 161**: $^{1}H$ NMR of beta-Ala-linked PGA-PPz before deprotection (blue, PROTON, $D_2O$) and after (red, ZGESGP, 10% $D_2O$ +$H_2O$); 500 MHz

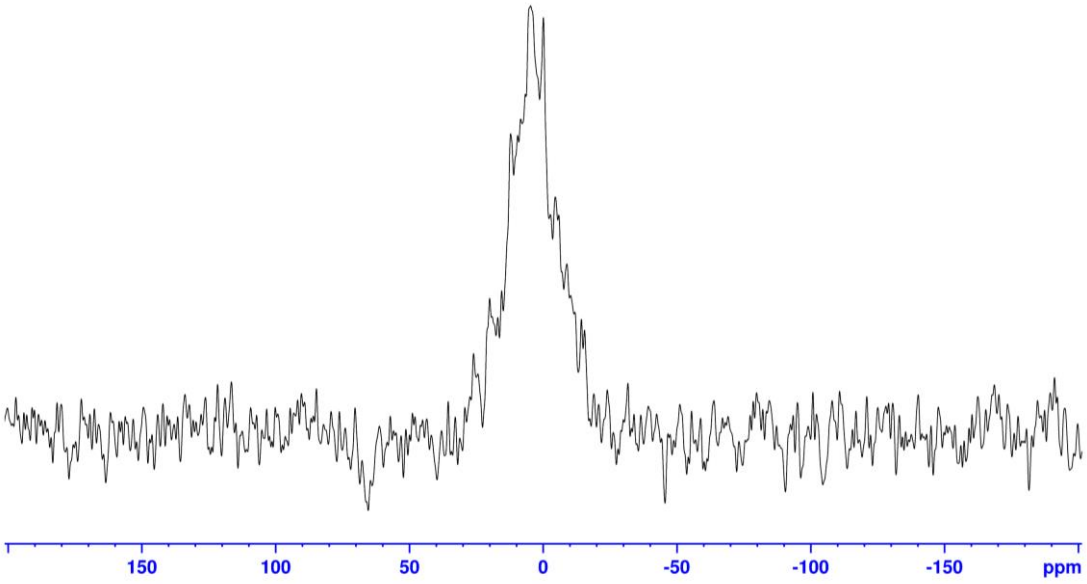


**Figure 162**: $^{31}P$ NMR of derotected beta-Ala-linked PGA-PPz;P31IG, 500 MHz, 10% $D_2O$ +$H_2O$

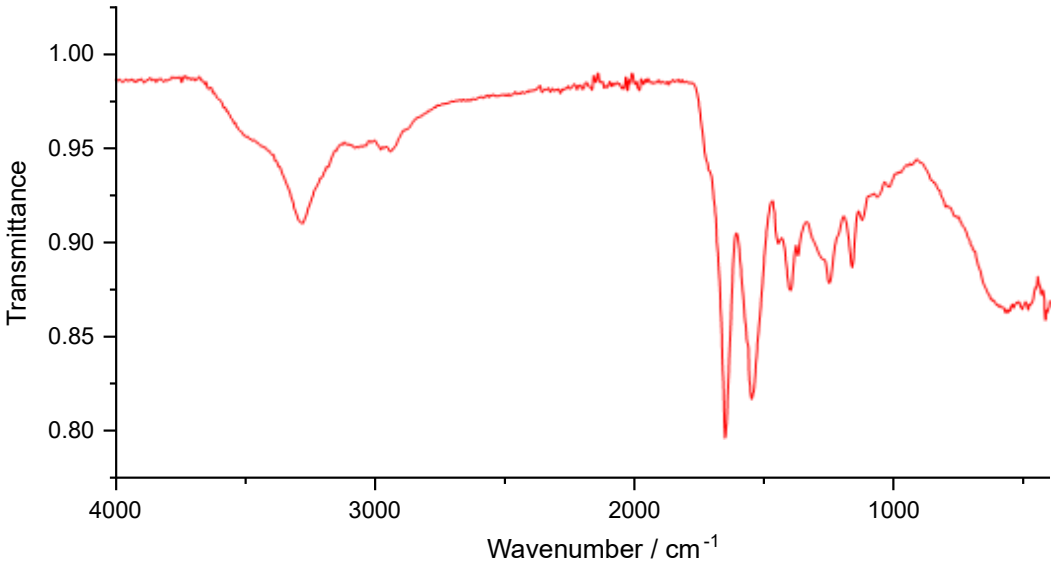


**Figure 163**: IR spectrum of beta-Ala-linked PGA-PPz before deprotection; Bruker Alpha II FT-IR spectrometer

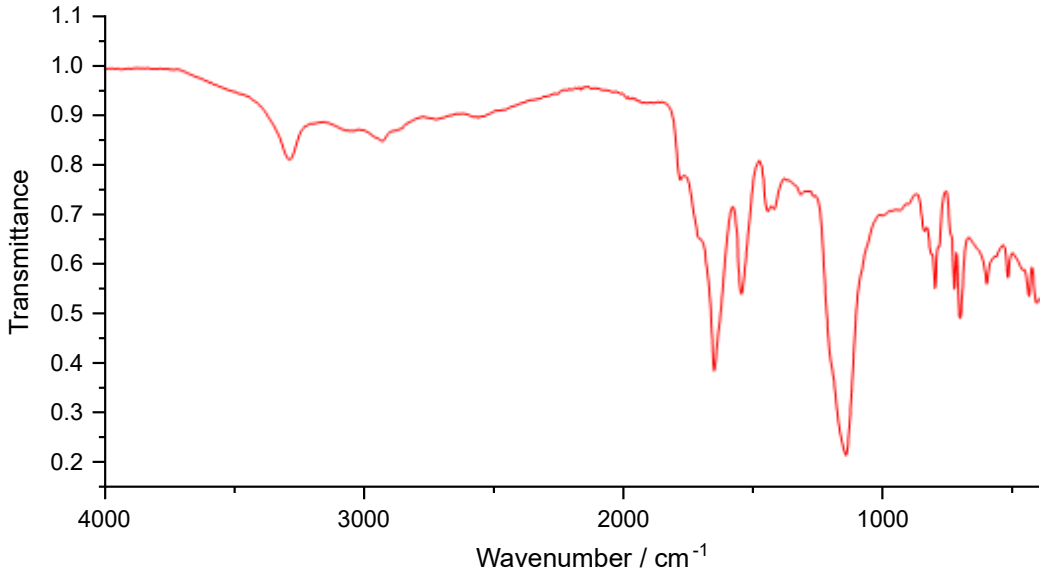


**Figure 164:** IR spectrum of beta-Ala-linked PGA-PPz before deprotection; Bruker Alpha II FT-IR spectrometer

**Characterization of SA-401-conjugated β-Ala-hydrazide-linked PPz-PGA**

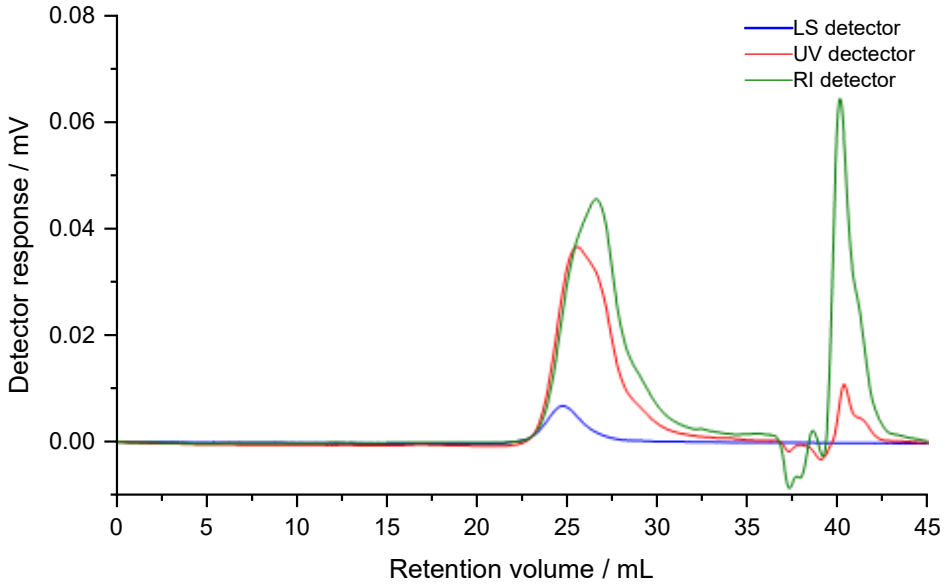


**Figure 165**: GPC chromatogram of SA-401-conjugated β-Ala-hydrazide-linked PPz-PGA; aqueous, light scattering (LS), refractive index (RI), and UV detection

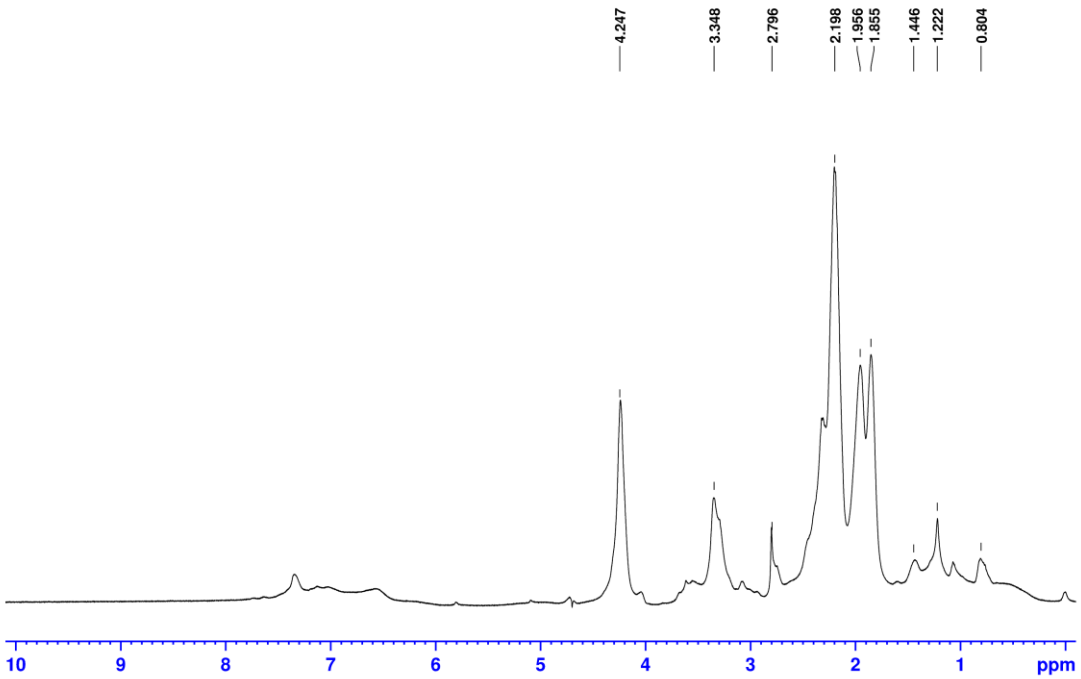


**Figure 166**: $^{1}H$ NMR of SA-401-conjugated β-Ala-hydrazide-linked PPz-PGA; ZGPR, 500 MHz, $D_2O$

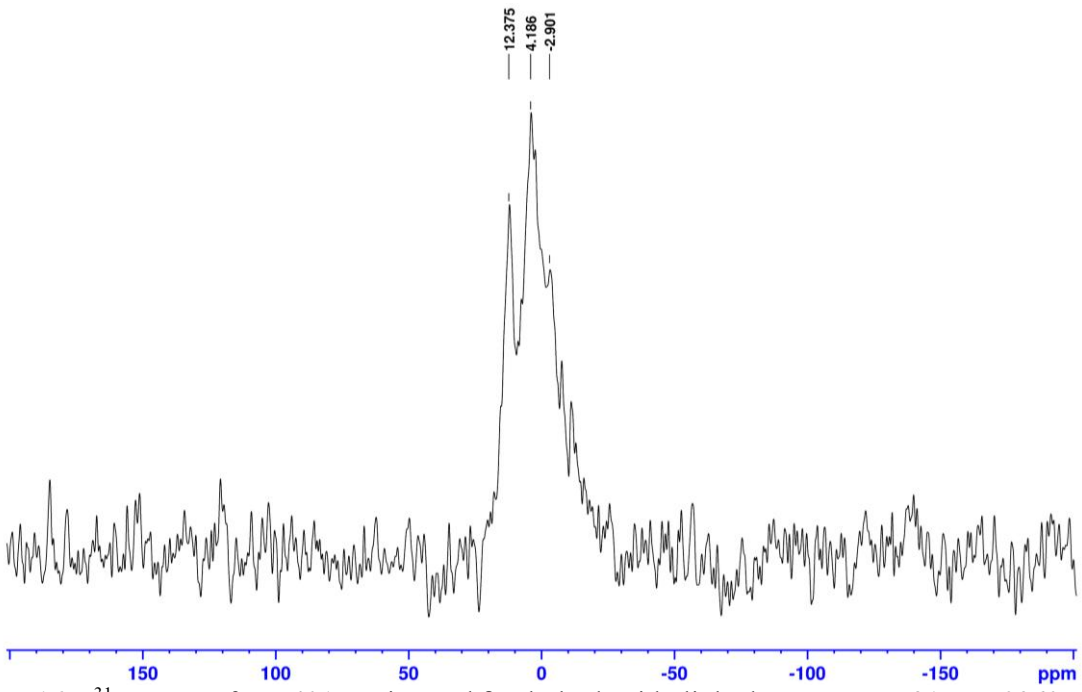


**Figure 167**: $^{31}P$ NMR of SA-401-conjugated β-Ala-hydrazide-linked PPz-PGA; P31IG, 50960 scans, 202 MHz, $D_2O$

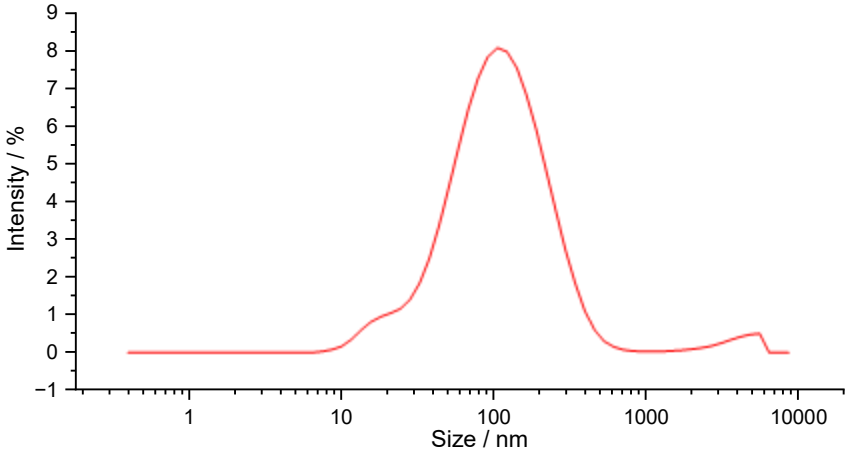


**Figure 168**: Size distribution (d.nm, by intensity) of SA-401-conjugated β-Ala-hydrazide-linked PPz-PGA determined by DLS measurements; 1xPBS

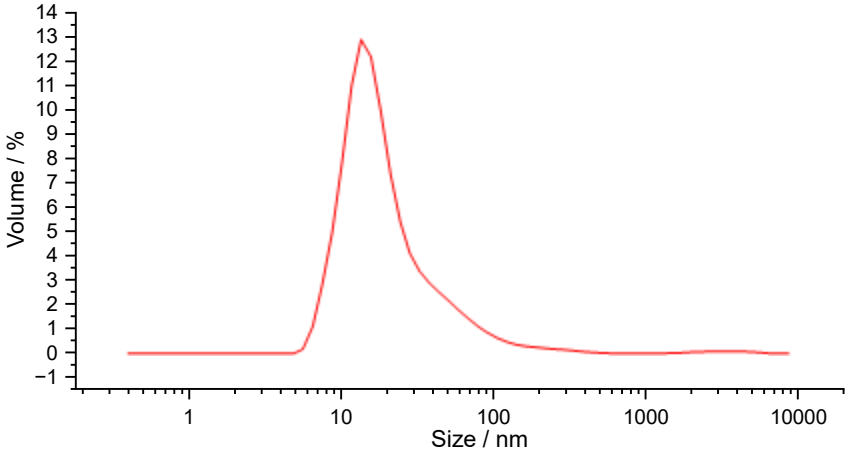


**Figure 169**: Size distribution (d.nm, by volume) of SA-401-conjugated β-Ala-hydrazide-linked PPz-PGA determined by DLS measurements; 1xPBS

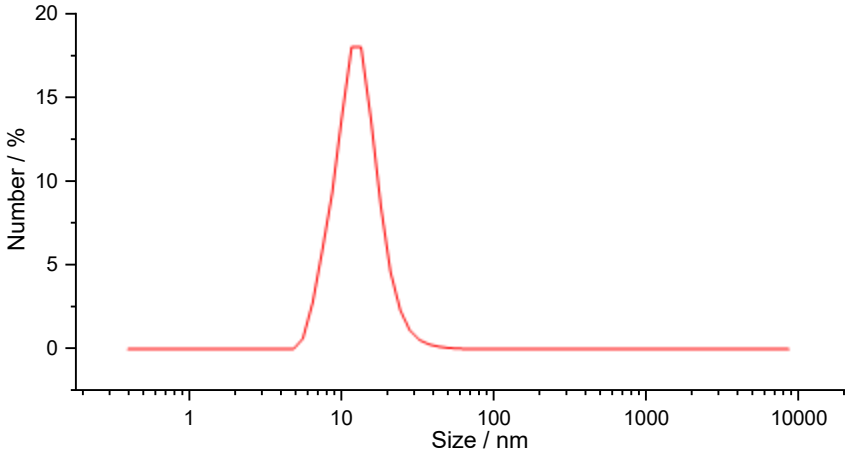


**Figure 170**: Size distribution (d.nm, by number) of SA-401-conjugated β-Ala-hydrazide-linked PPz-PGA determined by DLS measurements; 1xPBS

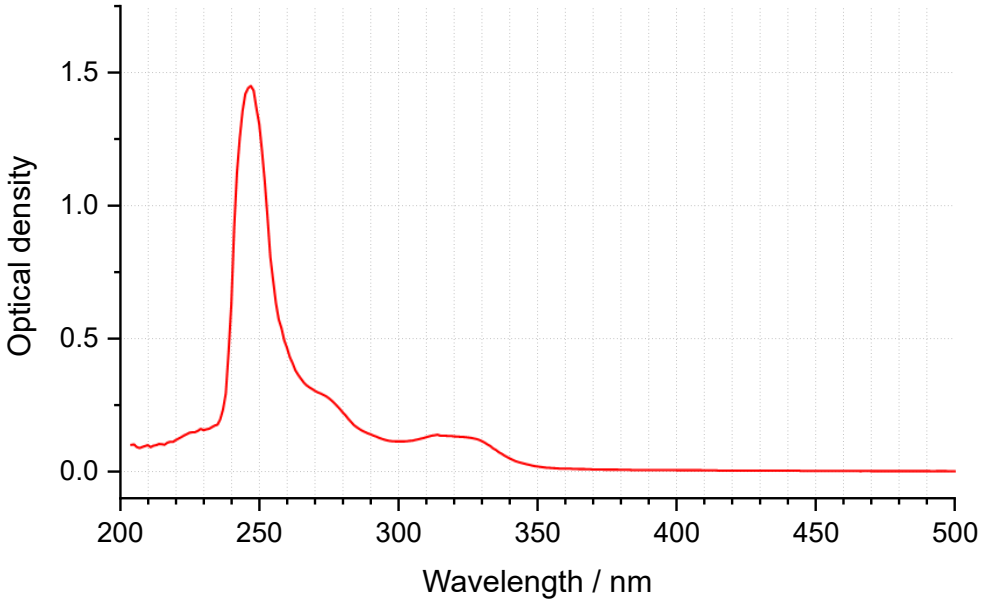


**Figure 171**: UV-Vis spectrum of SA-401-conjugated β-Ala-hydrazide-linked PPz-PGA; 0.175 mg/mL, 1.5:2.5 DMSO:1xPBS

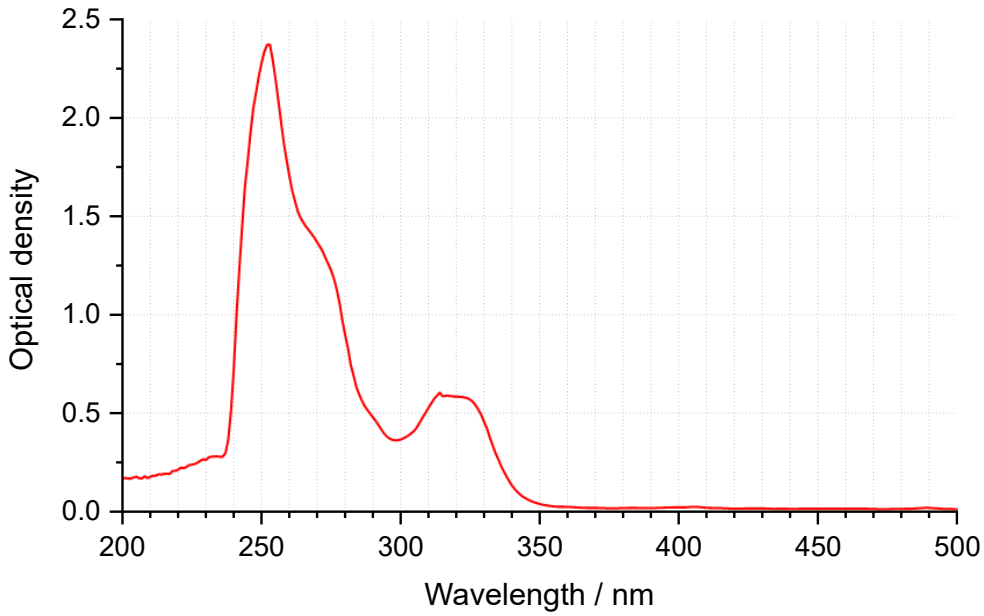


**Figure 172**: UV-Vis spectrum of SA-401; 0.075 mg/mL, 1.5:2.5 DMSO:1xPBS

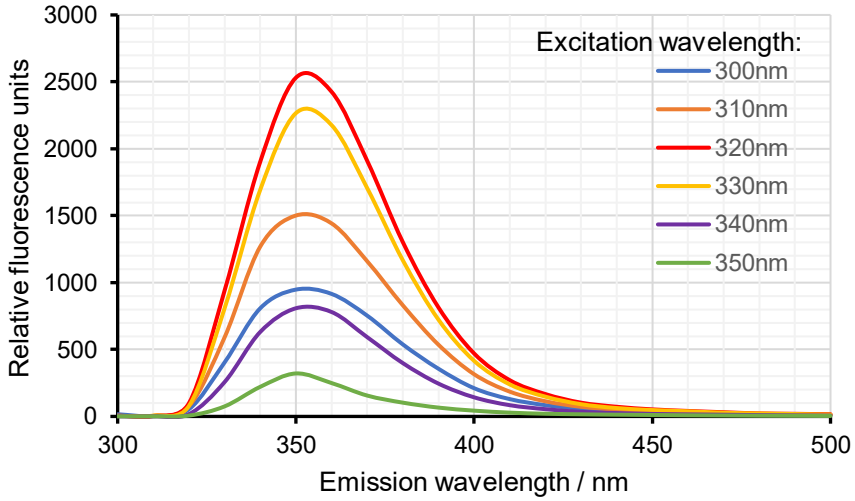


**Figure 173**: The sample (SA-401) was excited at 300, 310, 320, 330, 340 and 350 nm, and fluorescence intensity was measured as a function of emission wavelength.

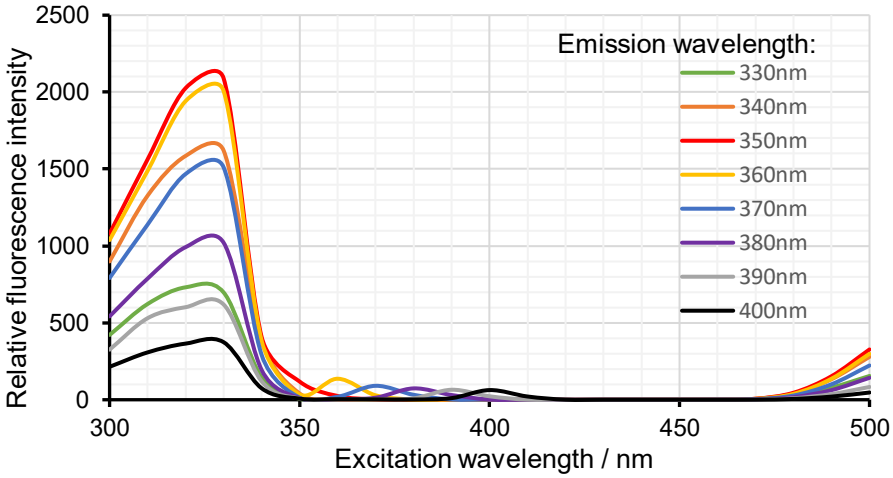


**Figure 174**: Fluorescence emission of SA-401 was monitored at 330, 340, 350, 360, 370, 380, 390, and 400 nm, and intensity was measured as a function of excitation wavelength.

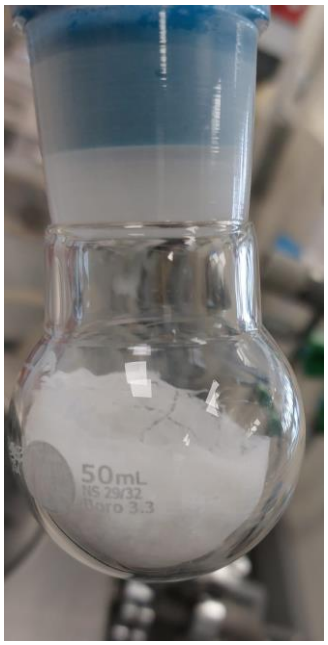


**Figure 175:** Physical appearance of SA-401-conjugated β-Ala-hydrazide-linked PPz-PGA

## Microscopy imaging of bone marrow-derived macrophages (BMMs)

### Day 0

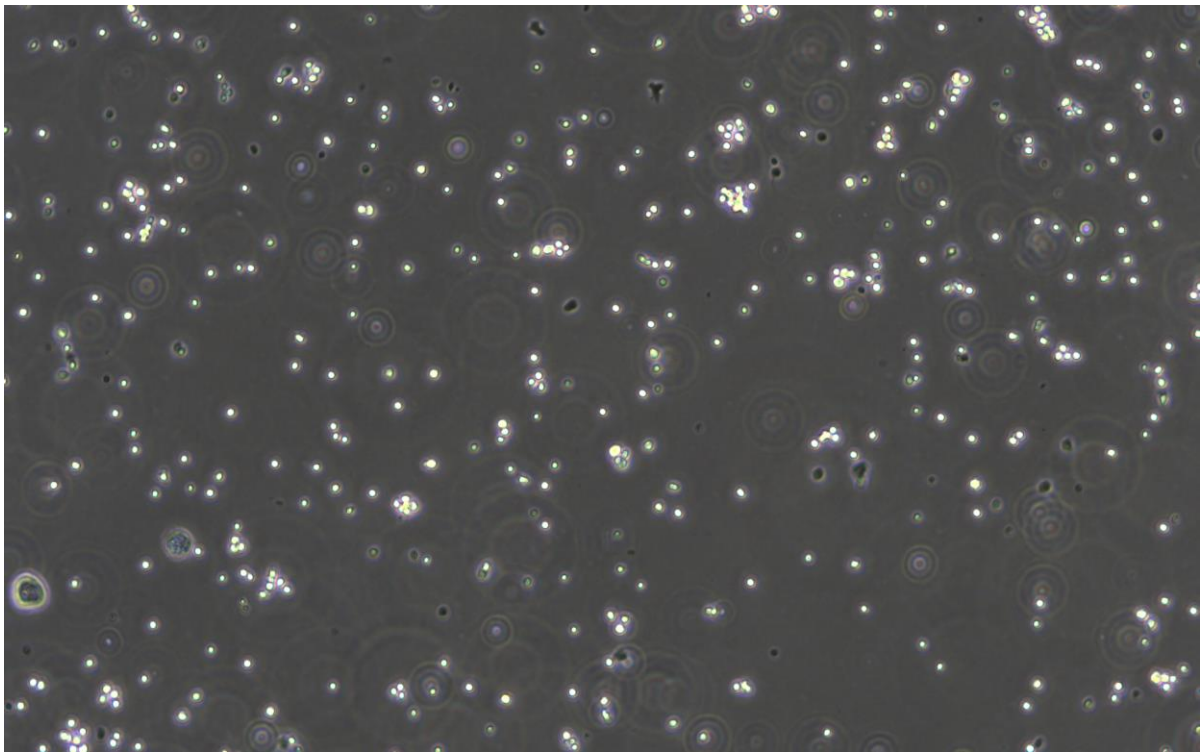

**Figure 176**: Cells observed under microscope following bone marrow isolation and seeding for differentiation; imaged at 100x magnification

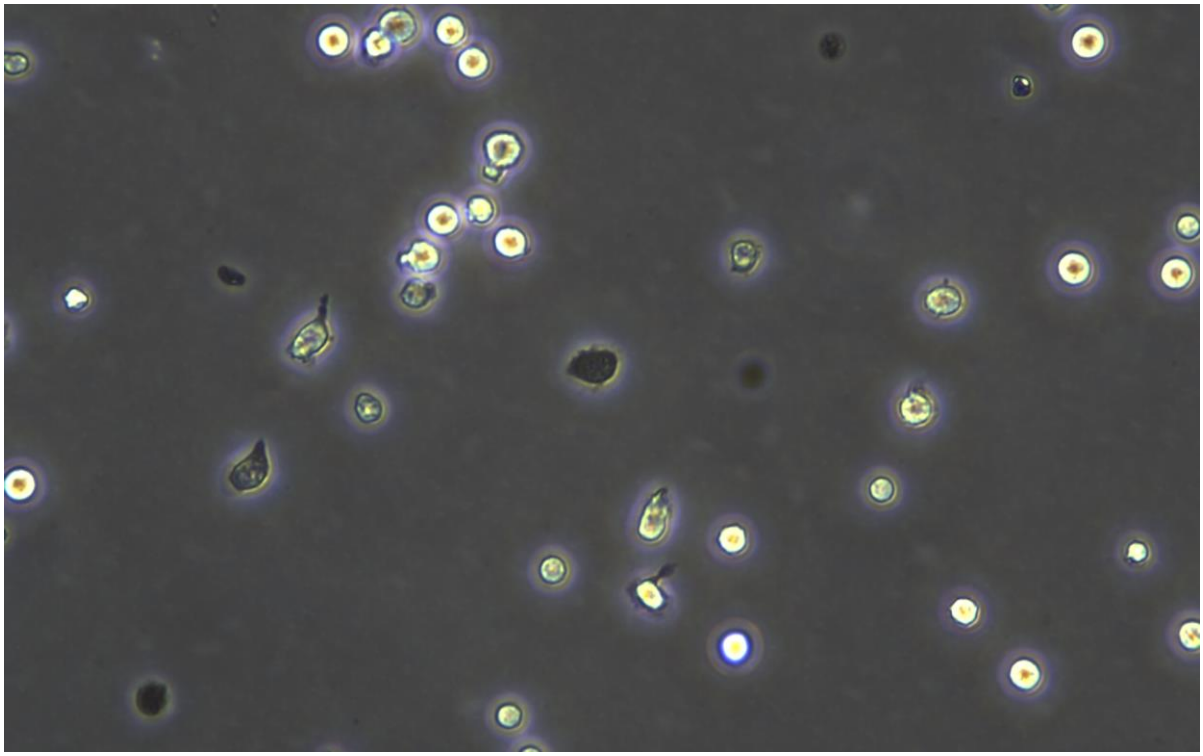

**Figure 177**: Cells observed under microscope following bone marrow isolation and seeding for differentiation; imaged at 400x magnification

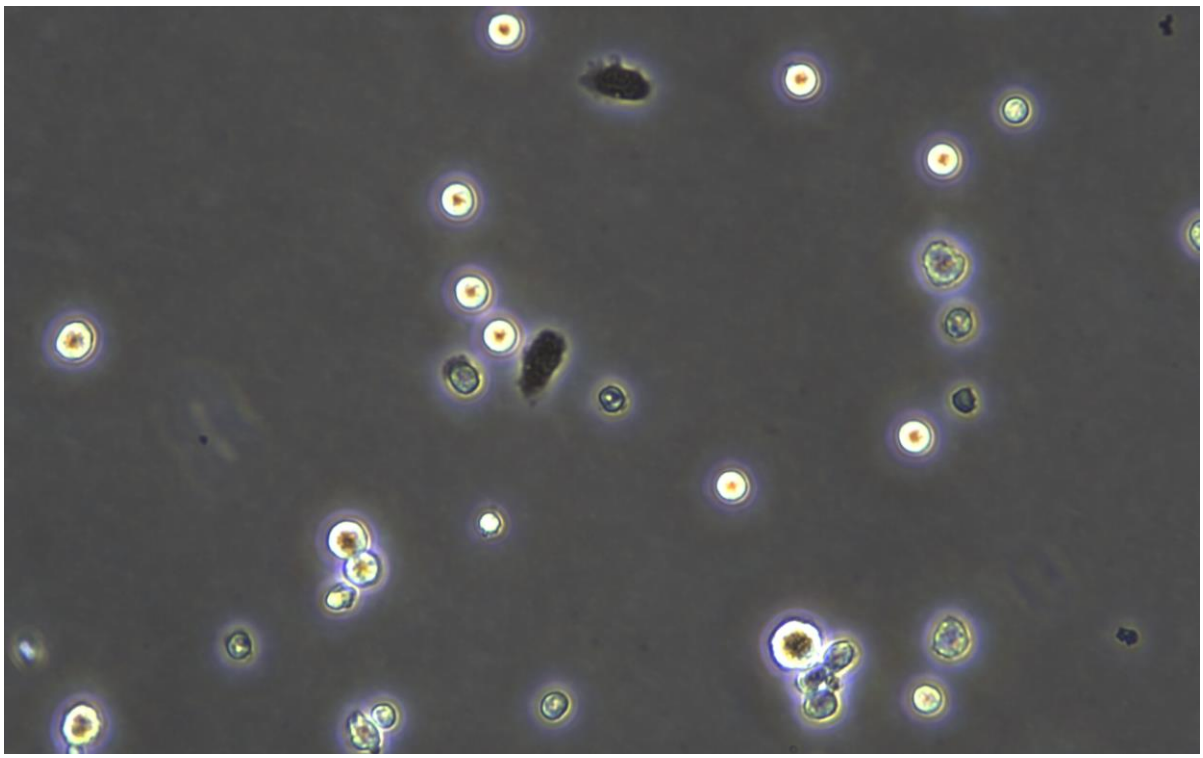

**Figure 178**: Cells observed under microscope following bone marrow isolation and seeding for differentiation; imaged at 400x magnification

**Day 3**

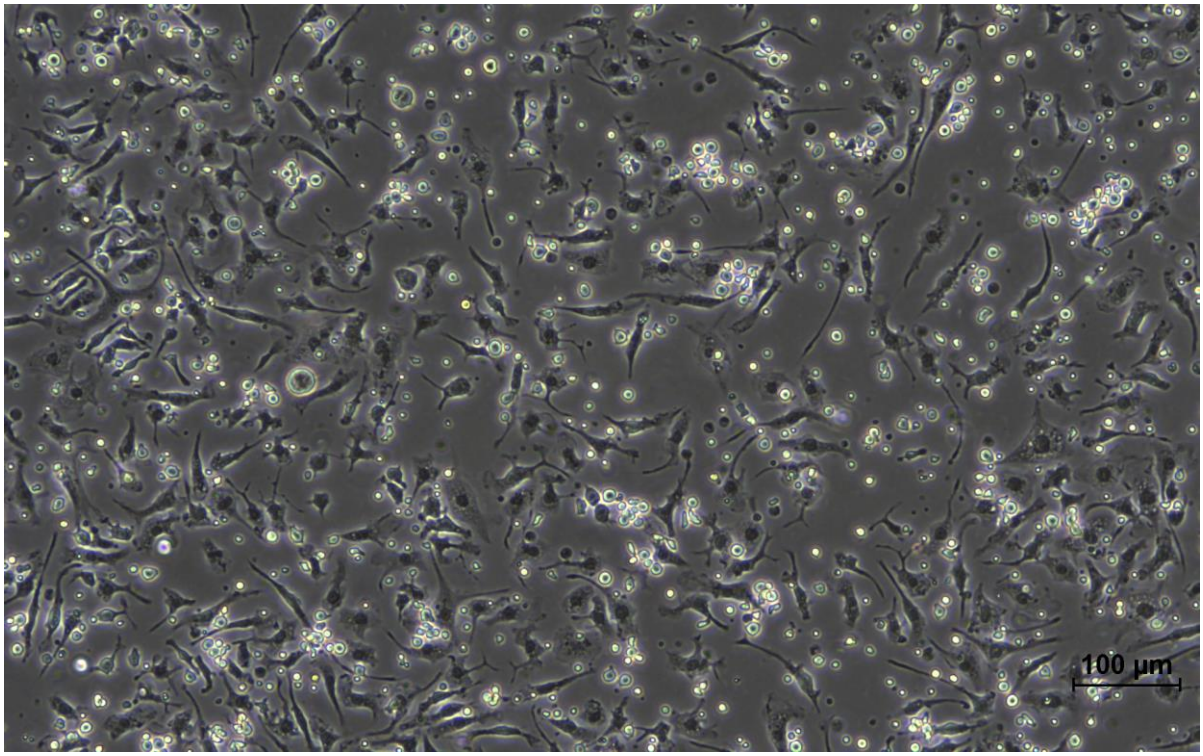


**Figure 179**: Cells observed under microscope on the 3rd day of differentiation; imaged at 100x magnification

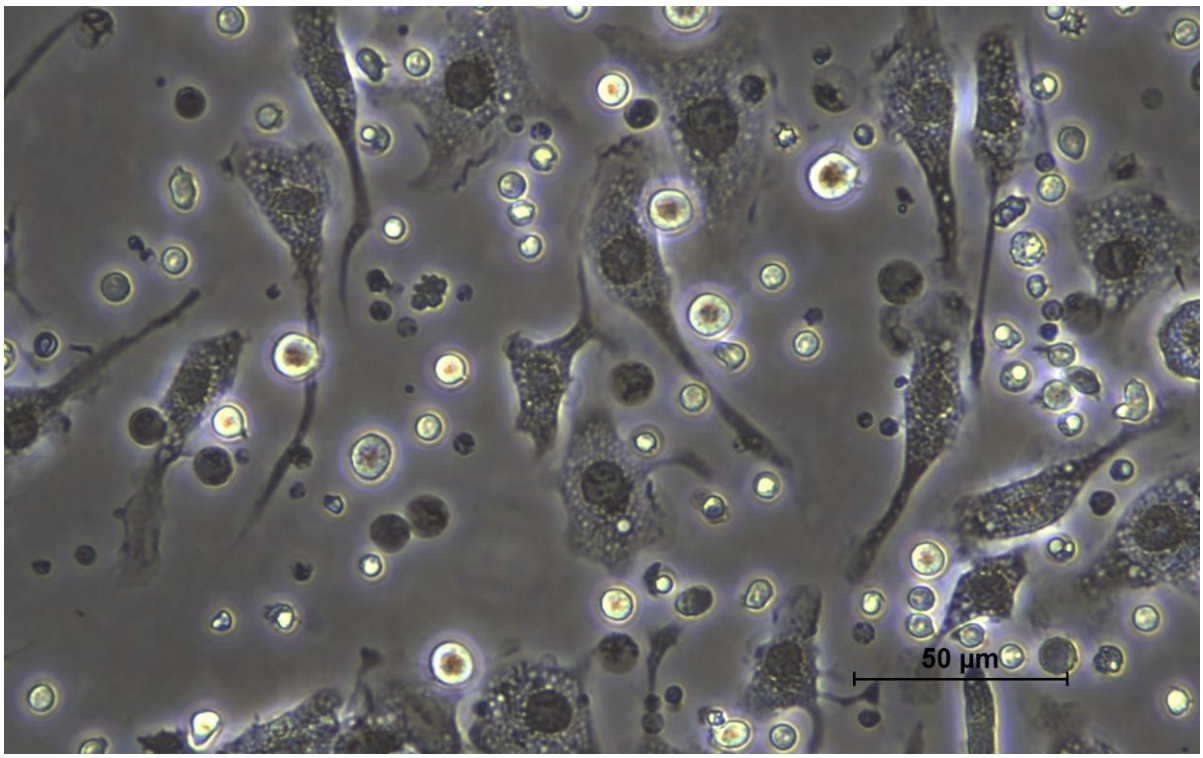


**Figure 180**: Cells observed under microscope on the 3rd day of differentiation; imaged at 400x magnification

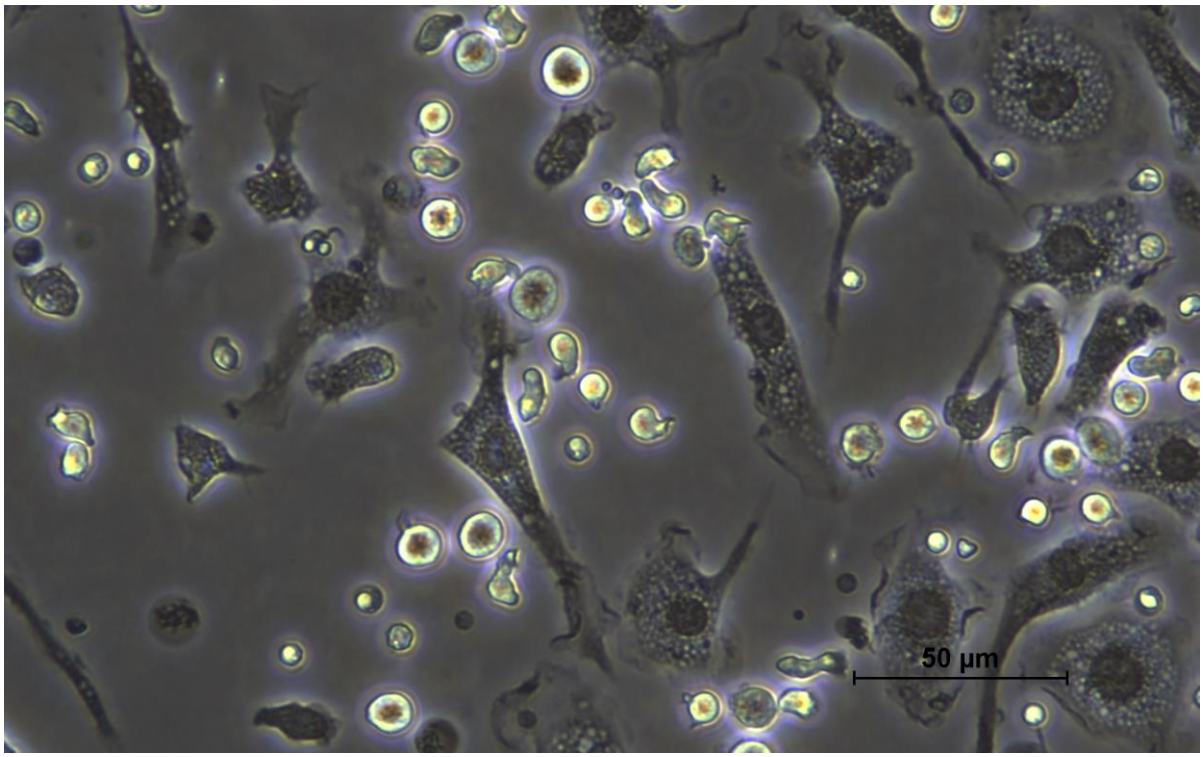


**Figure 181**: Cells observed under microscope on the 3rd day of differentiation; imaged at 400x magnification

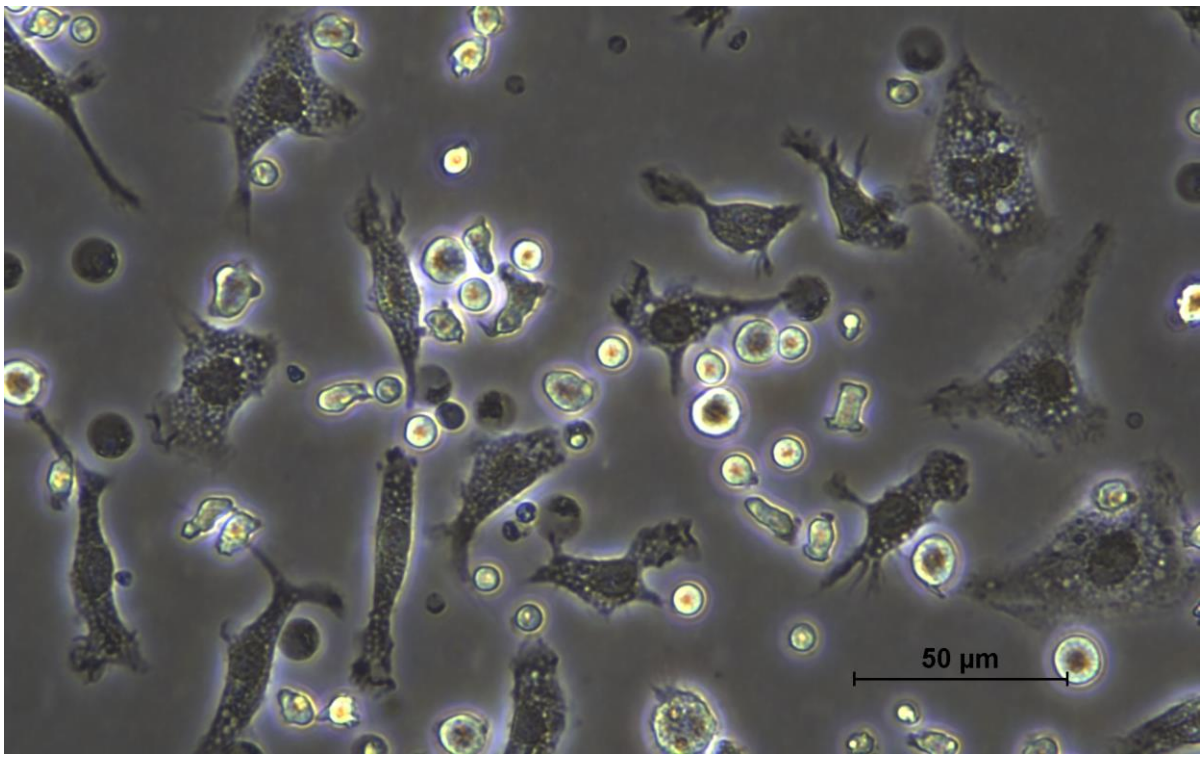


**Figure 182**: Cells observed under microscope on the 3rd day of differentiation; imaged at 400x magnification

**Day 7**

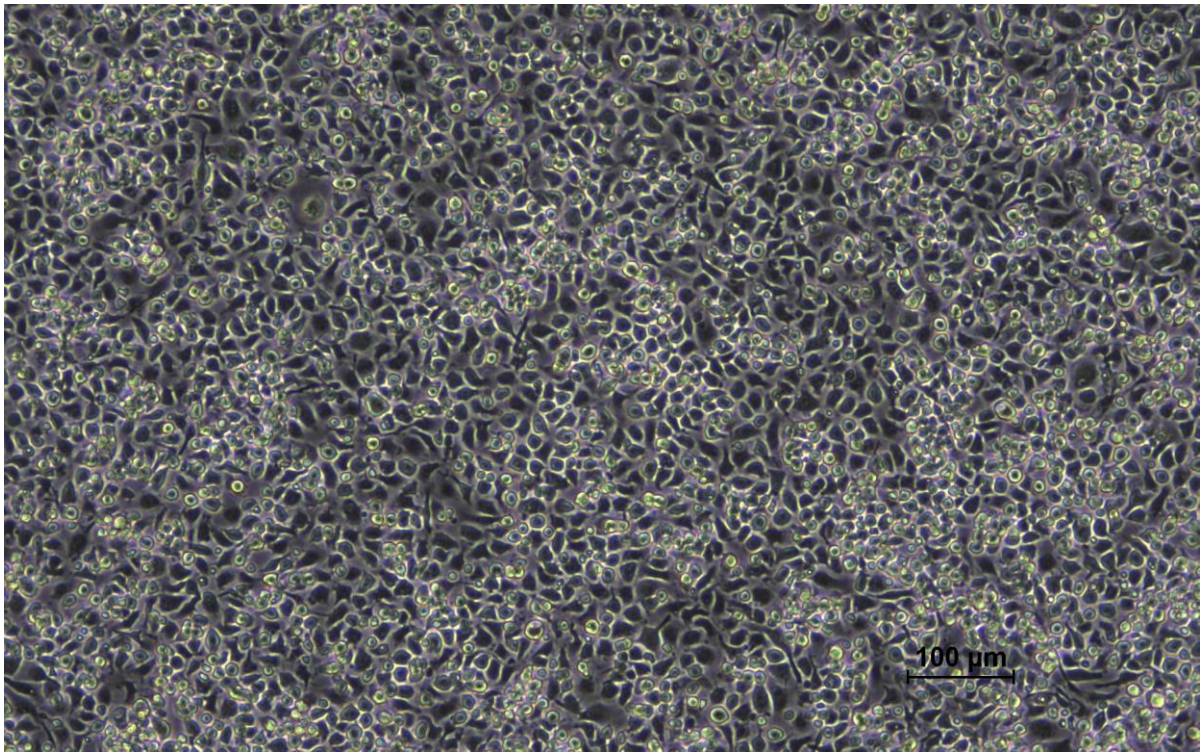


**Figure 183**: Cells observed under microscope on the 7th day of differentiation; imaged at 100x magnification

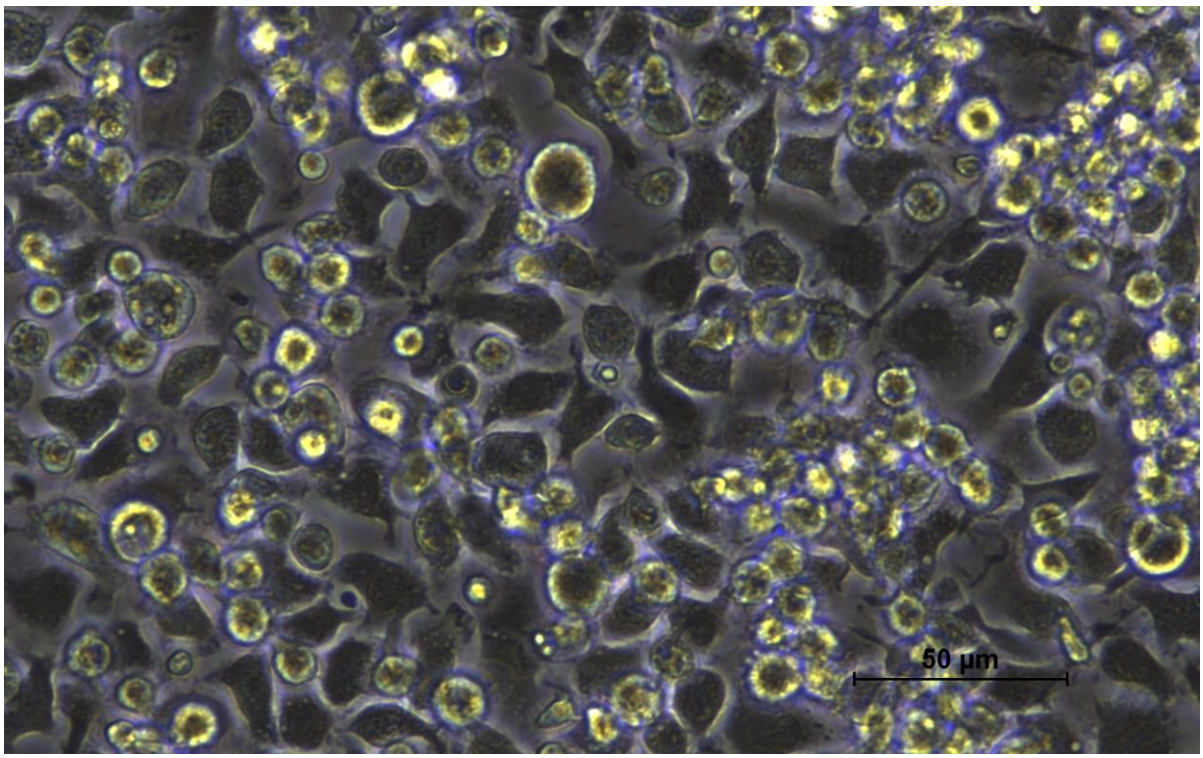


**Figure 184**: Cells observed under microscope on the 7th day of differentiation; imaged at 400x magnification

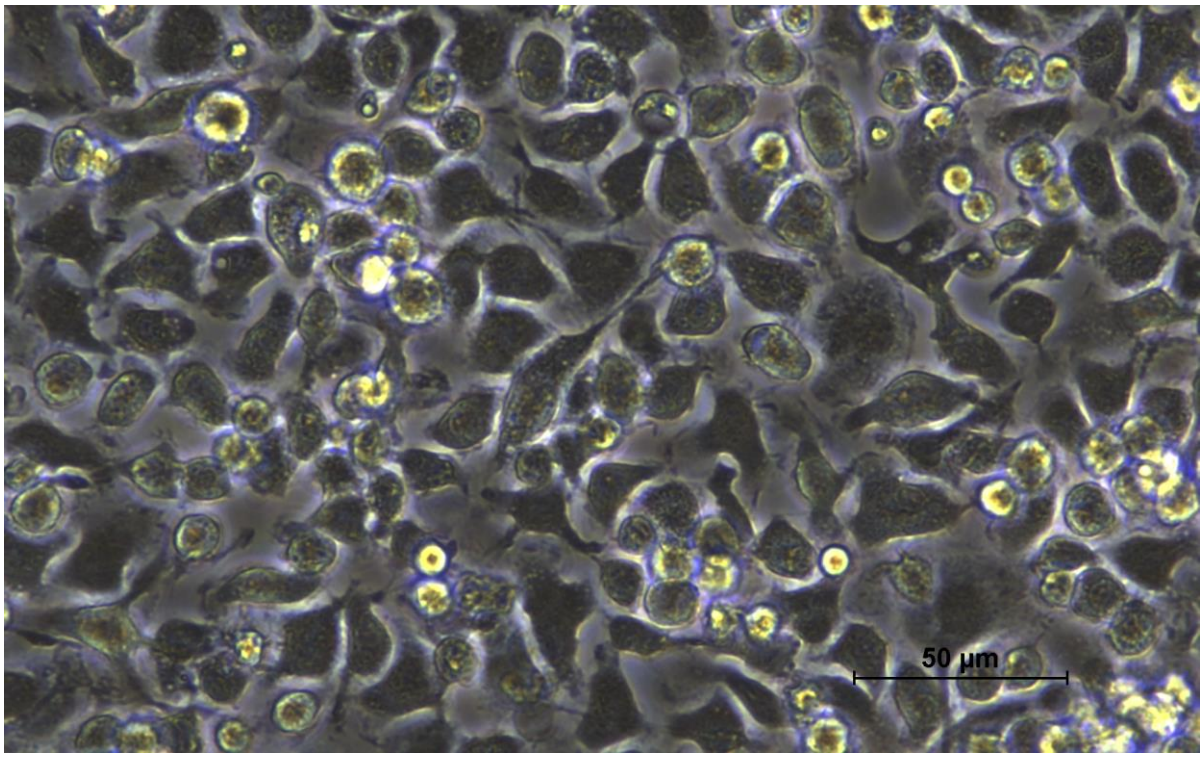


**Figure 185**: Cells observed under microscope on the 7th day of differentiation; imaged at 400x magnification

**Day 8**

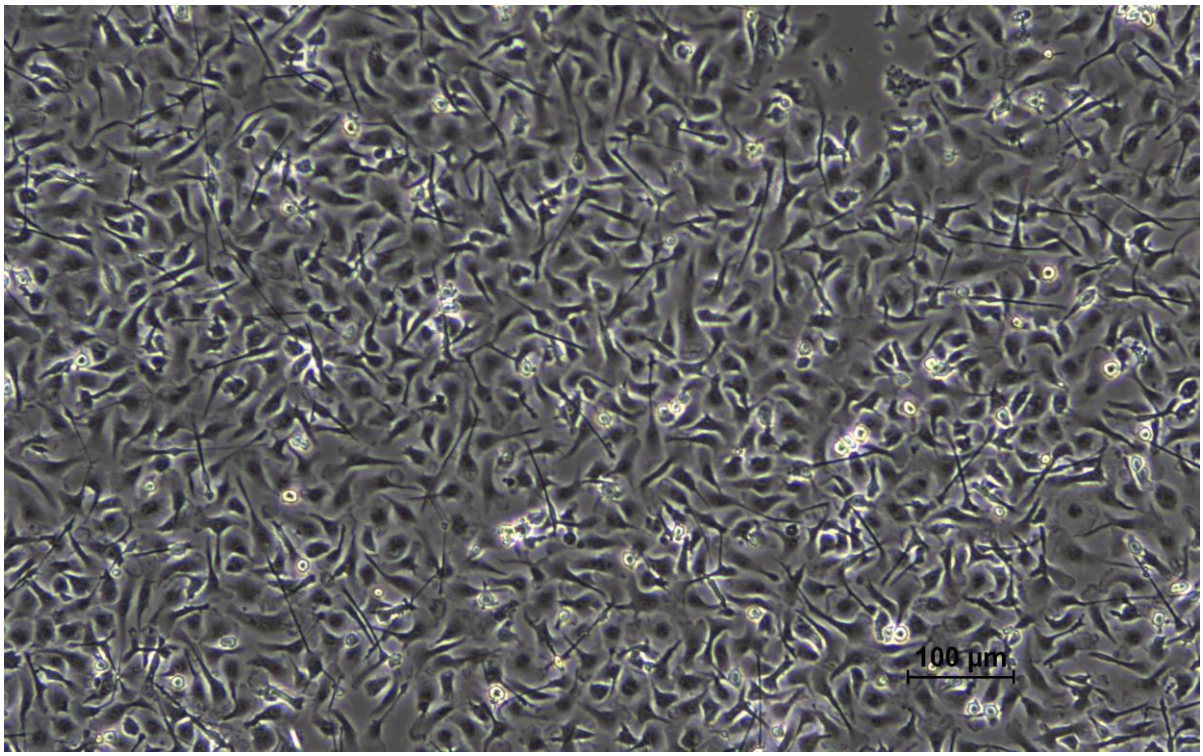


**Figure 186**: Cells observed under microscope on the 8th day of differentiation seeded with 10% FBS; imaged at 100x magnification

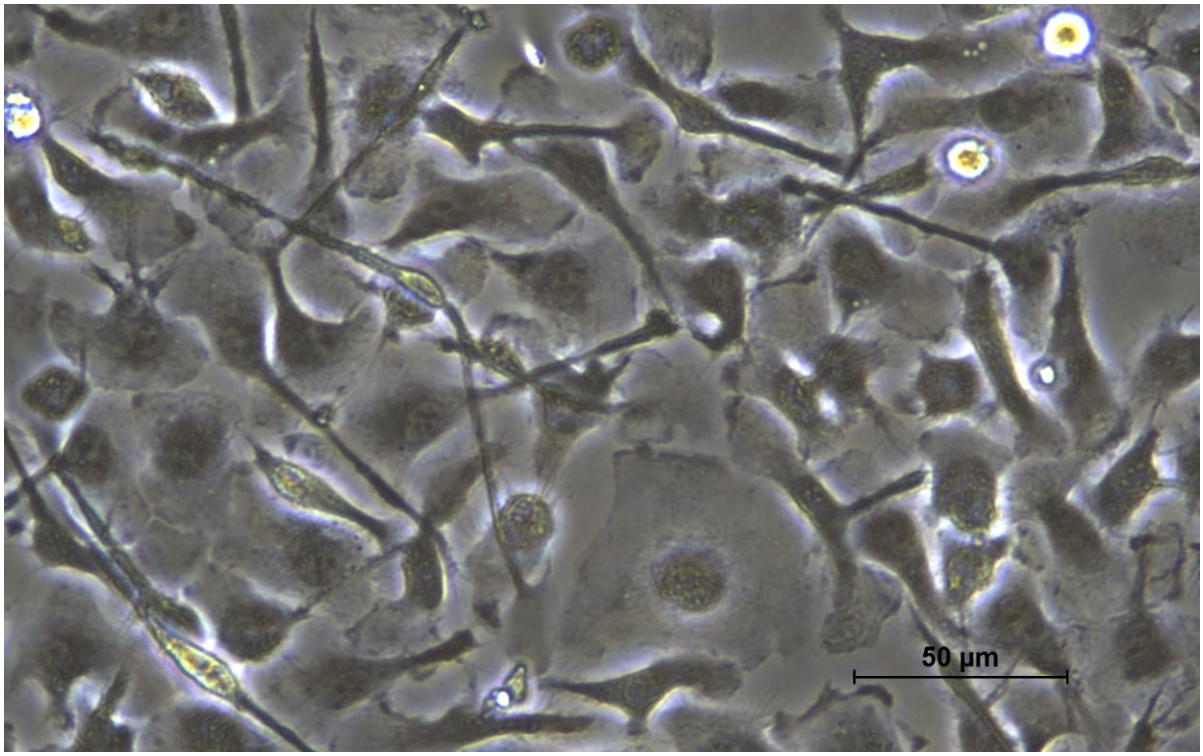


**Figure 187**: Cells observed under microscope on the 8th day of differentiation seeded with 10% FBS; imaged at 400x magnification

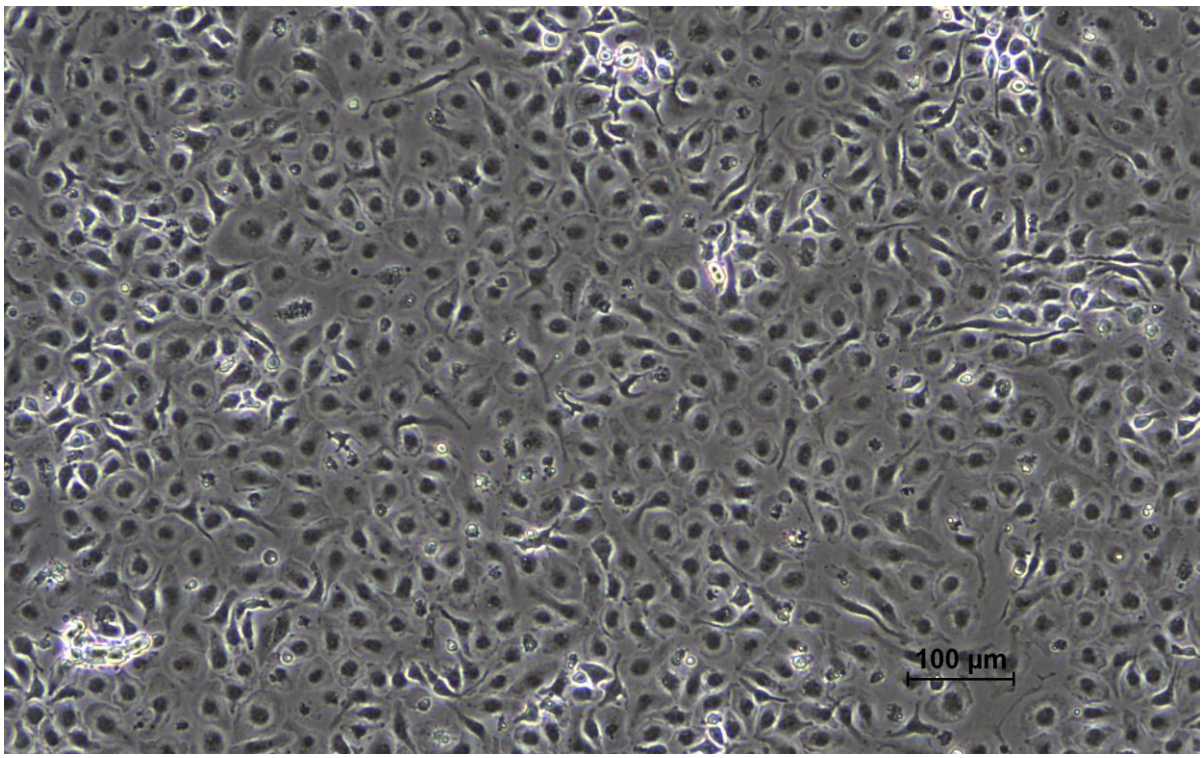


**Figure 188**: Cells observed under microscope on the 8th day of differentiation seeded without FBS; imaged at 100x magnification

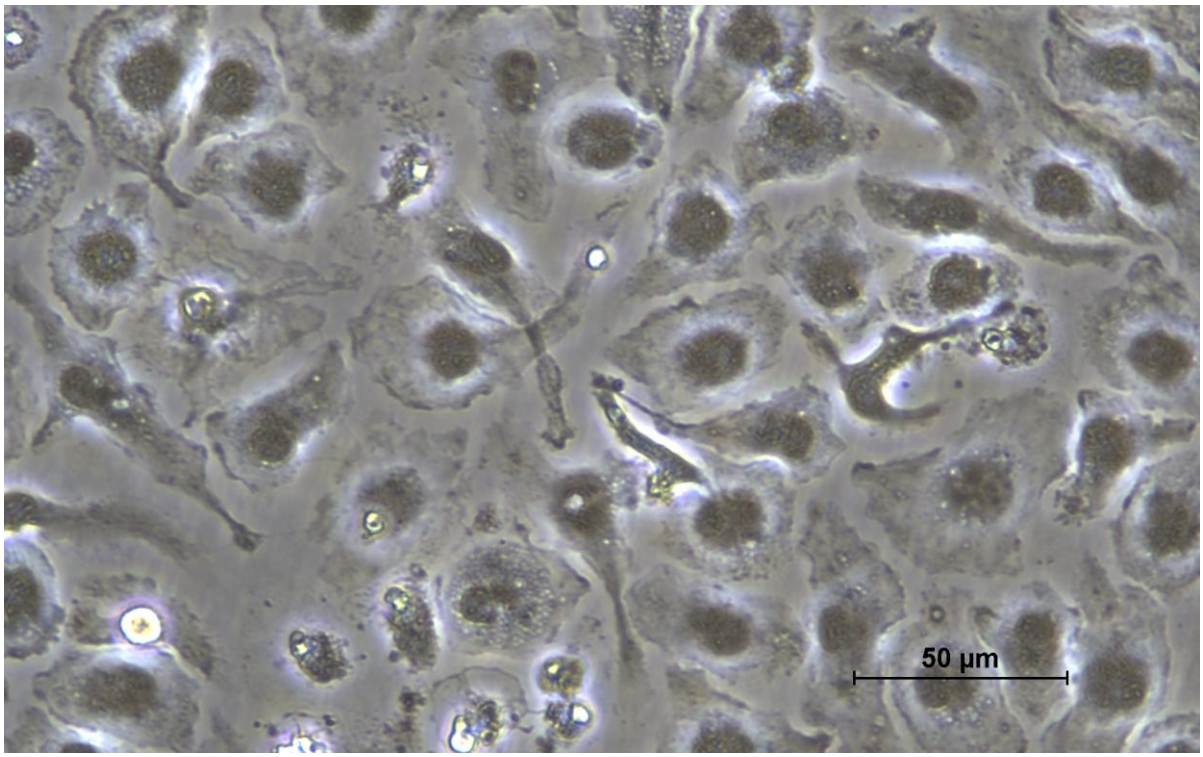


**Figure 189**: Cells observed under microscope on the 8th day of differentiation seeded without FBS; imaged at 400x magnification

**Day 9**

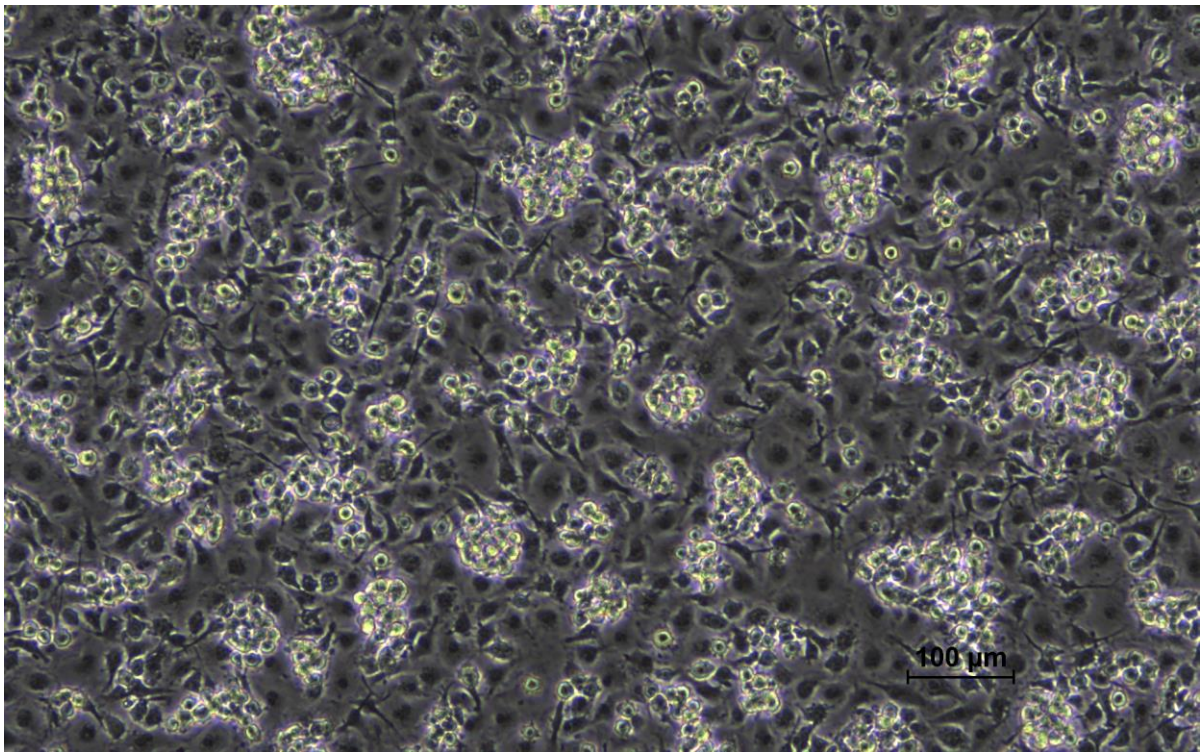


**Figure 190**: Cells observed under microscope on the 9th day of differentiation 24 hours post-activation with ligands; A1 culture dish (1.3 ug/mL SA-401, 10% FBS) imaged at 100x magnification

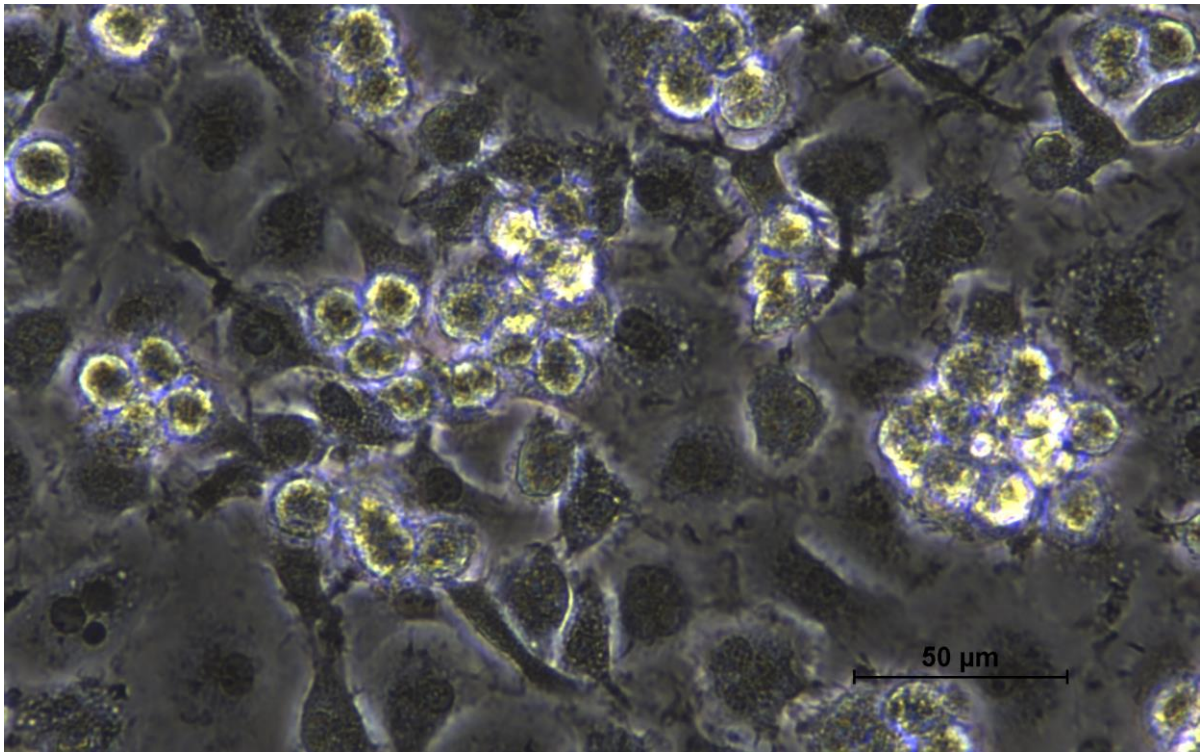


**Figure 191**: Cells observed under microscope on the 9th day of differentiation 24 hours post-activation with ligands; A1 culture dish (1.3 ug/mL SA-401, 10% FBS) imaged at 400x magnification

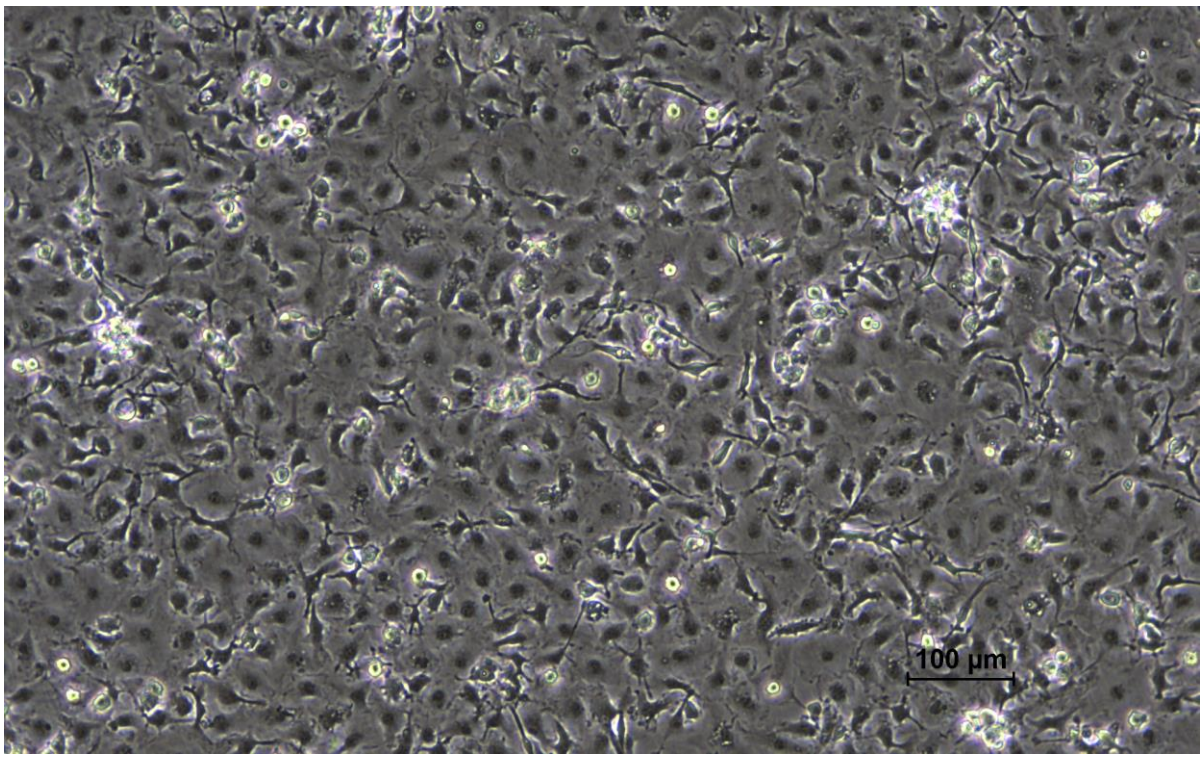


**Figure 192**: Cells observed under microscope on the 9th day of differentiation 24 hours post-activation with ligands; B5 culture dish (1.0 ug/mL R848, 10% FBS) imaged at 100x magnification

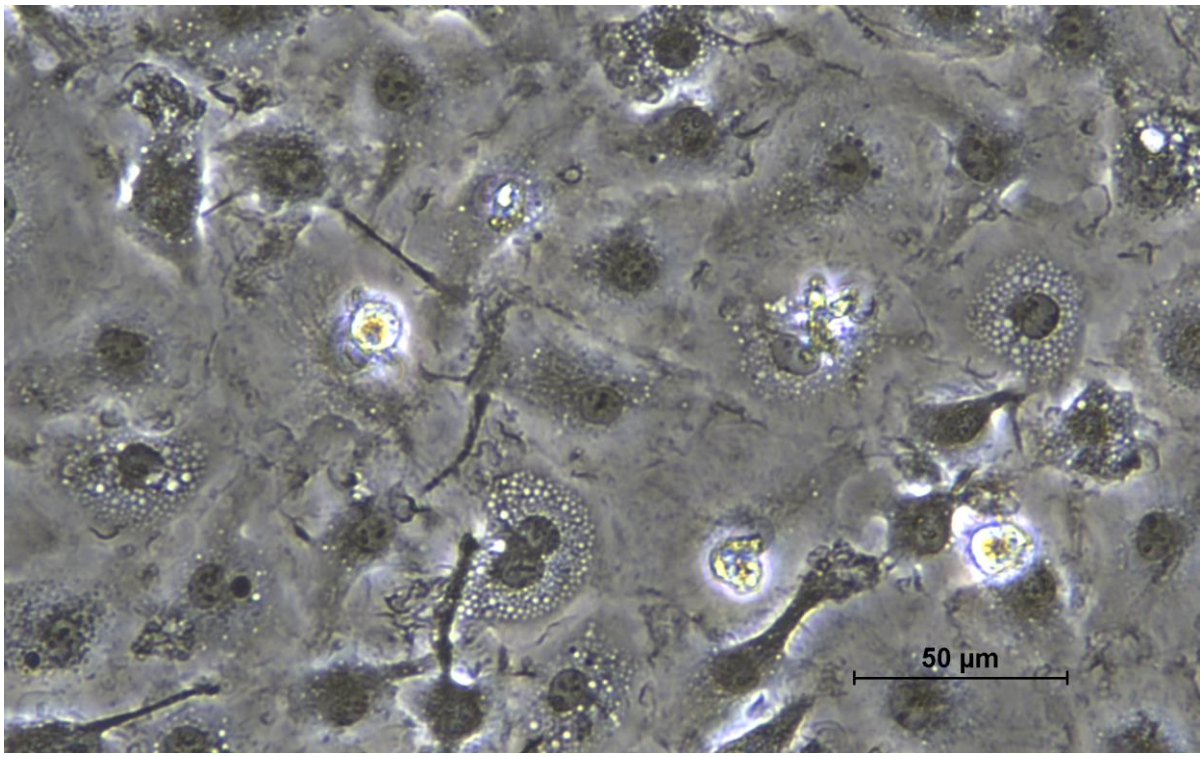


**Figure 193**: Cells observed under microscope on the 9th day of differentiation 24 hours post-activation with ligands; B5 culture dish (1.0 ug/mL R848, 10% FBS) imaged at 400x magnification

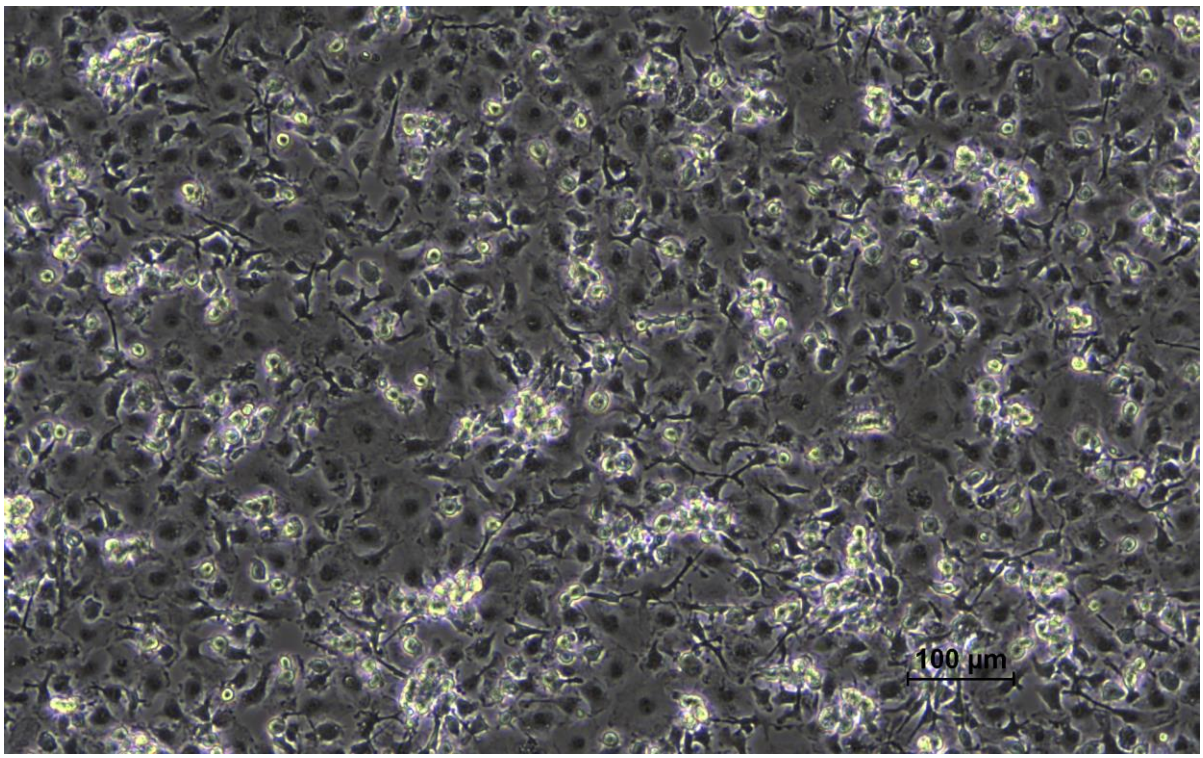


**Figure 194**: Cells observed under microscope on the 9th day of differentiation 24 hours post-activation with ligands; C5 culture dish (0.5 ug/mL LPS, 10% FBS) imaged at 100x magnification

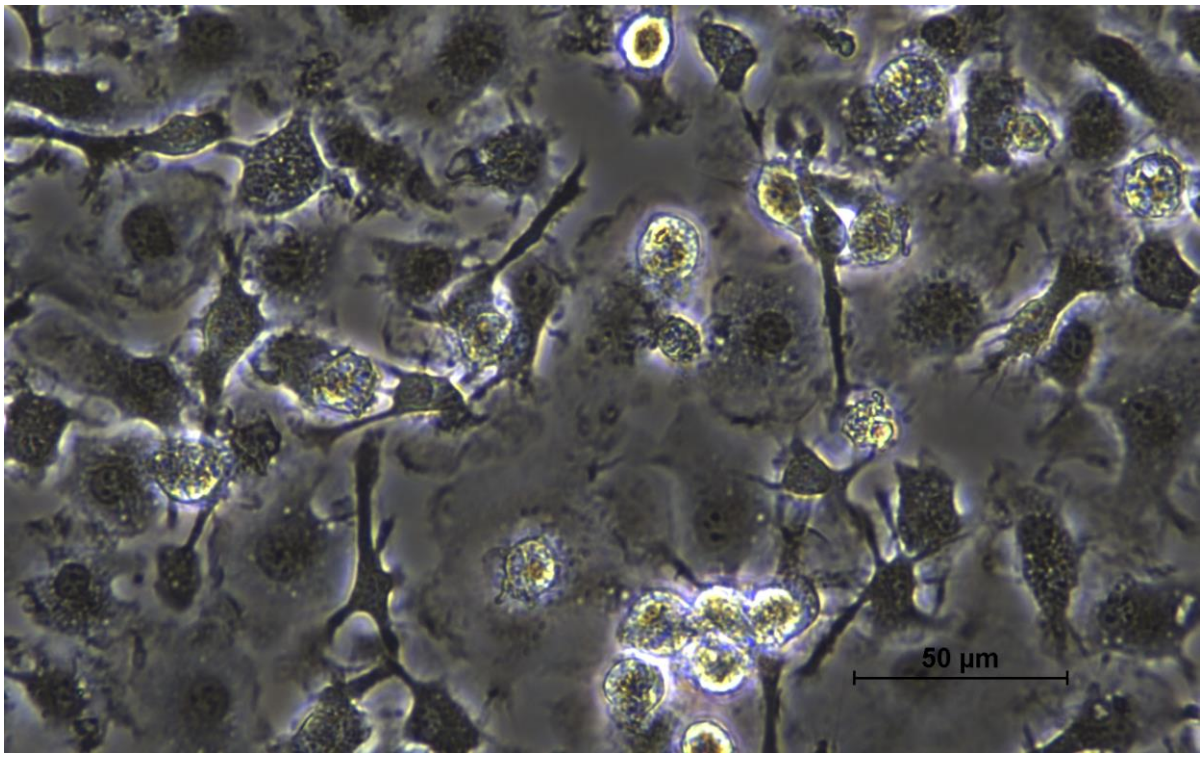


**Figure 195**: Cells observed under microscope on the 9th day of differentiation 24 hours post-activation with ligands; C5 culture dish (0.5 ug/mL LPS, 10% FBS) imaged at 400x magnification

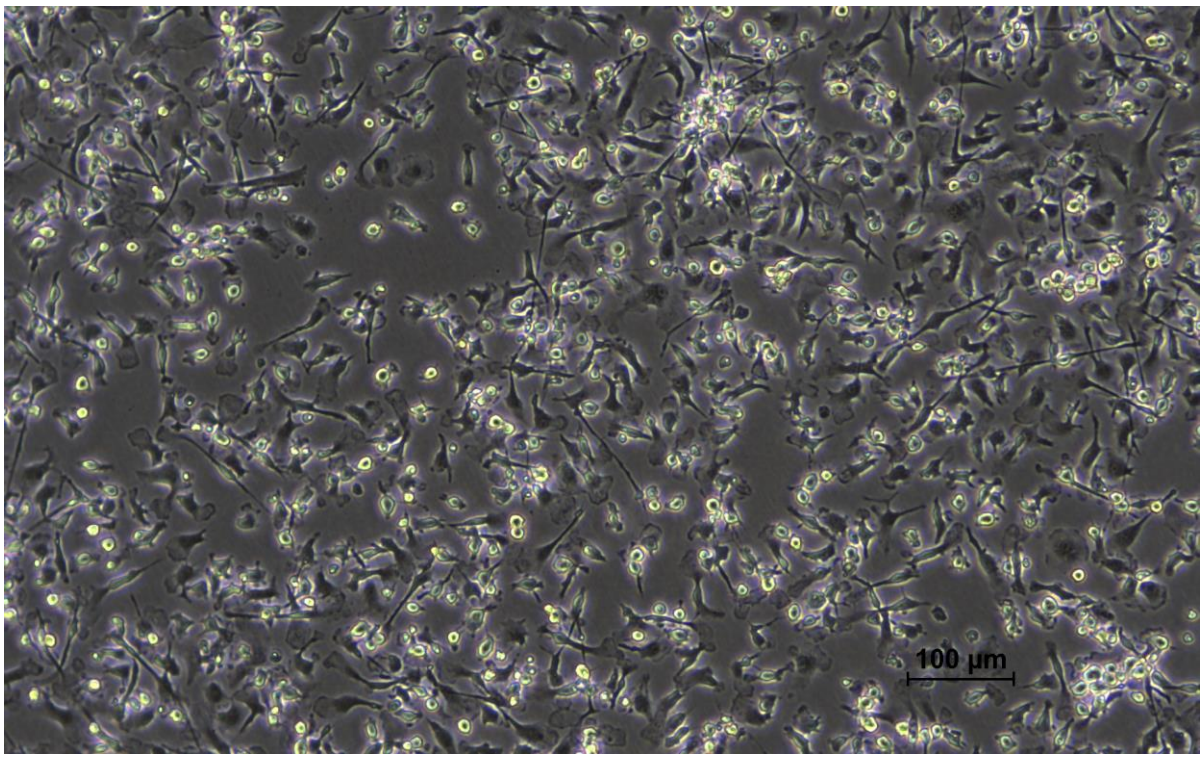


**Figure 196**: Cells observed under microscope on the 9th day of differentiation 24 hours post-activation with ligands; D5 culture dish (0.000022% HCl, 10% FBS) imaged at 100x magnification

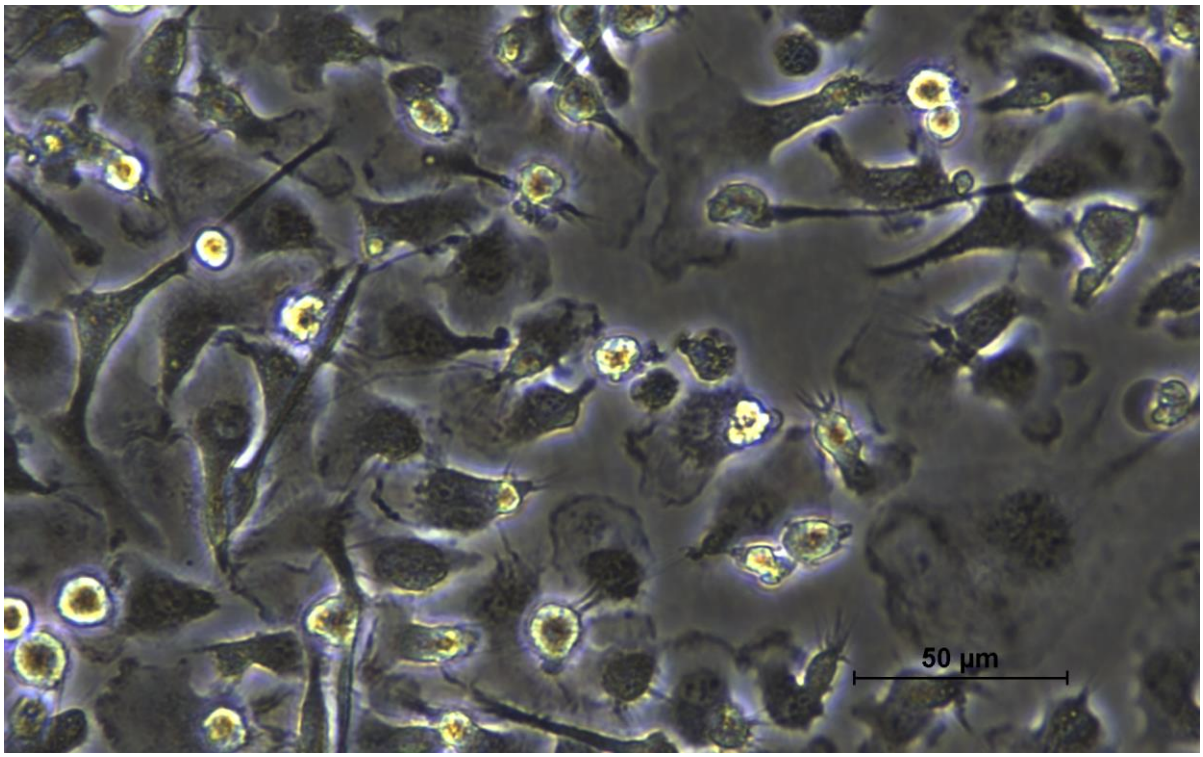


**Figure 197**: Cells observed under microscope on the 9th day of differentiation 24 hours post-activation with ligands; D5 culture dish (0.000022% HCl, 10% FBS) imaged at 400x magnification

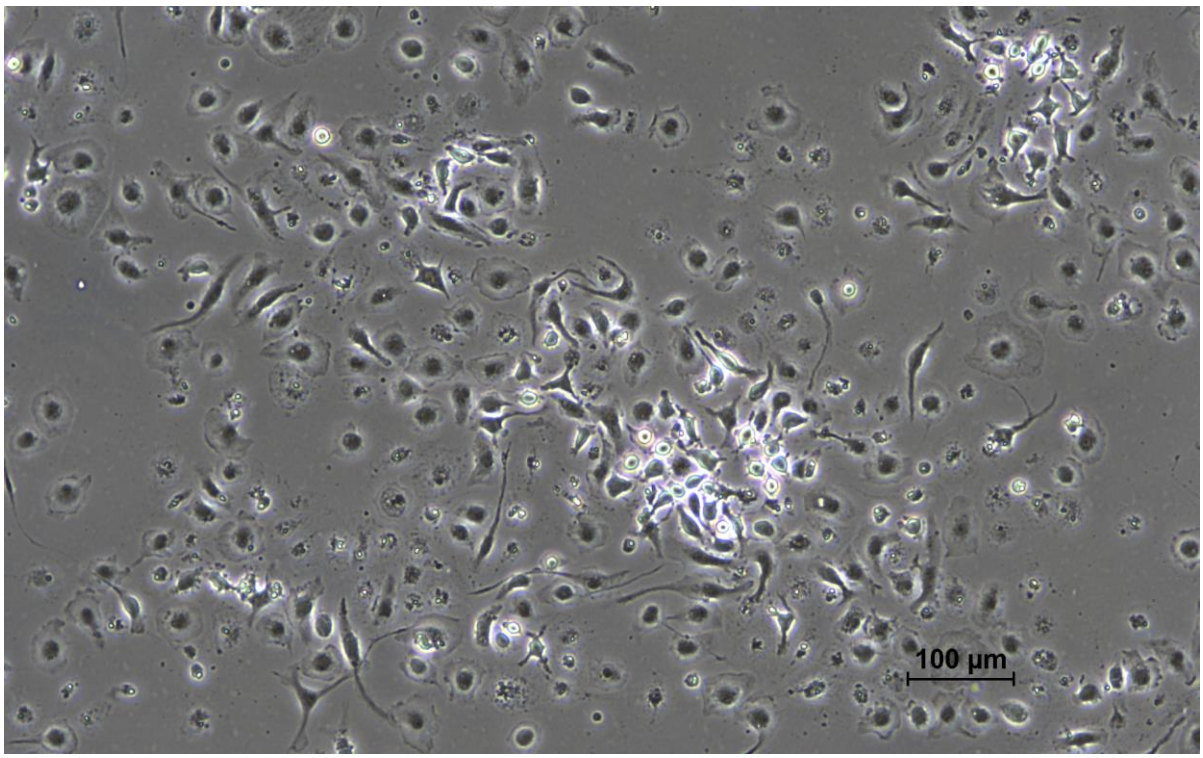


**Figure 198**: Cells observed under microscope on the 9th day of differentiation 24 hours post-activation with ligands; E5 culture dish (1.3 ug/mL SA-401, without FBS) imaged at 100x magnification

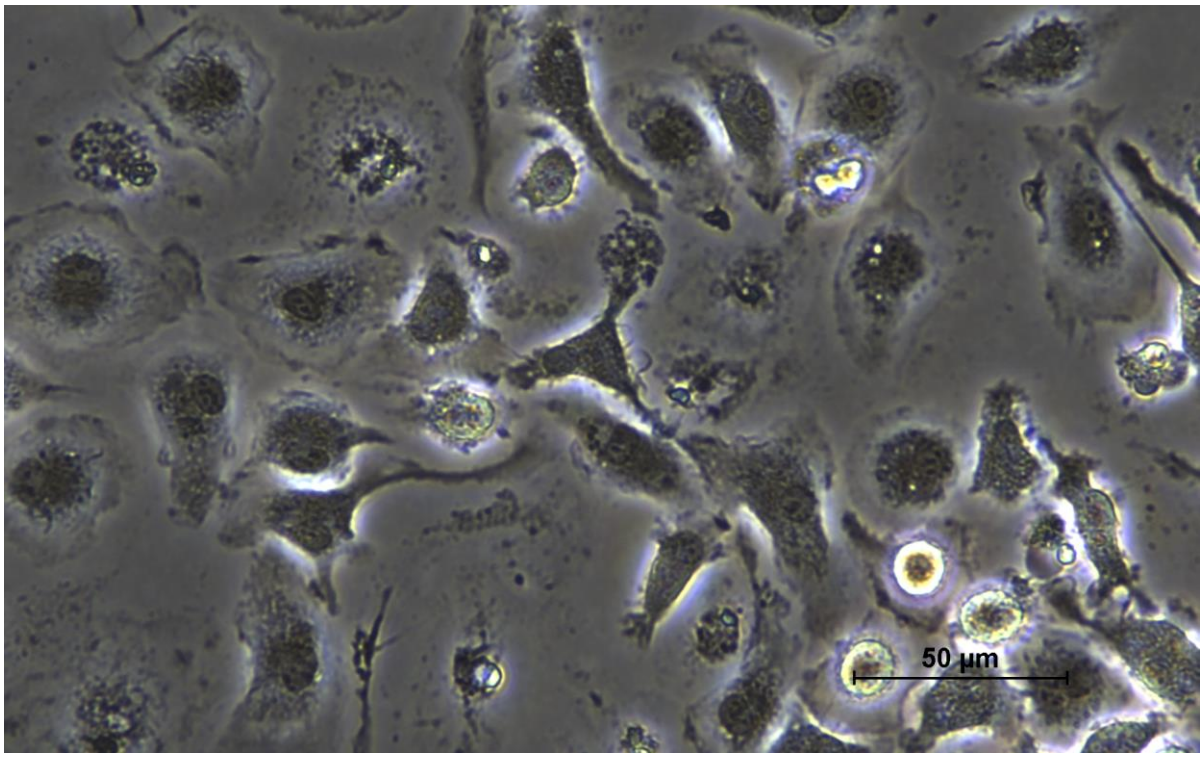


**Figure 199**: Cells observed under microscope on the 9th day of differentiation 24 hours post-activation with ligands; E5 culture dish (1.3 ug/mL SA-401, without FBS) imaged at 400x magnification

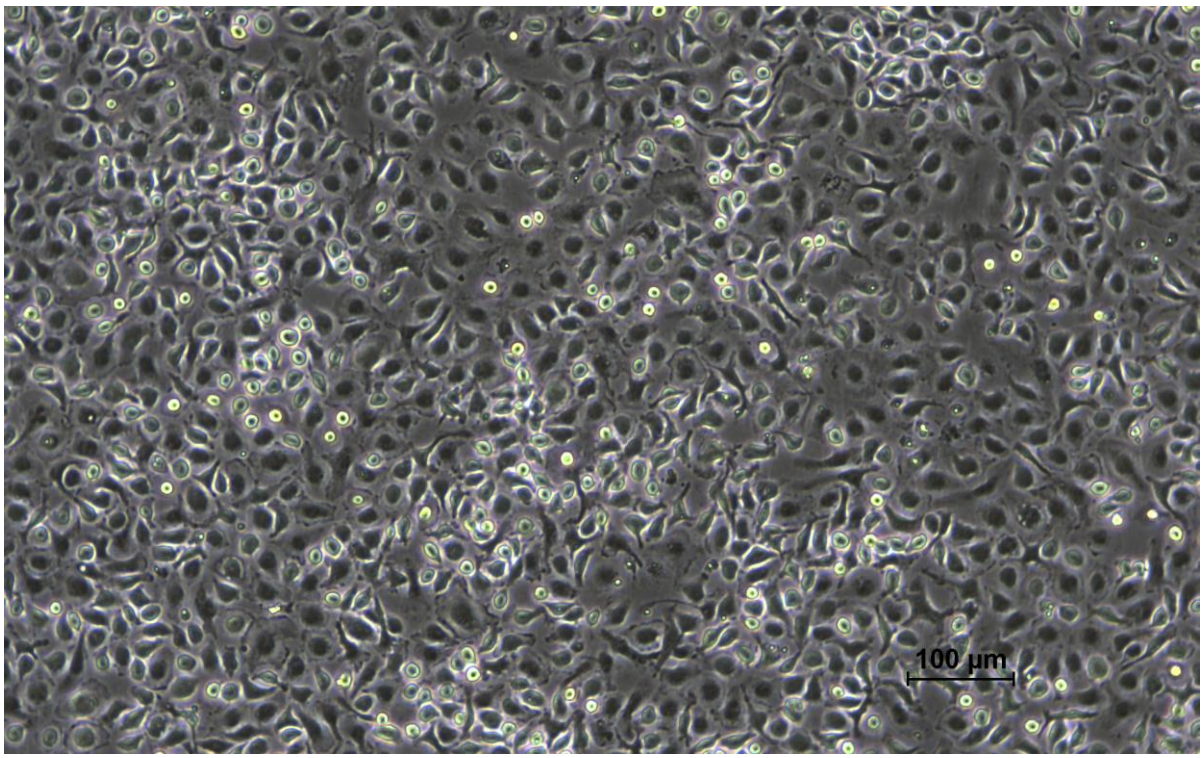


**Figure 200**: Cells observed under microscope on the 9th day of differentiation 24 hours post-activation with ligands; F5 culture dish (1.0 ug/mL R848, without FBS) imaged at 100x magnification

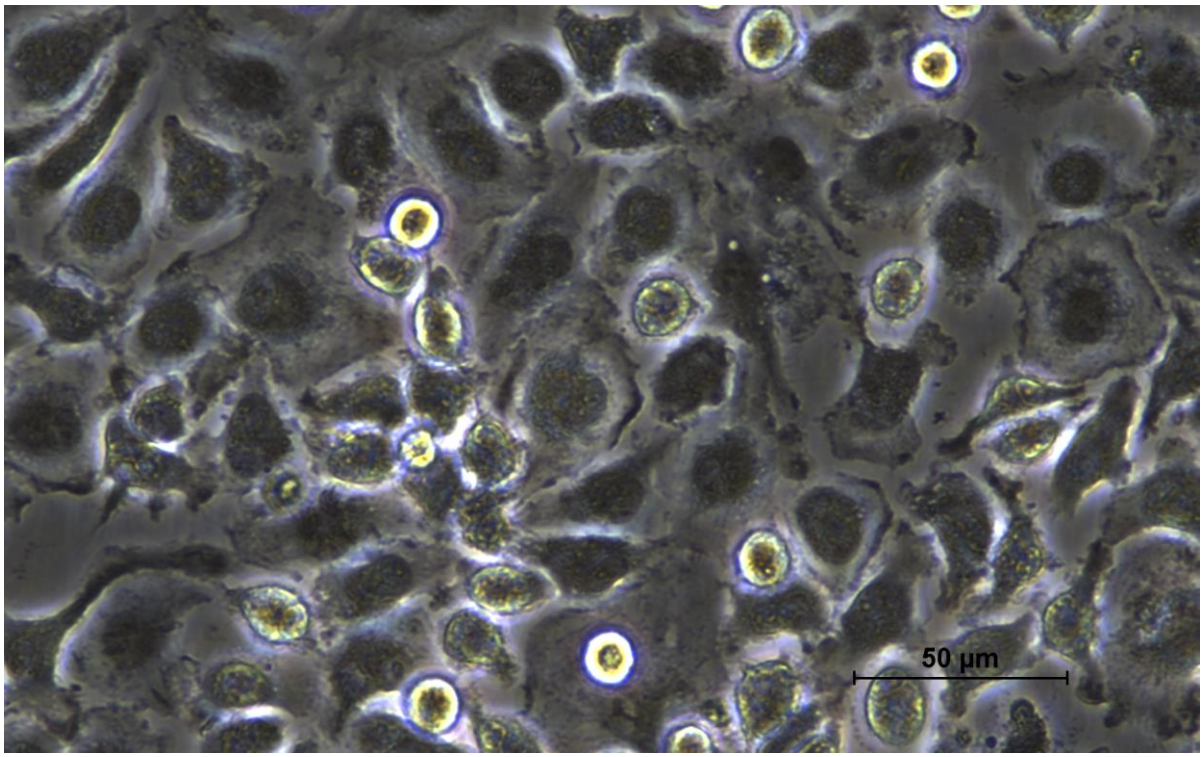


**Figure 201**: Cells observed under microscope on the 9th day of differentiation 24 hours post-activation with ligands; F5 culture dish (1.0 ug/mL R848, without FBS) imaged at 400x magnification

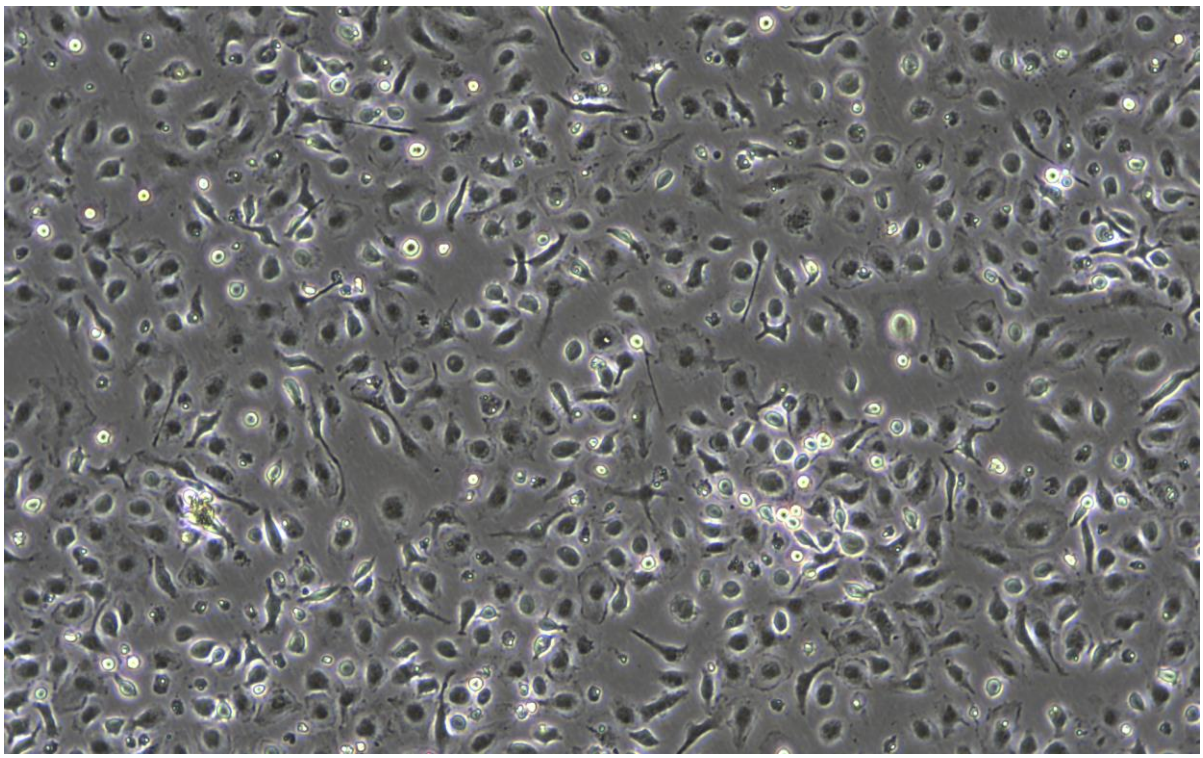

**Figure 202**: Cells observed under microscope on the 9th day of differentiation 24 hours post-activation with ligands; G5 culture dish (0.5 ug/mL LPS, without FBS) imaged at 100x magnification

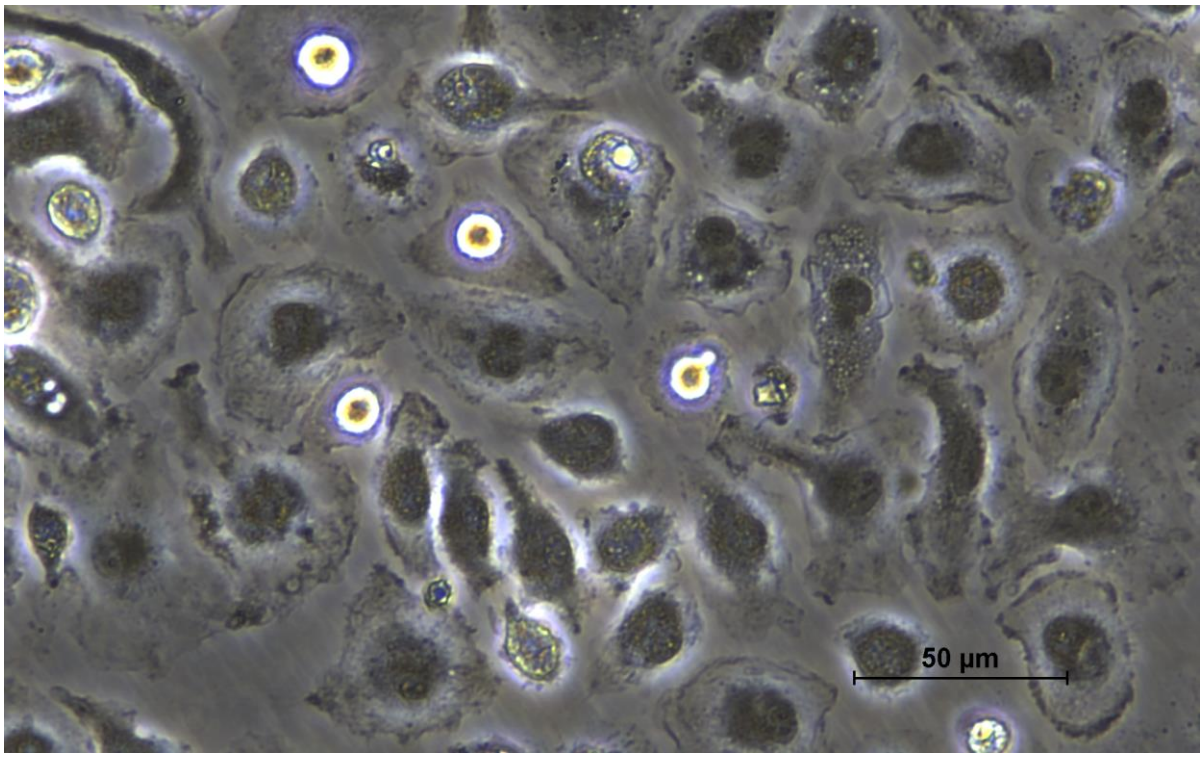


**Figure 203**: Cells observed under microscope on the 9th day of differentiation 24 hours post-activation with ligands; G5 culture dish (0.5 ug/mL LPS, without FBS) imaged at 400x magnification

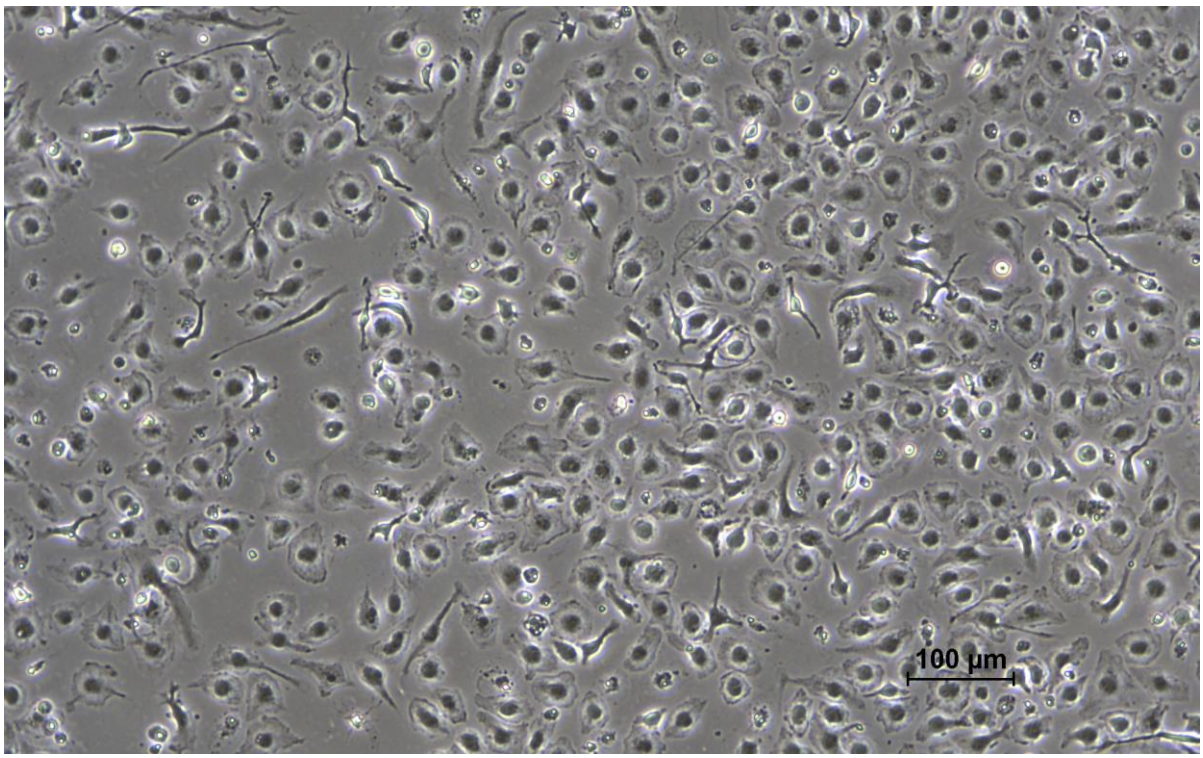


**Figure 204**: Cells observed under microscope on the 9th day of differentiation 24 hours post-activation with ligands; H5 culture dish (0.000022% HCl, without FBS) imaged at 100x magnification

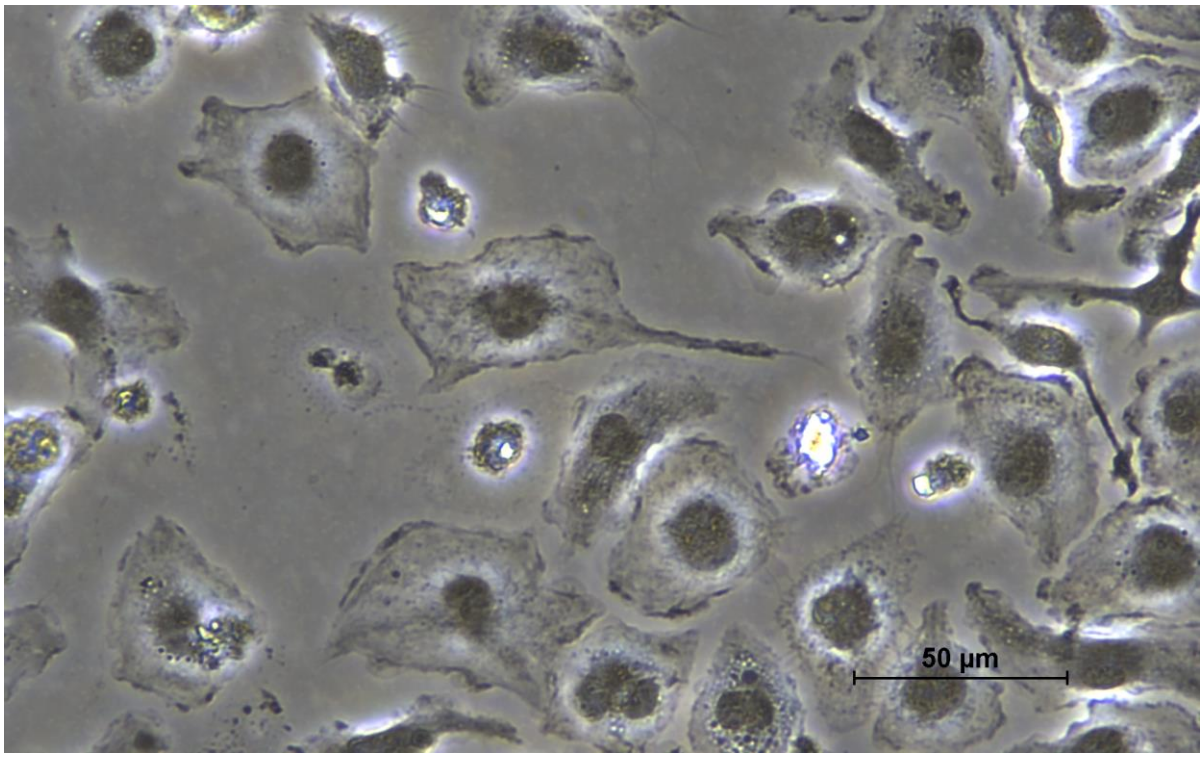


**Figure 205**: Cells observed under microscope on the 9th day of differentiation 24 hours post-activation with ligands; H5 culture dish (0.000022% HCl, without FBS) imaged at 400x magnification

## MD simulation inputs

### Ionizaton of the system (ions.mdp)

```
; LINES STARTING WITH ';' ARE COMMENTS
title           = Minimization     ; Title of run
```

```
; Parameters describing what to do, when to stop and what to save
integrator       = steep       ; Algorithm (steep = steepest descent
minimization)
emtol            = 1000.0      ; Stop minimization when the maximum
force < 10.0 kJ/mol
emstep          = 0.01      ; Energy step size
nsteps           = 50000       ; Maximum number of (minimization)
steps to perform

; Parameters describing how to find the neighbors of each atom and
how to calculate the interactions
nstlist          = 1              ; Frequency to update the neighbor
list and long range forces
cutoff-scheme   = Verlet
ns_type          = grid        ; Method to determine neighbor list
(simple, grid)
rlist            = 1.0         ; Cut-off for making neighbor list
(short range forces)
coulombtype      = cutoff      ; Treatment of long range
electrostatic interactions
rcoulomb         = 1.0         ; long range electrostatic cut-off
rvdw             = 1.0         ; long range Van der Waals cut-off
pbc             = xyz          ; Periodic Boundary Conditions
```

**Energy minimization (em.mdp)**

```
; LINES STARTING WITH ';' ARE COMMENTS
title            = Minimization     ; Title of run

; Parameters describing what to do, when to stop and what to save
integrator       = steep       ; Algorithm (steep = steepest descent
minimization)
emtol            = 1000.0      ; Stop minimization when the maximum
force < 10.0 kJ/mol
emstep          = 0.01      ; Energy step size
nsteps           = 50000       ; Maximum number of (minimization)
steps to perform

; Parameters describing how to find the neighbors of each atom and
how to calculate the interactions
nstlist          = 1                  ; Frequency to update the
neighbor list and long range forces
cutoff-scheme   = Verlet
ns_type          = grid           ; Method to determine neighbor
list (simple, grid)
rlist            = 1.2            ; Cut-off for making neighbor list
(short range forces)
coulombtype      = PME            ; Treatment of long range
electrostatic interactions
rcoulomb         = 1.2            ; long range electrostatic cut-off
vdwtype         = cutoff
```

```
vdw-modifier    = force-switch
rvdw-switch     = 1.0
rvdw             = 1.2            ; long range Van der Waals cut-off
pbc             = xyz            ; Periodic Boundary Conditions
DispCorr        = no
```

**NVT equilibration (nvt.mdp)**

```
title                    = Protein-ligand complex NVT equilibration
; Run parameters
integrator               = md        ; leap-frog integrator
nsteps                   = 50000     ; 2 * 50000 = 100 ps
dt                       = 0.002     ; 2 fs
; Output control
nstenergy                = 500   ; save energies every 1.0 ps
nstlog                   = 500   ; update log file every 1.0 ps
nstxout-compressed       = 500   ; save coordinates every 1.0 ps
; Bond parameters
continuation             = no        ; first dynamics run
constraint_algorithm     = lincs     ; holonomic constraints
constraints              = h-bonds   ; bonds to H are constrained
lincs_iter               = 1         ; accuracy of LINCS
lincs_order              = 4         ; also related to accuracy
; Neighbor searching and vdW
cutoff-scheme            = Verlet
ns_type                  = grid      ; search neighboring grid cells
nstlist                  = 20        ; largely irrelevant with Verlet
rlist                    = 1.2
vdwtype                  = cutoff
vdw-modifier             = force-switch
rvdw-switch              = 1.0
rvdw                     = 1.2       ; short-range van der Waals
cutoff (in nm)
; Electrostatics
coulombtype              = PME       ; Particle Mesh Ewald for long-
range electrostatics
rcoulomb                 = 1.2       ; short-range electrostatic
cutoff (in nm)
pme_order                = 4         ; cubic interpolation
fourierspacing           = 0.16      ; grid spacing for FFT
; Temperature coupling
tcoupl                   = V-rescale                     ; modified
Berendsen thermostat
tc-grps                  = Protein_MOL Water_and_ions    ; two
coupling groups - more accurate
tau_t                    = 0.1   0.1                     ; time
constant, in ps
ref_t                    = 300   300                     ; reference
temperature, one for each group, in K
; Pressure coupling
pcoupl                   = no        ; no pressure coupling in NVT
; Periodic boundary conditions
```

```
pbc                     = xyz       ; 3-D PBC
; Dispersion correction is not used for proteins with the C36
additive FF
DispCorr                = no
; Velocity generation
gen_vel                 = yes       ; assign velocities from Maxwell
distribution
gen_temp                = 300       ; temperature for Maxwell
distribution
gen_seed                = -1        ; generate a random seed
```

**NPT equilibration (npt.mdp)**

```
title                   = Protein-ligand complex NPT equilibration
; Run parameters
integrator              = md        ; leap-frog integrator
nsteps                  = 50000     ; 2 * 50000 = 100 ps
dt                      = 0.002     ; 2 fs
; Output control
nstenergy               = 500       ; save energies every 1.0 ps
nstlog                  = 500       ; update log file every 1.0 ps
nstxout-compressed      = 500       ; save coordinates every 1.0 ps
; Bond parameters
continuation            = yes       ; continuing from NVT
constraint_algorithm    = lincs     ; holonomic constraints
constraints             = h-bonds   ; bonds to H are constrained
lincs_iter              = 1         ; accuracy of LINCS
lincs_order             = 4         ; also related to accuracy
; Neighbor searching and vdW
cutoff-scheme           = Verlet
ns_type                 = grid      ; search neighboring grid cells
nstlist                 = 20        ; largely irrelevant with Verlet
rlist                   = 1.2
vdwtype                 = cutoff
vdw-modifier            = force-switch
rvdw-switch             = 1.0
rvdw                    = 1.2       ; short-range van der Waals
cutoff (in nm)
; Electrostatics
coulombtype             = PME       ; Particle Mesh Ewald for long-
range electrostatics
rcoulomb                = 1.2
pme_order               = 4         ; cubic interpolation
fourierspacing          = 0.16      ; grid spacing for FFT
; Temperature coupling
tcoupl                  = V-rescale                     ; modified
Berendsen thermostat
tc-grps                 = Protein_MOL Water_and_ions    ; two
coupling groups - more accurate
tau_t                   = 0.1   0.1                     ; time
constant, in ps
```

```
ref_t                    = 300   300                    ; reference
temperature, one for each group, in K
; Pressure coupling
pcoupl                   = Berendsen                    ; pressure
coupling is on for NPT
pcoupltype               = isotropic                    ; uniform
scaling of box vectors
tau_p                    = 2.0                          ; time
constant, in ps
ref_p                    = 1.0                          ; reference
pressure, in bar
compressibility          = 4.5e-5                       ; isothermal
compressibility of water, bar^-1
refcoord_scaling         = com
; Periodic boundary conditions
pbc                      = xyz       ; 3-D PBC
; Dispersion correction is not used for proteins with the C36
additive FF
DispCorr                 = no
; Velocity generation
gen_vel                  = no        ; velocity generation off after
NVT
```

**MD production run (md.mdp)**

```
title                    = Protein-ligand complex MD simulation
; Run parameters
integrator               = md        ; leap-frog integrator
nsteps                   = 100000000   ; 2 * 100000000 = 200000000 ps
(200 ns)
dt                       = 0.002     ; 2 fs
; Output control
nstxout          = 0        ; Save coordinates every 20 ps
nstvout          = 0        ; Save velocities every 20 ps
nstenergy        = 1000         ; Save energies every 2 ps
nstlog           = 1000         ; Log every 2 ps
nstxout-compressed = 10000      ; Save compressed trajectory every 20
ps
; Bond parameters
continuation             = yes       ; continuing from NPT
constraint_algorithm     = lincs     ; holonomic constraints
constraints              = h-bonds   ; bonds to H are constrained
lincs_iter               = 1         ; accuracy of LINCS
lincs_order              = 4         ; also related to accuracy
; Neighbor searching and vdW
cutoff-scheme            = Verlet
ns_type                  = grid      ; search neighboring grid cells
nstlist                  = 20        ; largely irrelevant with Verlet
rlist                    = 1.2
vdwtype                  = cutoff
vdw-modifier             = force-switch
rvdw-switch              = 1.0
```

```
rvdw                    = 1.2       ; short-range van der Waals
cutoff (in nm)
; Electrostatics
coulombtype             = PME       ; Particle Mesh Ewald for long-
range electrostatics
rcoulomb                = 1.2
pme_order               = 4         ; cubic interpolation
fourierspacing          = 0.16      ; grid spacing for FFT
; Temperature coupling
tcoupl                  = V-rescale                     ; modified
Berendsen thermostat
tc-grps                 = Protein_MOL Water_and_ions    ; two
coupling groups - more accurate
tau_t                   = 0.1   0.1                     ; time
constant, in ps
ref_t                   = 300   300                     ; reference
temperature, one for each group, in K
; Pressure coupling
pcoupl                  = Parrinello-Rahman             ; pressure
coupling is on for NPT
pcoupltype              = isotropic                     ; uniform
scaling of box vectors
tau_p                   = 2.0                           ; time
constant, in ps
ref_p                   = 1.0                           ; reference
pressure, in bar
compressibility         = 4.5e-5                        ; isothermal
compressibility of water, bar^-1
; Periodic boundary conditions
pbc                     = xyz       ; 3-D PBC
; Dispersion correction is not used for proteins with the C36
additive FF
DispCorr                = no
; Velocity generation
gen_vel                 = no        ; continuing from NPT
equilibration
```